JOURNAL OF APPLIED PHYSICS

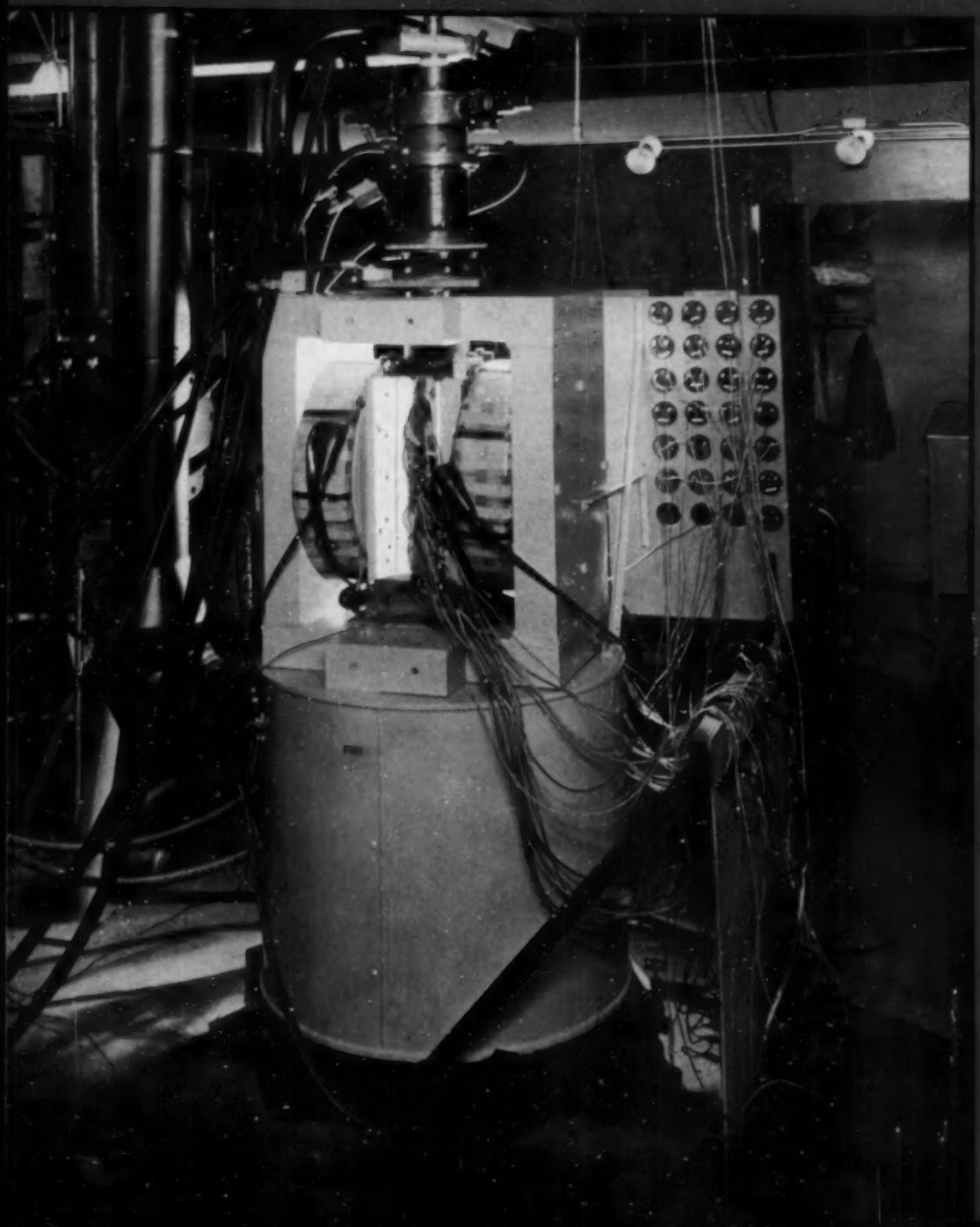

April
1960
Vol. 31 No. 4

Experimental M H D Generator Facility.

See Page 735.

WRITTEN BY THE WIND

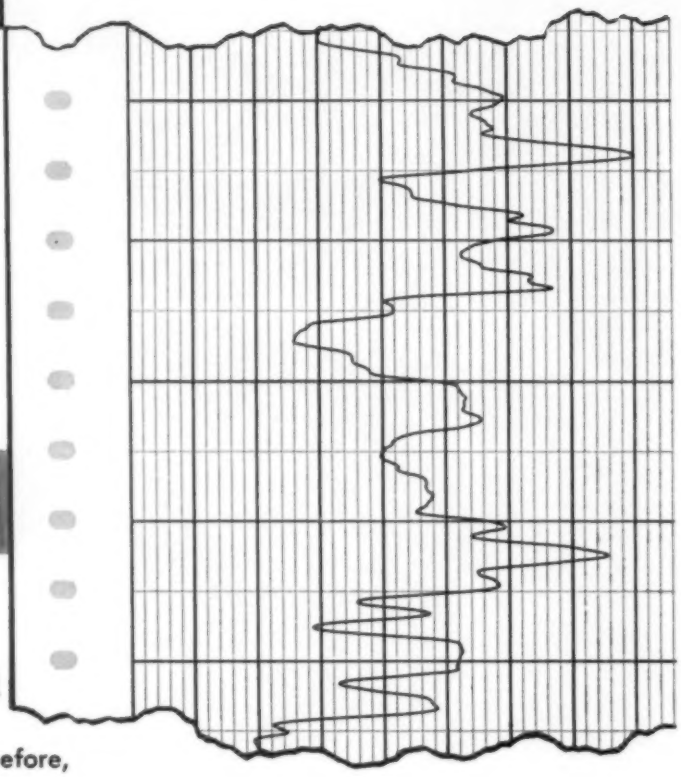

high resolution recording system

Sliced up thinner than ever before, the wind can record itself with a new maximum of resolution in the Beckman & Whitley Type F System. This not only permits a more intimate documentation of the features of the winds, but, even where detailed records are not required, offers many advantages for fixed-station and system-telemetering uses.

Operating from standard 115-volt 60-cps supply, the Type F can be used in portable applications where the increased resolution is needed, by the addition of an accessory battery-operated power supply.

Sample chart illustrated, produced by typical recorder shown, reveals fine, smooth detail recorded where maximum chart width is six miles per hour at a chart speed of 6-in. per min. Translator unit, designed for either bench-top or rack mounting, permits instantaneous switching between the four scales calibrated to maxima of 6, 12, 30, and 60 miles per hour.

For further information write:

Beckman & Whitley INC.

SAN CARLOS 8, CALIFORNIA

JOURNAL OF APPLIED PHYSICS

Vol. 31, No. 4 APRIL, 1960

In This Issue

Lattice Displacements by Fast Electrons . . . . . W. Dale Compton and George W. Arnold 621

X-Ray Examination of Brittle Fractures in Extruded Chromium . . . . . C. W. Weaver and K. A. Gross 626

Dislocation Multiplication in Lithium Fluoride Crystals . . . . . W. G. Johnston and J. J. Gilman 632

Mobility of Hydrogen and Deuterium Positive Ions in their Parent Gases . . . . . D. J. Rose 643

Elastic Constants of Yttrium Single Crystals in the Temperature Range 4.2–400°K . . . . . J. F. Smith and J. A. Gjevre 645

Optical Absorption by Free Carriers in a Semiconductor Containing a Dispersed Colloidal Phase . . . . . B. R. Gossick 648

Correlation between Certain Extinction Bands of Solids and Plasma Resonance . . . . . B. R. Gossick 650

Solutions of the Equations of Space Charge Flow for Radial Flow between Concentric Spherical Electrodes . . . . . I. Itzkan 652

Attenuation of the Shock Wave Produced in a Solid by a Flying Plate . . . . . G. R. Fowles 655

Motion of 180° Domain Walls in Metal Electroded Barium Titanate Crystals as a Function of Electric Field and Sample Thickness . . . . . Robert C. Miller and Albert Savage 662

Formation and Initial Growth of Single-Asperity Solid-State Bonds . . . . . F. C. Holden, J. B. Melehan, H. R. Ogden, and R. I. Jaffee 670

A Dynamic Hard Sphere Model . . . . . D. Turnbull and R. L. Cormia 674

On the Yield and Energy Distribution of Secondary Positive Ions from Metal Surfaces . Henry E. Stanton 678

Origin of the "First-Order Structure" of CP4-Etched Ge Surfaces . G. Bonfiglioli, A. Ferro, and A. Mojoni 684

Behavior of Individual Dislocations in Strain-Hardened LiF Crystals . . J. J. Gilman and W. G. Johnston 687

Piezoresistive Effect in *P*-Type PbTe . . . . . Lewis E. Hollander and T. J. Diesel 692

Molecular Trajectories in Electric Fields and State Selection in a Beam of Sodium Chloride . . . . . M. Peter, H. G. R. Venkates, and M. W. P. Strandberg 693

Polyhedral Holes in Evaporated AuCu Films . . . . . Victor A. Phillips 697

Analysis of Composite X-Ray Diffraction Profiles . . . . . J. J. Slade, Jr., and L. F. Nanni 699

Precipitation in Silicon Crystals Containing Aluminum . . . . . R. Bullough, R. C. Newman, J. Wakefield, and J. B. Willis 707

Production and Demonstration of Atomically Clean Metal Surfaces . . . H. D. Hagstrum and C. D'Amico 715

Efficiency of the Plasma Thermocouple . . . . . H. W. Lewis and J. R. Reitz 723

Effect of Viscosity on the Splash Caused by a Drop of Water Falling into a Mixture of Glycerol and Water . . . . . A. G. Davis Philip 727

Temperature-Dependence of the Electrical Resistivity of bcc Cr-Fe Alloys . . . . . N. S. Rajan, R. M. Waterstrat, and Paul A. Beck 731

Letters to the Editor:

Heating in Liquid Helium Resulting from Neutron and Gamma Bombardment by a Fission Source . . . . . M. G. Chasanov 733

Gamma-Ray Induced Conductivity in Polyethylene Coaxial Cable . . . Kichinosuke Yahagi and Akibumi Danno 734

Microwave Noise from Low-Pressure Arcs . . . . . R. M. Hill and S. K. Ichiki 735

Experimental Magnetohydrodynamic Power Generator . . . . . Richard J. Rosa 735

Improvements on the Pedestal Method of Growing Silicon and Germanium Crystals . . . . . W. C. Dash 736

Method for Determining the Thermal Conductivity of Incandescent Solids . . B. B. Brenden and H. W. Newkirk 737

Generation of Dislocations by an Electric Field in MgO . . . . . E. Mendel and S. Weinig 738

Total Electromagnetic Cross Sections of Imperfectly Conducting Cylinders . . . . E. S. Cassedy and J. Fainberg 739

Spontaneous Emission from an Inverted Spin System . . . . . Amnon Yariv 740

Backscattering of Carbon-14 Beta Radiation . . . . . George L. Gaines, Jr. 741

CW Millimeter Wave Maser Using Fe^{3+} in TiO_2 . . . . . S. Foner and L. R. Momo 742

Dislocation Etch Pits on the {111} and {$\bar{1}\bar{1}\bar{1}$} Surfaces of InSb . . . . . Harry C. Gatos and Mary C. Lavine 743

Monte Carlo Calculations of the Motions of Electrons in Helium . . . . . T. Itoh and T. Musha 744

Transistor with Base Containing a Dispersed Colloidal Phase . . . . . B. R. Gossick 745

Books Reviewed 746

Announcements 746

JOURNAL OF APPLIED PHYSICS

A journal of general physics and its applications to other sciences and to industry

Published by the

American Institute of Physics

GOVERNING BOARD

Ralph A. Sawyer, *Chairman*

Walter S. Baird
J. G. Baker
Jesse W. Beams
R. H. Bolt
Harvey Brooks
J. W. Buchta
J. H. Dillon
Vernet E. Eaton
Herbert A. Erf
S. A. Goudsmit
W. W. Havens, Jr.
Winston E. Kock
R. Bruce Lindsay
Walter C. Michels
C. J. Overbeck
G. E. Pake
Joseph B. Platt
John Strong
George E. Uhlenbeck
V. F. Weisskopf

ADMINISTRATION

Elmer Hutchisson
Director

Henry A. Barton
Associate Director

Wallace Waterfall
Secretary and Treasurer

Ruth F. Bryans
Publication Manager

W. C. Kelly
Director of Education Projects

Eugene H. Kone
Director of Public Relations

Alice Mastropietro
Circulation Manager

Kathryn Setze
Assistant Treasurer

Edward Tober
Manager, Production and Distribution

Theodore Vorburger
Advertising Manager

Emily Wolf
Office Manager

Editor
James A. Krumhansl

Assistant Editor
Ethel McMillan

Editorial Board

J. H. Crawford
Arthur Kantrowitz
A. F. Kip
J. E. Goldman
J. L. Tuck
C. A. Wert
Herman A. Haus
C. Lester Hogan
R. S. Rivlin

THE JOURNAL OF APPLIED PHYSICS is devoted to general physics and its applications to other sciences, to engineering, and to industry. Previous to 1937, this journal was called PHYSICS.

The JOURNAL OF APPLIED PHYSICS welcomes articles of two distinct kinds: (1) Descriptions of new results in experimental or theoretical physics which are of general interest to physicists. The author should explain his contribution in such a way that a physicist or engineer in another field of specialization can appreciate its objectives and essential features. (2) Critical reviews of particular areas of physics or surveys of extensive investigations at a single laboratory. Authors contemplating writing such should correspond with the Editor before they begin writing.

The JOURNAL OF APPLIED PHYSICS welcomes letters to the editor which describe in a few words the content of laboratory reports and theses and which tell readers how they may obtain copies of such reports.

Manuscripts should be submitted to the Editor, James A. Krumhansl, Rockefeller Hall, Cornell University, Ithaca, New York. Authors should read the "Information for Contributors," facing page 1 of the January issue, before writing articles or letters. The *Style Manual* of the American Institute of Physics is also helpful to writers preparing manuscripts for journals published by the American Institute of Physics. It can be obtained for $1.00 from the American Institute of Physics, 335 East 45 Street, New York 17, New York.

Corrected proofs and all correspondence concerning papers in the process of publication should be addressed to the Publication Manager, American Institute of Physics, 335 East 45 Street, New York 17, New York.

Subscriptions, renewals, and orders for back numbers should be addressed to the American Institute of Physics, 335 East 45 Street, New York 17, New York.

Subscription Price	**U.S. and Canada**	**Elsewhere**
To members of member organizations of the American Institute of Physics and Affiliated Societies ..	$12.00	$13.00
To all others	14.00	16.00

Back Number Prices

Yearly back number rate when complete year is available: $17.00.
Single copies: $1.75 each (exception: March, 1958—$3.00 each).

Changes of address should be sent to the American Institute of Physics.

Advertising rates supplied on request. Orders, advertising copy, and cuts should be sent to the American Institute of Physics.

Second-class postage paid at Lancaster, Pa.

For the ultimate in —

RELIABILITY
REPEATABILITY
SUPERIOR PERFORMANCE

Specify —

"MAG MOD"®

MAGNETIC MODULATORS

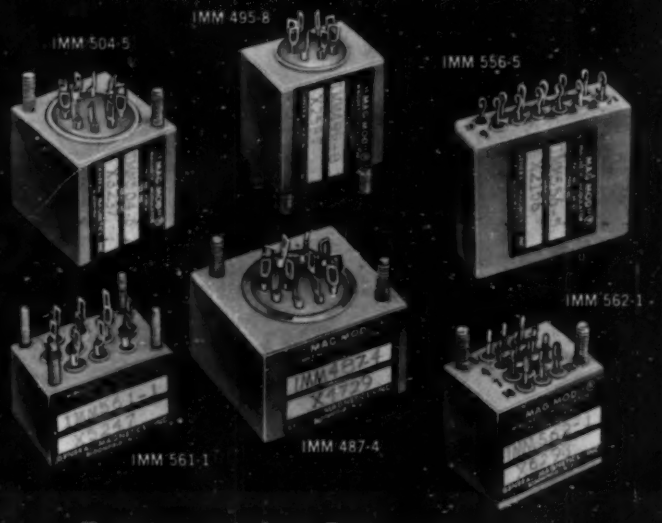

Designed for Subminiature
Circuit Assemblies and Printed Circuit Card Configurations

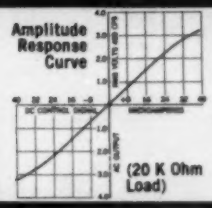

Input Magnetic Modulator
Type No. IMM 487-4

Subminiature "MAG MOD"® featuring high input signal sensitivity and high AC output impedance. Male or female mounting.

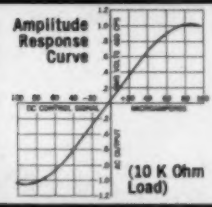

Input Magnetic Modulator
Type No. IMM 495-8

Subminiature "MAG MOD"® featuring wide band width, multiple signal input circuits, extreme zero stability from −65°C to +135°C, low null amplitude or noise level. Mounting available male or female.

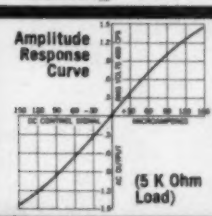

Input Magnetic Modulator
Type No. IMM 504-5

Subminiature "MAG MOD"® featuring low input and output impedance, resistance vs. temperature compensated input, extreme zero stability, repeatability and insignificant hysteresis. Supplied with male or female mounting.

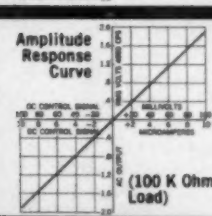

Input Magnetic Modulator
Type No. IMM 562-1

Subminiature "MAG MOD"® featuring 4 KC carrier operation, wide frequency band width, high output impedance and voltage range. Mounting male or female.

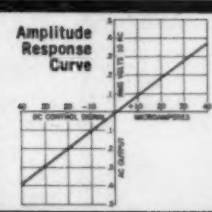

Input Magnetic Modulator
Type No. IMM 561-1

Subminiature "MAG MOD"® featuring low carrier energy level operation, very wide frequency band width, wide output operating range, minimum size and weight. Mounting male or female. May be mounted directly on printed circuit boards.

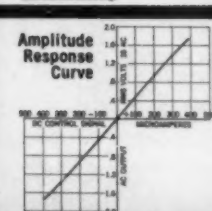

Input Magnetic Modulator
Type No. IMM 556-5

Subminiature "MAG MOD"® featuring high frequency carrier operation (35 KC), flat construction for printed circuit mounting, low output impedance and clean output fundamental frequency wave form. Mounting supplied male or female.

New miniature designs of these reliable "MAG MODS"® make them ideal for incorporation into transistorized printed circuit assemblies. There is no sacrifice of dynamic response. They offer the engineer/designer the solution to problems involved in a wide range of data systems where analog circuit operations are encountered. To insure complete flexibility, the mechanical mounting on any "MAG MOD" may be modified to conform to your particular packaging requirements.

- 1% repeatability throughout entire service life
- Negligible hysteresis
- Faster response time
- Extreme stability over a wide temperature range
- Infinite service life
- Extremely lightweight — compact design

GENERAL MAGNETICS • INC
135 BLOOMFIELD AVENUE, BLOOMFIELD, NEW JERSEY, U. S. A.

GM INC.

See reverse side for specifications

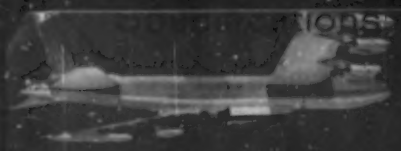

"MAG MOD" miniaturized MAGNETIC MODULATORS

TYPE NUMBER	IMM 487-4	IMM 495-8	IMM 504-5	IMM 562-1	IMM 561-1	IMM 556-5
Excitation Carrier Voltage and Frequency	115 V @ 400 cps	115 V @ 400 cps	115 V @ 400 cps	2.5 V RMS @ 4 KC	1.0 V RMS @ 10 KC	6 to 10 V RMS @ 35 KC
Control Signal Winding DC Resistance	Winding No. 1 6200 ohms Winding No. 2 7400 ohms	Signal Winding No. 1 550 ohms Signal Winding No. 2 600 ohms	1000 ohms	Signal Winding 1300 ohms Feedback Winding 160 ohms	200 ohms	5000 ohms
Input Control Signal Range	0 to ±40 μa Each Winding	0 to +100 μa (Both Sig. Windings in Series)	0 to ±100 μa	0 to ± 100 μa 0 to ± 1 V Bipolar	0 to ±400 μa	0 to ±400 μa
Amplitude Modulated AC Output Range	3 V RMS @ 400 cps Phase Reversing	0 to 1 V RMS @ 400 cps Phase Reversing	0 to 1.5 V RMS @ 400 cups Phase Reversing	0 to 6 V RMS @ 4000 cps Phase Reversing	0 to 3 V RMS @ 4 KC Phase Reversing	0 to 1.0 V RMS @ 35 KC Phase Reversing
Differential Gain RMS mv AC Out/μa Signal In	100 mv/μa	15 mv/μa	10 mv/μa	200 mv/μa	10 mv/μa	4.2 mv/μa
Null Amplitude (Noise Level) mv RMS	25 mv RMS Maximum	5 mv RMS Maximum	10 mv RMS Maximum	30 mv RMS Maximum	10 mv RMS Maximum	20 mv RMS Maximum
Output Impedance	Approx. 30 K ohms	1000 ohms	1000 ohms	Approx. 70 K ohms	Approx. 40 K ohms	900 ohms Each Output Wind.
External Load (Suggested)	Approx. 20 K ohms	Approx. 10 K ohms	Approx. 5 K ohms	Approx. 100 K ohms	Approx. 100 K ohms	1000 ohms Each Output Wind.
Null Drift (In terms of Input Signal) −65°C to +135°C	Less than ±0.25 μa Over Temp. Range	Less than ±0.25 μa Over Temp. Range	±1 μa Maximum Over Temp. Range	±0.5 μa Maximum Over Temp. Range	±1 μa Over Temp. Range	±2 μa Over Temp. Range
Hysteresis (% of Input Control Signal)	0.5% Maximum	0.5% Maximum	0.5% Maximum	Approx. 0.5%	0.5% Maximum	0.5% Maximum
% Harmonic Distortion in Output AC Modulated Envelope	Approx. 40% (3rd Harmonic)	Approx. 25% (3rd Harmonic)	Approx. 30% (3rd Harmonic)	Approx. 15% (3rd Harmonic)	Less Than 10% (3rd Harmonic)	Approx. 5% (3rd Harmonic)
Overall Dimensions (In Inches)	1¼ x 1½ x ⅝	⅝ x 1 x 1	1 x 1 x 1	1 x 11/16 x ⅞	11/16 x 1 x ⅝	7/16 x 1⅜ x 1⅛
Type of Mounting	4-40 Studs or Inserts	4-40 Studs or Inserts	4-40 Studs or Inserts	4-40 Studs or Inserts	2-56 Studs	4-40 Tapped Holes or Studs
Weight in Ounces	Approx. 1.25	Approx. 1	Approx. 1.1	0.75	0.6	1
Response Time (Band Width cps)	0.01 sec. for 15 K Sig. Source Imp. (12 cps Corner Frequency)	20 cps for 10 K Sig. Source Imp. 25 cps for 20 K Sig. Source Imp. (Both Sig. Windings in Series)	5 cps for 1 K Sig. Source Imp. 10 cps for 5 K Sig. Source Imp. 20 cps for 10 K Sig. Source Imp.	70 cps for 10 K Sig. Source Imp. (Time Constant Approx. 2 Milli-Seconds)	Corner Frequency 2 KC for Sig. Source Imp. of Approx. 6 K ohms	Corner Frequency 200 cps for 600 ohm Signal Source Imp. or 1000 cps for 5 K Source

Magnetic Multiplying Modulator Model MCM 515-1

The MAGNETIC MULTIPLIER is a miniaturized magnetic modulator specifically designed to deliver an analog output voltage which is the continuous product of two variable input voltages. One of these is an excitation voltage which varies over a pre-determined range; in this case, 0 to 1 VRMS 400 cycles per second. The other signal is a DC current which varies between 0 and ±400 μa. The output voltage is 400 cycles AC, and is always in phase or 180° out of phase with the variable excitation or fixed reference, i.e., in phase when the variable amplitude DC signal is positive, and 180° out of phase when the DC signal is negative. The general schematic is illustrated in Fig. 1. The relationship between variable alternating supply signal voltage E_B, variable direct current control signal E_C, and the alternating load voltage E_L having a sinusoidal wave shape is denoted by the equation—

$E_L = \text{Constant} \times E_B \times E_C$.

Figure 1

This expression, which defines the fundamental principle of the four quadrant MAGNETIC MULTIPLYING MODULATOR, can be clearly illustrated by linear transfer response curve families as shown at right, in Figure 2-A and Figure 2-B.

Illustrating:

(1) Load voltage E_L as a function of alternating supply signal voltage E_B with control DC signal voltage E_C as a parameter.

(2) Load voltage E_L as a function of control DC signal voltage E_C with alternating supply voltage, E_B as a parameter.

With linearity response curves held to within approximately 1 to 2% of theoretical straight lines, the product accuracy of the fundamental equation will be within 2 to 5% of the theoretical product.

SPECIFICATIONS MODEL MCM 515-1	
Variable Excitation Carrier Voltage and Frequency	Variable AC Signal 0 to 1 V RMS 400 cps
Control Signal Winding DC Resistance	DC Signal Winding Resistance 2650 ohms
Input Control Signal Range	Variable DC Signal 0 to ±400 μa
Amplitude Modulated AC Output Range	0 to 0.9 V RMS @ 400 cps Phase Reversing
Null Amplitude (Noise Level) mv RMS at Max. AC Excitation	5 mv RMS
Output Impedance	Approx. 3500 ohms
External Load (Suggested)	Approx. 25 K ohms
Null Drift (In terms of Input Signal) −65°C to +135°C	±2 μa over Temperature Range
Hysteresis (% of Input Control Signal)	0.5% Maximum
% Harmonic Distortion in Output AC Modulated Envelope	Less than 5%
Overall Dimensions (In Inches)	27/32 x 27/32 x 1 3/16
Type of Mounting	4-40 Insert or Stud
Weight	Approx. 1 Ounce

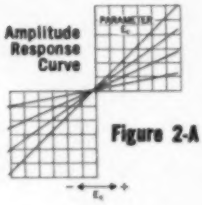

Figure 2-A

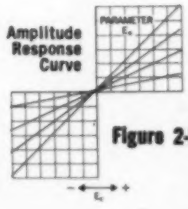

Figure 2-B

Typical "Mag Mod"® Applications—Circuit applications for MAGNETIC MODULATORS include algebraic addition, subtraction, multiplying, raising to a power, controlling amplifier gain, mechanical chopper replacement in DC to fundamental frequency conversion, filtering and low signal level amplification.

Consult General Magnetics—For magnetic amplifier components of proven reliability. These dependable instruments are widely employed in automatic flight systems, fire control, analog computers, guided missiles, nuclear equipment, antennas, gun turrets, commercial power amplifiers and complete control systems. Miniature, subminiature, standard and customized types available.

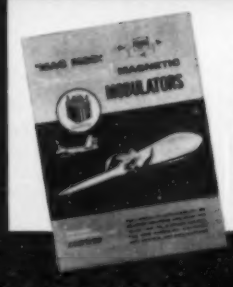

Call or write for new Brochure 102 on "MAG MOD" Miniaturized Magnetic Modulators and Magnetic Multiplying Modulators. Please address inquiries on company letterhead.

GENERAL MAGNETICS • INC
135 BLOOMFIELD AVENUE, BLOOMFIELD, NEW JERSEY, U.S.A.

THE IDEA THAT GREW FOR 100 YEARS

At Bell Laboratories, M. Uenohara (left) adjusts his reactance amplifier, assisted by A. E. Bakanowski. Extremely low "noise" is achieved when certain diodes are cooled in liquid nitrogen.

This is the first practical diode for amplifier as developed by A. E. Bakanowski and A. Uhlir.

How basic scientific ideas develop in the light of expanding knowledge is strikingly illustrated by the development of Bell Laboratories' new "parametric" or "reactance" amplifier.

Over 100 years ago, scientists experimenting with vibrating strings observed that vibrations could be amplified by giving them a push at strategic moments, using properly synchronized tuning forks. This is done in much the same way a child on a swing "pumps" in new energy by shifting his center of gravity in step with his motion.

At the turn of the century, scientists theorized that *electrical* vibrations, too, could be amplified by synchronously varying the *reactance* of a capacitor. Later amplifiers were made to work on this principle but none at microwave frequencies.

Then came the middle 50's. Bell Telephone Laboratories scientists, by applying their new transistor technology, developed semiconductor diodes of greatly improved capabilities. They determined theoretically *how* the electrical capacitance of these new diodes could be utilized to amplify at *microwave* frequencies. They created a new microwave amplifier with far less "noise" than conventional amplifiers.

The new reactance amplifier has a busy future in the battle with "noise." At present, it is being developed for applications in tropospheric transmission and radar. But it has many other possible applications. It can be used, for instance, in the reception of signals reflected from satellites. It is still another example of the continuing efforts to improve your Bell System communications.

BELL TELEPHONE LABORATORIES

WORLD CENTER OF COMMUNICATIONS RESEARCH AND DEVELOPMENT

TRANSISTOR MEN

Your future advancement lies in Delco Radio's Semiconductor Program in the fields of germanium and silicon transistors, silicon rectifiers, and solar cells.

In expanding its semiconductor line, Delco Radio offers unusual opportunities in research engineering and production. We are vitally interested in hiring men with experience in the following areas:

- **SEMICONDUCTOR DEVICE DEVELOPMENT**

  We need men with experience in the techniques of semiconductor device development including alloying and diffusion.

  We need a man with experience in the chemistry of semiconductor devices.

  We need a man with experience in semiconductor materials to lead a program on metallurgical research of new semiconductor materials.

  We need a man with experience in semiconductor device encapsulation.

- **PROCESS ENGINEERING**

  We need several men for production set-up and trouble shooting.

- **EQUIPMENT DEVELOPMENT**

  We need men to develop automatic and semi-automatic fabrication equipment.

PROGRESS=OPPORTUNITIES

Delco Radio has long been the World Leader in the production of auto radios and is becoming a leader in the semiconductor field. The semiconductor applications which we see are staggering. We're anxious to get more experienced personnel, and responsible positions are open to those who qualify.

GM
DELCO RADIO

If you're interested in becoming a member of our GM team, send your resume today to the attention of Mr. Carl Longshore, Supervisor Salaried Employment.

DELCO RADIO DIVISION OF GENERAL MOTORS
KOKOMO, INDIANA

X-RAY DIFFRACTION AND SPECTROSCOPY EQUIPMENT

ANOTHER WAY RCA SERVES INDUSTRY ... THROUGH ELECTRONICS

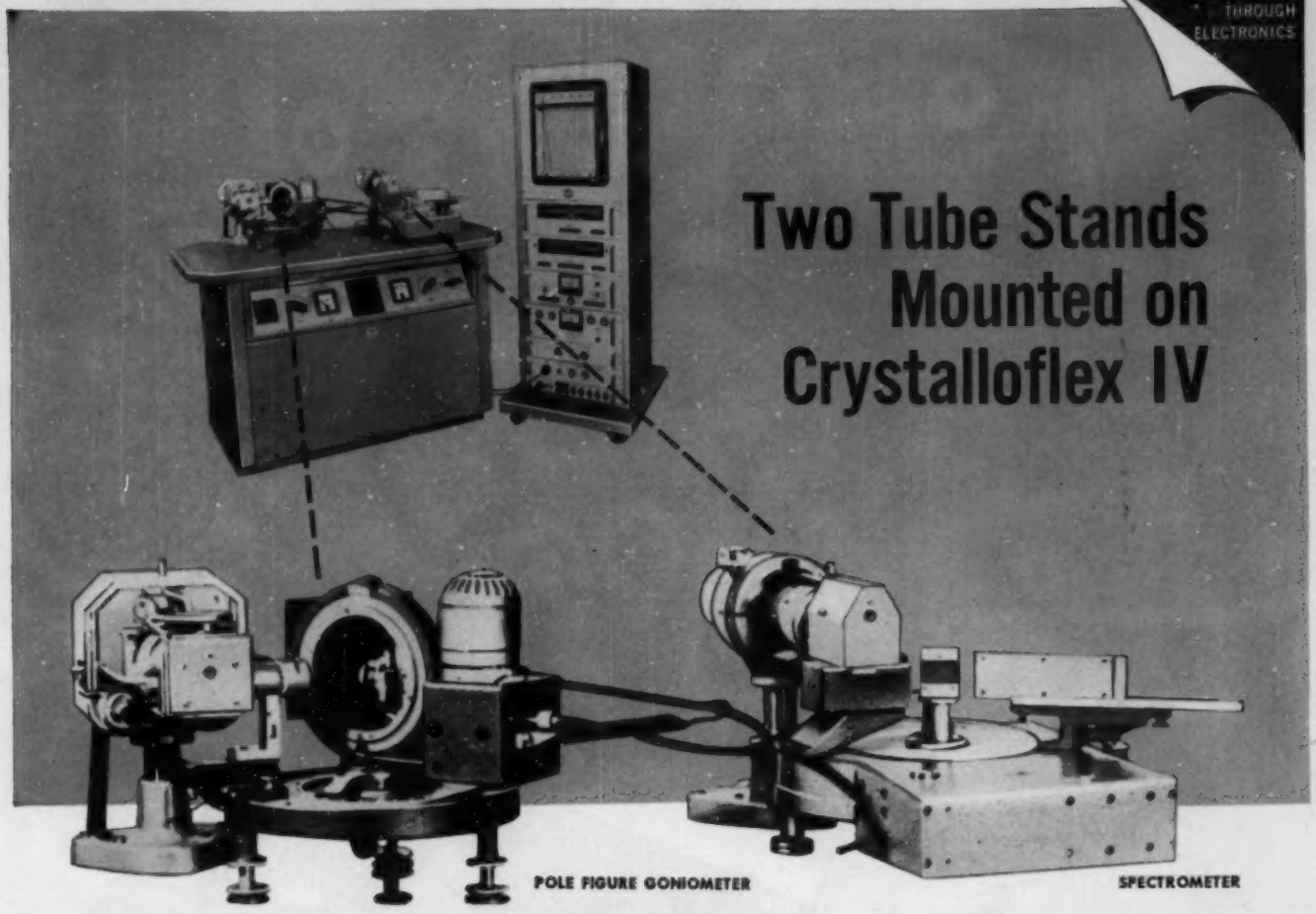

Fast change-over without realignment!

With two tube stands mounted at once on the RCA Generator, you're ready for either x-ray diffraction or spectroscopy. Change-over is made by merely moving the cable connection from one stand to the other. It saves time in set-up and alignment . . . in switching from spectroscopy to diffraction or vice-versa.

Conveniences such as this, as well as unusual flexibility and fine craftsmanship, are making this RCA equipment one of today's most frequently specified lines. Installations have already been made in a number of the nation's foremost research laboratories where these instruments are demonstrating their efficiency and versatility.

A Vacuum Spectrometer for analysis of elements with atomic numbers below 22 is but one of a wide range of attachments and accessories available. For spectrochemical analysis, the regulated and filtered DC power supply will prove invaluable. Also contributing to the unequalled adaptability of this equipment is the compact electronic circuit panel complete with built-in pulse height analyzer and convenient plug-in components.

As a basic facility for x-ray diffraction film studies, RCA offers a Table Model Generator, complete with an assortment of cameras *at a cost of less than $4000.00.*

RCA also offers the EMU-3 Electron Microscope—the most widely used instrument of its kind—providing direct electron image magnification to 200,000X.

Service and installation supervision on all RCA Scientific Instruments are available everywhere through the offices of the RCA Service Company, Inc.

For further information, write to Radio Corporation of America, Dept. E-65, Building 15-1, Camden, N.J. In Canada: RCA VICTOR Company Limited, Montreal.

RCA Tmk(s)®

RADIO CORPORATION of AMERICA

SCIENTIFIC INSTRUMENTS ■ CAMDEN, NEW JERSEY

EXPANDING THE FRONTIERS OF SPACE TECHNOLOGY

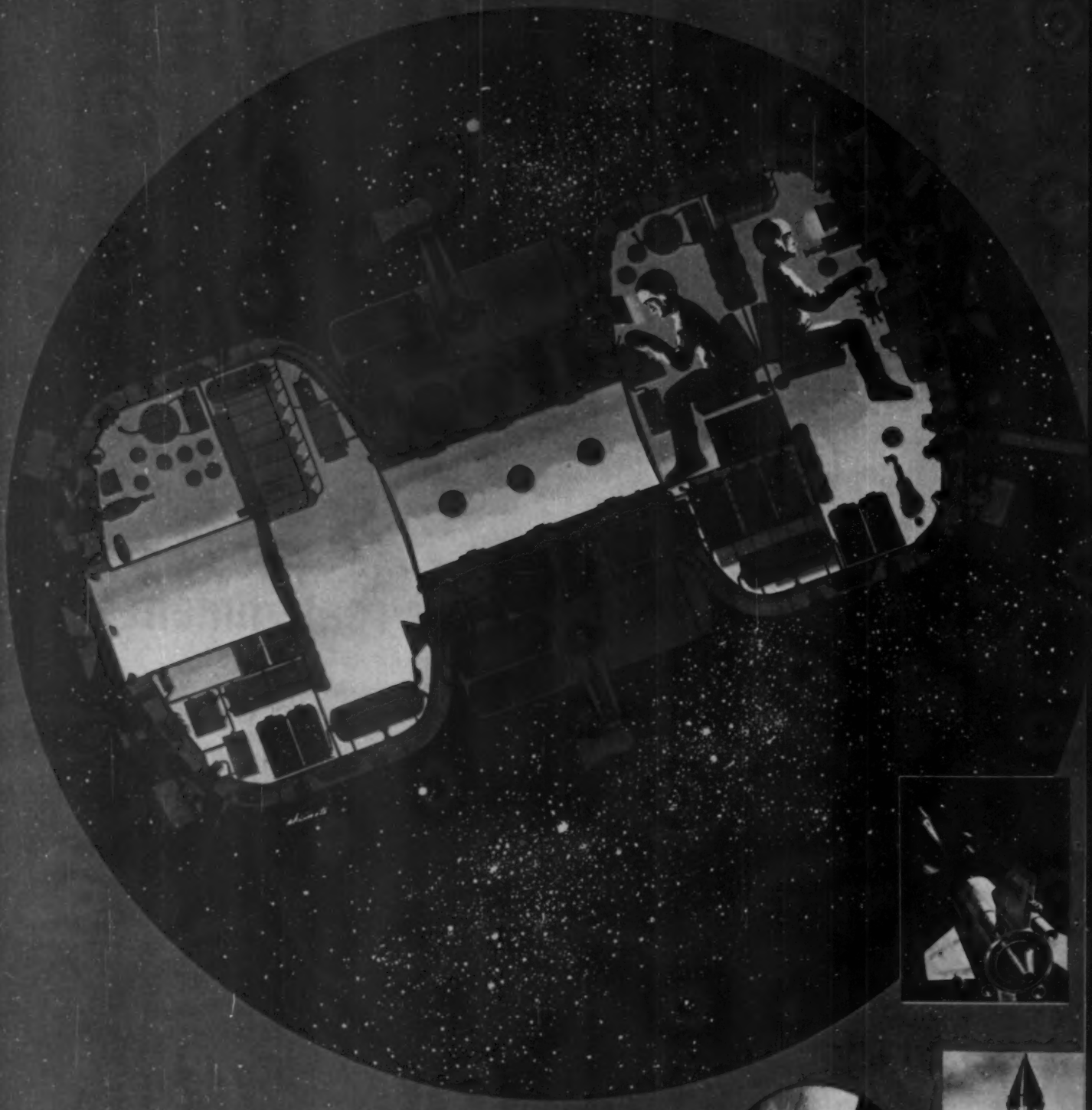

THE ASTROTUG

Tugboat for Space: Spaceborne scientific laboratories and platforms for further exploration into space are an accepted concept based on established engineering techniques. Components would be fired as individual units into space, on precalculated orbits, and there assembled. To solve the major problems of how men are to live and work in space during the assembly process, Lockheed has prepared preliminary engineering design of an astrotug – a manned vehicle housing a crew of three, capable, launch-to-dock, the astrotug will be capable of supporting its crew for a number of days in an environment of suitable atmosphere, artificial gravity, power provisions for exercise, relaxation, bathing facilities, medical care, sanitation and adequate food and water.

The Lockheed astrotug is a completely independent working vehicle. Personnel need not suit up in space suits in order to work on the project of assembling the space station components. As shown in the diagram, the tug consists of two double-walled pressure vessels approximately 20 feet long overall and 9 feet in inside diameter. Propelling rocket nozzles are arranged for maneuvering. On the forward end, extending out are four mechanical manipulator arms with interchangeable "hands" for such specialized functions as gripping, welding, hammering, cutting, running screws, etc. "Hands" can be changed by remote control from inside. Viewing ports provide uninterrupted observation. Radar antennas, searchlights, and other equipment necessary to the tug's work are mounted externally. Main controls and instruments including radar, radio, infrared, computers and navigation consoles are duplicated in each of the two major compartments as a safety measure.

Men working in single units afloat in space suits would have little applicable force and could work for very limited periods of time. With the Lockheed astrotug, personnel could carry on the work in relative safety and comfort with maximum efficiency. A special reentry vehicle, separate from the astrotug, has been conceived for ferrying to and from earth. Tugs themselves would remain floating in orbit indefinitely, being reprovisioned and refurbished as fresh crews arrive in relief.

Space vehicle development is typical of Lockheed Missiles and Space Division's broad diversification. The Division possesses complete capability in more than 40 areas of science and technology – from concept to operation. Its programs provide a fascinating challenge to creative engineers and scientists. They include: celestial mechanics; computer research and development; electromagnetic wave propagation and radiation; electronics; the flight sciences; human engineering; magnetohydrodynamics; man in space; materials and processes; applied mathematics; oceanography; operations research and analysis; ionic, nuclear and plasma propulsion and exotic fuels; sonics; space communications; space medicine; space navigation; and space physics.

Engineers and Scientists: Such programs reach far into the future and deal with unknown and stimulating environments. It is a rewarding future with a company that has an outstanding record of progress and achievement. If you are experienced in any of the above areas, or in related work, we invite your inquiry. Please write: Research and Development Staff, Dept. D-32, 962 W. El Camino Real, Sunnyvale, California. U.S. citizenship or existing Department of Defense clearance required.

Lockheed

MISSILES AND SPACE DIVISION

Systems Manager for the Navy POLARIS FBM; the Air Force AGENA Satellite in the DISCOVERER Program and the MIDAS and SAMOS Satellites; Air Force X-7; and Army KINGFISHER.

SUNNYVALE, PALO ALTO, VAN NUYS, SANTA CRUZ, SANTA MARIA, CALIFORNIA
CAPE CANAVERAL, FLORIDA • ALAMOGORDO, NEW MEXICO • HAWAII

Diverse applications prove the quality of CERAMELEX® ...the original barium titanate piezoelectric elements

Designers and manufacturers of ultrasonic microphones, phono cartridges, IF transformers, sonic devices, delay lines and ultrasonic cleaning devices rely on CERAMELEX piezoelectrics for efficient energy conversion.

Barium titanate, first artificially polarized* by Erie Resistor, is the base material of CERAMELEX. This precision-produced material has qualities not found in the conventional single crystal piezoelectrics:

Variety of sizes and shapes . . . ceramic composition allows molding and pressing;

Wide temperature range . . . operating temperatures as high as 100°C;

Efficient performance . . . higher degree of energy conversion than possible with natural crystals.

You're invited to contact Department 81 of Erie Technical Ceramics for literature and information regarding further capabilities, tolerances and availability of Erie CERAMELEX products.

*U.S. Patent 2,486,560

NOMINAL CHARACTERISTICS OF CERAMELEX® BODIES

	PZ 1005	PZ 1006	PZ 1007*	PZ 1009
Density gm/cc	5.6	5.5	5.4	5.6
Young's Modulus X 10^{10} Newton/m^2	10.2	11.5	10.1	11.0
Dielectric Constant	1800	1200	1200	1400
Diss. Factor %	0.8	0.9	2.5	0.8
Radial Coup. Coeff. k_r	.33	.31	.37	.32
k_{31}	0.20	0.18	0.22	0.19
k_{33}	.47	.48	.55	.52
d_{31} x 10^{-12} m/v	77	56	71	62
d_{33} x 10^{-12} m/v	180	148	177	168
g_{31} x 10^{-3} v.m/New.	4.9	5.2	6.7	5.1
g_{33} x 10^{-3} v.m/New.	11.5	13.7	16.7	13.8
Frequency Constant (fc) cyc. m	1440	1560	1465	1500
Aging %/decade	2	1	4	1½
Maximum Temperature 1°C	100	100	45	110

*Phono Pick-up units only

Write for Erie Bulletin 454, which gives complete technical data on CERAMELEX.

ERIE

TECHNICAL CERAMICS
DIVISION

ERIE RESISTOR CORPORATION
Erie, Pennsylvania

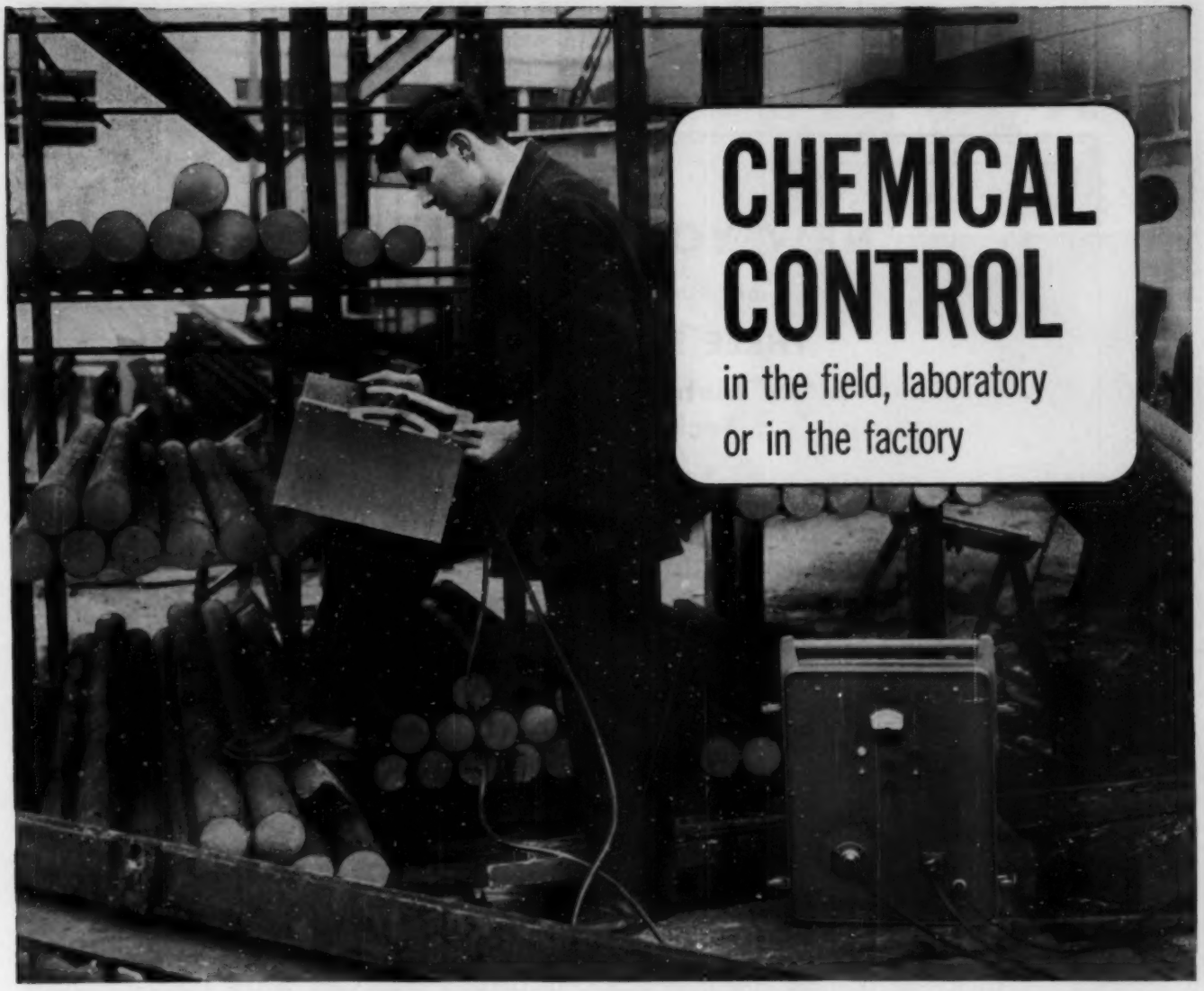

Progress and growth means bigger industries—our technology must grow in proportion. As specialization widens, skilled professional help is naturally more scarce.

Analytical tools, combining the miracles of X-rays and electronics, can provide reproducible, accurate, non-destructive chemical analyses with speeds undreamed of by wet chemical means. These units, operable by the relatively unskilled, can release chemists for research or non-routine analysis.

In the illustration above, you see a new lightweight portable X-ray Spectrograph. This exciting device may be used *anywhere*—factory, field, mine or even flying from site to site. It will provide element identity, alloy sorting, and plating thickness with excellent accuracy in a fraction of the time you would expect.

From this small unit upward there are laboratory tools like the Norelco X-ray Diffractometer, X-ray Spectrograph, 100 KV X-ray Spectrograph—providing higher energy for higher element studies. There is also the Autrometer—a 24 element automatic spectrograph. In many instances, these apparatus have been engineered into continuous process lines for on-the-spot and feed-back controls.

Let us tell you how you can apply these tools to improving your process and lowering your production costs.

Norelco

PHILIPS ELECTRONIC INSTRUMENTS

A Division of Philips Electronics and Pharmaceutical Industries Corp.

750 SOUTH FULTON AVENUE, MOUNT VERNON, N.Y.

In Canada: Research & Control Instruments • Philips Electronics Industries Ltd. • 116 Vanderhoof Ave. • Leaside, Toronto 17, Ont.

NEW YORK UNIVERSITY

announces the presentation of

THREE SUMMER MEETINGS

in its Metallurgy and Solid State Technology Program

Conference on Vacuum Metallurgy

June 1-2-3, 1960

A conference on new research and advanced engineering information in vacuum metallurgy.

Fee: $20.00

COURSE ON THERMOELECTRIC MATERIALS AND DEVICES

June 13-17, 1960

An intensive lecture series designed to bring engineers up to date with the theory and state of the art of materials and devices based on the thermoelectric effects. Speakers represent both industrial and research organizations and are currently engaged in work on thermoelectricity. For the benefit of those not thoroughly familiar with the subject the lecture sequence is arranged to include both fundamental and advanced information.

Fee: $110.00

Conference on Titanium Metallurgy

September 12-13, 1960

The 6th Annual Titanium Conference will be concerned with progress in welding, heat treatment, alloy development and corrosion of titanium.

Fee: $15.00

Dormitory accommodations are available at $3.50 a night. Registration will be limited. For further information contact Mr. M. Berk, New York University, University Heights, Bronx 53, N. Y. LUdlow 4-0700, Ext. 205.

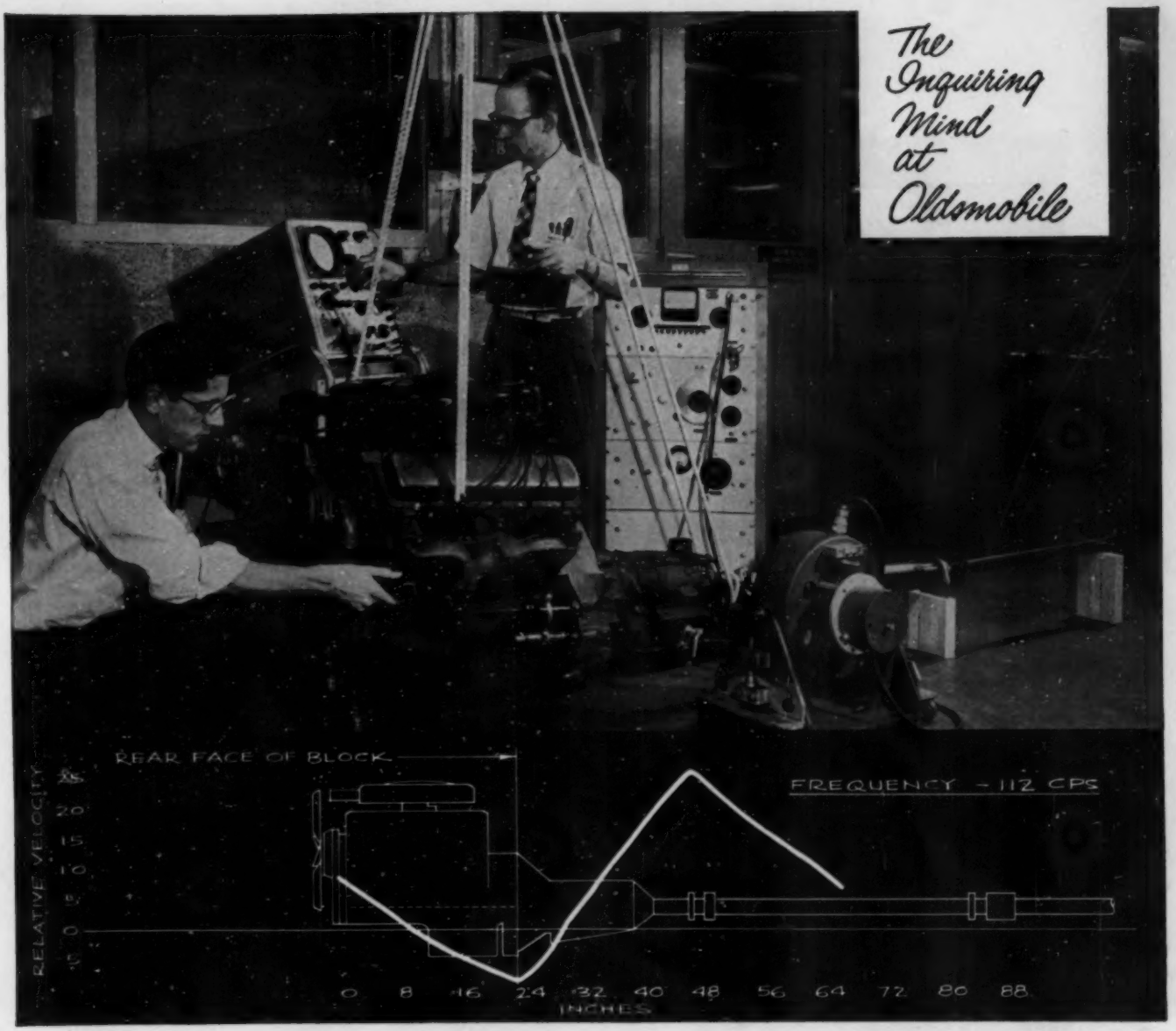
The Inquiring Mind at Oldsmobile
REAR FACE OF BLOCK
FREQUENCY - 112 CPS
RELATIVE VELOCITY
INCHES
0 8 16 24 32 40 48 56 64 72 80 88

no. 11 OF A SERIES

SHAKE-DOWN TEST FOR A ROCKET!

Intricate vibration studies that determine proper engine mounting points help Oldsmobile engineers design smooth, balanced Rocket Engine power.

To tame the explosive fury of the modern high compression engine, Oldsmobile engineers have developed highly specialized techniques in the field of vibration studies. The results of these studies produce Rocket Engine power that is balanced, controlled and exceptionally quiet under nearly every operating condition. Vibrations caused by the multitude of explosions in the cylinders—4800 per minute at 30 mph—are almost imperceptible in the passenger compartment.

To thoroughly study an engine's "bending" characteristics, in both horizontal and vertical planes, the engine is suspended from a low spring rate nylon rope that isolates external interference. A shaker is used to excite the entire power plant and drive line to find the resonant vibration frequencies, generally in the 25 to 55 mph speed range. Then intensive analysis of the engine begins. At four inch intervals, a transducer in contact with the engine translates movement into a reading on an oscilliscope. From this information, a displacement curve is plotted showing exactly the ideal locating points for the engine mountings—the "nodal points".

In addition, each engine accessory—generator, air cleaner, power steering pump, etc.—is studied so that no undesirable resonant vibrations will occur.

The quiet power, brilliant performance and solid quality of the 1960 Oldsmobile is a tribute to modern technology and craftsmanship. There's never been another car like it! Visit your Quality Dealer soon and Quiet-Test Olds for '60.

OLDSMOBILE DIVISION • GENERAL MOTORS CORPORATION

OLDSMOBILE **Where Proven Quality Is Standard**

Timely McGRAW-HILL Books

MISSILE AERODYNAMICS

By JACK N. NIELSEN, VIDYA, Inc. *McGraw-Hill Series in Missile and Space Technology.* 450 pages, $12.50

This volume presents a rational and connected account of principles of missile aerodynamics. It treats the subjects of wings, bodies, and tails and the interactions between them which are particularly important to missiles.

SOME MATHEMATICAL METHODS OF PHYSICS

By GERALD GOERTZEL and NUNZIO TRALLI, both of the Nuclear Development Corporation of America. Ready in May.

This modern book presents a common set of mathematical techniques as useful background for a variety of fields of theoretical and applied physics; quantum mechanics, acoustics, electromagnetic theory, reactor physics, etc. The authors do not try to cover the entire field of mathematical methods of physics. Rather, they attempt to give non-mathematicians a well-rounded and thorough indication of the basic concepts involved in the study of linear systems.

REACTOR ANALYSIS

By ROBERT V. MEGHREBLIAN, California Institute of Technology; and DAVID K. HOLMES, Oak Ridge National Laboratory. *McGraw-Hill Series in Nuclear Engineering.* Ready in June.

An outstanding contribution to the field of reactor theory. In developing the mathematical basis for each of the principal topics, a special effort has been made to provide several analytical methods for treating the relevant physical phenomena, and comparisons have been drawn between them when instructive.

FIRE CONTROL PRINCIPLES

By WALTER WRIGLEY and JOHN HOVORKA, both of Massachusetts Institute of Technology. *McGraw-Hill Series in the Aeronautical Sciences.* 113 pages, $10.00

A graduate level textbook which is the outgrowth of several years of teaching courses on weapons systems at Massachusetts Institute of Technology to Army, Navy, and Air Force officers. The work attempts to resolve the existing multiplicity of viewpoints by separating the fire control problem from its solution, and the principles from the systems.

Send for copies on approval

McGraw-Hill
BOOK COMPANY, INC.
330 West 42nd Street New York 36, N.Y.

At Los Alamos, the mysteries of the universe provide the dynamics for projects ranging from space propulsion to nuclear research.

Original painting by Emil Bisttram, Taos, N. M.

For employment information write:
Personnel Director
Division 80-88

los alamos
scientific laboratory
OF THE UNIVERSITY OF CALIFORNIA
LOS ALAMOS, NEW MEXICO

ARL
Applied Research Laboratory

RESEARCH POSITIONS
in Suburban Boston

Sylvania's new programs of expansion, enhanced by its merger last year with General Telephone & Electronics, offer increased opportunities for independent research at the Applied Research Laboratory. You will work with a distinguished organization of engineer-scientists whose achievements have already won them wide recognition in their fields. This laboratory is concerned with new approaches in:

• INFORMATION & COMMUNICATION THEORY • ELECTROMAGNETIC PROPAGATION • SOLID STATE PHYSICS • MICRO-ELECTRONICS • HYPERSONIC GASDYNAMICS • MATHEMATICAL ANALYSIS & OPERATIONS RESEARCH

If you hold a graduate degree or have equivalent experience in an applicable technical field, the advantages of a position with the Applied Research Laboratory merit your consideration—

• Problems of Major Magnitude in Advanced Areas • Ample Opportunity to Publish • Informal Professional Atmosphere & Extensive Opportunity for Creative Research

Write in confidence directly to Dr. L. S. Sheingold, Director, Applied Research Laboratory

Waltham Laboratories / **SYLVANIA ELECTRONIC SYSTEMS**
A Division of

SYLVANIA
Subsidiary of GENERAL TELEPHONE & ELECTRONICS

100 First Avenue—Waltham 54, Massachusetts

superb new null detector and dc microvoltmeter

Model 151 offers non-linear and linear ranges, 10^{-17} watt sensitivity, 2 x 10^{-13} ampere current sensitivity.

The new Keithley 151, incorporating a unique photo-conductive modulator of Keithley design, is useful wherever a suspension galvanometer can be used and where a galvanometer is not sufficiently sensitive, fast or rugged.

As a null detector, has five non-linear ranges as well as linear ranges. Non-linear ranges each cover three decades, with full scale sensitivities of 0.001 to 10 volts. Center 10% of the log scale is linear, permitting extremely critical readings near null.

As a microvoltmeter or dc amplifier, has eleven linear ranges in 1x and 3x steps from 100 microvolts to 10 volts full scale. Input resistance on all ranges is ten megohms, yielding a maximum power sensitivity of better than 10^{-17} watt. Currents as low as 2 x 10^{-13} ampere can be detected. Output of 10 volts at 1 ma full scale permits use as a dc amplifier with gains to 100,000.

Other Features. Greater than 60 db rejection to 60 cps ac signals; zero drift below 10 microvolts per day; short-term noise within ± 2 microvolts.

MODEL 151 has 10^{-17} watt sensitivity, 2 x 10^{-13} ampere current sensitivity.

SPECIFICATIONS

Ranges: 11 linear ranges in 1x and 3x steps, from 100 μv to 10 v f.s.; 5 non-linear ranges of 0.001, 0.01, 0.1, 1.0 and 10 v f.s., each covering three decades.

Accuracy: Linear ranges, ± 3% of f.s. Non-linear ranges, ± 10% of input.

Input Resistance: 10 megohms on all ranges.

Response Speed: On 100 μv range, 2.5-sec.; 1-sec. on all others.

Noise: Less than 2% f.s. on all ranges.

Zero Drift: Less than 10 μv per day after warm-up.

Output: 10 volts at 1 ma f.s.; resistance, less than 50 ohms.

Price: Model 151, Cabinet Model $395.00
Model 151R, Rack Model $385.00

For complete details, write:

KEITHLEY INSTRUMENTS, INC.
12415 EUCLID AVENUE CLEVELAND 6, OHIO

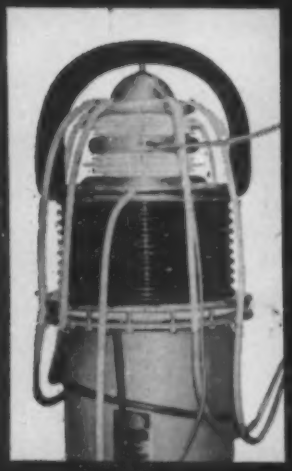

600,000 amperes help harness H-power

At the historic Geneva Atoms-For-Peace Conference, Los Alamos scientists unveiled Scylla—a fusion device used to heat a plasma of ionized heavy hydrogen particles millions of degrees by blasting it with a 600,000-ampere thunderbolt.

Surrounding the heart of this thermonuclear machine is a bank of Tobe low-inductance, energy-storage capacitors...each rated at 100,000 volts, each capable of a 20,000 megawatt peak surge.

Why Tobe capacitors? Because only Tobe, with over 30 years of capacitor experience, could meet the rigid design specifications set for the project. Tobe capacitors can meet yours, too. We invite inquiries for a single energy storage capacitor or a complete energy storage system including capacitors, racks, interconnecting lines, protective devices and charging power supply.

For further technical information or engineering aid, write to Cornell-Dubilier Electric Corp., Marketing Office, Norwood, Mass.

CDE CORNELL-DUBILIER ELECTRIC CORPORATION
Affiliated with **Federal Pacific Electric Company**

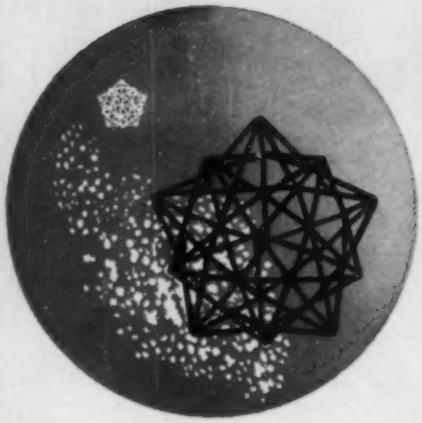

ENGINEERS
SCIENTISTS

FUTURISM in contemporary R&D

Radical departures from traditional forms of scientific investigation are the keynote of Republic Aviation's forward-looking programs in space exploration and upper atmosphere flight. In an environment that regards with skepticism the seeming validity of conventional conclusions, engineers and scientists seek below-the-surface solutions of problems... bypassing the superficial.

Expanding the scope and depth of present programs is Republic's recently completed $14 million Research and Development Center. Extensive facilities here are an invitation to professional men to realize the future by solving today's most perplexing problems.

• • • • • • • • • • • • • • • • • • •

SENIOR LEVEL OPENINGS EXIST IN THESE IMPORTANT AREAS:

Navigation & Guidance Systems / Radar Systems / Information Theory / Radio Astronomy / Solid State & Thermionic Devices / Microwave Circuitry & Components / Countermeasures / Digital Computer Development / Radome & Antenna Design / Receiver & Transmitter Design / Miniaturization-Transistorization / Radiation & Propagation (RF, IR, UV) / Telemetry-SSB Technique

Please forward resumes to:
Mr. George R. Hickman
Technical Employment Manager,
Department 17D

REPUBLIC AVIATION

Farmingdale
Long Island, New York

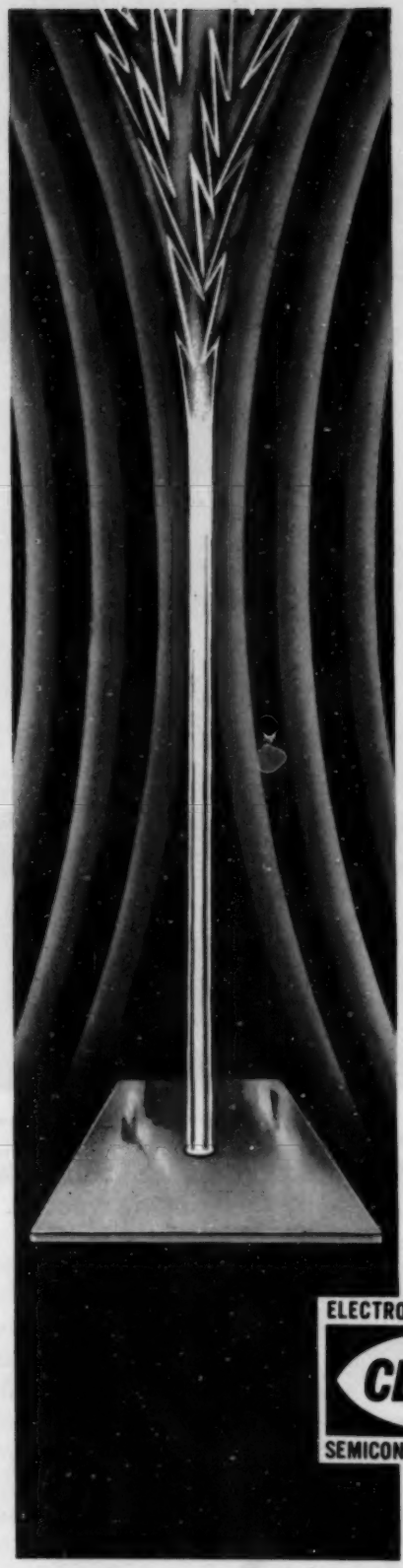

ELECTRON TUBES
CBS
SEMICONDUCTORS

A SIGNIFICANT PROFESSIONAL CAREER ANNOUNCEMENT TO SEMICONDUCTOR ENGINEERS, CHEMISTS and PHYSICAL CHEMISTS...

CBS ELECTRONICS*

sets-up important NEW MADT PROGRAM

THE PROGRAM... This is a major long range program in the mass production of Micro Alloy Diffused-base Transistors (FAST SWITCHES, HF AMPLIFIERS and HF POWER OSCILLATORS) through the use of electro-chemical jet etching and plating. These high-frequency transistors with extreme accuracy and uniformity for use in industrial and military computers are acknowledged to be the most challenging phase of *tomorrow's* data processing systems.

THE OPPORTUNITY... Engineers, Chemists and Physical Chemists with competence in semiconductors can now apply their full technical capabilities on CBS Electronics' new MADT program which offers exceptional ground-floor opportunities. Positions are available at all levels. Degree in one of the physical sciences required.

***THE COMPANY...** CBS ELECTRONICS is the engineering and manufacturing arm of COLUMBIA BROADCASTING SYSTEM, Inc. Supported by its full resources and under engineering-oriented management, we continue our sound expansion... with products characterized by ultra-high quality to meet the most exacting reliability standards.

As a member of the CBS professional family, you will work in our new $5,000,000 facility now nearing completion. You and your family will live in a pleasant New England community... with beaches, mountains, educational and cultural advantages nearby... and only 45 minutes from Metropolitan Boston.

Qualified applicants are invited to send resume to Mr. H. C. Laur. In replying, kindly designate Dept. 2950.

CBS ELECTRONICS
A Division of Columbia Broadcasting System, Inc.
900 Chelmsford Street, Lowell, Mass.

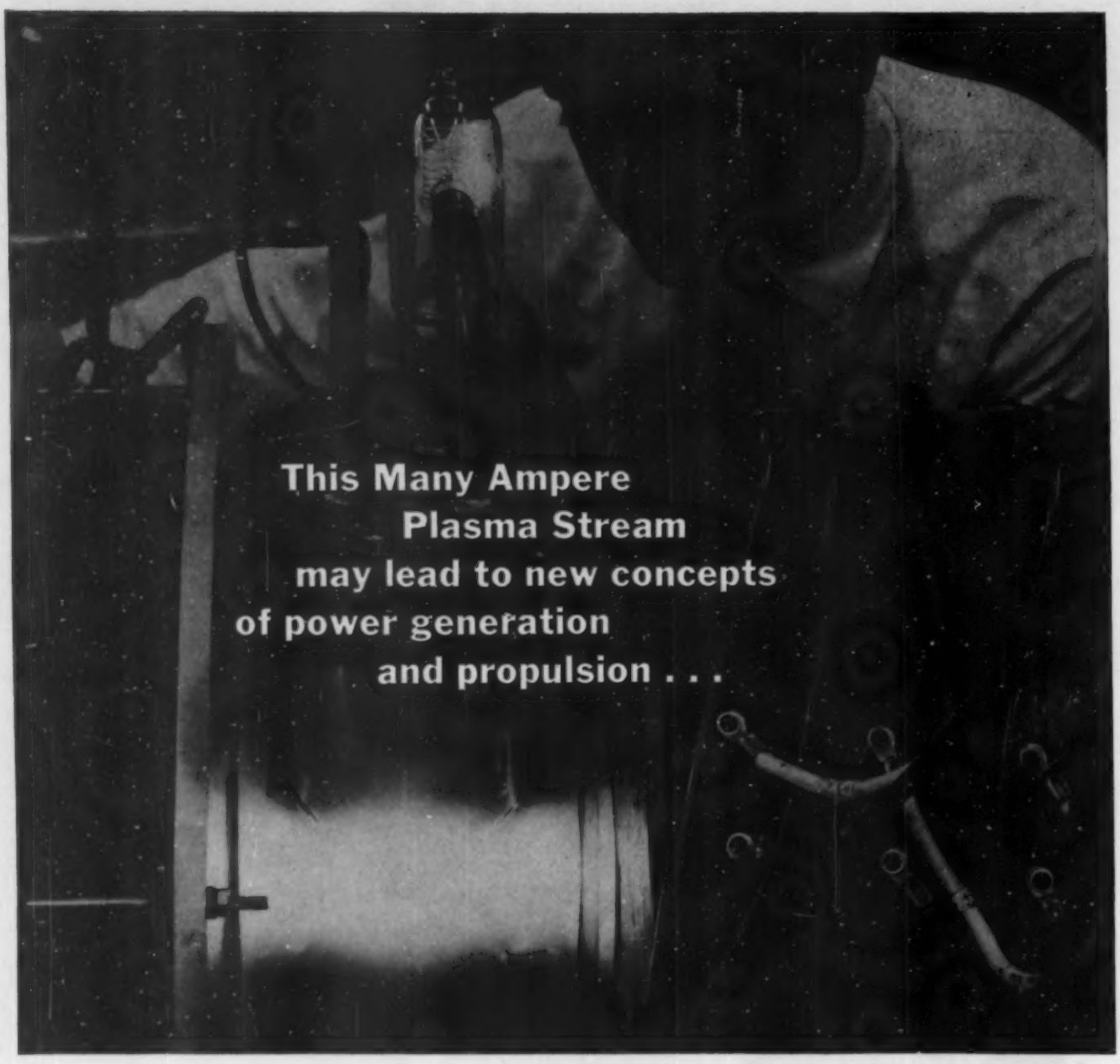

A many-ampere source of ions, this device is believed to be the most powerful in operation in any laboratory Already it is providing new insight into thermonuclear fusion. It may lead to new concepts in propulsion including a method of producing thrust for missions beyond the earth's atmosphere.

Accomplishments like this are the result, we believe, of a unique research environment. Among other things, we encourage independence of scientific thought and action. And, we make determined efforts to free scientists from tedious routine — help direct their full mental powers towards scientific achievement.

Complex calculations, for instance, are handled by the nation's largest industrial computational facility. Unusual assistance — at operational and theoretical levels — is available from outstanding leaders in other disciplines.

We believe that this combination of facilities and services is unequaled. If you are interested in corporate-sponsored studies into the fundamental nature of matter in an environment where success comes easier, write today.

Please write to Mr. W. N. Walsh, or phone Hartford, Conn., JAckson 8-4811, Ext. 7145

Research Opportunities
in many areas...

Solid State Physics
Plasma Physics
Gaseous Electronics
Chemical Kinetics
Particle Physics
Nuclear Engineering
Surface Chemistry
Cryogenics
Energy Conversion

RESEARCH LABORATORIES
UNITED AIRCRAFT CORPORATION
400 Main Street, East Hartford 8, Conn.

Symbol of UAC RESEARCH ... creative research

RESEARCH AT COLLINS

$$p(\lambda)d\lambda = \frac{C_1}{\lambda^5}\,\frac{1}{\exp(C_2/\lambda T)-1}$$

$$C_1 = 8\pi h c$$

$$C_2 = \frac{hc}{k}$$

THE UNUSUAL SHAPE OF PROGRESS

The principles of spectral energy distribution of the radiation from a black body, announced by Max Planck in 1900, were of intense interest to the theoretical physicists of the day. Since then, these principles have paved the way for major advances in marine navigation and radio astronomy. For example, Collins new Radio Sextant pictured here is capable of continuously tracking the sun or the moon under any weather conditions, furnishing both the ship's location and heading with high precision.

Max Planck's work was done in an atmosphere of unrestricted scientific freedom. Such an atmosphere is provided in Collins Radio Company Research laboratories for physicists, mathematicians and engineers engaged in basic research. These are men capable of looking beyond man's present limitations, with the ability and ambition to analyze man's progress and envision his future environment. To further implement the advancement of scientific knowledge at Collins, with the resultant development of new technologies, unique professional opportunities are now being offered in the fields of radio astronomy, circuits, advanced systems, antennas and propagation, mechanical sciences and mathematics. Your inquiry is invited.

COLLINS

COLLINS RADIO COMPANY • CEDAR RAPIDS, IOWA • DALLAS, TEXAS • BURBANK, CALIFORNIA

We promise you a reply within one week

The complexity of modern technology...the rapid increase in the number of specializations...and the frequent shifts in technological emphasis all have combined to require a staff of alert, aggressive, creative teams of engineering specialists. Their responsibility is to assist management in the formulation of plans for future efforts.

For our purposes the teams should be staffed by graduate Electronic Engineers and Physicists who have acquired several years of experience with radar, guided missiles, computers, infrared detection, nuclear radiation equipment, micro-electronics, underwater

Opportunities in:

Exploratory Studies · Advanced Planning · Systems Analysis

detection, space propulsion systems or related areas. Several of the positions require the ability to present contract proposals to both technical and non-technical officials. Other positions require the ability to do preliminary systems design. There are twenty-three openings in the above areas at the present time.

All of the positions involve close associations with senior engineers. All of the salaries reflect the unusual backgrounds required.

Please airmail your resume to

Mr. Robert A. Martin
Supervisor, Scientific Employment
Hughes Engineering Division
Culver City, California

Creating a new world with ELECTRONICS

HUGHES

©1960, HUGHES AIRCRAFT COMPANY
ENGINEERING DIVISION

many new developments

INCREASE PERFORMANCE, RUGGEDNESS, RELIABILITY

CRL manipulators... as obedient as your hand

Central Research Laboratories brings you important refinements in lateral rotation, azimuth assembly, wrist joint, tong, handle, roller mounts, load hook, and booting. Each is the result of CRL's continuing program to give you the finest in master-slave manipulators . . . manipulators which duplicate the natural motions of the operators' hand. Many of these improved features can be added to manipulators already in service. This program of improvement without obsolescence plus CRL's policy of immediate shipment on spare parts insures continued customer satisfaction.

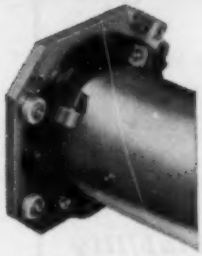

Improved *roller mount:* More rugged, more serviceable, less wear on through tube.

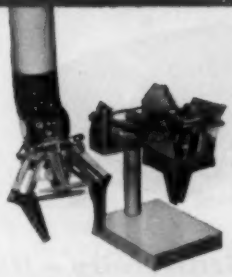

Improved *wrist joint, tong,* and *tong jig:* Greater protection of gears, more rugged, easier interchange.

Improved *handle:* More rugged, more satisfactory control of separation indexing and squeeze motion lock.

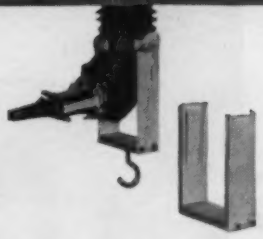

Improved *booting* and *load hook: Partial or* complete booting possible, load hook fits on booted or unbooted arm.

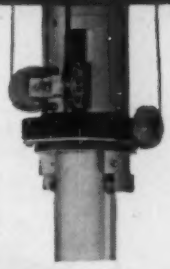

Improved *azimuth assembly:* Eliminates exposed rollers, provides greater "Z" motion or shorter collapsed length.

for thru-wall installation

CRL MODEL 8

Thru-wall installation for intermediate to high-level shielding. Separation indexing and lateral rotation keeps operator close to window with full visibility over large area. Easy to relocate —one man with a light crane can remove and relocate in less than five minutes.

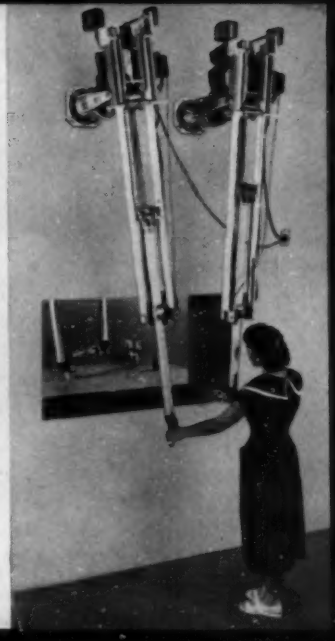

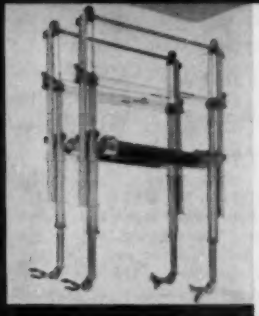

for over-wall installation

CRL MODEL 4

General purpose — for installation over a barrier wall or through ceiling opening of protective enclosure.

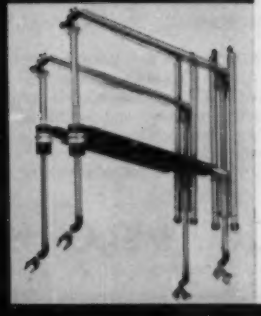

for restricted-space installation

CRL MODEL 7

Space saving, light weight — for use in "junior caves" or over thin walls where minimum clearance and easy portability are important factors.

Central Research Manipulators from basic Argonne National Laboratory designs

write today for complete information to:

Central Research laboratories, inc.

Red Wing, Minnesota, Dept. 302

Welch DENSICHRON® ELECTRONIC DENSITOMETER

Makes Precision Light Measurements—Quickly—Accurately

NO. 3830A DENSICHRON AND PROBE

ASSURES EXCEPTIONALLY STABLE READINGS OF TRANSMISSION AND REFLECTION DENSITIES

REFLECTION UNIT NO. 3832A

Good Sensitivity—High Stability

—SPECIAL FEATURES—

Patented Magnetic Modulation

Simple to Use

Convenient Small Size—5″ x 7¼″ x 13″

Light in Weight—only 11½ pounds

NO. 3830A. DENSICHRON WITH BLUE PROBE, including amplifier with logarithmic-scale meter, metal probe support, five different measuring apertures, a cone with ¼ inch aperture and a set of instructions. The amplifier operates on 115 volts, 60 cycle, A.C. only, except on special order.
Each $250.00

NO. 3830B. WITH RED PROBE. Each $265.00

NO. 3832A. REFLECTION UNIT. When coupled to the Densichron amplifier this unit becomes a convenient reflectance meter. It has a self-contained light source, filter wheel and phototube, and includes optics for both small and large spot work, a calibrated gray scale, and three Carrara working standards.
Each $160.00

W. M. WELCH SCIENTIFIC COMPANY

DIVISION OF W. M. WELCH MANUFACTURING COMPANY

ESTABLISHED 1880

1515 Sedgwick Street, Dept. C-1 Chicago 10, Illinois U. S. A.

Manufacturers of Scientific Instruments and Laboratory Apparatus

Journal
of
Applied Physics

Volume 31, Number 4 April, 1960

Lattice Displacements by Fast Electrons

W. Dale Compton and George W. Arnold
U. S. Naval Research Laboratory, Washington, D. C.
(Received October 15, 1959)

A discussion is given of the processes by which atoms are displaced from their lattice sites by incident fast electrons. In addition to direct displacement by the incident electron, expressions are derived for the fraction of atoms displaced by fast moving atoms and by fast secondary electrons, both of which are generated initially by the incident electron. A discussion of thermal spikes is given. A thermal spike process is discussed that might lead to the generation of defects with x irradiation in materials that exhibit a threshold energy for a displacement by a charged particle.

INTRODUCTION

THE displacement of atoms in a solid by irradiation with fast electrons, neutrons, heavy charged particles, and high energy photons has been studied by many investigators. Many of the investigations have dealt with the changes in properties of a material as a result of the displacement of the atoms. Other investigations have been primarily concerned with determining the processes by which the atoms are displaced and have used property changes of the material merely as indicators of such displacements.

This paper discusses the processes by which lattice atoms are displaced when fast electrons are incident upon the material. These processes may be listed as: (1) Displacements by direct interaction of the incident electron with the lattice atom. (2) Displacements by fast moving atoms which have been dislodged by the incident electron. (3) Displacements by secondary electrons which are generated in the solid by collisions between the incident electron and the bound electrons of the atoms. (4) Displacements arising from thermal spikes which are produced when a moving atom is brought to rest or when a slow electron is stopped. Quantitative calculations are possible for the first three of these processes. Numerous publications have dealt with the first process. An outline of this work will be given here for completeness. Explicit calculations are given here for the fraction of atoms displaced by processes two and three. Quantitative calculations are not possible for process four. It is argued, however, that defects may be produced in nonmetallic materials by thermal spikes that are generated by the low energy photo-electrons arising from soft x rays.

DISPLACEMENTS BY PRIMARY ELECTRONS

The number of lattice atoms that are displaced per incident electron can be calculated if the cross section for the displacement is known. A theoretical expression for the cross section exists. This expression contains one adjustable parameter T_d, the minimum kinetic energy that must be transferred to the lattice atom to displace it. It is assumed here that T_d does not depend upon the crystallographic direction taken by the displaced atom. A family of curves, with T_d as the parameter, can be plotted for the fraction of atoms displaced as a function of incident electron energy. A comparison of the experimental data with these curves fixes T_d. Once T_d is fixed, the absolute cross section is known and the number of displacements produced by a given electron flux can be determined.

A fast electron incident upon an atom will penetrate the electronic cloud of the atom and be scattered by the entire nuclear charge Z. The probability that the electron of energy E will be scattered into an angle θ between θ and $\theta+d\theta$ has been derived for relativistic electrons when $Z/137 \ll 1$.[1] The combination of this with the requirement that energy and momentum be

[1] W. A. McKinley and H. Feshbach, Phys. Rev. 74, 1759 (1948); N. F. Mott and H. S. W. Massey, *The Theory of Atomic Collisions* (Oxford University Press, London, 1952), second edition, p. 82.

Copyright © 1960 by the American Institute of Physics.

conserved gives the probability that the scatterer will have kinetic energy T between T and $T+dT$ after the collision.[2] The differential cross section for a displacement is

$$d\sigma=\frac{\pi b^2}{4}T_m\left[1-\beta^2\frac{T}{T_m}+\pi\alpha\beta\left\{\left(\frac{T}{T_m}\right)^{\frac{1}{2}}-\frac{T}{T_m}\right\}\right]\frac{dT}{T^2}, \quad (1)$$

where

$$b^2=4Z^2e^4(1-\beta^2)/m^2c^4\beta^4 =0.3177Z^2(1-\beta^2)/(\beta^4) \text{ barns}. \quad (2)$$

T_m is the maximum energy that the electron can transfer to the struck nucleus, m is the electronic rest mass, $\beta=v/c$ (v is the relativistic electron velocity), $\alpha=Z/137$, and π, e, and c have the usual definitions. If A is the atomic mass of the struck atom, then T_m can be conveniently calculated from[2]

$$T_m=2147.8E(E+1.0220)/A, \quad (3)$$

where T_m will be given in ev if E is given in Mev.

If the struck atom must receive a minimum energy T_d in order to dislodge it from its lattice site, then the total cross section for a displacement is obtained by integrating (1) between T_m and T_d. This procedure assumes that $T_d \ll E$ since the loss of an amount of energy T_d was neglected in writing the conservation of energy equations. This is not serious since E is usually many kilovolts and T_d is characteristically less then 30 ev for most materials. The integration gives

$$\sigma=\frac{\pi b^2}{4}\left[\left(\frac{T_m}{T_d}-1\right)-\beta^2\ln\frac{T_m}{T_d} +\pi\alpha\beta\left\{2\left[\left(\frac{T_m}{T_d}\right)^{\frac{1}{2}}-1\right]-\ln\frac{T_m}{T_d}\right\}\right]. \quad (4)$$

The number of displacements N_d produced by an incident flux ϕ electrons/cm^2 of energy E is simply

$$N_d=N_0\phi(E)\sigma(E,T_d), \quad (5)$$

where N_0 is the number of atoms/cm^3 of a given specie in the sample. From this the

Fraction of atoms displaced $=N_d/N_0=\phi(E)\sigma(E,T_d)$. (6)

A plot of the fraction of atoms displaced vs E for various values of the parameter T_d and for equal electron flux can now be made. A comparison with the experimental data is easier, however, if the fraction displaced by electrons of energy E relative to those displaced by electrons of the maximum attainable electron energy is plotted as a function of E. Figure 1 is a plot of these curves for T_d of 5, 15, and 30 ev for carbon where the maximum attainable energy is arbitrarily taken to be 2.0 Mev. Contrary to most discussions, it is seen that the cross section for a displacement can increase with decreasing electron energy. A comparison between the theoretical cross section (Eq. 4) and the experimental data is usually made by plotting N_d/N_0 and $\sigma(E,T_d)$ on the same energy scale. This assumes that the experimental points are taken with a constant electron flux $\phi(E)$. This is valid only if the electron energy is sufficiently high that an appreciable amount of scattering of the electron does not occur. The scattering produces an increased path length for the electron. The longer the path of the electron in the sample, the higher the probability for producing damage. A correction for this effect can be made using the theory of Yang.[3] This correction can be quite important in such high Z materials as Ge. For example, the actual path length of an 0.5-Mev electron in passing through an 0.008-in. thickness of Ge will be 0.0212 in. or 2.72 times the thickness of the material. The path length for a 2.0-Mev electron in an 0.008-in. thick Ge sample would be only 1.17 times the actual sample thickness. Thus, a significant error could be made if this correction is not applied.

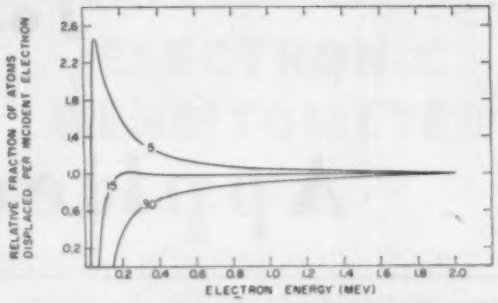

FIG. 1. Relative fraction of atoms displaced per incident electron in carbon as a function of the energy of the incident electron for $T_d=5$, 15, and 30 ev.

DISPLACEMENTS BY PRIMARY ELECTRONS AND FAST MOVING ATOMS

An atom that has been displaced by an electron may have sufficient energy to displace other atoms. The number of such secondary displacements may be quite important when T_d is small. In comparing the experimental data with theoretical calculations, one should include this secondary displacement process in making the calculations. This can be done with the help of the work of Seitz and Koehler.[2]

Let $g(T/T_d)$ be the total number of atoms that are displaced when a primary atom is produced with a kinetic energy T. Then the fraction displaced, both by direct interaction with the incident electron flux $\phi(E)$

[2] This development is given in more detail by F. Seitz and J. Koehler, in *Solid State Physics*, edited by F. Seitz and D. Turnbull (Academic Press, Inc., New York, 1955), Vol. 2, p. 305.

[3] C. N. Yang, Phys. Rev. 84, 599 (1951).

and by fast moving atoms, is given by

$$\text{Fraction displaced} = \phi(E)\int_{T_d}^{T_m} g(T/T_d)\frac{d\sigma(T,E,T_d)}{dT}dT. \quad (7)$$

Note that according to the definition of g that $g(T/Td)\geqslant 1$.

Seitz and Koehler[2] give the general form of $g(T/T_d)$. Equation 7 was explicitly calculated for various ratios of T/T_d and applied to the problem of calculating the total displacements in copper.[4] Figure 2 is a plot of this computation where T_d was taken to be 20 and 28 ev. The solid curves were calculated from Eq. 7 whereas the dashed curves were calculated from Eq. 6. Consideration of the displacements by fast moving atoms is thus seen to be very significant.[5]

This treatment of secondary atomic displacements has neglected replacement collision processes whereby a moving copper atom recombines with a previously formed vacancy thereby eliminating both defects from the material.

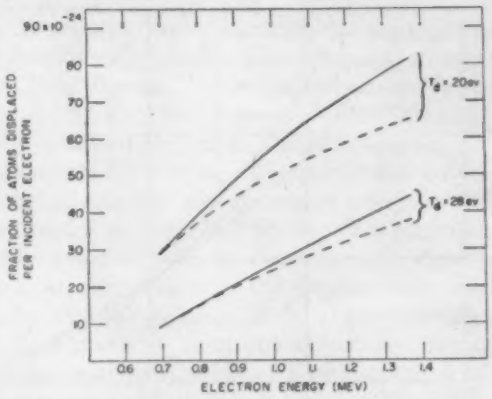

FIG. 2. Fraction of atoms displaced per incident electron in copper as a function of the energy of the incident electron. - - -, displacements arising only from direct interactions with the incident electron. ——, displacements arising from direct interactions with the incident electron and from fast moving atoms.

DISPLACEMENTS BY PRIMARY ELECTRONS, FAST MOVING ATOMS, AND SECONDARY ELECTRONS

Secondary electrons are produced by collisions between the incident electron and the orbital electrons of the atoms. Some of these may be energetic enough to displace atoms. In order to account for displacements by this process, the spectrum of secondary electrons must be calculated. This will be done in the following paragraphs.

The incident electron loses energy primarily by collisions with atomic electrons in which a few electron volts are transferred to the orbital electron. Occasionally, however, an event will occur which results in a fast secondary electron. The probability that the incident electron of energy E will produce a secondary electron W_i in a range between W_i and W_i+dW_i is given by the differential Møller cross section $d\sigma_m$.

$$d\sigma_m=\frac{2\pi e^4}{mc^2\beta^2}\left[\frac{1}{W_i}-\frac{1}{(E-W_i)}\frac{mc^2(2E+mc^2)}{(E+mc^2)^2}+\frac{W_i}{(E-W_i)^2}+\frac{W_i}{(E+mc^2)^2}\right]d(\ln W_i). \quad (8)$$

The secondary electrons then serve as a source for a cascade process in which electrons of all energies less than W_i are generated. If one assumes that all the secondaries and their cascade products remain in the sample and that the sources of the cascade process are uniformly distributed throughout the sample, then the results of a calculation by McGinnies can be used to obtain the final electron spectrum.[6] This calculation gives $y(W_i,W)$, the equilibrium number of electrons/unit source strength that have energy W in a range between W and $W+dW$ for a sample containing a uniformly distributed source that emits monoenergetic electrons of energy W_i. The only complication is the fact that the sources of the cascade process generated in the sample, the fast secondary electrons, are not of constant energy.[7]

Let $\phi(W,E)$ be the number of secondary electrons of energy W in a range between W and $W+dW$ that are generated by the incident electron flux, $\phi(E)$. Then

$$\phi(W,E)=\phi(E)\sum_{W_i}^{E/2} N_e d\sigma_m(W_i,E)y(W_i,W)\Delta W_i. \quad (9)$$

If N_e is the number of atomic electrons/cm³ in the sample, then $N_e d\sigma_m(W_i,E)$ is the number of source electrons for the cascade process that are generated by the incident electron of energy E. This quantity multiplied by $y(W_i,W)\Delta W_i$ gives the number of secondary electrons of energy W in range W to $W+dW$ produced by the electron of energy W_i. The summing over W_i and multiplying by the incident electron flux $\phi(E)$ gives the total number of secondary electrons of energy W produced by the incident electrons. Figure 3 is a plot of the secondary electron spectrum generated in SiO_2 by electrons of incident energy 2.1, 1.3, 0.5, and 0.3 Mev.[8]

[4] The general equations used in calculating these curves are given in the Appendix.

[5] The importance of secondary displacements has been recognized by many people; e.g. Corbett *et al.* consider this explicitly in evaluating their data on the electron irradiation of copper. They apparently used unpublished calculations of R. Fuchs in making this evaluation. See Phys. Rev. **108**, 954 (1957).

[6] R. T. McGinnies, NBS Circular 597, "Energy Spectrum Resulting from Electron Slowing Down" (1959).

[7] The electron having energy greater than $E/2$ after the scattering event is arbitrarily taken to be the primary electron.

[8] The authors are greatly indebted to Dr. Rosemary McGinnies for the special calculation of the quantity $y(W_i,W)$ specifically for fused silica, i.e., with the parameters $I=135.1$ ev and $Z/A=0.49920$.

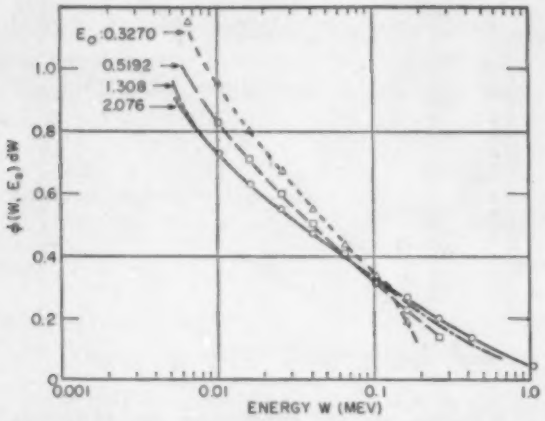

FIG. 3. Number of secondary electrons of energy W in the range between W and $W+dW$ generated by each incident electron of energy E as a function of W. The material is SiO_2 for which $I=135.1$ ev and $Z/A=0.49920$.

The combination of the effects of the displacements by the primary electron with those by the secondary electrons gives

Fraction displaced

$$=\phi(E)\int_{T_d}^{T_m} g(T/T_d)\frac{d\sigma(T,E,T_d)}{dT}dT$$

$$+\sum_W \phi(W,E)\int_{T_d}^{T_m} g(T/Td)\frac{d\sigma(T,W,T_d)}{dT}dT. \quad (10)$$

For low-threshold values and light elements, significant numbers of displacements can occur by this process.

DISPLACEMENTS BY THERMAL SPIKES

If sufficient energy is lost to a number of neighboring atoms, that small region of the crystal may reach a local temperature that is well above the melting point of the bulk material. If this condition persists for a sufficiently long time the atoms may undergo sufficient motion to jump from their lattice sites into interstitial positions and diffuse away, leaving vacancies behind. This is often referred to as the "thermal spike" process.

Thermal spikes are generated by the slowing down of displaced atoms. Because of the low energy of the displaced atoms, the probability of a collision between a displaced atom and an atom on a lattice site is very large. This results in a mean free path that approaches the lattice spacing. Essentially all of the energy of the displaced atom will be lost in a very small volume, thus giving a thermal spike whose magnitude is determined by the initial energy of the displaced atom. A brief calculation may be useful to illustrate the possible magnitude of these effects. The maximum energy that can be transferred to a silicon atom by a 2-Mev electron is 461 ev. By using $T_d=12.9$ ev[9] one finds that the average energy of all silicon atoms displaced by 2-Mev electrons is about 37 ev.[10] Thus, the average thermal spike arising from the stopping of displaced silicon atoms will have an energy of about 37 ev. The magnitude of the temperature attained in the center of this hot spot is evident when one notes that the average thermal energy of a silicon atom at the melting point is only 0.45 ev. Although the temperature is initially very high, it also drops very rapidly. By using the formalism of Seitz and Koehler,[2] one finds that in a time of about 10^{-14} sec the temperature will have dropped below that corresponding to the melting point of the material. This is a time somewhat shorter than the period of vibration of the atoms. It is not now possible to compute the number of displacements that may occur during such a thermal spike. It is often thought that this will be a negligible number. Until a detailed theory has been developed, however, one should not accept this with great certainty.

One needs to ask whether an incident electron can generate a thermal spike in its normal motion through the material. The vast majority of interactions which the electron makes as it moves through the lattice is such as to give up bundles of about 10 ev energy or less in the form of electronic excitation or ionization. As computed from the stopping power, an incident 2-Mev electron will interact about every 300 A losing about 10 ev at each interaction. The extent of the hot spots generated by these 10 ev bundles will be smaller than those discussed above. The same conclusion is valid for this type of spike as for the hotter one; i.e., one is not sure whether defects can be generated by such a short lived spike or not. There is evidence that indicates that defects are generated in such materials as the alkali halides by low energy x rays.[11] Although thermal spikes are not the only mechanism that should be considered as giving these defects, it is one of the more likely.

X-ray absorption may indeed result in the generation of very extensive thermal spikes. This can be seen as follows. Absorption of soft x rays results in the generation of photoelectrons whose energy spectrum, although complicated, contains many electrons of one kilovolt energy and greater. The stopping power of an electron in the kilovolt range is so high that it will essentially suffer an interaction at each lattice site and lose about 10 ev at each interaction.[12] An electron that interacts

[9] This value of T_d is the experimental value determined by Loferski and Rappaport, Phys. Rev. 111, 432 (1958).

[10] The average energy of the displaced atoms was calculated from Eq. (11.12) of Reference 2.

[11] The authors are indebted to Dr. H. Rabin and Dr. C. C. Klick of this laboratory for many discussions of their unpublished results which deal with this problem.

[12] The stopping power of a 1-kev electron in a given material is essentially equivalent to that of a 1.84-Mev proton in the same material. Values of the latter can be found in the Range-Energy Tables compiled by Rich and Madey, U. S. Atomic Energy Commission Rept. UCRL-2301.

at each lattice site will move through the lattice by diffusion. That is, its motion can be approximated by a random walk process. The root mean square distance that the electron will move from an initial point of interaction is $X(N)^{\frac{1}{2}}$ where N is the number of interactions and X is the distance between interactions. If an electron of one kilovolt energy loses 500 ev in steps of 10 ev at each interaction, all of this energy will be lost in a sphere with a diameter of about 7 lattice spaces. If the lattice spacing is taken as the interaction distance and if the energy is assumed to be distributed uniformly in the spherical volume, then some 170 atoms will share the energy. The result would be a hot zone containing these 170 atoms. If the 500 ev is assumed to originate at a point source, then the temperature at the surface of the hot zone will drop to the melting point in a time long compared to the period of vibration of an atom. Thus, defects might easily be generated by this process. The point source approximation overestimates this time. However, the assumption that all atoms in the volume share the energy underestimates the temperature that many of the atoms will experience. It seems likely that under the conditions just described that defects may be generated. The experiment by McKay *et al.*[13] strongly suggests that electrons of insufficient energy to produce direct displacements can cause radiation annealing of damage. This annealing presumably results from thermal spikes generated by these low energy electrons. If the above discussion is valid, then soft x rays should also cause similar annealing.

The authors know of no experiment that shows that lattice displacements are generated solely by such a thermal spike as described above. One might expect that this could be seen in a non-metallic material in which a threshold exists for the displacement of lattice atoms by charged particles. If the above thermal spike mechanism operates, then one should see damage in such a material as a result of x-irradiation, if all the photoelectrons have energies below the threshold.[14]

ACKNOWLEDGMENT

The authors would like to acknowledge many helpful discussions with Mr. Frank H. Attix.

APPENDIX

The following equations give the fraction, N_d/N_0, of atoms displaced by an incident electron of energy E in terms of the parameter X_m where $X_m=T_m/T_d$. T_m is defined by Eq. (3). α, β, and b are defined above.

$$X_m \geqslant 5$$

$$N_d/N_0=\frac{\pi b^2}{4}\{0.2737X_m+1.2891\beta^2-(0.4428X_m^{\frac{1}{2}}-0.1671)\pi\alpha\beta+0.561[(X_m-\beta^2-\pi\alpha\beta)\ln X_m+(\pi\alpha\beta-\beta^2)X_m-1]\}$$

$$4\leqslant X_m\leqslant 5$$

$$N_d/N_0=\frac{\pi b^2}{4}\{2.7652X_m-1.4444\beta^2+(25.0313X_m^{\frac{1}{2}}-25.4444)\pi\alpha\beta-2(1+6\pi\alpha\beta)\ln X_m-(1+3\pi\alpha\beta)(\ln X_m)^2-0.1667(1+3\pi\alpha\beta+\beta^2)(\ln X_m)^3-0.04167(\beta^2+\pi\alpha\beta)(\ln X_m)^4-2\}$$

$$3\leqslant X_m\leqslant 4$$

$$N_d/N_0=\frac{\pi b^2}{4}\{2.4140X_m-0.6374\beta^2+(12.5067X_m^{\frac{1}{2}}-12.6374)\pi\alpha\beta-2(1+3\pi\alpha\beta)\ln X_m-0.5000(1+\beta^2+3\pi\alpha\beta)(\ln X_m)^2-0.1667(\beta^2+\pi\alpha\beta)(\ln X_m)^3-2\}$$

$$2\leqslant X_m\leqslant 3$$

$$N_d/N_0=\frac{\pi b^2}{4}\{1.8466X_m-2-(1+\beta^2+3\pi\alpha\beta)\ln X_m-0.5000(\beta^2+\pi\alpha\beta)(\ln X_m)^2+0.2402\beta^2-5.7598\pi\alpha\beta+5.8087\pi\alpha\beta X_m^{\frac{1}{2}}\}$$

$$1\leqslant X_m\leqslant 2$$

$$N_d/N_0=\frac{\pi b^2}{4}\{X_m-1-\beta^2\ln X_m+\pi\alpha\beta[2(X_m^{\frac{1}{2}}-1)-\ln X_m]\}.$$

[13] MacKay, Klontz, Goheli, Phys. Rev. Letters **2**, 146 (1959).

[14] The authors have looked for such an effect in *n* type InSb, x-irradiated at 77°K. No evidence was found for the generation of defects which give rise to low lying acceptor levels.

X-Ray Examination of Brittle Fractures in Extruded Chromium

C. W. WEAVER AND K. A. GROSS
Australian Defence Scientific Service, Defence Standards Laboratories, Department of Supply, Maribyrnong, Victoria, Australia
(Received September 3, 1958)

X-ray examinations of brittle fractures in polycrystalline chromium, produced at temperatures between 193°K and 623°K, have been made. Estimates of the amount of deformation present at the fracture surfaces showed that very large plastic strains were associated with brittle cleavage fracture at the higher temperatures, such that the length of a self-sustaining crack calculated according to the modified Griffith crack formula of Hall, was more than an order greater than the mean grain diameter of the material. Plastic strains of this order would be expected to result in ductile behavior. It is suggested that brittle failure was caused by the presence of a fine dispersion of precipitate particles, which delayed the action of cross slip in sealing off the early stages of cracking. The spacing of the precipitate particles was estimated to be between 6000 and 7000 A.

INTRODUCTION

X-RAY examinations of low-temperature brittle fractures in iron and zinc[1–4] have shown that measurable plastic deformation is associated with the growth of cleavage cracks, even though no signs of macroscopic strain appear in the body of the material. These observations were made on fractures produced at low temperatures, where the "Cottrell locking" of dislocations by trace impurities is believed to strongly affect the yield stress.[5]

At these low temperatures, Chang[4] found by x-ray microbeam methods that the amount of plastic work involved in the fracture process (i.e., the plastic work factor), depended on the temperature and on the grain size of the material, and the minimum length of a self-sustaining crack as calculated by the modified Griffith crack formula of Hall[3] was approximately equal to the mean grain diameter. Stroh's[6–8] theoretical model of crack nucleation and growth also establishes a similar relation under conditions where Cottrell locking applies. The incidence of brittle fracture may also occur at higher temperatures, as for example in molybdenum between 248°K and 298°K[9] and in tungsten between 423°K and 723°K,[10] but here again it is associated with a temperature-dependent yield behavior similar to that found in α-iron. In the case of annealed chromium, however, anomalous behavior is found in that, although the brittle fracture strength exhibits a strong temperature-dependence between about 173°K and 373°K,[11] brittle fractures occur at temperatures up to 623°K under conditions which, from a consideration of the behavior of other metals having the body-centered cubic structure, would be expected to produce ductile behavior. The present investigation was therefore made to determine the extent to which current models of brittle fracture were applicable in the case of annealed chromium.

EXPERIMENTAL

Arc-melted electrolytic chromium of high purity* was extruded, machined to tensile specimens, and electro-polished to a mirror finish on the gauge length. Specimens were annealed 2 hr at 1523°K *in vacuo* and strained to fracture at a rate of 0.008 in./min in a Hounsfield tensile machine fitted with a strain-gauge autographic recorder.

The autographic record showed no signs of macroscopic strain in any of the specimens fractured up to 623°K and no signs of slip lines were observed in the gauge length behind the fracture, though there were occasional signs of local deformation immediately adjacent to the fracture surface itself.

A conventional x-ray tube and back reflection camera were used to examine the fracture surfaces, using copper

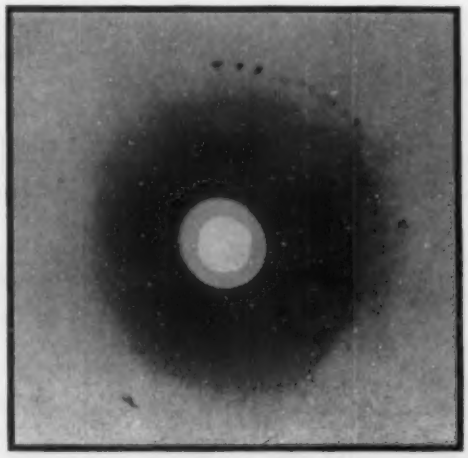

FIG. 1. Back-reflection pattern from surface fractured at 288°K.

* The major impurities were nitrogen, 0.002%, carbon, 0.002%, and oxygen, 0.02%.

[1] E. Orowan, *Fatigue and Fracture of Metals* (John Wiley & Sons, Inc., New York, 1950), p. 155.
[2] E. P. Klier, Trans. Am. Soc. Metals **43**, 935 (1951).
[3] E. O. Hall, J. Mech. Phys. Solids **1**, 227 (1953).
[4] L. C. Chang, J. Mech. Phys. Solids **3**, 212 (1955).
[5] A. H. Cottrell and B. A. Bilby, Proc. Phys. Soc. (London) **A62**, 49 (1949).
[6] A. N. Stroh, Proc. Roy. Soc. (London) **A223**, 404 (1954).
[7] A. N. Stroh, Phil. Mag. **46**, 968 (1955).
[8] A. N. Stroh, Proc. Roy. Soc. (London) **A232**, 548 (1955).
[9] A. P. Carreker, Jr., and R. W. Guard, J. Metals **8**, 178 (1956).
[10] J. H. Bechtold and P. G. Shewmon, Trans. Am. Soc. Metals **46**, 397 (1954).
[11] C. W. Weaver (to be published).

radiation, with a nickel filter in contact with the film. The area irradiated was 1 sq mm and beam divergence approximately 1°. The (310) and (222) reflections were recorded together with some Laue spots. The use of a large beam reduced the precision of measurement of plastic strain compared with micro-beam methods[4] because of the overlapping of the circumferential broadening of the reflections, which precluded direct measurement of this broadening. A calibration series in ductile chromium was therefore used to establish the degree of circumferential broadening produced by specific applied strains, and the strains at the brittle fracture surfaces were estimated by direct comparison with these.

At low temperatures, the amount of plastic deformation was very small, and usually only slightly distorted Laue spots were obtained. Calculations showed, however, that the presence of a layer of distorted material less than 0.1 μ thick would not be detected by the x-ray beam (see Appendix), which is a greater depth than that estimated by Hall in the case of iron.[3] It was estimated that the bulk of the diffraction pattern originated from material less than 3 μ below the surface.

RESULTS

A large increase in the amount of distortion at the fracture surfaces occurred as the temperature of testing was raised. In the specimen fractured at 153°K, only a slight distortion of Laue spots was found, but fracture at 288°K produced severe distortion of the Debye spots as shown in Fig. 1, and some signs of residual elastic strains were also evident. Distortion of the Debye spots increased with temperature until at 623°K an almost complete ring was produced (Fig. 2), but at these higher temperatures the elastic strains were relieved before the specimens were cooled to room temperature. These early results showed that the degree of plastic deformation, which occurred at the higher temperatures, was much greater than that previously reported for other brittle fracture surfaces. When the surface strain data for the present work were plotted (Fig. 3) against temperature, together with Chang's data[4] on iron and zinc, the trends of the curves suggested that the present method of measuring strain may have given low results at the lower temperatures. At elevated temperatures, however, the strains recorded in the chromium were very high, often in excess of 15%. Further signs of large plastic deformations were also found in the presence of long ductile ribbons of metal which had been raised from the surface during cleavage, as described recently in cast chromium by McNeil and Limb,[12] and to a lesser degree in iron by Low.[13] Repeated x-ray examination of the fracture surfaces also revealed that, particularly in the low-temperature fractures (153°K and 288°K), the amount of plastic strain varied considerably from place to place, corresponding to some extent with changes in the appearance of the fracture which presumably arose from changes in the velocity of the crack. Fractures produced at higher temperatures (423°K and 623°K) were more uniform in appearance and the amounts of plastic strain recorded, though very large, were much more uniform.

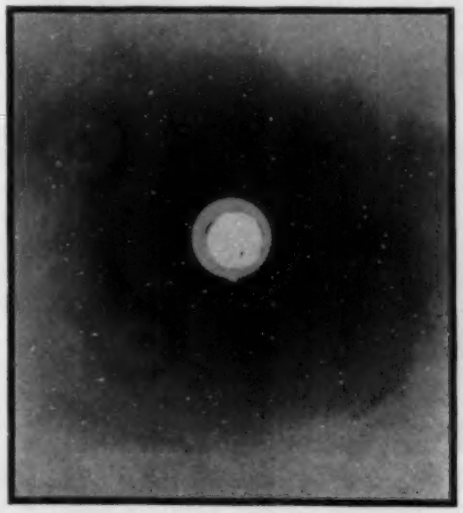

FIG. 2. Back-reflection pattern from surface fractured at 623°K.

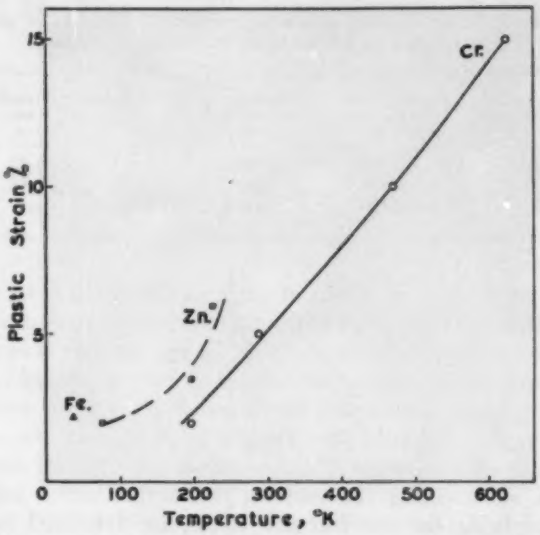

FIG. 3. Effect of temperature on the plastic strain at the brittle fracture surfaces of chromium (present work), iron and zinc (Chang[4]).

The depth of the deformed layer was measured by removing successive layers from the surface by electropolishing, followed by further x-ray examinations, to a total depth of 20 μ. The sides of the specimens along the gauge length were also examined both microscopically and by x-rays for signs of deformation, but none were found, which accords with the absence of macroscopic deformation in the tensile records.

[12] J. F. McNeil and H. R. Limb, "Cleavage fracture in cast chromium of high purity" (to be published in J. Inst. Metals).

[13] J. R. Low, *Deformation and Flow of Solids* (Springer-Verlag, Berlin, 1956), p. 60.

TABLE I. Effect of temperature on the plastic work factor and critical crack length in chromium brittle fractures.

Temperature, °K	Plastic work factor ω ergs/cm²	Surface energy γ ergs/cm²	Crack length $2C$ μ	Grain size μ
288	2×10^6	2000	47	42
473	4.6×10^5	2000	250	44
623	6.4×10^4	1900	1060	40

The amount of strain in each specimen fell from a maximum at the original fracture surface to a constant value of about 2% in the body of the specimen, in a manner closely similar to that found experimentally by Chang[4] and theoretically by Gilman.[14] The plastic work factor ω was obtained graphically by plotting curves of plastic strain against distance below the fracture surface, substracting the uniform prefracture strain and multiplying by the fracture stress, as described by Chang.[4] These results are given in Table I.

DISCUSSION

The factors governing the propagation of brittle fracture in a metal may be expressed according to the modified Griffith crack formula of Hall,[3] as

$$\sigma_f=[2E(\omega+\gamma)/\pi C]^{\frac{1}{2}}, \qquad (1)$$

where σ_f=the brittle fracture stress, E=Young's modulus, ω=the plastic work factor, γ=the surface energy of the crack, and $2C$=the minimum length of an internal self-sustaining crack.

The surface energy term γ is usually small compared with ω[3,4] but may be found from[6]

$$\gamma=\alpha Gb, \qquad (2)$$

where α=const, a=approx. 0.06, b=Burgers vector, and G=the rigidity modulus.

Values of G for chromium were calculated from elasticity modulus data[15] and Poisson's ratio.[16] γ was slightly temperature dependent, as the data in Table I shows, but was of the same order (i.e., $\sim10^3$ ergs/cm²) as in iron.

The critical crack lengths $2C$ calculated according to Hall's formula are also listed in Table I together with the mean grain diameters of the individual specimens. It is immediately apparent that at elevated temperatures, the crack lengths as calculated are greatly in excess of the mean grain diameters of the specimens, and that the correspondence between grain diameter and critical crack length found by Chang[4] and Stroh[8] no longer holds.

The models of crack nucleation and growth currently proposed[6–8,14] are based on the three major premises.

(a) Interstitial locking of dislocations is required to limit the number of slip sources operating and to provide an avalanche of dislocations from the few operating sources.

(b) Grain boundaries form impenetrable barriers to this slip, thus promoting the conditions for the formation of crack nuclei.

(c) Plastic deformation at the tip of the crack will reduce the velocity of the crack, or stop it altogether if sufficient deformation can occur during the time that the tip of the crack is passing a Frank-Read source.

The data of Fig. 3 suggest that the high deformations observed at the fracture surfaces should have been sufficient to stop the growth of the cracks to an unstable size (the limiting crack size in ductile material being about 1 μ[17]) and the very large crack sizes calculated from Eq. (1) and shown in Table I suggest that the grain boundaries themselves do not offer very great resistance to their spread at elevated temperatures. Thus, the influence of two of the factors most strongly affecting brittle fracture was probably quite small at these temperatures and other contributory causes of the brittle fractures must be sought. On the other hand, despite the high plastic strains present, the plastic work factors in these specimens were not as high as those found in zinc and iron[4] at lower temperatures, due in part to the moderately low stresses at which fracture occurred.

Under a constant applied shear force, a crack of subcritical size will grow only if it has enough energy to maintain a high velocity, sufficient to propagate it across a grain and through the enclosing boundaries. Local structural factors such as grain boundaries (the grain size effect), changes in orientation or the presence of precipitate particles and inclusions may, however, considerably decrease the velocity by absorption of

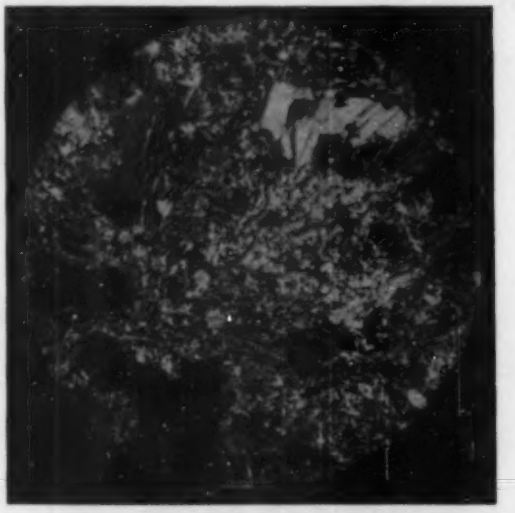

FIG. 4. Brittle fracture surface produced at 193°K. ×15.

[14] J. J. Gilman, J. Appl. Phys. **27**, 1262 (1956).
[15] D. J. Maykuth and R. I. Jaffee, Trans. Am. Soc. Metals **49**, 948 (1957).
[16] H. Pursey, Nature **169**, 150 (1952).
[17] N. F. Mott, *Deformation and Flow of Solids* (Springer-Verlag, Berlin, 1956), p. 53.

energy in multiple cleavage[13,14] and cross slip, both of which will cause an increase in the plastic work factor.[3,14] Since cross slip is dependent to a large extent on the degree of Cottrell locking and the velocity of the crack, slip should be more easily initiated at slightly elevated temperatures where the locking forces are reduced, than at low temperatures. The velocity of the crack should therefore be low, with consequent high-energy absorption as plastic strain. Thus, the surface of a fracture produced at 193°K contained large smooth areas near the source of the fracture surrounded by areas of more complex cleavage (as shown in Fig. 4). This indicates the operation of only one or two cracks at high velocity, whereas a fracture at 473°K contained no large smooth areas nor any single well-defined source of fracture, but rather a homogeneous appearance, indicating the operation of many crack nuclei simultaneously (Fig. 5).

The operation of several sources simultaneously would serve merely to delay the growth of the cracks by mutual relief of stress at points of overlap and by the occurrence of ductile yielding between cracks,[13] unless the initial interactions were delayed by a mechanism which would hinder cross slip and keep the energy absorption due to plastic work below the limit required to stop the crack. Such a mechanism could perhaps be provided by the presence of a finely dispersed precipitate, the influence of which has previously been reported in chromium.[18,19] The back-stress or hardening effect of precipitation could materially affect the velocity of the crack by absorbing energy and restricting the propagation of slip, and these processes may be invoked here to explain the present combination of high plastic strains with brittle fractures.

The operation of delayed yielding effects must also be considered even at these relatively high temperatures, since sharp yield points have been observed even in the purest available material at 623°K and 473°K.[11] Delayed yielding does not, however, account for the high plastic strains in these specimens since large amounts of stored energy would be available on yielding which would result in a crack of high velocity with little plastic deformation. On the other hand, interstitial impurities appear to be completely removed from solution as precipitates after small plastic strains[18] with elimination of the upper yield point and an increase in flow stress. The complete absence of interstitial damping peaks in internal friction measurements on chromium[20] provides further evidence for the extremely low solubilities of nitrogen and carbon at these temperatures.

A distinct difference in behavior during the early stages of plastic flow also arises from the two mechanisms. With simple dislocation locking the stress falls

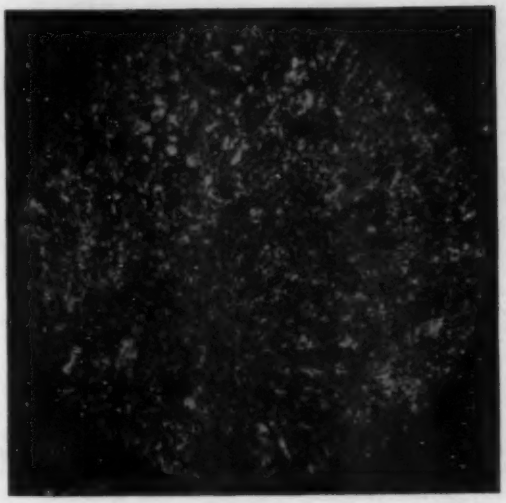

FIG. 5. Brittle fracture surface produced at 473°K. ×15.

rapidly to a low value once the dislocation is freed from its attendant atmosphere, and no further solute effects occur so long as the velocity of the dislocation exceeds the diffusion rate of the solute. A precipitate array on the other hand offers a barrier of an order intermediate between the upper and lower yield conditions. The "back stress" or resistance to flow offered by an array of precipitate particles is an additional stress superimposed on the normal driving stress of the dislocation in an unimpeded state, and depends to a first approximation on the distribution of the precipitate particles (or nuclei) according to the relation[21] $\tau_{\text{total}}=\tau_d+\tau_p$, where

$$\tau_d=qG(b/d), \tag{3}$$

and τ_p = the driving stress of a dislocation, τ_p = the back stress produced by precipitation, $q=a$ const$\simeq 1$, G = the rigidity modulus, b = Burgers vector, d = the spacing of precipitate particles, and on their size as it affects the ability of the particles to support the imposed shear stresses. The effective size of the particle also increased with the passage of dislocation lines by the accumulation of rings of dislocations to a limiting diameter of approximately 2.3 times the diameter of the precipitate particle,[22] and the resulting back stress will therefore increase slightly to a steady value in the early stages of deformation.

Some preliminary evidence for the presence of a structure (e.g. precipitates) which could exert a "back stress" corresponding to τ_p in Eq. (3) is provided by the following experiment: a specimen, previously annealed *in vacuo* at 1523°K, was strained in tension to beyond the yield point at 673°K (Curve *A*, Fig. 6). After re-annealing at 1523°K, tensile straining was repeated, when yielding occurred at a much lower load and no upper yield appeared (Curve B, Fig. 6).

[18] C. W. Weaver, Nature **180**, 806 (1957).
[19] Wain, Henderson, Johnstone, and Louat, J. Inst. Metals **25**, 281 (1958).
[20] M. E. DeMorton, "Preliminary internal friction experiments in chromium" (to be published).
[21] E. Orowan, "Dislocations in metals," Am. Inst. Mining Met. Engrs. (1954), p. 133.
[22] Fisher, Hart, and Pry, Acta Met. **1**, 336 (1953).

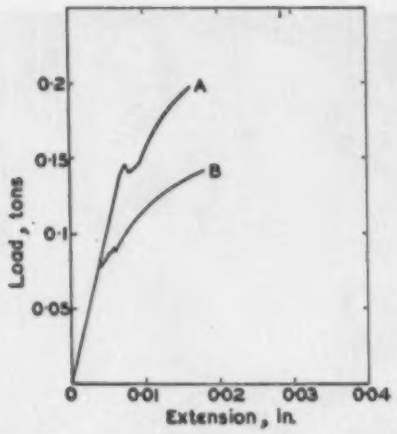

FIG. 6. Tensile tests on extruded chromium at 683°K. Curve A. Specimen annealed for 1 hr at 1523°K. Strained in tension. Curve B. Same specimen, reannealed for 1 hr at 1523°K and subsequently restrained.

In the first test, it is thought that two processes were operating together, namely strain-aging which occurred during the heating of the specimen before test to produce the upper yield point, and precipitation which occurred partly during heating before test, but mostly during the straining before yielding. In the second test, most of these precipitates would be expected to have dispersed during annealing, but it is though that sufficient nuclei remained to cause rapid over-aging prior to test, with the result that (a) the material was softened and (b) the upper yield point was eliminated because not enough interstitial impurities (i.e., nitrogen or carbon) remained in solution to produce it.

Equation (3) may now be used to calculate the spacing of the precipitate particles. If we take τ_p, the "back stress" caused by precipitation as the difference between the lower yield stress of Curve A and the yield stress of Curve B in Fig. 6, i.e., 3 ton/in.^{2} (or $3\times1.544\times10^8$ d/cm^2), $q=1$, $G=11\times10^{11}$ d/cm^2 and $b=2.88\times10^{-8}$ cm, the distance d between particles is

$$d=\frac{11\times10^{11}\times2.88\times10^{-8}}{3\times1.544\times10^8}\text{ cm},$$

i.e. $d=6650$ A, which is very similar to the spacing (7000 A) between precipitate particles in iron-carbon alloys at 585°K found by Wert.[23] In the presence of interstitial carbon and nitrogen totalling 150 parts per million, about 10^6 impurity atoms are available for precipitation at each of these sites in combination with chromium, which in view of the extremely low solid solubilities of these elements[24] at these temperatures, is more than sufficient to provide particles of sizes up to 600 A diam.

Although these tests were made in the ductile condition at a temperature slightly higher than those producing brittle fracture, they do provide a measure of the structural conditions in the material which may contribute toward the observed anomalous behavior.

The total effects of a precipitate array on a system also containing "locked" sources of slip in the presence of a moving crack may therefore be as follow.

1. Shear stresses normal to the plane of the crack would operate nearby Frank-Read sources causing local yielding, and release the first of an avalanche of dislocations.
2. The movement of dislocations across the path of the crack would be delayed by the precipitate arrays because of (a) the increase in length required to permit expansion through each barrier and form loops around the particles, and (b) the back stress thus induced.
3. The continued operation of the sources combined with the low rate of cross slip would set up a balance between the terminal velocity of the crack under the continuing high stress occasioned by the presence of the precipitates, and the amount of local cross slip which could penetrate the precipitate barriers, Under these conditions, a crack would be slowed down but not stopped, and high local deformations would occur, as in the present case, in combination with brittle cleavage fractures.

It is significant that high plastic work factors and critical crack lengths greatly in excess of the mean grain diameter, have also been reported in zinc[4] at 195°K and 225°K, behavior which again could arise from the inhibition of cross slip (or equivalent deformation) ahead of the crack, in this case arising from the absence of a sufficient number of slip systems in the hexagonal structure.

CONCLUSIONS

X-ray examination of brittle fractures obtained in chromium at slightly elevated temperatures has revealed the presence of very large plastic strains in the fracture surfaces. Calculations of the critical crack lengths by Hall's modified Griffith crack formula suggests that cracks of more than an order greater than the mean grain diameter of the material had existed before catastrophic failure commenced. This differs markedly from the fracture behavior of iron and zinc at low temperatures, where the critical crack length is usually of the same order as the mean grain diameter. Consideration of the effects of structural factors present in chromium, such as precipitate particles, on the velocity of the crack shows that the existence of a back stress (hardening effect) in the slip planes, due to the presence of a dispersed precipitate may serve to (a) maintain a high driving stress on the crack and further its growth and (b) delay the rapid development of cross-slip (but not its inhibition).

Under these conditions, it is suggested that the crack would propagate only very slowly owing to the con-

[23] C. Wert, J. Appl. Phys. 20, 943 (1949).
[24] Caplan, Fraser, and Burr, "Ductile Chromium," Am. Soc. Metals (1957), 196.

tinuous absorption of energy as local deformation, but too fast for the deformation to operate sufficiently ahead of the tip of the crack to stop it. Brittle fracture accompanied by high deformations, instead of ductile behavior, therefore results.

Calculation shows that the spacing of the precipitate particles in chromium at 673°K (i.e., at a temperature slightly above the ductile-brittle transition) is approximately 6650 A, and similar to that of precipitates in iron-carbon alloys at slightly lower temperatures.

ACKNOWLEDGMENTS

Thanks are due to Dr. R. I. Garrod of the Aeronautical Research Laboratories for suggestions on the x-ray data, and to the Chief Scientist, Australian Defence Scientific Service, Department of Supply, Melbourne, Australia, for permission to publish this work.

APPENDIX

Estimate of the Minimum Amount of Surface Deformed Material Detectable

Consider a layer of deformed material, thickness t on the surface of a grain. This layer will give rise to a diffraction *arc* of area A_2 and integrated intensity I_2. If it is less than the depth of penetration of the x-ray beam, then a second superimposed spot of intensity I_1 and area A_1 will appear.

The deformed material will be observed if

$$\frac{I_2}{A_2} \geqslant \frac{1}{M}\left(\frac{I_1}{A_1}+\frac{I_2}{A_2}\right), \tag{1}$$

where M is the range of relative exposure detectable on a photographic film. Now

$$A_2 = mA_1, \tag{2}$$

where m is a factor which can be obtained by direct measurement from our calibration series on ductile chromium.

Combination of Eqs. (1) and (2) gives

$$I_2\left(1-\frac{1}{M}\right) \geqslant \frac{m}{M}\cdot I_1,$$

but since M is large we may write

$$I_2 \geqslant (m/M)\cdot I_1. \tag{3}$$

Now, consider the radiation diffracted by a small lamina δx thick at a depth x below the surface. The path length l in the specimen for this radiation will be

$$l = x(1-\sec 2\theta)$$

and the intensity of the diffracted beam on emerging from the specimen,

$$\delta I = I_0 f \exp[-\mu x(1-\sec 2\theta)]\delta x, \tag{4}$$

where I_0 is the incident x-ray intensity, f a factor which represents the proportion of radiation diffracted, and μ is the linear absorption coefficient. It is assumed that the x-ray beam is of uniform and constant cross section and that f is independent of the state of deformation.

The total diffracted intensity, in each case, is then

$$I_1 = I_0 f \int_t^\infty e^{-\mu k x} dx \tag{5a}$$

and

$$I_2 = I_0 f \int_0^t e^{-\mu k x} dx, \tag{5b}$$

where

$$k = (1-\sec 2\theta).$$

Integration and substitution in Eq. (3) leads to

$$t \geqslant \frac{1}{k}\cdot \log_e\left(1+\frac{m}{M}\right). \tag{6}$$

Finally, substitution of the appropriate values of μ, θ, M, and m leads to the values in Table II. The value of M used is 100; for accurate intensity measurements it would be lower, ~20 (Klug and Alexander[25]).

TABLE II. Relation between the amount of deformation and the minimum thickness of the deformed layer detectable by x-ray measurements.

Deformation (%)	Min. detectable layer (222) reflection	Min. detectable layer (310) reflection
1 to 2.5	0.1 μ	0.05 μ
6.3	0.1 μ	0.10 μ
15.0	0.2 μ	0.15 μ

[25] H. Klug and L. Alexander, *X-ray Diffraction Procedures* (John Wiley & Sons, Inc., New York, 1956), p. 367.

JOURNAL OF APPLIED PHYSICS VOLUME 31, NUMBER 4 APRIL, 1960

Dislocation Multiplication in Lithium Fluoride Crystals

W. G. JOHNSTON AND J. J. GILMAN
General Electric Research Laboratory, Schenectady, New York
(Received October 12, 1959)

Experimental observations are presented of dislocation multiplication, of the defect structure left behind by a moving dislocation, and of cross-glide of individual dislocations in LiF crystals. New dislocation loops form at many different sites in the wake of a moving dislocation. These loops have the same Burgers vector as the parent dislocation but do not, in general, lie on the same atomic plane. The rate of formation of new loops depends upon the magnitude of the applied stress. Such creation of new loops leads eventually to the formation of a wide glide band.

A moving screw dislocation trails many line defects behind it that lie parallel to its direction of motion. The existence and nature of these trails and the observed dislocation multiplication can be explained in terms of a mechanism which involves the formation, by cross-glide, of jogs on a screw dislocation. This cross-glide multiplication mechanism was originally proposed by Orowan and by Koehler. It is demonstrated that cross glide occurs easily in LiF, so that this mechanism is plausible. Some interesting complications arise when jogs are formed that are longer than several atomic spacings but less than several hundred. The defect trails exert a dragging of the screw dislocations that is not negligible compared to the yield stress of a crystal.

INTRODUCTION

ETCH pit studies of dislocation multiplication and glide band formation in LiF single crystals have led to a simple description of the multiplication.[1] During plastic deformation new dislocation loops arise in the wake of a moving dislocation. The new loops arise at many different points near the glide plane of the original dislocation, and have the same Burgers vector as that dislocation. As each new loop expands, small new loops are formed in its wake; so that an entire wide glide band forms, almost catastrophically, from the one initial mobile dislocation. The conventional Frank-Read source that is formed from network dislocations cannot account for the major part of dislocation multiplication in LiF, because it is observed that the new loops form at very many sites that are not located at the original network.

Hirsch[2] and Lomer[3] suggested that the above behavior might result from a double cross-glide mechanism such as that proposed by Koehler[4] and Orowan.[5] According to this mechanism, a length of a gliding screw dislocation moves by cross-glide onto a nearby plane parallel to the original glide plane (see Fig. 1 and description below). Amelinckx and Dekeyser[6] proposed that the multiplication in LiF resulted from prismatic loops formed by jogs on moving screw dislocations. The prismatic loops could act as Frank-Read sources to produce new loops under either sign of applied stress.

When our earlier work was reported,[1] it appeared that dislocations could be formed in dislocation-free regions of LiF crystals at stresses as low as $10^{-4}\,G$, where G is the shear modulus. Since this stress is far too low to allow homogeneous nucleation of dislocations,[7] Fisher,[8] and Weertman[9] suggested that there may be present many small, undetected, prismatic loops, formed by vacancy precipitation in an as-grown crystal, and that such loops could act as dislocation sources. Recently Kuhlmann-Wilsdorf, Maddin, and Kimura[10] have further examined this possibility, and suggested that multiplication would result if the stress field of a moving dislocation could activate such sources on nearby planes. These authors showed that many of our earlier observations could be explained in terms of prismatic loops resulting from vacancy condensation. However, more recent careful work by Gilman[11] has shown that dislocations form in dislocation-free regions of LiF crystals only if small precipitates or other stress raisers are present. Gilman has also shown that dislocations *do not* form in completely defect-free regions of LiF at stresses as high as $G/85$. This later work eliminates the possibility that there exist many small sources capable of creating dislocations at low stresses, and therefore rules out the possibility that the multiplication involves such sources.

In the light of further observations to be presented here, it appears that dislocation multiplication in LiF results from a cross-glide mechanism similar to that proposed by Koehler[4] and Orowan,[5] and somewhat similar to the mechanism of Amelinckx and Dekeyser.[6] It may, therefore, be worthwhile to review how the double cross-glide mechanism might operate in LiF, as shown in Fig. 1. We start with a single dislocation half-loop as in Fig. 1(a). This half-loop lies on the (110) plane and has a [1$\bar{1}$0] Burgers vector. Under an applied

[1] J. J. Gilman and W. G. Johnston, *Dislocations and Mechanical Properties of Crystals*, ed. by Fisher et al. (John Wiley & Sons, Inc., New York, 1957), p. 116.
[2] P. B. Hirsch, (private communication, 1956).
[3] W. M. Lomer (private communication, 1956).
[4] J. S. Koehler, Phys. Rev. **86**, 52 (1952).
[5] E. Orowan, in *Dislocations in Metals* (American Institute of Mining and Metallurgical Engineers, New York, 1954), p. 103.
[6] S. Amelinckx and W. Dekeyser, J. Appl. Phys. **29**, 1000 (1958).
[7] See, for instance, A. H. Cottrell, *Dislocations and Plastic Flow in Crystals* (Oxford University Press, Oxford 1953) p. 53.
[8] J. C. Fisher, footnote 1, p. 153.
[9] J. Weertman, J. Appl. Phys. **28**, 1068 (1957).
[10] D. Kuhlmann-Wilsdorf, R. Maddin, and H. Kimura, Z. Metallk. **49**, 584 (1958).
[11] J. J. Gilman, J. Appl. Phys. **30**, (1959).

stress the half-loop expands as in Fig. 1(b). Its screw components cannot cross-glide on a primary glide plane (each ⟨110⟩ Burgers vector has only one {110} plane associated with it in the rocksalt structure), but they can cross-glide on {100} planes as at *MNOP* in Fig. 1(b). Short segments of edge dislocations (*MN* and *PO*) are thus produced. These segments can glide under high stress along the screw dislocation in the $[1\bar{1}0]$ direction, but they cannot glide at all in the direction of motion of the original screw dislocation, the [001] direction. Therefore these jogs can act as pinning points, tending to restrain the forward motion of the screw segments as in Fig. 1(c). Now, depending on how large *MN* and *OP* are, either the configuration shown in Fig. 1(d) results (case of large jogs) or the configuration of Fig. 1(f) (case of small jogs).

When *MN* and *OP* are large enough to allow the applied stress to push the dislocations of opposite sign (*MS* and *NT*) past each other, the segment *NO* can act like a Frank-Read source as shown in Figs. 1(d) and (e). The original screw dislocation can be restored by the "pinching off" process shown in Fig. 1(d). Further motion gives the original screw dislocation, plus a new glide loop, and a loop (*MNOP*) as in Fig. 1(e).

If *MN* and *OP* are too small to allow the above process to operate, then the situation shown in Fig. 1(f) can arise. The two glide planes are too close together to allow *MS* to pass by *NT* and *OV* to pass by *PU* under the applied stress. In this case, long dislocation dipoles *MNST* and *OPUV* trail out behind the moving screw dislocation. Amelinckx and Dekeyser[6] have suggested that such dislocation pairs may break up into prismatic loops that can act as dislocation sources. If the jogs, *MN* and *OP*, are very small, the dislocation dipoles become equivalent to rows of ion vacancies or interstitial ions.

We will first present a description of observations of dislocation multiplication, of the defect structure left by a moving dislocation, and of cross-gliding of individual dislocations. Then we will show how the proposed dislocation mechanism is in detailed agreement with the observations.

EXPERIMENTAL WORK

A. Techniques

Lithium fluoride crystals were obtained from the Harshaw Chemical Company. The etch pit techniques for revealing dislocations in them have been described elsewhere in detail.[1,12] Specimens are made by cleavage along (100) planes, and dislocation etch pits are formed on the cleavage faces. The (100) surfaces can be dissolved by chemical polishing[1] so that dislocation lines can be followed into the crystal by alternately polishing and etching.

[12] J. J. Gilman and W. G. Johnston, J. Appl. Phys. **27**, 1018 (1956).

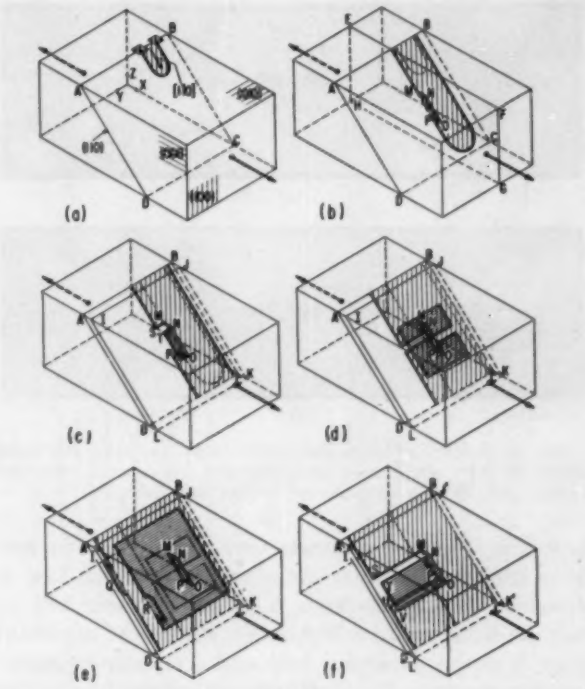

FIG. 1. Showing the operation of a cross-glide multiplication mechanism (after Koehler[4] and Orowan[5]). As the small loop of (a) expands there is cross-glide of the portion *NO*, shown in (b). If the separation of the two glide planes is large, *MP* and *NO* can both act as Frank-Read Sources, as in (c), (d), and (e). If the two glide planes are closely spaced, *SM* and *TN* cannot by-pass one another, and neither can *UP* and *VO*, as shown in (f).

Much of the work to be described involves single dislocation loops of the type depicted in Fig. 1(a). Such loops can be deliberately introduced into a crystal.[1] They will expand if a tensile stress is applied along the length of the crystal, and they will contract if the stress is compressive. Stresses are conveniently obtained by applying a bending moment about axis *AB* (Fig. 1) with a four point bending jig, so that the loops lying near one of the faces experience the maximum stress.

The segments of the dislocation loop that cut the surface in Fig. 1(a) are predominantly screw in character because they lie parallel to the Burgers vector. The loops will become elongated in the direction of the Burgers vector as they expand, because the edge components of dislocation loops move much faster (by ~50 times) than the screw components.[13]

B. Multiplication of Loops

A single dislocation loop such as that in Fig. 1(a) will expand when a sufficiently high tensile stress is applied to it. The rate at which it will expand depends upon the magnitude of the applied stress, and the hardness of the crystal.[13] The rate at which it multiplies also depends on the magnitude of the applied stress. If the stress is

[13] W. G. Johnston and J. J. Gilman, J. Appl. Phys. **30**, 129 (1959).

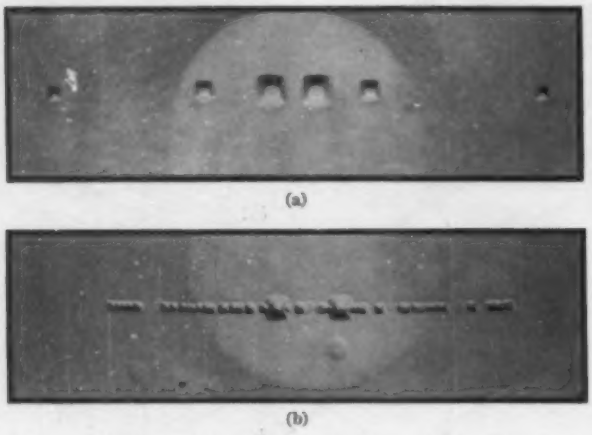

FIG. 2. Multiplication of dislocation loops. (a) Loop expanded slowly in two stages—no multiplication. (b) Loop expanded rapidly with 30% greater stress—profuse multiplication.

kept low, the loop expands very slowly and no new dislocations appear. On the other hand, if the loop is expanded rapidly under a high stress, there will be profuse dislocation multiplication within the expanded loop. A slowly expanded loop and a rapidly expanded loop are shown in Fig. 2. Numerical values showing the dependence of multiplication rate on applied stress were given in a previous paper.[13]

When a single loop is expanded slowly under a tensile stress, etching will form only two etch pits on the crystal surface to indicate the presence of the single loop. If then a higher stress, *either tensile or compressive*, is applied, the original loop will expand further or contract and, upon etching, new etch pits will appear within it. In Fig. 3(a) a crystal is shown that was given this treatment. The two large flat-bottomed pits show where the ends of the enlarged loop were before the crystal was given a short pulse of high stress. The outermost small pits mark the position of the enlarged loop after the stress pulse. The other small pits show the positions of some new dislocation loops. By alternately polishing and etching such a crystal, it can be shown that the new dislocations came from various places near the active glide plane [Fig. 3(b)].

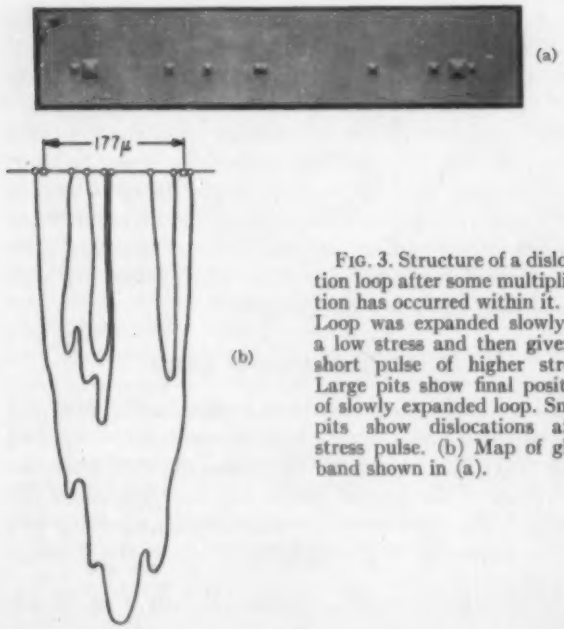

FIG. 3. Structure of a dislocation loop after some multiplication has occurred within it. (a) Loop was expanded slowly at a low stress and then given a short pulse of higher stress. Large pits show final position of slowly expanded loop. Small pits show dislocations after stress pulse. (b) Map of glide band shown in (a).

If instead of being subjected to a stress pulse, an enlarged loop is traced through the crystal by alternate polishing and etching, no dislocations are encountered within the loop. There is *occasional* evidence of "debris" left by the passing dislocations (Fig. 4), but there is nothing that etches like a dislocation. Small circular loops might be overlooked, but since dislocation loops in LiF become greatly elongated because of the difference between edge and screw dislocation velocities, most loops could not escape detection by the chemical sectioning technique.

When a small loop ($\sim 10\,\mu$ diam) is pushed out of a crystal by a compressive stress, it *usually* leaves no trace behind, and subsequent stress applications do not produce dislocations at the same site. However, when an enlarged loop (say $>20\,\mu$ diam or so) is pushed out,

FIG. 4. Round etch pits caused by "debris" left in glide plane of an expanded dislocation loop. The loop was expanded and the crystal was then polished to remove $60\,\mu$ from the surface, and etched. Large pyramidal pits mark the ends of the loop.

the crystal will retain some memory of it. There will be no effect when stresses are applied that are barely sufficient to move glide dislocations; but higher stresses (either tensile or compressive) produce dislocations in the region traversed by the original loop. This is shown in Fig. 5.

The foregoing observations are summarized schematically in Fig. 6. Figure 6(a) represents a loop that has been slowly enlarged by a tensile stress. The etch pits appear as shown on Surface I. Two flat-bottom pits correspond to the original small loop, and two sharp pits mark the ends of the enlarged loop. Chemical sectioning reveals no structure within the loop when Surface I is etched after polishing. If a pulse of higher tensile stress is applied, the original loop expands and new loops with the same Burgers vector appear as in Fig. 6(b). If a pulse of higher compressive stress is applied to the slowly enlarged loop, the loop contracts slightly, and new loops appear with Burgers vector opposite in sign to the original loop, as in Fig. 6(c). If the enlarged loop of Fig. 6(a) is collapsed slowly, a subsequent pulse of either tensile stress or compressive stress will form new loops within the region formerly encompassed by the enlarged loop. In all these cases

the new dislocation loops have either the Burgers vector of the parent dislocation, or a Burgers vector that differs only in sign. Pulses as high as 20 kg/mm² have been applied without forming loops with any other Burgers vectors.

A final aspect of the multiplication process is that the new loops apparently do not necessarily lie on the same atomic plane as the parent loop. This is inferred from the fact that when many dislocations are made by repeated multiplication from one initial loop, wide glide bands are formed [Fig. 7(a)]. As the deformation proceeds, the individual bands widen as shown in Fig. 7(b). This widening has been shown to occur in direct proportion to the total plastic strain in a crystal.[13]

C. Structure within an Enlarged Loop

When an enlarged loop is mapped in depth by alternate polishing and etching of Surface I (Fig. 8), no structure is encountered within the loop that etches like a dislocation. The result is much different, however, when the interior of the same loop is approached from the side i.e., from the surface that is perpendicular to Surface I and contains the Burgers vector. Two ways

FIG. 5. The "memory effect" in LiF. The large loop was pushed out of the crystal, and then a pulse of tensile stress was applied. New dislocations (small pyramidal pits) formed within the former loop (marked by large flat-bottomed pits) 500×.

for doing this are shown in Fig. 8. In the first method, a loop is first enlarged, and then the crystal is cleaved through the loop. In the second method, a small loop near an edge is expanded until one end moves around the edge. When the side surface (Surface II) is etched many etch pits are formed along the trace *OE* which look like dislocation etch pits, as shown in Fig. 8(c). If an enlarged loop is pushed out of the crystal before the crystal is split, etch pits will still form on the cleaved face along the trace of the enlarged loop, i.e., the internal structure is not completely eliminated when a loop is removed from the crystal.

The etch pits within an expanded loop (Fig. 9) are usually quite numerous, they are deeper than pits formed at screw dislocations, and during even short etching periods some of the pits become flat-bottomed. This might imply that small loops are being etched, and each time a loop is etched out a pair of flat-bottomed pits appears.[1] This inference is incorrect for the present case. Close examination reveals the etching effect is not due to small loops. Instead there are line defects that etch much like dislocations, except that they etch intermittently (as shown in the sequence of photographs

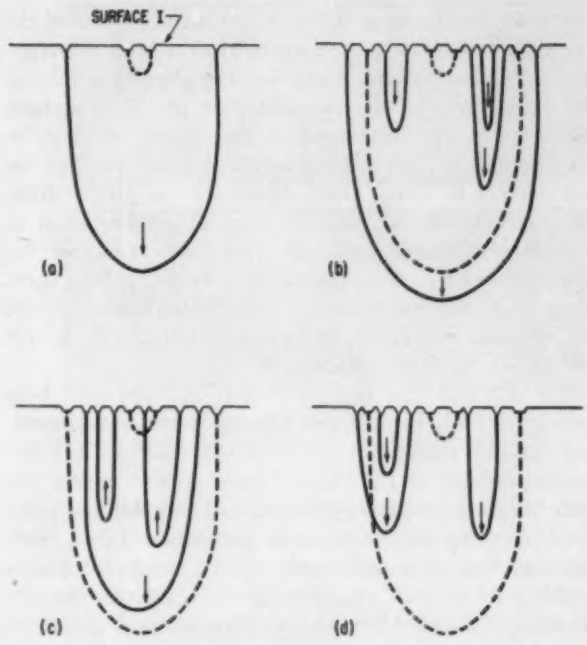

FIG. 6. Schematic summary of dislocation multiplication determined by etching and polishing Surface I. (a) Loop expanded slowly by tensile stress—no new loops appear. Arrow indicates Burgers vector. (b) Expanded loop subjected to higher tensile stress-pulse. New loops appear with Burgers vector of same sign as parent loop. (c) Expanded loop subjected to high compressive stress-pulse. New loops appear with Burgers vector of opposite sign. (d) Large loop pushed out of crystal, and then the crystal was subjected to a high tensile stress-pulse. New loops appear within the former enlarged loop.

of Fig. 9). Some of the line defects etch continuously for tens of microns without interruption, and for others the etching is interrupted every few microns.

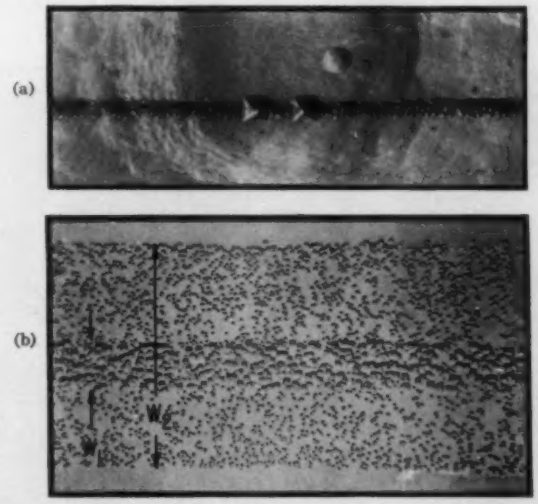

FIG. 7. Lateral growth of glide bands in LiF. (a) Glide band formed at a single loop. Large pits show the position of the single loop. Small pits show that new dislocations lie on both sides of the glide plane of the original loop. (b) Widening of a glide band. Crystal was deformed twice and etched after each deformation. W_1 and W_2 show the glide band widths after the two deformations. 300×

It may also be seen in Fig. 9(c) that when one of the line defects begins to etch again after a brief interruption, the new pit that forms is very slightly displaced from the center of the flat-bottomed pit. Such etching implies that the interruptions correspond to steps in the line defect. The etching behavior indicates that the line defects lie along ⟨100⟩ directions (as judged from the symmetry of the pits), so they lie perpendicular to the Burgers vector and the screw component of the loop. In addition to the pyramidal pits in Fig. 9(c) there are some round, indistinct pits which indicate the presence of other defects, perhaps defects of a less severe nature than a dislocation.

The stepped line defects within an expanded loop appear to trail behind the moving screw component, and for this reason we call them "trails." In any deformed crystal of LiF, these trails appear within the glide bands in which edge dislocations normally appear. Two types of glide bands can be seen on an etched (100) cleavage face of a deformed crystal, one band makes a ⟨010⟩ trace, and the other a ⟨011⟩ trace (see, for example, *AB* and *AD* in Fig. 1). Pure screw dislocations appear in the former, and pure edge dislocations in the latter, hence we refer to the two types of bands as "screw bands" and "edge bands." The pits in a screw band always etched continuously [Fig. 10(a)], while many of the pits in the edge bands etch discontinuously [Fig. 10(b)]. It appears that many of the pits in an edge band correspond to trails rather than to normal dislocation lines.

The trails do not move in response to the same stresses that move normal dislocations. When a crystal is deformed lightly, etched, deformed further, and etched again, it is observed (Fig. 11) that the large etch pits in a screw band almost all become flat bottomed, showing that the initial dislocations moved during the second deformation. In contrast, most of the pits in the edge band continue to etch undisturbed, indicating that the trails did not move during the second deformation.

In summary, enlarged dislocation loops seem to contain stepped line defects, as shown schematically in Fig. 12. The portions of these lines that etch (*AB* and *CD*) lie perpendicular to the Burgers vector, and cannot be revealed by etching a surface that is parallel to themselves (e.g., Surface I). These "trails" can be revealed by etching the surface that is perpendicular to them (Surface II), and they etch in an interrupted manner. The sharp etch pits that form at the trails are usually deeper than those formed at screw dislocations, and in addition some indistinct pits form on Type II surfaces. The trails are not moved by stresses which will move fresh dislocations.

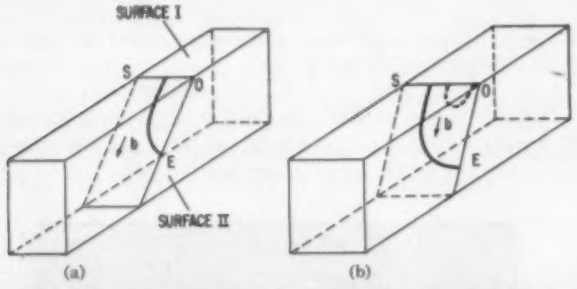

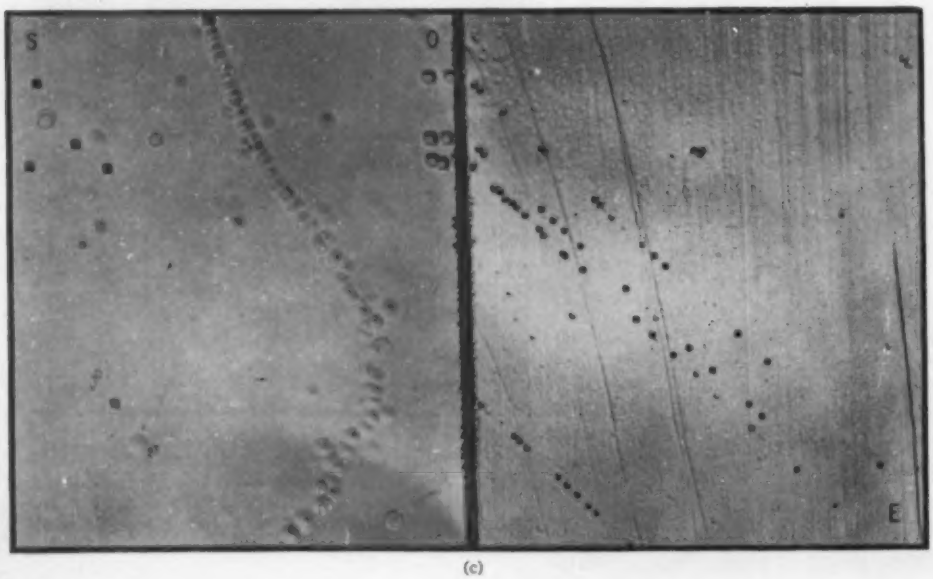

FIG. 8. (a) Crystal with expanded loop cleaved so as to bisect loop. (b) Small loop near edge (dotted) expanded around corner (full line). (c) Photograph of Surface I (left) and Surface II (right) of a split crystal that had several loops. The vertical black strip is the edge of the crystal.

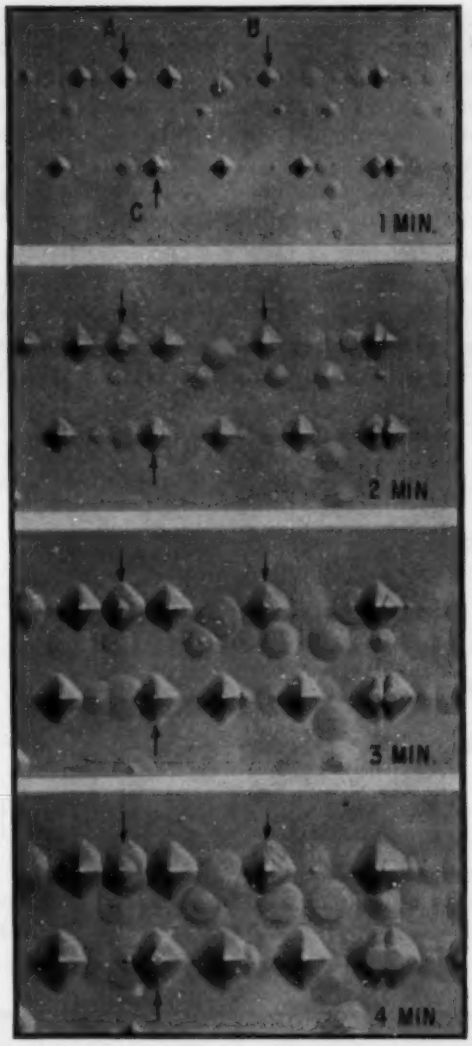

FIG. 9. Etching behavior of Type II Surface. The sequence of photographs was taken after one minute etching intervals. The intermittent etching of some of the pits within the glide bands may be seen in pits *A*, *B*, and *C*. Slight displacements of the bottoms of the pits may also be seen from time to time. 300×.

D. Etch Pit Densities in Edge and Screw Glide Bands

The existence of trails in deformed crystals of LiF resolves an apparent contradiction that existed with regard to densities of pits in edge versus screw glide bands. We have shown[13] that edge dislocations move about fifty times as fast as screw dislocations, so in a deformed crystal there should be fifty times as much length of screw dislocation as edge dislocation. However, etch pit counts do not agree with this. For example, consider the crystal shown in Fig. 13. The crystal measured $\frac{1}{4}$ in. × $\frac{1}{4}$ in. × 1 in. and was compressed slightly and then cleaved into four pieces as shown in Figs. 13(a) and (b). After the crystal was etched, densities of pits in the edge and screw projections of the same band were compared [Fig. 13(c)]. There were more pits (by ~40%) in the edge band, whereas there should have been only about 2% as many. We now believe that most of the pits in an edge band correspond to trails. It follows that there is about seventy times as much length of trails in a glide band as there is length of edge dislocation.

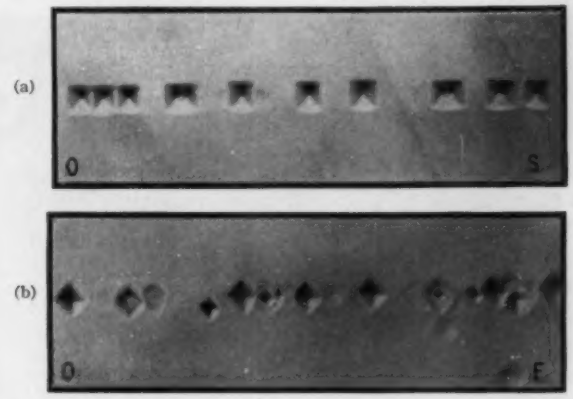

FIG. 10. Difference in etching behavior of bands of screw and edge dislocations. (a) Screw band. (b) Edge band 300×.

Note added in proof. A. A. Urusovskaia [Kristallografiya **3**, 726 (1958)] has observed the effect shown in Fig. 11 and inferred that edge dislocations are less mobile than screws. This conclusion does not agree with our measurements of dislocation velocity,[13] which demonstrated that edge dislocations move faster than screw dislocations at any stress sufficiently high to produce dislocation motion. Our suggestion that the defects in an edge band are immobile because they are not single edge dislocations is compatible with all existing information.

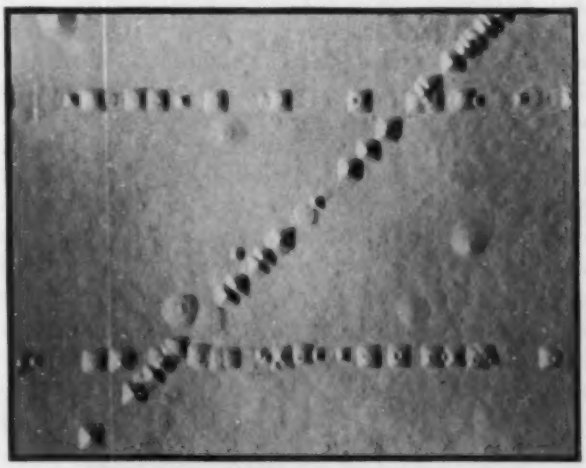

FIG. 11. Crystal with two screw bands (horizontal) and one edge band (diagonal), which was deformed twice and etched after each deformation. Practically all of the line defects in the screw bands moved during the second deformation, while most of those in the edge band did not move. 300×.

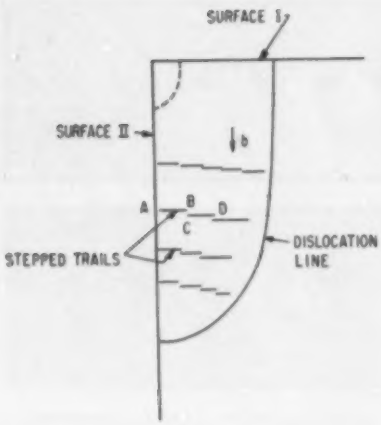

FIG. 12. Schematic representation of stepped trails within an expanded dislocation loop.

E. Cross-Glide in LiF

Since the possibility has been suggested of a dislocation multiplication mechanism which involves cross-glide, it is of interest to examine the occurrence of cross-glide in LiF. We have shown in the past[1] that dislocations in LiF can move out of their normal (110) glide plane onto an (001) plane. It often happens that when a freshly bent crystal is etched, dislocations move out of some of the screw bands. In particular, they tend to move out of screw bands that have a gradient of plastic strain along their length. Figure 14 shows such a screw band in a crystal that was bent and etched immediately. Some of the dislocation ends moved during the etching time in a direction perpendicular to the glide band, and a few of the dislocations moved along paths not quite normal to the glide band.

The motion of dislocation ends shown in Fig. 14 seems to be always directed towards the acute angle formed by the glide band and the surface. In Fig. 15 are shown the matching cleavage surfaces of a crystal that was deformed, then immediately cleaved, after which both surfaces were etched. The cross-glide was in opposite directions in the two surfaces, consistent with the observation that the motion is always towards the acute angle.

The possibility that the observed cross-glide occurs only during etching can be eliminated by deforming a crystal and then waiting a short time before etching as was done for Fig. 16. In that photograph it is clear that some of the dislocations were far from the glide band when the etching was begun. Also, some dislocations left the glide band during the etching. It appears that some dislocations leave the band immediately after deforming, while others leave at later times. The velocity of cross-glide of dislocation ends in Figs. 15 and 16 is as high as 3 or 4 μ/sec in some cases.

Although the cross-glide appears to be always in the direction dictated by the line tension of the dislocation, it can be shown that the line tension cannot be the main driving force for the motion. The calculated elastic energy of a dislocation gives a good approximation to the line tension, and the resistance to cross-glide can be taken equal to the measured resistance to dislocation motion in the primary glide plane. The radius of curvature of a dislocation that is calculated from these two quantities gives a rough approximation to the distance that the dislocation end should pull out of the glide band at the surface. Such a calculation indicates that the line tension is sufficient to cause a motion of only about one micron. Since the observed cross-glide is often one hundred times that amount, we must infer that the line tension is not the principal driving force. The driving force may well be due to the residual elastic strains near the glide band.

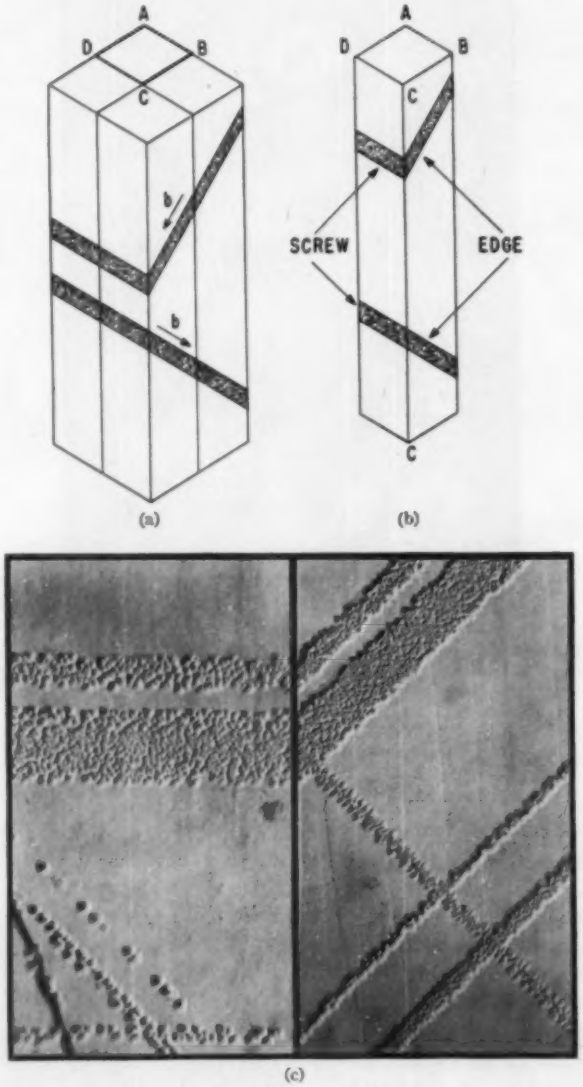

FIG. 13. Comparison of etch pit densities in screw and edge views of a glide band. (a) Deformed crystal to be cleaved into four sections. (b) One section showing two glide bands. (c) Photographs of screw and edge views of glide bands taken at a corner (vertical black stripe). 250×.

DISCUSSION

A. Multiplication Mechanism

If very small jogs are formed on a moving screw dislocation, they may move with the dislocation leaving behind trails of point defects; and if very large jogs are formed the double cross-glide mechanism shown in Fig. 1(a)–(e) will operate. The intermediate case [shown in Fig. 1(f)] of jogs too large to create point defects, and too small to cause immediate multiplication is also of interest. We may consider such a jog, *AD*, on a predominantly screw dislocation *SS'* in Fig. 17(a). The jog, being too long to move with the dislocation, and too short for by-passing remains connected to the parent dislocation by the two parallel lines *AX* and *DY* [Fig. 17(b)].

In general, *SS'* will not be a perfectly straight, pure screw dislocation, so that the two trailing dislocations will not be perpendicular to the Burgers vector, and the situation depicted in Fig. 17(c) will prevail. Such a configuration can reduce its energy by changing to the one in Fig. 17(d), where the double dislocation trail has become stepped and the screw portions (*CE* and *BF*) have annihilated by cross-glide. This leaves prismatic loops such as *ABCD* that lie perpendicular to the screw dislocation. This mechanism requires only glide and cross-glide and so should operate at any temperature. Furthermore, the configuration of Fig. 17(d) has the minimum length of dislocation line, and thus seems to be the lowest energy configuration that can be achieved by glide and cross-glide during the motion of a predominantly screw dislocation containing an intermediate size jog.

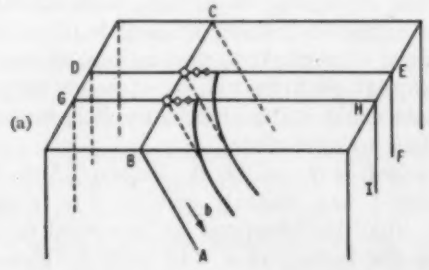

(b)

FIG. 14. Cross-glide of (110) $\langle 1\bar{1}0 \rangle$ dislocations. (a) Sketch of two dislocations, the ends of which have moved by cross-glide out of the normal glide plane (*ABC*) along the (001) planes (*DEF*) and (*GHI*). (b) Photograph showing motion towards the right of the ends of screw dislocations out of their (110) glide plane. 300×.

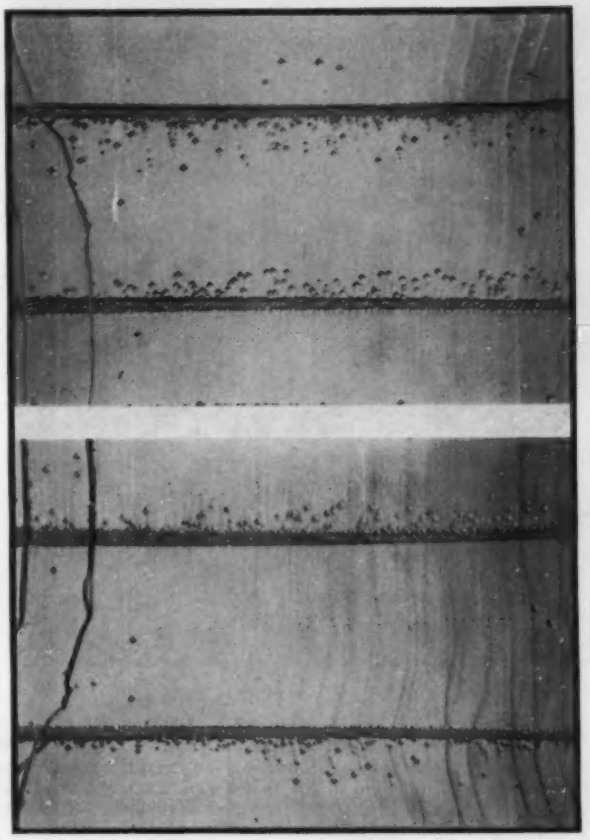

FIG. 15. Cross-glide on two matching cleavage faces of a crystal that was deformed and cleaved, and both halves were then etched. 300×.

The stepped trail left by a large jog depicted in Figure 17(d) would exhibit the etching characteristics that we have observed in LiF. The etching would be

FIG. 16. Etching was begun 3 min after deformation. By that time many dislocations had moved out of the screw band, and they continued to move during the etching. 500×.

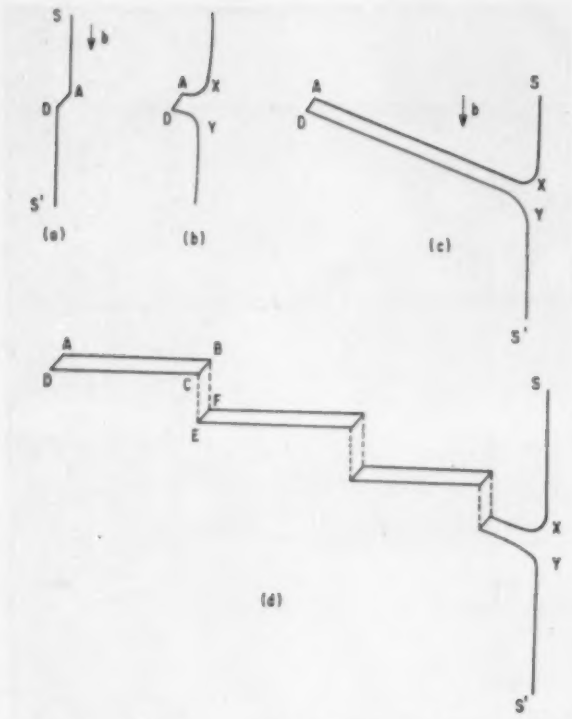

FIG. 17. (a)–(c) show how a jog on a screw dislocation causes formation of a double trail, AX and BY, as the dislocation moves while the jog is immobile. If SS' is not a pure screw dislocation, the double trail will tend to break up as in (d), by glide of AB and DC, and cross-glide and annihilation of CE and BF.

interrupted, with a slight displacement at each interruption. The double dislocation line AB-CD would etch more rapidly than a single dislocation, accounting for the rapid etching that is observed in edge bands.[14] The trails lie parallel to the edge component, and might not be observed during etching on the surface through which the screw component emerges. Finally, the trails would not be expected to move readily at the low stresses that are needed to move individual dislocations.

Upon application of sufficiently high stress the prismatic loops of Fig. 17(d) could operate as dislocation sources, and such sources should exhibit all the characteristics we have observed in the multiplication. The two glide dislocation loops that could form from such a source would lie on closely spaced planes, but not on the same plane, so that this mechanism would naturally lead to a formation of ever-widening glide bands. The sources would produce dislocations with the same Burgers vector as the original loop, and operate under either sign of applied stress. When an enlarged loop is collapsed, it cannot be expected to retrace its movements exactly so that all of the trails would not be removed, and further, new trails would be formed during the collapse. This accounts for the so-called "memory effect."

[14] J. J. Gilman, W. G. Johnston, and G. W. Sears, J. Appl. Phys. **29**, 747 (1958).

The stress required to activate a long prismatic loop source is roughly the stress required to move two parallel edge dislocations of opposite sign [AB and CD in Fig. 17(d)] that lie on parallel planes spaced a distance d apart, past one another. This stress is

$$\sigma = Gb/8\pi(1-\nu)d,$$

where G is the shear modulus and ν is Poisson's ratio.[15] Hence, the stress required to activate such a source is inversely proportional to the size of the jog which led to its formation.

The jogs in a dislocation probably range in size from one atomic distance upwards, with very few large ones and many small ones. At relatively low stresses only the sources formed by very large jogs will be activated, and the parent dislocation may move a large distance before a sufficiently large jog is formed. At higher stresses the smaller sources will be activated, so the apparent rate of multiplication should increase rapidly with increasing stress as we have reported.[13]

B. Plausibility of the Suggested Mechanism

The proposed double cross-glide mechanism accounts for the observed multiplication and structure within glide bands in LiF. However, the nature of the driving force for cross-glide is not clear. It cannot be caused directly by the applied stress because the shear component of this stress on the cross-glide plane equals zero. Also, it does not seem to be caused by long range internal stresses because it was found that the superposition of torques (to produce shear stress on the cross-glide planes) during the bending of crystals had little or no effect on the rate of multiplication or the amount of cross-glide. When they originally discussed the double cross-glide mechanism, both Koehler[4] and Orowan[5] suggested that the cross-glide might occur as the result of thermal stress fluctuations. However, it is not clear that such fluctuation at room temperature and below could cause sufficiently long segments of dislocations to cross-glide.

Note added in proof. G. A. Bassett [Acta Met. **7**, 754 (1960)] has recently published a photograph showing what he interprets as decorated monatomic steps on the surface of a KBr crystal. Bassett suggests that the monatomic steps were formed as screw dislocations moved across the crystal. The decorated lines are not straight nor perfectly parallel, and they sometimes cross one another. Therefore, if we accept Bassett's interpretation of the decoration, we must conclude that cross-glide of screw dislocations occurs very commonly during deformation of KBr. This agrees with our proposal that such cross-glide occurs during deformation of LiF, and leads to the proposed multiplication mechanism.

One cause of cross-glide is the interaction of screw dislocations with the external surface. Whenever a

[15] See footnote 7, p. 152.

screw dislocation intersects a surface at an angle, and there is a possible cross-glide plane, some cross-glide must occur because there will be a stress singularity unless the end of the dislocation line is oriented normal to the surface. In the LiF crystals we have studied, the end of the dislocation should move about a micron. We observe cross-glide over much longer distances than that near glide bands that do not lie near other glide-bands. This latter fact suggests that internal stress concentrations cause the additional cross-glide. Such stress concentrations are to be expected in the elastic matrix of a crystal adjacent to a plastically relaxed region.

The jogs formed by cross-glide near a crystal surface could account for the formation of trails near that surface. However, trails also form inside crystals and we have observed that they are no more numerous near a surface than in the interior of the crystal when a screw dislocation is moved that extends completely through a crystal. The nature of the driving force for this internal cross-glide has not yet been established.

When a glide band is fully established in a crystal, the forces that cause it to grow laterally seem to be readily explained. It appears reasonable to suppose that dislocations that move along the edge of a glide band will be deflected by encounters with other dislocations that lie near the edge of the band. If they are deflected inward they will slow down because of work-hardening and if they deflected outward far enough they will multiply.

The existence of trails left by moving dislocations has been reported by Dash[16] for the case of silicon, and by Amelinckx[17] for the case of KCL. Dash found that moving screw dislocations left trails during glide, and that often there were cusps in the dislocations where the trails joined them, indicating that the trails exerted a dragging force on the dislocations. Dash has suggested that the trails are formed by nonconservative jog motion. It is interesting to note in Fig. 18 (courtesy of W. C. Dash) that when a trail in silicon causes a large cusp in a dislocation, the trail tends to become serrated, and the portions of the stepped trail that lie parallel to the screw dislocation do not etch well, if at all. These serrated trails may have resulted from the mechanism we have described above.

Attempts to obtain conclusive evidence to show that the trails consist of double dislocation lines have not been successful. Electron microscopic examinations of etch pits at trails have failed to detect double pits. However, the search for double etch pits is difficult because the bottoms of etch pits in LiF are not sharp enough to permit resolution better than several hundred angstroms, while only a small fraction of the double dislocation lines need be spaced more than several hundred angstroms apart in order to account for the observed multiplication at low stresses.

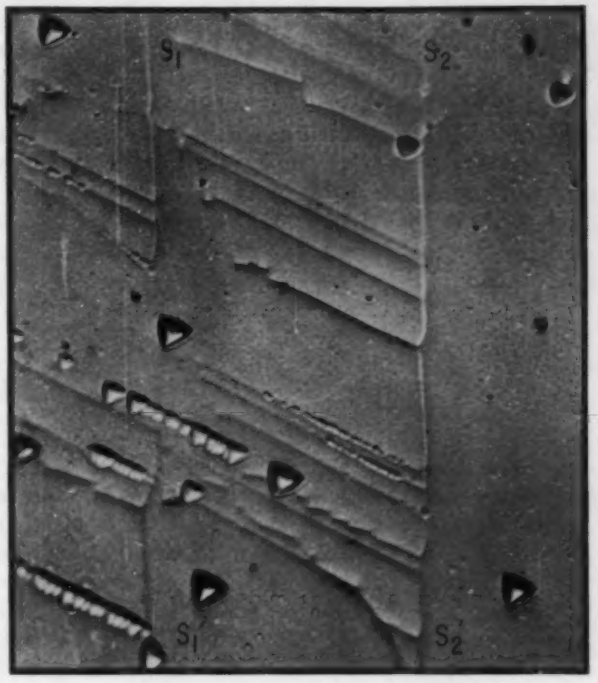

FIG. 18. Screw dislocations SS' and trails in silicon (courtesy of W. C. Dash).

C. Generality of the Multiplication Mechanism

The mode of dislocation multiplication and of glide band formation, and the structure within enlarged dislocation loops is almost the same in MgO crystals as in LiF. In MgO, as in LiF, edge dislocations move much faster than screws,[18] and again the etch pit densities in screw and edge glide bands do not reflect the anisotropy of velocity. It is believed that this results from the many trails that form etch pits in the edge bands. The behavior of MgO is so similar to LiF that it will not be described in detail. Stokes, Johnston, and Li[19] have reported some etch pit studies on dislocation behavior in MgO, and in Figs. 13 and 14 of their paper many of the flat-bottomed pits in edge bands that result from intermittent etching of trails can be seen.

We have observed in NaCl crystals that when a freshly introduced dislocation loop is stressed, it leads to the formation of a wide glide band. Thus the multiplication mechanism must involve cross-glide, as in LiF and MgO. It appears then that this mode of multiplication is definitely a characteristic of ionic crystals.

Low and Guard[20] have inferred from etching studies that dislocation multiplication in silicon iron (Fe-3% Si) proceeds by the cross-glide mechanism. In silicon

[16] W. C. Dash, J. Appl. Phys. **29**, 705 (1958).
[17] S. Amelinckx, Acta. Met. **6**, 34 (1958).
[18] W. G. Johnston (to be published).
[19] R. J. Stokes, T. L. Johnston, and C. H. Li, Trans. Am. Inst. Met. Engrs., **215**, 437 (1959).
[20] J. R. Low and R. W. Guard, Acta Met. **7**, 171 (1959).

iron, as in the ionic crystals, glide bands grow by spreading laterally. Therefore, cross-glide plays an important role in metal crystals as well as ionic crystals. In fact, whenever glide bands of appreciable width result from an initiating event at some point in a crystal, the regenerative mechanism for dislocations probably involves cross-glide.

D. Drag Due to Trails

The trails left by a moving screw dislocation are lattice defects, and their energy of formation must be supplied in order to move the dislocation. Therefore, the trails must exert a dragging force on the dislocation. In the case of silicon (Fig. 18) it is clear from the existence of the cusps that the trails do exert a drag. Dash concluded that the drag due to trails is small compared to the driving forces that he applied to dislocations in silicon in order to move them.

In the case of LiF, the effect of trails on dislocation mobility may not be negligible. From the spacing of pits in Fig. 9(a) there are $\sim 3\times 10^8$ trails per cm. This figure includes *all* pits, the round indistinct pits as well as the sharp pyramidal pits. A lower limit can be placed on the energy of the trails. A unit jog would leave behind point defects, and in LiF, as in the other alkali halides, the lower energy defects are ion vacancies. According to Haven[21] it requires about 2.7 ev to make a separated positive and negative ion pair in LiF. In the present case, the pairs would be associated, so the energy would probably be somewhat more than half of the above figure, say 1.5 ev per atom spacing. For a larger jog of about 100 A, which would form a double dislocation line as a trail, the elastic and core energies would amount to about 3 ev per atom distance. We conclude that *most* of the trails have energies in the range of 1.5–3 ev per atom distance. The stress required to overcome this drag is given by

$$\sigma_d = nE/b = 75\text{–}150 \text{g/mm}^2,$$

where n is the number of trails per cm of dislocation, E is the energy per unit length of trail, and b is the Burgers vector.

This estimate of 75 to 150 g/mm^2 for the stress required to overcome the drag of trails should be compared with the yield stress which was about 500 g/mm^2. Since the estimated drag due to trails is not negligible compared to the yield stress of the crystal, it may account for the fact that, in LiF, edge dislocations move much faster than screw dislocations at the same stress.

E. Some Possible Implications of the Multiple-Cross-Glide Mechanism

The multiple-cross-glide mode of dislocation multiplication leads to a different distribution of dislocations in strained crystals than the distribution that results from the operation of prolific Frank-Read sources. The former mode leads to a random but more or less uniform distribution of dislocation loops plus trails, while the latter mode leads to sets of concentric loops and not necessarily to the formation of trails. Interpretations of the properties of cold-worked crystals depend sensitively on the distributions of dislocations in the crystals, so account must be taken of the multiplication mode in interpreting many mechanical properties. Detailed interpretations will not be attempted here, but some features of processes like strain-hardening, creep, internal friction, and fatigue may be affected by the multiple cross-glide process, and some surface effects may be given a more natural interpretation in terms of this process. The various processes will be considered briefly in turn:

(*a*) *Strain-hardening.* The drag forces resulting from trails on a dislocation that moves on a virgin glide plane are not negligible (Sec. *D*). It can be expected that still more drag will be experienced by a dislocation that moves in a glide plane that has already been traversed and hence is strewn with trails. This type of strain-hardening would be expected to be proportional to both plastic strain and dislocation density, which is in better agreement with experiments[13] than are the usual theories of strain-hardening.

(*b*) *Creep.* Transient creep is determined by the viscosities of dislocations plus strain-hardening, and hence is covered by our previous discussion. Steady-state creep, on the other hand, depends on the additional process of recovery. It may be that recovery is simply the process of dissolution of trails through vacancy diffusion, and is thus the inverse of strain-hardening.

(*c*) *Internal friction.* As we have mentioned previously the trails that we discuss may be described as edge dislocation dipoles. Such dipoles have two stable positions of their individual dislocations and they can pass from one stable position to the other by gliding past one another under the influence of an applied shear stress. Such a relaxation process could contribute to the internal-friction in deformed crystals.

(*d*) *Fatigue.* Since some trails are incipient rows of vacancies, if their concentration becomes sufficiently large in a crystal, a fatigue crack may form.

(*e*) *Surface effects.* One of the causes of cross-glide and hence of dislocation multiplication is the line tension of a screw dislocation that cuts a free surface at an acute angle. When such a dislocation cross-glides, it leaves a monomolecular step in the surface. Therefore, various types of surface films can be expected to affect the rate of cross-glide if they modify the surface energy or form a rigid film which resists the formation of a step. Changes of the cross-glide rate will, in turn, influence the rate of strain-hardening and hence the stress-strain curve.

(*f*) *Charge effects.* Multiple-cross-glide provides a simple means for the production of charged jogs on dislocation lines at low temperatures. If cross-glide

[21] Y. Haven, Rec. trav. chim. **69**, 1471 (1950).

occurs at a free surface, for example, the end of the dislocation will be normal to the surface, while the part of the dislocation line that is far from the surface will lie on a {110} plane that makes an angle of 45° with the surface. Somewhere along such a dislocation there must be one or more jogs of the type that are charged. Since positively charged jogs do not, in general, have the same energy as negatively charged jogs there will be a tendency for the cross-glide to occur in such a way that more of one type is produced than of the other. Thus charge will be carried from the surface into the interior of the crystal, and the surface will become charged.

CONCLUSIONS

The detailed observations that have been presented here of dislocation multiplication, glide band formation, and defect structure left by a moving dislocation can be understood in terms of the double cross-glide multiplication mechanism. It has been shown that cross-glide occurs at room temperature in LiF, so this mechanism is feasible. When a screw dislocation cross-glides, jogs are formed on it which must leave behind trails of defects as the dislocation moves. The structure of the defect trails depends upon the sizes of the jogs. A jog of intermediate size ($3b$ to $300\ b$) must leave behind a dislocation dipole, and such a dipole can subsequently lead to formation of new dislocation loops. The observations of the nature of trails left by screw dislocations, and the observations of dislocation multiplication support the cross-glide mechanism. The trails or dipoles exert a dragging force on a moving dislocation, and this dragging force is not negligible compared to the yield stress.

ACKNOWLEDGMENT

The authors are indebted to Miss A. M. Turkalo for making electron microscopic studies of etched LiF crystals, and for developing a method for making fine grained replicas of such surfaces.

JOURNAL OF APPLIED PHYSICS VOLUME 31, NUMBER 4 APRIL, 1960

Mobility of Hydrogen and Deuterium Positive Ions in their Parent Gases

D. J. Rose
*Bell Telephone Laboratories, Murray Hill, New Jersey**
(Received November 30, 1959)

The mobilities of positive ions in H_2 and D_2 have been measured, using a pulsed Townsend technique. For hydrogen, the mobility μ_0 corrected to 0°C was 11.8 (cm²/v×sec) at $E/p_0=26$(v/sec×mm Hg), increasing to a maximum of 15.3 at $E/p_0=48$, then decreasing to 11.6 at $E/p_0=150$. For deuterium, the mobility was about 0.75 the value for hydrogen throughout the range of E/p_0. The experiment was performed with uranium-purified gas in an ultra-high vacuum system. Ions were not identified as atomic, diatomic, or triatomic; there was no conclusive evidence of more than one ion at any value of E/p_0. The H_2 mobility data are significantly lower than those attributed to Mitchell in the range $20<E/p_0<40$, and lower than the value ≈12.5 for zero-field mobility generally reported.

I. INTRODUCTION

THE mobility of hydrogen ions in hydrogen gas has been measured by Bennett,[1] Bradbury,[2] Lauer,[3] and Mitchell.[4] The first three references quote values at low E/p (ratio of electric field strength v/cm to pressure mm Hg), and might be presumed to apply at $E/p\approx0$. Mitchell's data extend over the range $0<E/p<39$ v/cm×mm Hg; few experimental details are recorded. An additional indirect determination of the mobility can be made from Persson and Brown's measurement of the ambipolar diffusion coefficient in a hydrogen afterglow.[5] In the present work, the mobility of hydrogen and deuterium ions in their parent gases has been measured over the range $22<E/p_0<200$, where p_0 is the pressure reading reduced to the corresponding value for 0°C.

II. EXPERIMENT

The pulsed Townsend technique described by Hornbeck[6] was used. The experimental tube and general vacuum procedure are identical to those used by the author in measuring the first Townsend coefficient.[7] In essence, the tube contains parallel plates of adjustable gap, vertically mounted; in this way the anode could be supported by gravity on a quartz mount, and capacity thereby minimized. A preamplifier was attached adjacent to the tube wall; account was taken of the finite spark duration ($\approx10^{-7}$ sec), and of all time delays in cables and circuits. These steps were necessary in view of the short drift times (0.4–4 μsec, approximately).

Hydrogen or deuterium from flasks was purified by

* Now at Massachusetts Institute of Technology.
[1] W. H. Bennett, Phys. Rev. **58**, 992 (1940).
[2] N. E. Bradbury, Phys. Rev. **40**, 508 (1932).
[3] E. J. Lauer, J. Appl. Phys. **23**, 300 (1952).
[4] J. H. Mitchell, quoted in A. M. Tyndall, *The Mobility of Positive Ions in Gases* (Cambridge University Press, 1938).
[5] K-B. Persson and S. C. Brown, Phys. Rev. **100**, 729 (1955).
[6] J. A. Hornbeck, Phys. Rev. **83**, 374 (1951); **84**, 615 (1952).
[7] D. J. Rose, Phys. Rev. **104**, 273 (1956).

uranium, as described in reference 7. The actual data were obtained at temperatures 22–27°C.

III. RESULTS AND DISCUSSION

The drift velocity v of ions in hydrogen and deuterium is shown in Figure 1, plotted vs E/p_0. Typical data points are shown. Figure 2 shows the conventional atmospheric pressure mobility $\mu_0=vp_0/760E$ plotted vs E/p_0. The results of Bennett,[1] Bradbury,[2] and Lauer,[3] at low E/p_0 are indicated by arrows at the left, and those of Mitchell[4] are drawn. In each case, it is presumed that the data were taken at 20°C (Bradbury 22°C) and their data are correspondingly adjusted to 0°C. The value ascribed to Persson and Brown[5] (PB) and shown on the figure is derived from their measurement of the ambipolar diffusion coefficient,

$$D_a=(D_+\mu_-+D_-\mu_+)/(\mu_++\mu_-). \quad (1)$$

Here, $D_\pm$, $\mu_\pm$ are the diffusion coefficients and mobilities, respectively, of the ions and electrons. On the presumption that thermal equilibrium exists in the afterglow, $D_+/\mu_+=D_-/\mu_-=kT/e$, and one may write

$$\mu_+p=\{2[(D/\mu)/(D_ap)]-1/\mu_-p\}^{-1}. \quad (2)$$

The electron mobility term is small, amounting to about 3%. Persson and Brown quote $D_ap=700\pm50$ cm²×mm Hg/sec. Thus assuming $T=300°K$, one finds $\mu_+(273°\text{K}, 760\text{ mm Hg})\equiv\mu_0=16.6\pm1.2$ cm²/v-sec.

Considerable disagreement is evident. Three low-field values cluster about $\mu_0=12.5$. Bradbury's 7.6 value refers to ions$\approx10^{-2}$ sec old; these ions may not be hydrogen, as pointed out both by him and by Lauer. Bennett's value refers to an experiment where the gas may not have been pure.

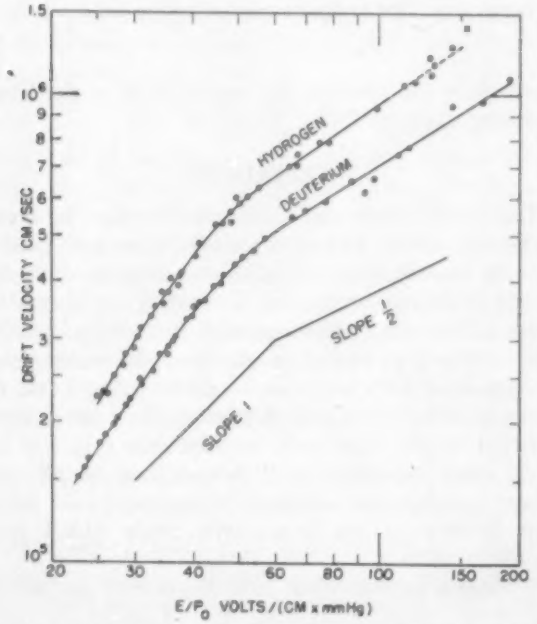

FIG. 1. Drift velocity of ions in the parent gases H_2 and D_2 vs E/p_0. Lines of logarithmic slope 1 and ½ are shown for reference.

The value derived from PB appears at odds with all other data. No precise reason can be given for the difference, but several effects could yield too high a mobility. First, the presence of higher diffusion modes in the discharge cavity increases the loss rate, as noted by PB. Their value applies to measurements late in the afterglow, when the higher modes have presumably decayed. If they have not decayed, the measured mobility is too high. Second, if the gas is heated by the discharge pulse, and stays hot during the afterglow ($\approx$60 msec), the mobility derived will be high (see Eq. (2) and associated discussion). Finally, the diffusion at these late times may not have been quite ambipolar. PB measure D_ap at a reduced time $t/p\Lambda^2\approx6$ msec/mm Hg×cm² where Λ is the diffusion length of the cavity. The density at that time is not given, but density plots for shorter times show $n\Lambda^2\approx6\times10^7$ electrons/cm at $t/p\Lambda^2=2.8$. If their plotted trends continue in time, one estimates $n\Lambda^2\approx10^7$ at the time of measurement. In this case $n\Lambda^2\mu/D\approx4\times10^8$ (v-cm)$^{-1}$. This may be compared with the calculation by Allis and Rose[6] of the effective diffusion coefficient in hydrogen, in cases where the charge density is too low for ambipolar theory to apply. Convergence difficulty precluded calculation for $n\Lambda^2\mu/D>2\times10^7$ (v-cm)$^{-1}$ in the isothermal case. The transition to ambipolar diffusion is very slow, extending over many orders of magnitude. Reasonable extrapolation of the calculation to $n\Lambda^2\mu D=4\times10^8$ indicates that ambipolar theory probably does not apply within 10 or 15%. If that be the case, the value of D_ap measured by PB would be correspondingly high at $t/p\Lambda^2=6$; D_ap would be expected to increase if data were taken at yet later times.

In order to check whether the present results were the result of contamination, the experiment was repeated several times with more vigorous outgassing. In these attempts, the base pressure was $\approx10^{-8}$ mm Hg with fresh uranium in the system at 800°C. The pressure did not rise above 10^{-7} mm Hg (no hydrogen in

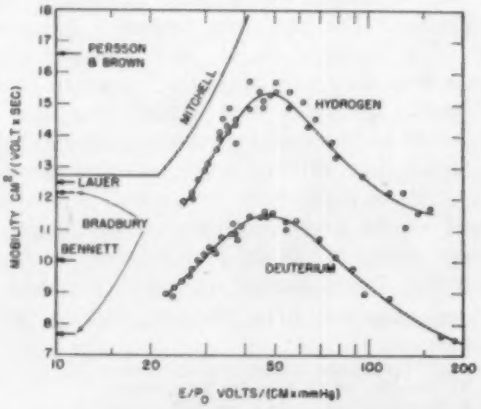

FIG. 2. Mobility μ_0 of ions in the parent gases H_2 and D_2 vs E/p_0. Low-field mobilities of Bennett, Bradbury, Lauer, and Persson and Brown, and μ_0 vs E/p_0 by Mitchell are also shown.

[6] W. P. Allis and D. J. Rose, Phys. Rev. 93, 84 (1954).

the system) over a time equal to that taken for the experiment. "Hydrogen" absorbed in the cool uranium left a rare gas residue of less than two parts in 10^6. As a final check, $\approx 5\mu$ mercury vapor was purposely admixed with 10 mm hydrogen. The slower Hg^+ ions formed by charge exchange (perhaps 10% of the total number) could readily be seen in the oscilloscope trace.

Only one ion could be seen at any value of E/p_0, with the exception to be noted below. A second ion could not have been observed (a) if it had much different mobility and contributed a few percent of the current, or (b) if it had the same mobility within about 5% and were present in large amount. It is tempting to speculate that the observed ion may change its nature over the range of E/p_0. Then it must do so frequently enough when both species are present that only one drift velocity is seen. This is apparently the case in nitrogen and carbon monoxide.[9]

The fact that a Townsend avalanche must be produced to obtain the ions in this technique precluded operation in the interesting region below $E/p_0=26$ in H_2 and 23 in D_2. On the other hand, there was also difficulty in obtaining data if the gap voltage was near breakdown, so that secondary avalanches formed and contributed significantly to the current. In such cases, the secondary emission coefficient at the molybdenum cathode could be approximately measured.[10] But the effect was much confused by the appearance also of a sizeable secondary photo-emission at the cathode. Thus successive avalanches formed $\approx 10^{-7}$ sec apart, and the arrival of ions was largely masked. In that regime, some evidence could be found of a faster particle (e.g., $\mu_0 \approx 16$ at $E/p_0=100$). The appearance was intermittent and variable, and it also seems unreasonable that the ions are aware of the secondary processes at the cathode. The data of Figs. 1 and 2 therefore refer to conditions far from breakdown, where the current could reasonably be analyzed in terms of a single avalanche of ions.

IV. CONCLUSION

The presently measured values of mobility of ions in H_2 lie significantly below previously reported data, for the range $E/p_0 > 25$ v/cm×mm Hg. No data in D_2 have been available hitherto. There remains considerable doubt regarding the mobility at $E/p_0 \approx 0$. It would be interesting to investigate the region $20 > E/p_0 > 0$, to see if mobility rises again with decreasing E/p_0. In addition, identification of the ions (e.g., by a mass-analyzer attached to the cathode) as H_2^+ or H_3^+ (H^+ seem unlikely) should shed some light on the heat of formation of H_3^+ by the reaction $H_2^+ + H_2 \rightarrow H_3^+ + H$. The same remarks apply to deuterium.

[9] R. N. Varney, Phys. Rev. 89, 708 (1953).

[10] D. J. Rose, 3rd International Conference on Ionization Phenomena in Gases, Venice (1957), p. 888.

JOURNAL OF APPLIED PHYSICS VOLUME 31, NUMBER 4 APRIL, 1960

Elastic Constants of Yttrium Single Crystals in the Temperature Range 4.2–400°K*

J. F. Smith and J. A. Gjevre†
Institute for Atomic Research and Departments of Chemistry and Physics, Iowa State University, Ames, Iowa
(Received November 16, 1959)

The five independent elastic constants for yttrium single crystals have been determined by the pulse-echo technique over the temperature range, 4.2–400°K. The experimental values extrapolated to 0°K are: $C_{11}=8.34\pm0.02$, $C_{33}=8.01\pm0.02$, $C_{44}=2.690\pm0.006$, $C_{12}=2.91\pm0.03$, and $C_{13}=1.9\pm0.4$ in units of 10^{11} d/cm². The degree of elastic anisotropy is low throughout the entire temperature range. The curves illustrating the temperature dependence of the elastic constants show several inflections, and the curve for C_{11} crosses that for C_{33} near 390°K. The behavior is somewhat unusual, and is probably explicable on the basis that the degree of band overlap in yttrium is quite sensitive to interatomic spacing. Such a sensitivity has previously been postulated to explain the temperature dependence of the Hall coefficient.

INTRODUCTION

BELOW 1490°C yttrium crystallizes in the hcp ($A3$) structure[1] while above 1490°C the bcc ($A2$) structure occurs.[2] Measurements of the elastic parameters of polycrystalline yttrium have been made at room temperature,[3] but no data were available concerning the elastic behavior of single crystals. Because of the current interest in yttrium, measurement of the single crystal elastic constants was undertaken in order to obtain some information about the interaction forces in the solid metal. These forces are closely related to the cohesive energy, vibrational behavior, and mechanical properties of the material. The elastic behavior of the

* Contribution No. 814. Work was performed in the Ames Laboratory of the U. S. Atomic Energy Commission.

† Present address: Physics Department, University of North Dakota.

[1] F. H. Spedding, A. H. Daane, and K. W. Herrmann, Acta Cryst. 9, 559 (1956).

[2] D. T. Eash and O. N. Carlson, Trans. Am. Soc. Metals, preprint No. 142 (1959).

[3] J. F. Smith, C. E. Carlson, and F. H. Spedding, J. Metals 9, 1212 (1957).

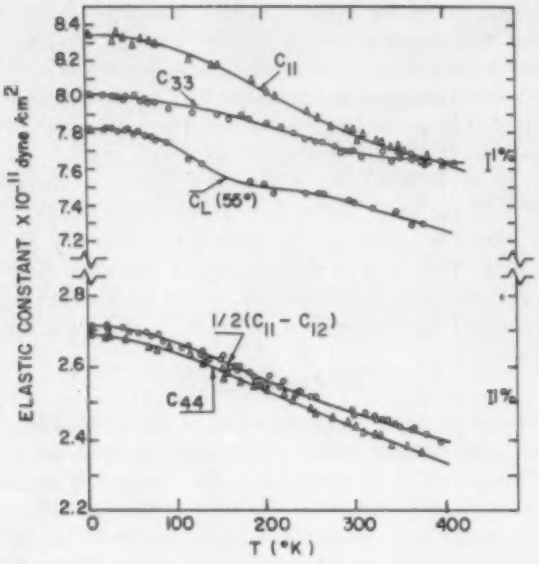

FIG. 1. The temperature dependence of the five independently determined adiabatic elastic constants for single crystalline yttrium.

hcp structure is specified by five independent constants,[4] and these constants have been determined for hexagonal yttrium in the temperature range 4.2–400°K by the pulse-echo technique.

PROCEDURE AND RESULTS

Single crystals were prepared by annealing machined cylinders of yttrium in tantalum crucibles in vacuo at 1300°C for 24 hr. This is essentially a strain-anneal technique since the machining operation presumably introduces a sufficient amount of residual strain to initiate grain growth at elevated temperature. The purity of the yttrium was >99% with titanium and oxygen being the major contaminants. Crystal orientations were determined by the back-reflection Laue technique to ±0.5°. Two crystals were selected for the experimental measurements. The first of these crystals was ground and lapped so that sonic waves could be propagated perpendicular to the c axis; the length perpendicular to the c axis was 2.1135±0.0003 cm. A second crystal was prepared so that waves could be propagated in a direction 55° from the c axis through a length of 1.0909±0.0003 cm. This latter crystal was subsequently further cut and surfaces prepared so that measurements could also be made along the c axis. In this latter case the length parallel to the axis was 1.0079±0.0003 cm. In all cases residual worked metal was removed from the crystal surfaces by etching before measurements were made. The transverse cross sections of the crystals were large with respect to the wave lengths propagated so that the boundary conditions for plane wave propagation were adequately fulfilled. A pycnometric determination of the crystal density gave a value of 4.477 g/cm³ which is within a 0.1% of the value, 4.472 g/cm³, obtained from x-ray measurements.[1] This latter density value with appropriate temperature correction was used to calculate the elastic constants from the measured sonic velocities.

Propagation velocities of sonic pulses were measured in the temperature range 4.2–400°K. Liquid helium, hydrogen, or nitrogen was used as a refrigerant in the various low-temperature ranges. A frequency of 10 Mc/sec was employed and longitudinal waves were induced with X-cut quartz transducers while shear waves were induced with Y-cut quartz transducers. The apparatus and modifications have been described in previous reports.[5,6] Transit times of the pulses were measured to ~0.1% which reflects a precision of the order of 0.2% in the independently measured elastic constants.

From the available crystalline orientations, measurements were made over the complete temperature range of the elastic constants: C_{11}, C_{33}, C_{44}, $(1/2)(C_{11}-C_{12})$, and $C_L(55°)$ where

$$\begin{aligned} C_L(55°) &= (1/2)(C_{11}+C_{44})\sin^2 55°+(1/2)(C_{33}+C_{44})\cos^2 55° \\ &\quad +(1/2)\{(C_{11}-C_{44})^2\sin^4 55°+(C_{33}-C_{44})^2\cos^4 55° \\ &\quad +2\sin^2 55°\cos^2 55°[(C_{11}-C_{44})(C_{44}-C_{33}) \\ &\quad +2(C_{13}+C_{44})^2]\}^{\frac{1}{2}}. \quad (1) \end{aligned}$$

The relationships between propagation velocities and elastic constants in hexagonal crystals have been discussed by Musgrave[7] and by Neighbours.[8] From the measured data, C_{12} and C_{13} were calculated. It may be noted that Eq. (1) is quadratic in C_{13} so that the lattice stability conditions of Alers and Neighbours[9] were employed to choose the correct root for the evaluation of C_{13}. A graphical representation of the experimental points is shown in Fig. 1, and a tabulation of the smoothed experimental data plus the calculated constants is shown in Table I. In both the figure and the table, the values have been corrected for dimensional and density changes due to temperature; these corrections were based upon the anisotropic thermal expansion measurements made below room temperature by Meyerhoff[10] and above room temperature by Hanak.[11]

The internal consistency of the data was checked by means of the following comparisons at room temperature. First, the experimental value of $C_{44}=2.433\times10^{11}$ d/cm² obtained from measurement perpendicular to the c axis on the first crystal is within 0.3% of a value of 2.440×10^{11} d/cm² obtained from measurement parallel to the c axis on the second crystal. In addition, measurements of the two shear-induced modes in the 55°

[4] A. E. H. Love, *A Treatise on the Mathematical Theory of Elasticity* (Dover Publications, Inc., New York, 1944).

[5] P. E. Armstrong, O. N. Carlson, and J. F. Smith, J. Appl. Phys. **30**, 36 (1959).

[6] J. F. Smith and C. L. Arbogast, J. Appl. Phys. **31**, 99 (1960).

[7] M. J. P. Musgrave, Proc. Roy. Soc. (London) **A226**, 339 (1954).

[8] J. R. Neighbors, J. Acoust. Soc. Am. **26**, 865 (1954).

[9] G. A. Alers and J. R. Neighbours, J. Appl. Phys. **28**, 1514 (1957).

[10] R. W. Meyerhoff, M. S. thesis, Iowa State University (1959).

[11] J. H. Hanak, Ph.D. thesis, Iowa State University (1959).

TABLE I. Adiabatic elastic constants of yttrium in units of 10^{11} d/cm².

Temp. (°K)	C_{11} (±0.02)	C_{33} (±0.02)	$C_L(55°)$ (±0.02)	$(1/2)(C_{11}-C_{12})$ (±0.006)	C_{44} (±0.006)	C_{12} (±0.03)	C_{13} (±0.4)
4.2	8.34	8.01	7.82	2.715	2.690	2.91	1.9
20	8.34	8.01	7.82	2.713	2.684	2.91	1.9
50	8.33	8.00	7.81	2.700	2.670	2.93	1.9
75	8.30	7.98	7.77	2.684	2.656	2.93	1.8
100	8.27	7.96	7.72	2.662	2.635	2.95	1.8
125	8.22	7.93	7.64	2.639	2.613	2.94	1.7
150	8.16	7.91	7.58	2.615	2.586	2.93	1.7
175	8.10	7.88	7.54	2.589	2.557	2.92	1.8
200	8.03	7.84	7.51	2.562	2.530	2.91	1.8
225	7.97	7.81	7.49	2.538	2.511	2.89	1.9
250	7.90	7.77	7.47	2.514	2.480	2.87	2.0
275	7.84	7.73	7.44	2.492	2.456	2.86	2.0
300	7.79	7.69	7.41	2.471	2.431	2.85	2.1
325	7.75	7.67	7.37	2.451	2.405	2.85	2.1
350	7.71	7.66	7.33	2.432	2.382	2.85	2.1
375	7.67	7.65	7.30	2.414	2.357	2.84	2.1
400	7.63	7.64	7.26	2.396	2.333	2.84	2.1

direction were used to obtain values for the constants:

$$C_T^I(55°) = (1/2)(C_{11}+C_{44})\sin^2 55° + (1/2)(C_{33}+C_{44})\cos^2 55° - (1/2)\{(C_{11}-C_{44})^2 \sin^4 55° + (C_{33}-C_{44})^2 \cos^4 55° + 2\sin^2 55° \cos^2 55° [(C_{11}-C_{44})(C_{44}-C_{33}) + 2(C_{13}+C_{44})^2]\}^{\frac{1}{2}}; \quad (2)$$

$$C_T^{II}(55°) = (1/2)(C_{11}-C_{12})\sin^2 55° + C_{44}\cos^2 55°. \quad (3)$$

The measured value of $C_T^{II}(55°)$ was 2.415×10^{11} d/cm² and agrees within 1.7% with the value of 2.458×10^{11} d/cm² calculated from values of C_{11}, C_{12}, and C_{44}. The sum of the measured values for $C_T^I(55°)$ and $C_L(55°)$ was 10.35×10^{11} d/cm² which is within 1.5% of the value, 10.19×10^{11} d/cm², calculated from values of C_{11}, C_{33}, and C_{44}. In view of the precision of the 55° crystallographic orientation as well as the precision of the determination of the individual constants, this agreement is considered quite satisfactory and is taken to indicate that both crystals were in a state of strain-free equilibrium.

DISCUSSION

Averaging of the single crystalline elastic constants at room temperature in the manner of Voigt[12] and in the manner of Reuss[13] gives values as follows:

	Voigt	Reuss
Shear Modulus$\times10^{-11}$ d/cm²	2.55±0.04	2.54±0.03
Young's Modulus$\times10^{-11}$ d/cm²	6.36±0.13	6.33±0.06
Poisson's Ratio	0.25±0.01	0.25±0.01
Compressibility$\times10^{6}$ cm²/kg	2.46±0.08	2.46±0.10

These two extremes of averaging represent limiting values to be expected from polycrystalline aggregates,[14] and the close agreement between the two sets of values indicates a relatively low-elastic anisotropy. A more direct measure of the degree of anisotropy can be obtained from the values of the ratios, $1.04>C_{11}/C_{33}>0.999$, $1.01<(C_{11}-C_{12})/2C_{44}<1.03$, and $1.7>C_{12}/C_{13}>1.4$, where the first figure is the low-temperature extreme and the second figure is the high-temperature extreme.

The Cauchy relations[15] for hexagonal yttrium are $C_{13}=C_{44}$ and $(C_{11}-C_{12})/2=C_{12}$. With increasing temperature the ratio, $(C_{11}-C_{12})/2C_{12}$, decreases from 0.93 to 0.84 while the ratio, C_{13}/C_{44}, increases from 0.7 to 0.9. Since central-force interactions are one criterion for the validity of the Cauchy relations and since central-force interactions are undoubtedly a poor approximation in the case of metals, the small deviations of the ratios from unity quite probably indicates some degree of cancellation of noncentral-force interactions.

It can be seen from Fig. 1 that inflections occur in all of the curves representing the temperature dependence of the elastic constants except that for C_{44}. In addition the curve for C_{11} crosses that for C_{33} near 390°K. The over-all behavior is somewhat unusual and indicates a change in the directionality of the interaction forces with temperature. A probable explanation is that the degree of band overlap in yttrium is quite sensitive to interatomic spacing. Such a sensitivity in the degree of overlap has previously been postulated to explain the temperature dependence of the Hall coefficient[16] and could also explain the observed behavior of the electrical resistivity which exhibits a pronounced and strongly temperature dependent anisotropy.[17]

ACKNOWLEDGMENTS

The authors wish to acknowledge the cooperation of Dr. F. H. Spedding in making possible this research and thank him for his active interest and encouragement throughout the course of the work. Appreciation is also extended to Dr. O. N. Carlson and Mr. E. D. Gibson for growing the yttrium single crystals and to Mr. M. L. Shepard for his assistance in accumulating the experimental data.

[12] W. Voigt, *Lehrbuch der Kristallphysik* (B. G. Teubner, Leipzig, 1928), p. 956.

[13] A. Reuss, Z. angew. Math. u. Mech. **9**, 49 (1929).

[14] H. B. Hungtington in *Solid State Physics*, edited by D. Turnbull and F. Seitz (Academic Press, New York, 1958), Vol. 7, p. 213.

[15] C. Zener, *Elasticity and Anelasticity of Metals* (University of Chicago Press, Chicago, 1948), p. 19.

[16] C. J. Kevane, S. Legvold, and F. H. Spedding, Phys. Rev. **91**, 1372 (1953).

[17] P. M. Hall, S. Legvold, and F. H. Spedding (submitted to Phys. Rev.).

Optical Absorption by Free Carriers in a Semiconductor Containing a Dispersed Colloidal Phase*

B. R. Gossick
Arizona State University, Tempe, Arizona
(Received September 24, 1959)

The optical absorption by free carriers in a semiconductor containing a dispersed colloidal phase is treated, taking into account the dipolar diffusion of minority carriers about the particles.

I. INTRODUCTION

THE optical absorption by solids is already complicated by a plethora of competing mechanisms. This paper introduces another mechanism, viz., dipolar diffusion,[1] which applies to the optical absorption by minority carriers in the regions which surround colloidal metal particles embedded in a semiconductor. Another suitable dispersed phase would be submicroscopic regions in the semiconductor of opposite type, e.g., a colloidal p-type phase within a predominately n-type sample. Such a colloidal phase might be produced by pile neutrons.[2,3]

A colloidal metal particle within a semiconductor is surrounded by a potential barrier, which arises because the position of the energy bands relative to the Fermi level differs within the particle from that outside. If the potential barrier blocks the passage of majority carriers, optical absorption by majority carriers is reduced, and the optical absorption by minority carriers is increased by the dipolar diffusion process.[1] As the particle becomes polarized by an electric field, and minority carriers are emitted on the side the barrier is reduced and collected on the opposite side where the barrier is increased, energy is absorbed from the field. The important cases are expected to be those in which the metal of the colloidal particles and the surrounding semiconductor together happen to yield metal-semiconductor barriers with high injection ratios.[4]

II. ABSORPTION COEFFICIENT

We consider only those cases in which the semiconducting medium is homogeneous, and the double layer surrounding each metal particle produces a potential well which is deep compared with kT/q, the thermal potential.[5] The following discussion refers to an n-type semiconducting medium. The dispersed phase consists of certain metal, or p-type semiconducting, particles. Minority carriers are designated by holes. The shape of the particles is assumed here to be spherical, and in many cases of interest the error introduced by this assumption is small.[3]

The absorption cross section of a particle may be determined by its polarizability. The following expression for the polarizability comes from relations given elsewhere[1,6]:

$$a_1-ia_2=4\pi r_0^3\left\{\frac{1}{1-f}+\frac{\sigma_{p0}r_0}{(1-f)\epsilon_0(8\omega D)^{\frac{1}{2}}}-\frac{i}{\omega\epsilon_0}\left[\frac{\sigma_{p0}r_0}{1-f}\left(\frac{\omega}{8D}\right)^{\frac{1}{2}}-\frac{\sigma_{n0}}{2+f}\right]\right\}. \quad (1)$$

The subscript 0 designates properties of the medium outside the double layers. For example, σ_{n0}, σ_{p0}, and ϵ_0 denote the conductivity by electrons, conductivity by holes and dielectric constant, respectively, of the semiconducting medium exclusive of the double layers. The radius of the double layer surrounding each particle is given by r_0, the fraction of volume surrounded by double layers by f, the angular frequency by ω, and the diffusion coefficient of holes by D. A small spherical particle with polarizability a_1-ia_2 has an optical absorption cross section[7]

$$S_a=2\pi a_2/\lambda, \quad \lambda\ll 2\pi r_0. \quad (2)$$

for incident radiation with wavelength, λ. If one determines the absorption coefficient for the particles on the basis of (1) and (2) and then adds the Drude free carrier absorption,[8] the following expression is obtained:

$$\alpha=\frac{\sigma_{n0}}{1+\omega^2\tau_n^2}\left(\frac{u}{\epsilon_0}\right)^{\frac{1}{2}}\frac{1-f}{1+f/2}+\frac{\sigma_{p0}}{1+\omega^2\tau_p^2}\left(\frac{u}{\epsilon_0}\right)^{\frac{1}{2}}\left[1+\frac{3fr_0}{1-f}\left(\frac{\omega}{8D}\right)^{\frac{1}{2}}\right]. \quad (3)$$

The magnetic permeability of the semiconducting medium is denoted by u, while τ_n and τ_p denote the carrier collision times for electrons and holes, respectively. The first term on the right side of (3) is the Drude absorption

* Work supported by U. S. Atomic Energy Commission contract.
[1] B. R. Gossick, J. Appl. Phys. **31**, 29 (1960).
[2] J. H. Crawford, Jr. and J. W. Cleland, J. Appl. Phys. **30**, 1204 (1959).
[3] B. R. Gossick, J. Appl. Phys. **30**, 1214 (1959).
[4] E. H. Borneman, R. F. Schwarz, and J. J. Stickler, J. Appl. Phys. **26**, 1021 (1955).
[5] Symbols k, T, and q denote Boltzmann's constant, absolute temperature, and electronic charge, respectively.
[6] J. H. Crawford, Jr., and B. R. Gossick (paper in preparation).
[7] H. C. van de Hulst, *Light Scattering by Small Particles* (John Wiley & Sons, Inc., New York, 1957).
[8] H. Y. Fan and M. Becker, *Semiconducting Materials*, edited by H. K. Henisch, (Butterworths Scientific Publications, Ltd., London, 1951), pp. 132–147.

TABLE I.

Curve	I	II	III	IV
$3fr_0/(2-2f)$[a] (μ)	0.4	4.0	0.4	4.0
τ_p[a] (Sec)	10^{-13}	10^{-13}	$0.5\cdot10^{-14}$	$0.5\cdot10^{-14}$

[a] These values of the parameter $3fr_0/(2-2f)$, and the collision time of holes τ_p were used in calculating the curves I, II, III, and IV in Fig. 1.

by conduction electrons, which is diminished by the presence of double layers through the factor $(1-f)/(1+f/2)$. The second term is the Drude absorption by free holes, which is enhanced by the dipolar diffusion process through the factor $[1+(3fr_0/1-f)(\omega/8D)^{\frac{1}{2}}]$. The effect of colloidal particles on optical absorption by dipolar diffusion of minority carriers appears to modify the Drude free carrier absorption.

III. DISCUSSION

Consider the frequency dependence of the contribution to the absorption coefficient

$$\alpha_1(\omega)=\sigma_{p0}\left(\frac{u}{\epsilon_0}\right)\frac{1+(3fr_0/1-f)(\omega/8D)^{\frac{1}{2}}}{1+\omega^2\tau_p^2}, \quad (4)$$

due only to dipolar diffusion. Four plots of the ratio $\alpha_1(\omega)/\alpha_1(0)$ are shown in Fig. 1. The curve designated I was calculated by taking the parameter $3fr_0/(2-2f)$ as $0.4\,\mu$ and the collision time τ_p as 10^{-13} sec (corresponding roughly to the room temperature collision time of a "heavy hole" in germanium). Curve III was calculated by taking the parameter $3fr_0/(2-2f)$ again as $0.4\,\mu$ and the collision time τ_p as $0.5\cdot10^{-14}$ sec (corresponding roughly to the room temperature collision time of a "light hole" in germanium). Curve III illustrates that a reduction in minority carrier collision time produces a significant increase in absorption. Increasing the outer radius of the double layer by an order of magnitude, and holding f constant, increases the absorption $\alpha_1(\omega)$, by approximately an order of magnitude, e.g., compare Curves I and II, and Curves III and IV. Values of the parameter $3fr_0/(2-2f)$ and collision time τ_p, which were used to calculate Curves I, II, III, and IV are summarized in Table I.

It should be mentioned that increasing the particle size also increases the extinction through the scattering contribution; the ratio of the scattering to absorption cross section S_s/S_a increases with the volume of the particle. Rayleigh scattering applies to the small particles under consideration. Therefore the cross section for scattering may be written[7]

$$S_s=(2\pi)^3(a_1^2+a_2^2)/(3\lambda^4), \quad \lambda\gg2\pi r_0. \quad (5)$$

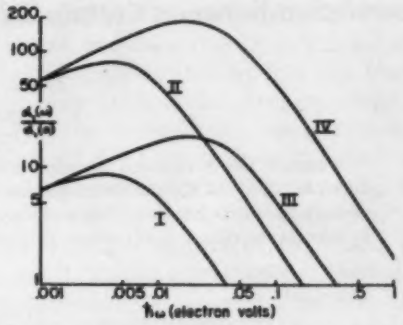

FIG. 1. The relative absorption coeff $\alpha_1(\omega)/\alpha_1(0)$ is plotted against energy $\hbar\omega$. Values of $3fr_0/(2-2f)$ and τ_p, which apply to Curves I, II, III, and IV, are listed in Table I.

If the colloidal phase is metallic, (5) applies only if the particle radius is small compared with the skin thickness.

On comparing the cross sections for absorption and scattering, one finds that for an n-type germanium medium with 10 ohm-cm resistivity, containing particles with radius 200 A, barrier height 0.4 v, the scattering and absorption cross sections are approximately equal at a photon energy of 0.05 ev, with scattering dominating at higher energies and absorption dominating at lower energies. It becomes clear that the absorption by colloidal particles can be determined only by measuring both transmission and scattering.

Germanium may exhibit high resistivity, and yet contain relatively large amounts of tin or gold,[9] and it should be possible to prepare an n type germanium sample with 20 ohm-cm resistivity containing one part in 10^5 tin or gold in the form of particles with diameters of a few hundred angstroms. In this instance, f could be as great as approximately 10%, in which case, the absorption at a wave length of $10\,\mu$ by dipolar diffusion would be comparable to the absorption by free carriers. The behavior of an n type germanium sample with 20 ohm-cm resistivity, containing $2\cdot10^{11}$ p-type disordered regions per cm^3, as induced by fast neutrons should be similar.

The following examples should be of interest: (1) III-V compounds with appreciable deviations from stochiometry, (2) semi-conductor samples which have been doped by diffusion of impurities, and (3) semiconductors which have been bombarded by fast neutrons.

ACKNOWLEDGMENTS

It is a pleasure to thank J. H. Crawford, Jr., and A. T. Wager for helpful discussions and comments.

[9] W. Crawford Dunlap, Jr., article in *Progress in Semiconductors* edited by A. F. Gibson (John Wiley & Sons, Inc., New York, 1957), Vol. 2.

Correlation between Certain Extinction Bands of Solids and Plasma Resonance*

B. R. Gossick
Arizona State University, Tempe, Arizona
(Received September 25, 1959)

A correlation is reported between certain optical extinction bands in sapphire, quartz, the silver and alkali halides, and the calculated plasma resonance of electrons in colloidal particles which are either known or expected to be present. This correlation suggests not only that pile neutrons produce lithium particles in lithium fluoride, but aluminum particles in sapphire, and silicon particles in quartz.

I. INTRODUCTION

HAMPE[1] has given a model for the optical extinction by quartz containing particles of gold, based on the plasma resonance of conduction electrons within the gold particles. He has tested the model also on an extinction band in KCl commonly attributed to particles of potassium. It appears worthwhile to test Hampe's model by applying it to other optical extinction bands which are either associated with, or might possibly be associated with, colloidal particles. The preliminary results of such a test reveal an interesting correlation between the calculated and observed resonances related to several bands, which are known to be induced by pile irradiation, e.g., a band in sapphire at 2600 A discussed by Levy and Dienes,[2] a familiar band around 2200 A in quartz,[3–6] and several other bands in the alkali and silver halides.[9–16]

The print-out process by which metal particles are formed in the halide crystals is well known.[17] Recently, evidence of the presence of lithium particles in pile irradiated LiF has been given on the basis of both nuclear magnetic and electron spin resonance measurements.[18] Therefore, it is not surprising that a band at 4500 A produced in the extinction spectrum of LiF by pile irradiation appears to be connected with the plasma resonance of electrons in particles of lithium. The correlation between electronic plasma resonance and extinction bands in sapphire and quartz, which suggests that the print-out process produces particles of aluminum in sapphire and particles of silicon in quartz, is somewhat surprising as these bands have been commonly attributed to electronic levels connected with point defects in the lattice.

The electronic plasma frequency ω_0 for spherical particles obeys the relation,

$$\omega_0^2 = \tfrac{1}{3}(nq^2/m\epsilon_c)\epsilon_c/\epsilon_m, \tag{1}$$

in which n is the density of the electrons, q the electronic charge, m the electronic mass, ϵ_c the dielectric constant of the bulk material of the particle accounting only for the core electrons not included in the density n, and ϵ_m the dielectric constant of the medium surrounding the particles. The familiar expression within parentheses gives the plasma frequency of the bulk material of the particle. The factor $\frac{1}{3}$ allows for the spherical form of the particles (after Jensen),[19] and the factor ϵ_c/ϵ_m allows for the polarizability of the medium surrounding the particles (after Hampe).[1]

II. REVIEW OF CERTAIN EXTINCTION BANDS WITH REFERENCE TO PLASMA RESONANCE

Table I refers to extinction bands, some of which are, and others which may be, produced by colloidal particles. The following information is listed by column: *I*, the chemical composition of the colloidal particles; *II*, the minimum plasmon energy $\hbar\omega_{\min}$ required for collective electronic action in the particles according to the criterion stated by Pines, Bohm, and Nozières; *III*, the chemical composition of the media; *IV*, the relative dielectric constants ϵ_m of the media based on the refractive indices; *V*, the photon energy $\hbar\omega_0$ corresponding to the observed extinction peaks; *VI*, the number of electrons per atom z participating in the

* Work supported by U. S. Atomic Energy Commission contract.

[1] W. Hampe, Z. Physik **152**, 476 (1958).
[2] P. W. Levy and G. J. Dienes, Phys. Rev. **94**, 1409 (1954).
[3] E. W. J. Mitchell and E. G. S. Paige, Phil. Mag. **46**, 1353 (1955).
[4] C. M. Nelson, reported by J. H. Crawford, Jr., and M. C. Wittels, *Proceedings of the International Conference on the Peaceful Uses of Atomic Energy* (United Nations, New York, 1956), Vol. 7, p. 654.
[5] C. M. Nelson, and J. H. Crawford, Jr., *Proceedings of Conference on Defect Structure of Quartz and Glassy Silicas* (1957). (To be published in J. Phys. Chem. Solids.)
[6] M. Lautout, J. Chim. Phys. **52**, 259 (1955).
[7] A. J. Cohen, J. Chem. Phys. **23**, 765 (1955).
[8] P. W. Levy, J. Chem. Phys. **23**, 764 (1955).
[9] C. J. Delbecq and P. Pringsheim, J. Chem. Phys. **21**, 794 (1953).
[10] J. J. Gilman, and W. G. Johnson, J. Appl. Phys. **29**, 877 (1958).
[11] M. Savostianowa, Z. Physik **64**, 266 (1930).
[12] D. R. Westervelt, Phys. Rev. **91**, 218 (1953).
[13] R. Kaiser, Z. Physik **132**, 482 (1952).
[14] F. Seitz, Revs. Modern Phys. **26**, 7 (1954).
[15] H. W. Etzel and J. H. Schulman, J. Chem. Phys. **22**, 1549 (1954).
[16] J. W. Mitchell, *Progress in Semiconductors* John Wiley & Sons, Inc., New York, (1958), Vol. 3, p. 61.
[17] N. F. Mott and R. W. Gurney, *Electronic Processes in Ionic Crystals* (Oxford University Press, London, 1948), 2nd ed.
[18] P. J. Bray, Nuclear Sci. Abstr., **13**, 1107 (1959); **13**, 1643 (1959).
[19] H. Jensen, Z. Physik, **106**, 620 (1937).

TABLE I.

	Particle		Medium				
	I Element	*II* $\hbar\omega_{\min}$ (ev)	*III* Compound	*IV* ϵ_m	*V* $\hbar\omega_0$ (ev)	*VI* z	*VII* Footnote
1	Al	14	Al_2O_3	3.2	4.8	3	2
2	Si	15	SiO_2	2.7	5.6	4	3–8
3	Na	3.2	NaCl	2.4	2.1	1	11, 12
4	Na	3.2	KCl	2.2	2.2	1	13
5	K	2.1	KBr	2.4	1.5	1	12
6	K	2.1	KI	2.8	1.4	1	14
7	Ag	5.5	NaCl	2.4	3.2	1	15
8	Ag	5.5	AgCl	4.3	2.3	1	16
9	Ag	5.5	AgBr	5.1	1.9	0.7	16
10	Li	4.7	LiF	1.9	2.8	0.8	9, 10

plasma resonance within the colloidal particles based on the density of bulk material; and *VII*, some of the references in which the extinction bands have been reported.

With metals, $\hbar\omega_{\min}$ equals the Fermi level measured from the bottom of the conduction band; the numbers in column *II* are estimates in which bulk density, free electronic mass, and spherical energy surfaces have been used. With silicon, $\hbar\omega_{\min}$ equals the width of the valence band,[20] ~14ev, plus the energy gap, 1.1 ev.

The following formula gives the plasmon energy $\hbar\omega_0$ in ev and is based on (1):

$$\hbar\omega_0 = 15.8(z\rho/A\epsilon_m)^{\frac{1}{2}}. \qquad (2)$$

The quantity ρ refers to the density in gm cm^{-3} and A to the atomic weight of the particle. Values of ϵ_m from column *IV* and $\hbar\omega_0$ from column *V* and handbook values of ρ and A have been inserted into Eq. (2) to yield z as tabulated in column *VI*. These numbers z have been determined from experimental values of $\hbar\omega_0$ which are approximate in the second significant figure. The numbers z which have been tabulated elsewhere,[21] are similarly uncertain because of experimental limitations.

III. DISCUSSION

In the examples cited here, would the plasma resonance occur through collective or individual action in terms of the model of Pines, Bohm and Nozières?[21–25] Whether or not the collective or individual modes of forced vibrations are excited by incident photons depends on the magnitude of the plasmon energy $\hbar\omega_0$. The electrons oscillate through collective action only if $\hbar\omega_0$ exceeds $\hbar\omega_{\min}$ (Table I). Otherwise, the electrons oscillate through individual action. For example, with unit amplitude of applied field, the individual (Drude) model gives a current density of amplitude, $i\omega\epsilon_c+\sigma_0/(1+i\omega\tau)$, which exhibits a resonance at the bulk plasma frequency, provided the collision time τ is large compared with the dielectric relaxation time ϵ_c/σ_0.

The fact that the separation between the lowest filled and empty states $\hbar\omega_{\min}$ exceeds the plasmon energy $\hbar\omega_0$ in all cases would by itself indicate that collective electronic action is ruled out for the entire list of examples. On the other hand, the number of electrons per atom participating in oscillations (Column *VI*) approximately equals the number of electrons in the outer shell except in the last two examples. The substantial deviation of z from its expected value, in the last two examples, could be caused by neglecting the size and number of particles in our calculations. Our method of calculation gives a number for z, which is too low if the particles are not small compared with both the "skin thickness" referred to the bulk metal, and the wave length,[11] or if the particles occupy more than a negligible part of the total volume. If z indeed equals the number of electrons in the outer shell, individual action would not be expected to occur. A plausible escape from this contradiction is to assume that the separation between the lowest filled and empty states, $\hbar\omega_{\min}$ is substantially lower for small particles surrounded by a polarizable medium than for bulk material.

Ideally, an experimental study of this subject should include observations on (a) extinction, (b) scattering, (c) number of particles per unit volume, and (d) the size of particles. In no instance are we in possession of all this information, and in the more interesting cases we have no direct evidence that there are even any particles.

ACKNOWLEDGMENTS

It is a pleasure to thank both J. H. Crawford, Jr., and A. T. Wager for discussion and helpful comments.

[20] H. D. Hagstrum, J. Phys. Chem. Solids **8**, 211 (1959).
[21] D. Pines, *Solid State Physics*, edited F. Seitz and D. Turnbull, (Academic Press, Inc., New York, 1955), Vol. 1, p. 367.
[22] D. Pines and D. Bohm, Phys. Rev. **85**, 338 (1952).
[23] D. Bohm and D. Pines, ibid. **92**, 609 (1953).
[24] D. Pines, ibid. **92**, 626 (1953).
[25] P. Nozières and D. Pines, Phys. Rev. **109**, 741 (1958); **109**, 762 (1958).

Solutions of the Equations of Space Charge Flow for Radial Flow between Concentric Spherical Electrodes

I. ITZKAN
Sperry Gyroscope Company, Great Neck, Long Island, New York
(September 21, 1959)

The solutions of the equations of space charge flow of electron beams for radial flow between concentric spherical electrodes are formulated in such a manner as to permit the introduction of arbitrary initial conditions. This allows one to solve a variety of physical problems with the aid of a table of Airy functions. A particular case, which exhibits a potential minimum between electrodes, is presented as an illustrative example.

LIST OF SYMBOLS

V	electrostatic potential
ρ	space charge density
v	electron velocity
ϵ_0	permittivity of free space
j	current density
e, m	charge and mass of electron
r	radius (position coordinate)
I	total current
b	constant defined in Eq. (5)
s and ψ	variables defined in Eq. (6)
p and q	variables defined in Eqs. (7) and (8)
x and y	variables defined in Eqs. (9) and (11)
$Ai(x)$ and $Bi(x)$	Airy functions of argument x
$Ai'(x)$ and $Bi'(x)$	derivatives of the Airy functions with respect to x
C_1, C_2, k	arbitrary constants
ϕ	normalized potential (to initial potential)
ϕ_f	normalized potential (to final potential)
σ	normalized radius
K_0	initial perveance
K_f	final perveance
t	transit time

1. INTRODUCTION

THE solutions of the equations of space charge flow between electrodes are of great interest to those working with many of the various electron-beam problems. It is not surprising, then, that most of the simpler, nonrelativistic, one-dimensional cases have been well covered in the literature, as shown by the comprehensive bibliography at the end of a recent review article by Ivey.[1] In a one-dimensional problem all variables are a function of a single spatial coordinate; the three electrode shapes which give rise to this situation are parallel planes, concentric cylinders, and concentric spheres. The equations of space charge flow for these cases reduce to nonlinear, ordinary differential equations of the second order.

Throughout the literature there is a tendency to evaluate the solutions of these differential equations in terms of the particular physical situations corresponding to particular values of the two arbitrary constants that enter into the solutions. For example, emission from a space-charge-limited cathode corresponds to the particular case where the electron velocity and potential gradient are zero at the same equipotential surface. Likewise, emission from a temperature-limited cathode corresponds to the case where the potential gradient is not zero at the equipotential surface where the velocity is zero.

The problem of flow between infinite planar electrodes for the space-charge-limited emission case was first solved by Child.[2] The more general case of arbitrary initial conditions (planar case) was considered by many but was worked out in great detail by Fay, Samuel, and Shockley.[3] Langmuir and Blodgett solved the cases of cylindrical electrodes and spherical electrodes for the space-charge-limited cathode.[4,5] Crank et al., by using mechanical integration, computed sets of curves for the cylindrical case with various initial conditions.[6] Subsequently, Page and Adams showed that both the linear and cylindrical cases with arbitrary initial conditions are derivable from pairs of master curves.[7] Kan derived an exact solution for the spherical case when the initial constants are both zero, that is, space-charge-limited emission[8]; and Poplovsky, following the procedure of Kan, derived the spherical solution corresponding to temperature limited emission, that is, where only one of the initial constants is zero.[9]

This paper derives the general spherical solution with arbitrary initial conditions in order to complete the solutions of the nonrelativistic, one-dimensional problems. Solutions for any pair of initial conditions are then derivable from a single pair of tabulated functions (and their first derivatives). Some sample solutions are also presented.

[1] H. F. Ivey, *Advances in Electronics and Electron Physics* (Academic Press, Inc., New York, 1954), Vol. VI, p. 137.

[2] C. D. Child, Phys. Rev. **32**, 492 (1911).
[3] C. F. Fay, A. L. Samuel, and W. Shockley, Bell System Tech. J. **17**, 49–79 (1938).
[4] I. Langmuir and K. Blodgett, Phys. Rev. **22**, 347–356 (1923).
[5] I. Langmuir and K. Blodgett, Phys. Rev. **24**, 49–59 (1924).
[6] J. Crank, D. R. Hartree, J. Ingham, and R. W. Sloane, Proc. Phys. Soc. (London) **A51**, 952 (1939).
[7] L. Page and N. I. Adams, Jr., Phys. Rev. **76**, 381 (1949).
[8] V. L. Kan, J. Tech. Phys. (U.S.S.R.) **18**, 483–494 (1948).
[9] R. P. Poplovsky, J. Tech. Phys. (U.S.S.R.) **20**, 149–159 (1950).

Applications of the space-charge-limited solutions of the three geometries in the design of Pierce guns, conventional diodes, and multi-element tubes are well known.[10] The general solutions of Fay, Samuel, and Shockley have found extensive application in the design of beam power tubes,[3] and they have been applied by Siekanowicz and Vaccaro to the design of periodic electrostatic focusing structures.[11] The present work opens up possibilities for extending these applications from parallel-flow beams to the case of convergent beams.

2. DESCRIPTION OF PROBLEM

The physical situation is as follows. We are given a pair of spherical surfaces, each at a given potential. Emanating from one of these and flowing toward the other is a beam of electrons which originated from a cathode at zero potential. The initial electron velocities are all radial and homogeneous, and since the geometries are such that only radial fields exist, the paths of motion remain radii and we have a one-dimensional problem. If the magnitude of the initial velocity (which must be compatible with the potential at the first surface) and the beam current are specified, then there is a unique solution for the potential distribution between the two surfaces. It is our problem to find this potential distribution. However, it is easier to solve the differential equations, given the value and slope at one end point rather than the values at both end points; therefore, in practice, one draws up families of curves with different initial slopes, from which the one with the correct final potential can be selected.

Physically, this situation corresponds to injecting a converging or diverging beam through a gridded surface toward another electrode, and examining the equilibrium potential distribution in the region between.

3. ANALYTICAL SOLUTION OF SPHERICAL CASE

The equations which govern space charge flow are

$$\nabla^2 V=\rho/\epsilon_0, \quad \text{Poisson's equation,} \tag{1}$$

$$\mathbf{j}=\rho\mathbf{v}, \quad \text{conservation of charge,} \tag{2}$$

$$eV=\tfrac{1}{2}\,mv^2, \quad \text{conservation of energy.} \tag{3}$$

If the current flow through any spherical surface is I, then the current density is given by

$$j=I/4\pi r^2,$$

and with spherical symmetry, $\nabla^2 V$ becomes

$$\frac{d}{r^2 dr}\frac{dV}{r^2 dr}.$$

On combining these, the differential equation of space charge flow between concentric spheres results:

$$\frac{d}{dr}\left(r^2\frac{dV}{dr}\right)=\frac{b^{\frac{1}{2}}I}{V^{\frac{1}{2}}}, \tag{4}$$

where

$$b=\frac{1}{4\pi\epsilon_0}\left(\frac{m}{2e}\right)^{\frac{1}{2}}, \tag{5}$$

where $b=612.4$ for electrons in mks units.

If we follow the substitutions proposed by Kan,[8] but do not introduce any initial conditions until the end, we have the following: Put

$$r=e^s \quad \text{and} \quad \psi=V/bI^{\frac{1}{2}}, \tag{6}$$

then

$$(d^2\psi/ds^2)+(d\psi/ds)=\psi^{-\frac{1}{2}}.$$

Put

$$p=d\psi/ds; \tag{7}$$

then

$$p(dp/d\psi)+p=\psi^{-\frac{1}{2}}.$$

Put

$$q=\psi^{\frac{1}{2}}; \quad \text{then} \quad pdp+2pqdq=2dq. \tag{8}$$

Put

$$x=2^{-\frac{1}{3}}(p+q^2); \quad \text{then} \quad pdx=2^{\frac{1}{3}}dq \tag{9}$$

and

$$dq/dx=2^{\frac{1}{3}}x-2^{-\frac{1}{3}}q^2. \tag{10}$$

Put

$$q=2^{\frac{1}{3}}(1/y)(dy/dx);$$

then

$$y''=xy. \tag{11}$$

The solutions of Eq. (11) are the Airy functions $Ai(x)$ and $Bi(x)$. These functions are tabulated in the references and are defined by[12,13]:

$$Ai(x)=\frac{1}{\pi}\int_0^\infty \cos(\tfrac{1}{3}t^3+xt)dt, \tag{12}$$

and

$$Bi(x)=\frac{1}{\pi}\int_0^\infty [\exp(-\tfrac{1}{3}t^3+xt)+\sin(\tfrac{1}{3}t^3+xt)]dt. \tag{13}$$

An important relationship between $Ai(x)$ and $Bi(x)$ is that

$$Ai(x)Bi'(x)-Bi(x)Ai'(x)=1/\pi. \tag{14}$$

Airy functions are also expressible as Bessel functions of the order $\pm\frac{1}{3}$.[14]

It is now necessary to recover the potential as a function of radius. This can be done in parametric form with x as the parameter as follows

$$y=C_1Ai(x)+C_2Bi(x); \tag{15}$$

$$dy/dx=C_1Ai'(x)+C_2Bi'(x). \tag{16}$$

[10] J. R. Pierce, J. Appl. Phys. **11**, 548–554 (1940).
[11] W. W. Siekanowicz and F. E. Vaccaro, Proc. Inst. Radio Engrs. **47**, 451 (1959).
[12] V. A. Fock, Government Information Pamphlet HNN-108 (Moscow, 1946).
[13] J. C. P. Miller, *Tables of Airy Functions* (Cambridge University Press, New York, 1946).
[14] G. N. Watson, *Theory of Bessel Functions* (Cambridge University Press, New York, 1952).

From the definition of q,

$$q=2^{\frac{1}{2}}\frac{y'}{y}=2^{\frac{1}{2}}\frac{C_1Ai'(x)+C_2Bi'(x)}{C_1Ai(x)+C_2Bi(x)}, \tag{17}$$

$$V=bI^{\frac{1}{2}}=bq^2I^{\frac{1}{2}}=b(2I)^{\frac{1}{2}}\left[\frac{kAi'(x)+Bi'(x)}{kAi(x)+Bi(x)}\right]^2, \tag{18}$$

where $k=C_1/C_2$. From the definition of x,

$$x=2^{-\frac{1}{2}}(p+q^2)=2^{-\frac{1}{2}}\left(\frac{d\psi}{ds}+\psi\right)=2^{-\frac{1}{2}}\left[\psi+\frac{d\psi}{dr}\frac{dr}{ds}\right] \tag{19}$$

and

$$x=2^{-\frac{1}{2}}\left[\psi+r\frac{d\psi}{dr}\right]=\frac{1}{b}\left[\frac{1}{2I}\right]^{\frac{1}{2}}\left[V+r\frac{dV}{dr}\right]. \tag{20}$$

Now, let us consider the initial conditions given at the point $r=r_0$, and then denote these by subscript zero, i.e.,

$$V=V_0, \quad dV/dr|_{r=0}=V_0', \quad x=x_0, \quad \text{etc.}$$

Then, we can use Eq. (18) to compute the value of k at $r=r_0$:

$$k_0=\frac{b^{\frac{1}{2}}(2I)^{\frac{1}{2}}Bi'(x_0)-V_0^{\frac{1}{2}}Bi(x_0)}{V_0^{\frac{1}{2}}Ai(x_0)-b^{\frac{1}{2}}(2I)^{\frac{1}{2}}Ai'(x_0)}. \tag{21}$$

And Eq. (20) can be used to compute x_0:

$$x_0=1/b(1/2I)^{\frac{1}{2}}(V_0+r_0V_0'). \tag{22}$$

To obtain r as a function of x, we have

$$\int_{r_0}^{r}\frac{dr}{r}=\int_{s_0}^{s}ds=\int_{\psi_0}^{\psi}\frac{d\psi}{p}=\int_{q_0}^{q}\frac{2qdq}{p}$$

$$=\int_{x_0}^{x}\frac{2qdx}{2^{\frac{1}{2}}}=\int_{y_0}^{y}\frac{2dy}{y}; \tag{23}$$

therefore,

$$\ln r/r_0=2\ln y/y_0 \tag{24}$$

and

$$\frac{r}{r_0}=\left[\frac{k_0Ai(x)+Bi(x)}{k_0Ai(x_0)+Bi(x_0)}\right]^2. \tag{25}$$

Let us use variables normalized to the initial conditions. Define

$$\sigma=r/r_0 \quad \text{and} \quad \phi=V/V_0. \tag{26}$$

Also, let

$$K_0=I/V_0^{\frac{1}{2}}; \quad a=b^{\frac{1}{2}}(2K_0)^{\frac{1}{2}}. \tag{27}$$

Then, K_0 is the initial perveance of the beam.

In terms of these variables, Eqs. (22), (21), (18), and (25) become, respectively,

$$x=\frac{1}{a^2}\left[\phi+\frac{d\phi}{d\sigma}\right]; \quad x_0=\frac{1}{a^2}[1+\phi_0']; \tag{28}$$

$$k_0=\frac{aBi'(x_0)-Bi(x_0)}{Ai(x_0)-aAi'(x_0)}; \tag{29}$$

$$\phi=a^2\left[\frac{k_0Ai'(x)+Bi'(x)}{k_0Ai(x)+Bi(x)}\right]^2; \tag{30}$$

and

$$\sigma=\left[\frac{k_0Ai(x)+Bi(x)}{k_0Ai(x_0)+Bi(x_0)}\right]^2. \tag{31}$$

Equations (28) to (31) constitute the solutions to the problem for general initial conditions.

4. SPECIAL CASES

If one wishes to recover the solutions of Poplovsky,[9] that is to solve for the particular cases where V_0 is zero (corresponding to emission from a unipotential cathode with radius r_0 and negligible initial velocity), one cannot normalize with respect to V_0. For these cases, substitution in the unnormalized equations will give the following results

Equation (22) becomes

$$x_0=1/b(1/2I)^{\frac{1}{2}}r_0V_0', \tag{32}$$

Eq. (21) becomes

$$k_0=-Bi'(x_0)/Ai'(x_0), \tag{33}$$

Eq. (25) becomes

$$r/r_0=\sigma=\pi^2[Ai(x)Bi'(x_0)-Bi(x)Ai'(x_0)]^2, \tag{34}$$

and Eq. (18) becomes

$$V=b(2I)^{\frac{1}{2}}\left[\frac{Ai'(x)Bi'(x_0)-Bi'(x)Ai'(x_0)}{Ai(x)Bi'(x_0)-Bi(x)Ai'(x_0)}\right]^2. \tag{35}$$

If K_f and V_f are the perveance and voltage at some final radius $K_f=I/V_f^{\frac{1}{2}}$, we can normalize with respect to V_f; that is, let $\phi_f=V/V_f$; then

$$\phi_f=b(2K_f)^{\frac{1}{2}}\frac{\pi^2}{\sigma}[Bi'(x)Ai'(x_0)-Ai'(x)Bi'(x_0)]^2. \tag{36}$$

Therefore, given the gradient at the cathode, one uses Eq. (32) to compute x_0; and then Eqs. (34) and (36) constitute the parametric solutions of the problem. For space-charge-limited flow, x_0 equals 0. Appropriate choice of the sign of V_0', and the decision of whether to let x either increase or decrease from x_0 yield the various cases of flow from concave or convex cathode surfaces.

Very often, the transit time is of interest in these problems. If one notes that $dt=dr/v$, where t is the transit time of an electron, then, by straight substitution one obtains

$$t=2^{1/6}(I^{-\frac{1}{2}})\left(\frac{m}{be}\right)^{\frac{1}{2}}r_0\int_{x_0}^{x}\sigma dx. \tag{37}$$

5. CONCLUSION

There are a number of physical problems involving the flow of charged particles between spheres, and these problems are essentially solutions of the same differential equation with different initial conditions. We

have seen how the solutions to all of these problems can be expressed in parametric form in terms of Airy functions. For a space-charge-limited diode, one sets x_0 equal to zero in Eqs. (34) and (36) and obtains normalized voltage and normalized radius as a function of x. If x is permitted to decrease from zero, one gets the case where the anode is smaller than the cathode; and if x increases, one gets the case where the anode is greater than the cathode.

For emission from a temperature-limited cathode, we must know the gradient at the cathode and also the total current. Then Eq. (32) can be used to obtain x_0; and then Eqs. (34) and (35) or (36) are used to obtain the voltage-radius curves. More often, one knows the current and the final voltage at a final radius. For such cases, a family of curves for different values of V_0' can be plotted and the appropriate curve selected.

For the general case, one needs to know the velocity of the electrons and the potential gradient at one electrode, in addition to the total current. One then uses Eq. (28) to obtain x_0, Eq. (29) to obtain k_0, and then Eqs. (30) and (31) to obtain the voltage-radius curves. More often, the current, initial potential, and final potential are known so that a family of curves for different values of ϕ_0' can be plotted and the appropriate curve selected. An example of such a plot is shown in Fig. 1. All the curves are for cases where $K_0=40\times10^{-6}$, but each curve is for a different ϕ_0'. The curves of the particular family selected for illustration show the interesting property of passing through a potential minimum. This is the case which Fay, Samuel, and Shockley[3] have called case "*C*." A preliminary survey of the possible solutions seems to indicate that all the cases found in the planar case also are present in the spherical case, including the bistable solutions found by Fay et al.

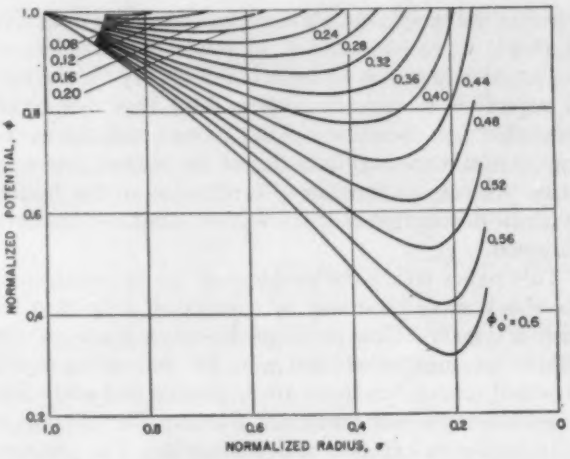

FIG. 1. Normalized potential vs normalized radius for the case where $K_0=40\times10^{-6}$ for various values of the initial slope.

ACKNOWLEDGMENTS

The author is deeply indebted in Dr. C. C. Wang for his suggestions, advice, and encouragement during the preparation of this paper; to Dr. R. R. Pepper and Mr. R. J. von Gutfeld for valuable discussions, and to Mr. A. Brandenstein who performed the computation.

JOURNAL OF APPLIED PHYSICS VOLUME 31, NUMBER 4 APRIL, 1960

Attenuation of the Shock Wave Produced in a Solid by a Flying Plate*

G. R. FOWLES
Stanford Research Institute, Menlo Park, California
(Received October 28, 1959)

The attenuation of the plane shock wave produced in a solid by a flying plate of the same material is treated neglecting dissipative processes and effects of material rigidity. Explicit formulas for the position of the shock front and the shape of the pulse as functions of time are obtained by application of Friedrich's method. A numerical example for an aluminum target and projectile is presented to illustrate some of the features of the calculation, and an experiment is proposed to test the theory. The experiment should also allow a reasonably precise measurement of sound velocity immediately behind the shock front to be obtained. This possibility applies equally well to the case of target and projectile of different materials.

I. INTRODUCTION

A NUMBER of investigations have shown that the mechanical behavior of solids at the high pressures produced by detonating explosive can be adequately described by assuming that the solid behaves as an ideal fluid. Among these are descriptions of the behavior of shaped charge jets[1,2] and high-pressure equations of state.[3,4] It is of considerable interest to determine

* Some of the results of this paper were submitted in partial fulfillment of the requirements for the degree of Doctor of Philosophy, Department of Geophysics, Stanford University. Work partially performed under U. S. Air Force contract, Air Force Office of Scientific Research (ARDC).

[1] J. M. Walsh, R. G. Shreffler, and F. J. Willig, J. Appl. Phys. **24**, 349 (1953); also E. M. Pugh, R. J. Eichelberger, and N. Rostoker, J. Appl. Phys. **23**, 532 (1952); also D. C. Pack, W. M. Evans, and H. J. James, Proc. Phys. Soc. **60**, 1 (1948).
[2] W. A. Allen, et al., Phys. Fluids, **2**, 329 (1959).
[3] G. E. Duvall and B. Zwolinski, J. Acoust. Soc. Am. **27**, 1054–1058 (1955).
[4] M. H. Rice, J. M. Walsh, and R. G. McQueen, *Solid State*

whether the theory can also be applied to the description of shock wave attenuation in solids. Calculations of attenuation based on hydrodynamic theory for the case of explosive in contact with a solid have been performed,[5,6] but these are subject to uncertainties in the equation of state and behavior of the burned explosive gases. As yet, no conclusive verification of the hydrodynamic description of shock wave attenuation has been obtained.

This paper treats the problem of the attenuation of the shock wave produced by collision of a flying plate with a target. This problem is not subject to the difficulties mentioned and can be solved explicitly provided entropy changes are negligible and plate and target are of the same material. Further, the calculation is amenable to experimental verification. The analysis follows closely the theory given in Courant and Friedrichs.[7] Many aspects of this problem as it applies to penetration, including effects of entropy change, have been considered by Duvall.[8]

A numerical example and an experiment to verify the theory are also described. The experiment should not only provide a test of the validity of hydrodynamic theory, but also should permit measurement of sound velocity at high pressure. Application of plasticity theory to a plane shock followed by a plane rarefaction[9] indicates that during loading the material first strains elastically, then plastically to peak strain. Upon unloading, the material again first strains elastically, then plastically when the yield criterion is again satisfied. Hence, one might expect the first relief wave to overtake the shock front to travel with the elastic dilatational velocity appropriate to the high pressure at the shock front. In the experiment described it appears feasible to determine whether the first relief wave travels with "hydrodynamic" sound velocity or with elastic dilatational velocity, and to measure this velocity with reasonable precision. It may be noted that the elastic dilatational velocity usually exceeds the "hydrodynamic" sound velocity at low pressure by about 20%.

Note added in proof.—In an important recent article L. W. Morland [Phil. Trans. Roy. Soc. London **A251**, 341 (1959)], treats the problem of the propagation of a plane compressional wave in an elastic-plastic medium. The theory confirms that the first relief wave to overtake the shock does travel with elastic dilatational velocity and has stress amplitude approximately equal to four times the yield strength in simple compression. For most materials this amplitude should be sufficient to be easily observable in the experiment described. Thus, the experiment should show unequivocally whether the hydrodynamic model or the elastic-plastic model is correct at the extreme strain rates concerned.

II. OUTLINE OF THE PROBLEM

A plate of thickness "d" and initial velocity u_0 strikes a semi-infinite plate of the same material normal to the boundary at $x=x_0$, $t=t_0$ (Fig. 1). Shock waves are produced in each medium traveling away from the collision boundary with velocity U_1' (with respect to materials). The shock wave in the projectile reflects from the rear free surface as a centered simple rarefaction wave, which eventually overtakes the shock in the target, reducing the peak pressure and the shock velocity. It is desired to compute the peak pressure in the two shock waves as a function of initial plate velocity for arbitrary projectile and target material, to determine the time and position at which the peak pressure of the shock in the target first begins to decay, and to describe completely the attenuation of the shock.

The principal assumptions are as follows:

1. The materials behave as fluids with negligible rigidity, viscosity, and heat conductivity. Thus, it is assumed that hydrodynamic theory for compressible, inviscid flow applies in all respects.

2. Entropy is everywhere constant, including the shock transition. Shock transitions are therefore taken to be equivalent to isentropic compressions. The validity of this assumption for moderate compressions has been discussed by Friedrichs.[7]

In addition to these assumptions, pressure, P, and particle velocity, u, are required to be continuous across the collision boundary for $P\neq 0$. Additional necessary information is knowledge of the Hugoniot equation of state, or shock polar, for each material considered.

III. METHOD OF CALCULATION

A. Equation of State

Various forms of equation of state have been proposed and applied to high-pressure shock wave data for solids.[3,4] Of these, some are semi-theoretical, while others are entirely empirical. For purposes of calculation there is little to choose between the various forms other than convenience of application since, in most cases, each fits available data within experimental error.

A semi-theoretical form derived by Murnaghan[10] on the basis of finite elastic strain theory is

$$P=A[(\rho/\rho_0)^{\gamma}-1], \tag{1}$$

where P is pressure, ρ and ρ_0 are final and initial

Physics, edited by F. Seitz and D. Turnbull (Academic Press, Inc., New York, 1958), Vol. 6.

[5] J. O. Erkman, Phys. Fluids **1**, 535 (1958).

[6] W. E. Drummond, J. Appl. Phys. **28**, 1437 (1957); J. Appl. Phys. **29**, 167 (1958).

[7] R. Courant and K. O. Friedrichs, *Supersonic Flow and Shock Waves* (Interscience Publishers, Inc., New York, 1948); also, K. O. Friedrichs, Appl. Math. **1**, 3 (1948).

[8] G. E. Duvall, "Penetration of matter by solid projectiles," Internal Rept. No. 002-55, Poulter Laboratories, Stanford Research Institute (1955).

[9] C. S. Gardner (private communication).

[10] F. D. Murnaghan, *Finite Deformation of an Elastic Solid* (John Wiley & Sons, Inc., New York, 1951).

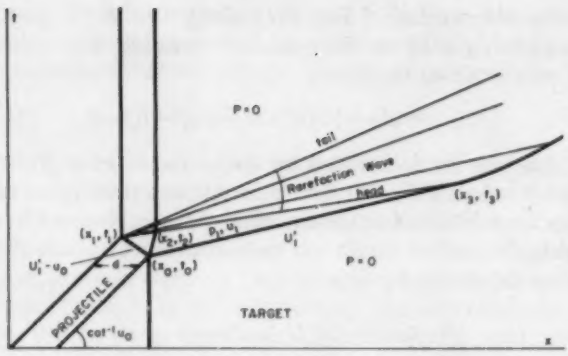

FIG. 1. Time-distance diagram illustrating collision of a plate with a target (case shown is for target and projectile of the same material).

densities, respectively, and A and γ are empirical constants.

This equation is especially convenient for hydrodynamic calculations since it gives a particularly simple form for the Riemann parameter "l" (Sec. III-C).

It is convenient at this point to introduce the definition of hydrodynamic sound velocity "c,"

$$c^2=(\partial P/\partial\rho)_s \quad \text{where} \quad s=\text{entropy}.$$

By virtue of assumption (2) this is equivalent to

$$c^2=(\partial P/\partial\rho)_H,$$

where the subscript H means the derivative is taken along the Hugoniot.

For Eq. (1) sound velocity is therefore given by

$$c^2=\gamma A/\rho_0(\rho/\rho_0)^{\gamma-1}=\gamma(P+A)/\rho. \tag{2}$$

B. Initial Conditions

The mechanical shock conditions expressing conservation of mass and momentum may be written,

$$\rho_0(U-u_0)=\rho_1(U-u_1) \tag{3}$$

$$P_1-P_0=\rho_0(U-u_0)(u_1-u_0), \tag{4}$$

where U and u are shock and particle velocities (lab. coordinates), respectively, P is pressure and ρ is density. Subscripts "0" refer to the state ahead of the shock and subscripts "1" refer to the state behind the shock. In the discussion, unprimed velocities are with respect to laboratory coordinates, primed are with respect to the material ahead of the shock.

For the problem under consideration therefore, ($P_0=0$),

$$\left.\begin{aligned}\rho_0U_1'&=\rho_1(U_1'-u_1)\\ P_1&=\rho_0U_1'u_1\end{aligned}\right\}\ \text{target} \tag{5,6}$$

$$\left.\begin{aligned}\rho_0U_1'&=\rho_1(U_1'-u_0+u_1)\\ P_1&=\rho_0U_1'(u_0-u_1)\end{aligned}\right\}\ \text{projectile,} \tag{7,8}$$

where u_0 is initial plate velocity.

By eliminating P_1 between (6) and (8) gives

$$u_1=u_0/2, \tag{9}$$

as is also evident from symmetry.

The solution for the density behind the shock is most easily obtained graphically or numerically. The combination of (1) with (5), (6), and (9) gives

$$\left(\frac{u_0}{2}\right)^2=\frac{A}{\rho_0}\left(\frac{\rho_1/\rho_0-1}{\rho_1/\rho_0}\right)[(\rho_1/\rho_0)^\gamma-1], \tag{10}$$

which gives ρ_1/ρ_0 implicitly as function of u_0. P_1 then follows from the equation of state (1), and shock velocity from (5) or (6).

The time required for the shock in the projectile to reach the rear free boundary is

$$t_1-t_0=d/U_1'. \tag{11}$$

The head of the reflected rarefaction then reaches the collision boundary at time t_2, given by

$$t_2-t_1=\rho_0d/\rho_1c_1, \tag{12}$$

where c_1 is sound velocity at pressure P_1.

The head of the rarefaction overtakes the shock front in the target at time t_3 given by

$$t_3-t_2=\frac{x_3-x_2}{u_1+c_1}=\frac{(t_3-t_0)U_1-u_1(t_2-t_0)}{u_1+c_1}, \tag{13}$$

or

$$t_3-t_0=\frac{(t_2-t_0)c_1}{u_1+c_1-U_1}. \tag{14}$$

On combining (11), (12), and (14),

$$t_3-t_0=\frac{c_1d}{u_1+c_1-U_1}\left(\frac{\rho_0}{\rho_1c_1}+\frac{1}{U_1}\right). \tag{15}$$

The distance the shock travels before the peak pressure changes is, therefore,

$$x_3-x_0=\frac{U_1c_1d}{u_1+c_1-U_1}\left(\frac{\rho_0}{\rho_1c_1}+\frac{1}{U_1}\right). \tag{16}$$

The calculation to this point is easily extended to the case in which target and projectile are of different materials. The initial state for that case is determined from the intersection of the Hugoniot curves $P=P(u)$ for each material. These curves may be calculated in terms of the intermediate parameter ρ/ρ_0. The formulas are

$$P=A[(\rho/\rho_0)^\gamma-1] \quad \text{(target and projectile)}$$

$$u=\left[\frac{P(1-\rho_0/\rho)}{\rho_0}\right]^{\frac{1}{2}} \quad \text{(target),}$$

and

$$u=u_0-\left[\frac{P(1-\rho_0/\rho)}{\rho_0}\right]^{\frac{1}{2}} \quad \text{(projectile).}$$

Formulas corresponding to (15) and (16) are

$$l_3-l_0=\frac{c_1{}^l d}{u_1+c_1{}^l-U_1{}^l}\left(\frac{\rho_0{}^p}{\rho_1{}^p c_1{}^p}+\frac{1}{U_1{}'^p}\right), \quad (17)$$

$$x_3-x_0=\frac{U_1{}^l c_1{}^l d}{u_1+c_1{}^l-U_1{}^l}\left(\frac{\rho_0{}^p}{\rho_1{}^p c_1{}^p}+\frac{1}{U_1{}'^p}\right), \quad (18)$$

where superscripts "p" refer to the projectile and superscripts "l" refer to the target.

The decay of the shock when target and projectile are of different materials is somewhat more complicated than for the case considered, due to the impedance mismatch at the collision boundary. Because of the mismatch, reflected waves are generated which modify the incident rarefaction. Consequently, the flow in the projectile and the initial conditions for the rarefaction in the target must be determined in general by stepwise integration. Where target and projectile are the same material, however, no interaction at the boundary takes place, and the attenuation of the shock in the target can be calculated explicitly by application of Friedrich's method.[7]

C. Decay of the Shock in the Target

When target and projectile are of the same material, the rarefaction is everywhere a simple wave centered at (x_1,t_1). The $C+$ characteristics[7] (trajectories of forward-facing sound waves) are, therefore, straight lines with slopes $dx/dt=u+c$. Further, the Riemann invariant l_0 given by

$$u-l=-l_0, \quad (19)$$

is constant everywhere, including the shock transition by virtue of assumption (2).

The quantity l in (19) is defined as

$$l=\int_{\rho'}^{p}\frac{dP}{\rho c}=\int_{,}^{\rho}\frac{c\,d\rho}{\rho},$$

where ρ' is arbitrary.

For the Murnaghan equation of state [Eq. (1)], l is the same as for an ideal gas,

$$l=2c/(\gamma-1), \quad (\rho'=0). \quad (20)$$

Since the rarefaction is a centered simple wave, it may be described by the equations

$$x-x_1=(u+c)(t-t_1)=c_0(\sigma+1)(t-t_1), \quad (21)$$

$$u=2\sigma c_0/(\gamma+1), \quad (22)$$

$$c=(c_0/\gamma+1)[(\sigma+1)(\gamma-1)+2], \quad (23)$$

where σ is defined as

$$\sigma=(u+c-c_0)/c_0,$$

and c_0 is the sound velocity ahead of the shock.

By differentiating Eq. (21) along the shock path, considering σ as the independent variable, and using $U=dx/dt$ along this path,

$$[U(\sigma)-c_0(\sigma+1)](dt/d\sigma)-c_0(t-t_1)=0, \quad (24)$$

which may be integrated for $t(\sigma)$ once $U(\sigma)$ is given. Shock velocity $U(\sigma)$ is determined from the mechanical shock conditions and the equation of state. Rather than using the explicit form, it is more convenient to use the series expansion for $U(\sigma)$.

Expansion of U in Powers of σ

From the equation of state (1) and the definition of sound velocity we have

$$c^2=\gamma(P+A)/\rho.$$

On eliminating P and ρ by Eqs. (3) and (4),

$$c^2=\gamma(U-u)[u+(A/\rho_0 U)]. \quad (25)$$

But,

$$\gamma A/\rho_0=c_0{}^2. \quad (26)$$

On substituting (26) into (25) and eliminating u and c by (22) and (23) gives, after some manipulation,

$$U^2-U\left[\frac{\sigma c_0(\gamma+1)}{2\gamma}+\frac{c_0(\gamma-1)}{\gamma}\right]-\frac{c_0{}^2}{\gamma}=0. \quad (27)$$

The solution is then

$$U=\frac{c_0(\gamma+1)}{2\gamma}\left\{\frac{\sigma}{2}+\frac{\gamma-1}{\gamma+1}\pm\left[\frac{\sigma^2}{4}+\frac{\sigma(\gamma-1)}{\gamma+1}+1\right]^{\frac{1}{2}}\right\}. \quad (28)$$

Expansion of Eq. (28) by the binomial theorem gives

$$U=\frac{c_0(\gamma+1)}{2\gamma}\left(\frac{\sigma}{2}+\frac{\gamma-1}{\gamma+1}\pm\left\{1+\frac{1}{2}\left[\frac{\sigma^2}{4}+\frac{\sigma(\gamma-1)}{\gamma+1}\right]-\frac{1}{8}\left[\frac{\sigma^2}{4}+\frac{\sigma(\gamma-1)}{\gamma+1}\right]^2+\cdots\right\}\right).$$

Keeping only terms to second order in σ yields

$$U=c_0\left[1+\frac{\sigma}{2}+\frac{\sigma^2}{4(\gamma+1)}+0(\sigma^3)\right]. \quad (29)$$

It will be noted that this expansion does not depend on the term "A" in the equation of state. Hence, it is also valid for a polytropic gas. It differs from the expansion given by Friedrichs[7] for a polytropic gas, however, in the coefficients of the square and higher order terms. The expansion given by Friedrichs is

$$U=c_0[1+(\sigma/2)+(\sigma^2/8)+0(\sigma^4)]. \quad (30)$$

The difference between Eqs. (29) and (30) results from somewhat different procedure in their derivation. For a polytropic gas, an exact expression including

entropy can be derived in place of (27). This derivation requires invoking the energy shock condition and the definition of internal energy. The resulting expression is

$$U^2-U[(\gamma+1/2)u]-c_0^2=0, \tag{31}$$

which upon substituting for u by (22) and expanding gives Eq. (30). It appears, therefore, that a contribution due to entropy change is concealed in (30). Further, this relation obviously does not apply to a Murnaghan solid, since in deriving (31) internal energy is assumed proportional only to temperature. The contribution of the second order term is small, however, for moderate compressions amounting to a few percent.

Substitution of Eq. (29) into (24) gives

$$c_0\left[1+\frac{\sigma}{2}+\frac{\sigma^2}{4(\gamma+1)}-(\sigma+1)\right]\frac{dt}{d\sigma}-c_0(t-t_1)=0$$

or,

$$\left[\frac{\sigma^2}{4(\gamma+1)}-\frac{\sigma}{2}\right]\frac{dt}{d\sigma}-(t-t_1)=0. \tag{32}$$

Equation (32) is a linear equation for the times along the shock path in terms of the parameter σ.

Separating variables in Eq. (32),

$$\frac{dt}{t-t_1}=\frac{4(\gamma+1)d\sigma}{\sigma[\sigma-2(\gamma+1)]}.$$

The solution is evidently

$$\log(t-t_1)\Big|_{t_3}^{t}=4(\gamma+1)\left[\frac{-1}{2(\gamma+1)}\log\left(\frac{\sigma}{\sigma-2(\gamma+1)}\right)\right]_{\sigma_0}^{\sigma}.$$

Hence,

$$t(\sigma)-t_1=(t_3-t_1)\left[\frac{\sigma_0}{\sigma_0-2(\gamma+1)}\right]^2\left[\frac{\sigma-2(\gamma+1)}{\sigma}\right]^2, \tag{33}$$

where σ_0 is the value of σ corresponding to the head of the rarefraction, or

$$\sigma_0=\frac{x_3-x_1}{c_0(t_3-t_1)}-1; \tag{34}$$

$x(\sigma)$ may then be determined from Eq. (21),

$$x(\sigma)-x_1=c_0(\sigma+1)(t_3-t_1)\times\left[\frac{\sigma_0}{\sigma_0-2(\gamma+1)}\right]^2\left[\frac{\sigma-2(\gamma+1)}{\sigma}\right]^2. \tag{35}$$

Equations (33) and (35) thus determine the shock path through the intermediate parameter σ.

Shock Profiles

Values of the shock-wave parameters (P, u, c, ρ) along the shock path may be calculated once the shock path is known. Profiles of the parameters as functions of distance behind the shock for fixed times may also be computed.

From Eq. (22) we have

$$u(x,t')=\frac{2\sigma(x,t')c_0}{\gamma+1}\quad 0<\sigma<\sigma_0$$

$$=\frac{2c_0}{\gamma+1}\left[\frac{x-x_1}{c_0(t'-t_1)}-1\right]. \tag{36}$$

Similarly,

$$c(x,t')=\frac{c_0}{\gamma+1}\left[2+\frac{\gamma-1}{c_0}\left(\frac{x-x_1}{t'-t_1}\right)\right]. \tag{37}$$

It is apparent from Eqs. (36) and (37) that particle velocity and sound velocity vary linearly with distance behind the shock for fixed times.

From the equation of state (1) and the definition of sound velocity we obtain

$$\rho_0/\rho=(A\gamma/\rho_0c^2)^{(1/\gamma-1)}=(c_0/c)^{(2/\gamma-1)}, \tag{38}$$

and

$$P=A[(\rho/\rho_0)^\gamma-1]=\rho c^2/\gamma-A. \tag{39}$$

Equations (33) through (39) provide a complete description of the attenuation of the shock, to the extent of course that dissipative processes and effects of material rigidity can be neglected.

IV. NUMERICAL EXAMPLE

As a numerical example, the following initial conditions are chosen for an aluminum target and projectile.

Equation of state (fitted to Los Alamos data[4]).

$$P=188.96[(\rho/\rho_0)^{4.286}-1]\text{ kb.}$$

Plate thickness	$d=0.125$ in. $=3.175$ mm.
Initial plate velocity	$u_0=1.63$ mm/μs.
Initial density	$\rho_0=2.785$ gm/cm^3.
Initial sound velocity	$c_0=5.38$ mm/μs.
Initial particle velocity	$u_1=0.815$ mm/μs.

Graphical solution of (10) gives

$$\rho_0/\rho_1=0.8736,$$

and, hence,

$$P_1=146.4\text{ kb},$$
$$c_1=\ 6.70\text{ mm}/\mu\text{s},$$
$$U_1=\ 6.45\text{ mm}/\mu\text{sec}.$$

Application of Eqs. (11) through (16) then gives

$$t_1-t_0=0.492\ \mu\text{s},$$
$$t_2-t_0=0.906\ \mu\text{s},$$
$$t_3-t_0=5.70\ \mu\text{s},$$

and

$$x_1-x_0=-2.37\text{ mm},$$
$$x_3-x_0=\ 36.76\text{ mm}.$$

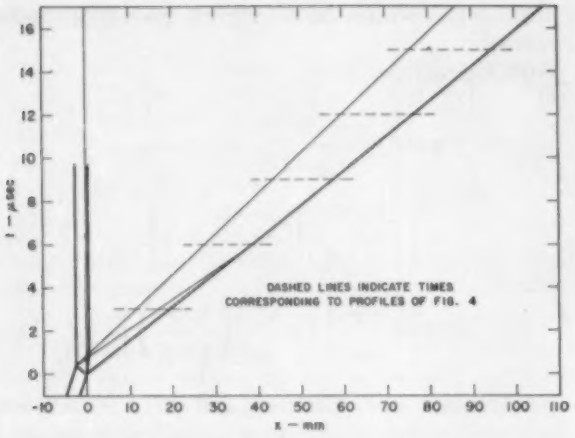

FIG. 2. Time-distance plot for numerical example treated.

The shock path computed from (33) and (35) is shown in Fig. 2. Peak pressure and peak particle velocity along the shock path as function of distance of travel of the shock are shown in Fig. 3. Figure 4 shows the position of the shock and profiles of the shock parameters (c and u) as functions of distance behind the shock at five different times and Fig. 5 shows the same for parameters p and ρ.

V. PROPOSED EXPERIMENT

A possible experimental arrangement to test the theory is illustrated in Fig. 6. The most important requirement is a means for accelerating the plate to uniform velocity so that it strikes nearly normal to the collision boundary. This can probably be done by using either a flying-plate plane-wave initiator[11] as shown, or by using a plane-wave lens. A wedge angle is cut on the face of the target plate opposite the collision boundary. The apparent velocity of the shock wave along the wedge face and the free-surface velocity across a known gap are measured by a streak camera using a reflected light technique.[12] The tilt of the shock about an axis perpendicular to the camera slits is determined from the apparent shock velocity along the wedge face, the measured free-surface velocity, and the equation of state. Argon gaps on either side of the free-surface gap are viewed by additional slits in the camera. These measure the tilt of the shock about an axis parallel to the camera slits.

Since the tilt of the shock is monitored, small departures from normality can be tolerated. Further, the initial free-surface velocity is measured so that the velocity of the projectile need not be known in advance. Necessary experimental conditions which are not moni-

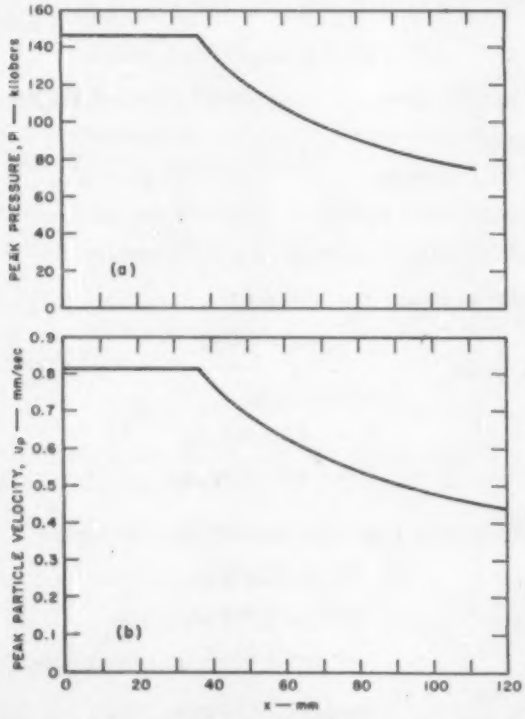

FIG. 3. Peak pressure and peak particle velocity at shock front as function of distance of travel of shock.

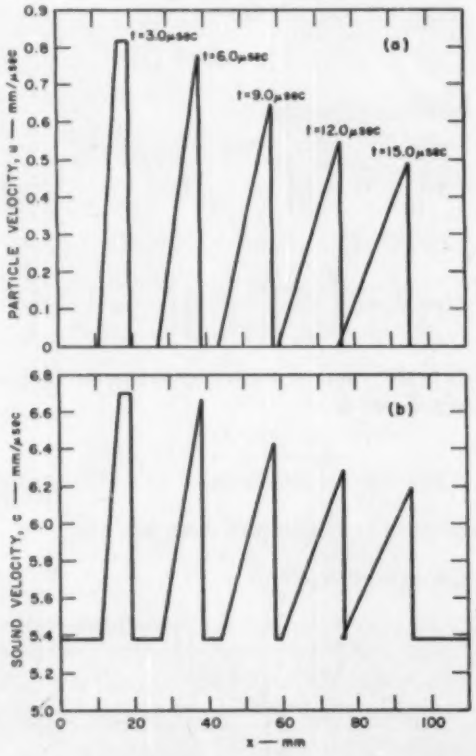

FIG. 4. Profiles of particle velocity and sound velocity behind shock at fixed times.

[11] D. E. Brink, R. F. Hurst, and M. C. Kells, "Plane wave generators," Lab. Tech. Rept. 001-58, Poulter Laboratories, Stanford Research Institute (1958).

[12] D. G. Doran, G. R. Fowles, and G. A. Peterson, Phys. Rev. Letters **1**, 402 (1958).

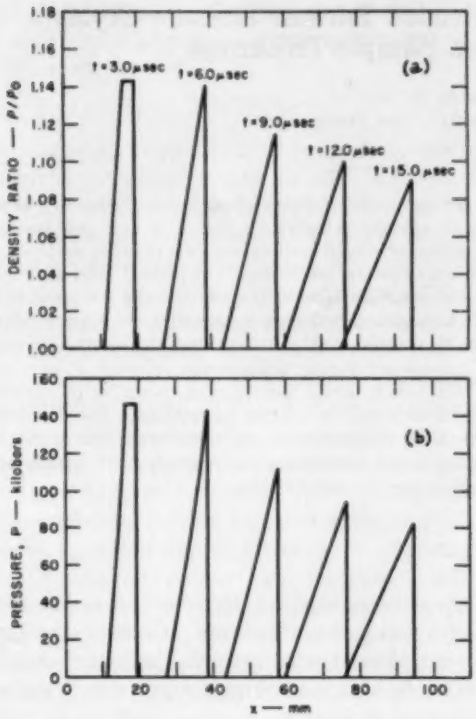

FIG. 5. Profiles of density ratio and pressure behind shock at fixed times.

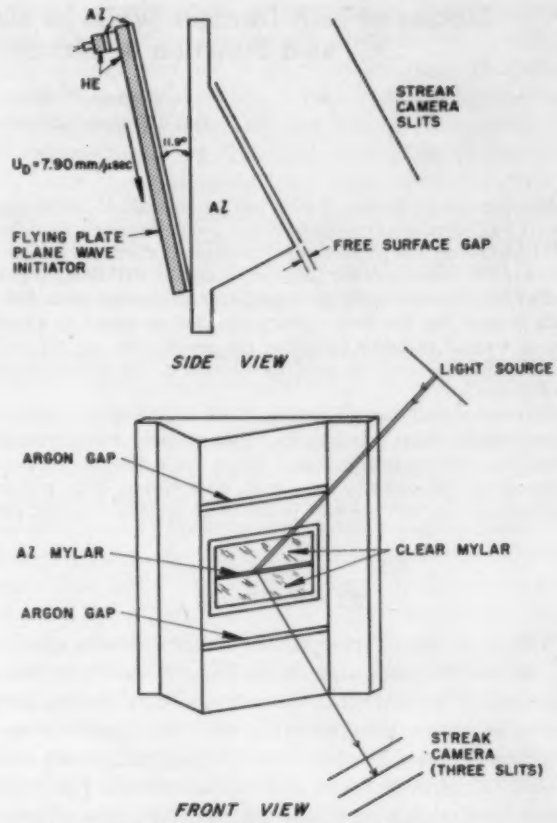

FIG. 6. Sketch of possible experimental arrangement.

tored, and which must therefore be known in advance are (1) uniformity of plate velocity and planarity of shock, (2) projectile thickness, and (3) zero pressure in the projectile at the time of impact.

The first of these could be monitored in independent experiments until reliable planarity is obtained. The second should not be a serious problem for the experiment shown and the third should not give rise to serious difficulties, except possibly in the very late stages of the shock attenuation.

The data obtained from the experiment would correspond to the curve of Figure 3(b). The abrupt change in free-surface velocity as the head of the rarefaction overtakes the shock suggests the important possibility that sound velocity at pressure P_1 can be measured. For an aluminum target and projectile, as illustrated, the distance (x_3) at which the head of the rarefaction overtakes the shock should be easily determinable to within 5%.

After solving Eq. (16) for c_1,

$$c_1=\frac{U_1(x_3-x_0+\rho_0 d/\rho_1)-u_1(x_3-x_0)}{x_3-x_0-d}. \tag{40}$$

After substituting for ρ_0/ρ_1 from Eq. (5),

$$c_1=\frac{(U_1-u_1)(x_3-x_0/d+1)}{(x_3-x_0/d-1)}, \tag{41}$$

in which all quantities may be considered known except c_1. For target and projectile of different materials the expression is slightly more complicated. However, the conclusion to be stated is not materially altered.

Equation (41) shows that c_1 is relatively insensitive to the value of the quantity $(x_3-x_0)/d$ for large values of that quantity. In the numerical example treated $(x_3-x_0)/d\cong 10$, and a 5% error leads to only a 1% error in c_1. Further, the value of U_1-u_1 should be easily measurable to within 1%. Hence, the method appears to offer better than 2% accuracy in determination of sound velocity at high pressure.

ACKNOWLEDGMENTS

The author wishes to express his appreciation to Dr. G. E. Duvall, G. M. Muller, Dr. S. Katz, and Dr. J. S. Koehler for many helpful suggestions; also to J. O. Erkman who supplied the fit of the Murnaghan equation to the Los Alamos data for aluminum.

Motion of 180° Domain Walls in Metal Electroded Barium Titanate Crystals as a Function of Electric Field and Sample Thickness

ROBERT C. MILLER AND ALBERT SAVAGE
Bell Telephone Laboratories, Murray Hill, New Jersey

(Received November 9, 1959)

The domain dynamics of polarization reversal in metal electroded $BaTiO_3$ single crystals have not been adequately described in the literature. The present paper contains quantitative measurements of the velocity of the sidewise motion of 180° domain-walls in $BaTiO_3$ crystals, most of which were electroded with 200-A thick films of Au. The wall velocity has been measured as a function of several variables including the applied electric field, the crystal thickness and the impurity content added to the crystal growth melts.

The wall velocity as a function of the field E is described by $v_\infty \exp(-\delta/E)$ where δ and v_∞ are constants over several decades of velocity. The quantities δ and v_∞ are the activation field and extrapolated wall velocity for $E=\infty$, respectively. This field dependence of the wall velocity is the same as that reported previously for liquid electroded specimens. The thickness dependence of the wall velocity, which is through δ, is very pronounced and similar to that observed in measurements of other variables under different experimental conditions. The present data are explained in terms of a surface layer estimated to be of the order of 100-A thick. It is suggested that high fields within the surface layer may give rise to electron field emission and the electroluminescence which is observed during polarization reversal. Effects on the wall motion which persist for times of the order of minutes are ascribed to dielectric relaxation phenomena. The observed dependence of the wall motion on the impurity content of the cyrstal, and several other parameters, may result from changes in the characteristics of the surface layer.

INTRODUCTION

SOME of the characteristics of the sidewise motion of 180° domain walls in $BaTiO_3$ crystals have been described in several recent papers.[1-3] These studies gave rise to important results which were not expected from an examination of the literature on polarization reversal in $BaTiO_3$. However, the wall motion studies just mentioned were made with liquid electroded crystals, whereas most of the other relevant published data,[4-7] which are largely electrical characterizations of polarization reversal, come from experiments with metal electroded crystals. Therefore, it was not clear that the wall velocity data obtained with the liquid electroded crystals applied to metal electroded specimens. In view of the rather large body of published material of a theoretical as well as experimental nature on polarization reversal in metal electroded $BaTiO_3$ crystals, wall motion studies similar to those mentioned in the foregoing, but with metal electroded crystals, were highly desirable.

Certain aspects of domain growth through sidewise 180° domain-wall motion in metal electroded $BaTiO_3$ crystals have recently been shown[8] to be similar to those found with liquid electroded samples. Extensive sidewise wall motion can occur in both liquid and metal electroded crystals; and in some instances, the entire electroded area, whether liquid or metal electroded, can be reversed with a single expanding domain. Over a measured range of several decades in velocity, the sidewise wall velocity v, for both types of electrodes, was found to be equal to $v_\infty \exp(-\delta/E)$ where E is the electric field and δ and v_∞ are constants. However, the limited data on metal electroded crystals[8] indicated that for a given field, the wall moved much more slowly than with liquid electroded samples.

The present paper contains quantitative wall velocity measurements as a function of the applied field for metal electroded crystals. The effects of crystal thickness on the wall velocity have been investigated in some detail; and to a lesser extent, the effects of sample purity and electrode material on the wall motion. These data indicate the presence of a surface layer whose electrical properties are different from those of the bulk ferroelectric material. These results, and others, are interpreted in terms of earlier published work with metal electroded $BaTiO_3$ crystals. It is suggested that during polarization reversal, electron field emission and electro-

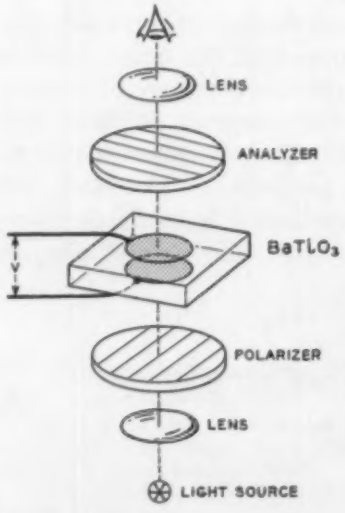

FIG. 1. Schematic drawing of the arrangement used for the direct observation of 180° domain walls during polarization reversal in $BaTiO_3$.

[1] R. C. Miller, Phys. Rev. **111**, 736 (1958).
[2] R. C. Miller and A. Savage, Phys. Rev. **112**, 755 (1958).
[3] R. C. Miller and A. Savage, Phys. Rev. **115**, 1176 (1959).
[4] W. J. Merz, Phys. Rev. **95**, 690 (1954).
[5] E. A. Little, Phys. Rev. **98**, 978 (1955).
[6] W. J. Merz, J. Appl. Phys. **27**, 938 (1956).
[7] R. Landauer, D. R. Young, and M. E. Drougard, J. Appl. Phys. **27**, 752 (1956).
[8] R. C. Miller and A. Savage, Phys. Rev. Letters **2**, 294 (1959).

luminescence[9] may result from these surface layers. Some direct measurements supporting this proposal are also described.

METHOD

The techniques employed in the present experiments to study the sidewise motion of 180° domain-walls in $BaTiO_3$ are considered to be vastly superior to those used in earlier investigations.[2] If a sample of $BaTiO_3$ is mounted between crossed polaroids and viewed through transparent or semi-transparent electrodes along the ferroelectric axis with transmitted light, one can discern the antiparallel domain configuration continuously during polarization reversal.[8] A schematic drawing of this arrangement is shown in Fig. 1. Thus, one has a very convenient and direct method to measure the velocities of the domain walls. In the present experiments, the wall velocities were calculated from measurements of the time required for the wall under direct observation to move through a known distance. A stop watch was used to obtain the relevant time interval. This method of measurement of the time interval imposes an upper limit of about 10^{-2} cm sec^{-1} on the wall velocity data.

The semi-transparent metal electrodes were in general 200 A films of Au, 2.5 mm in diam, evaporated on to opposite sides of the crystal.

The fields to reverse the polarization were in most cases cycled automatically in order to obtain reasonably reproducible domain configurations. The usual voltage cycle consisted of a positive voltage pulse, 50-sec long and of variable amplitude, followed immediately by a 50-sec long 22-v-negative pulse and finally a 50-sec interval with no voltage. The amplitude of the negative voltage was sufficiently large so as to reverse the polarization completely prior to its removal. The mensuration operations were performed during the positive voltage portion of the cycle. For low velocities, the duration of the positive voltage was extended beyond 50 sec.

RESULTS

Wall velocity data for a sample 4.0×10^{-3}-cm thick are shown in Fig. 2. These data are typical except that the measured range shown in the figure is somewhat greater than is usually obtained. The high velocity data, i.e., $v>10^{-4}$ cm sec^{-1}, can generally be fitted with a straight line, which when extrapolated to lower fields lies below the low field experimental points. The dashed line shown in Fig. 2 is an extrapolation of the straight line drawn through the data for $v>10^{-4}$ cm sec^{-1}. There are some time, or aging, effects which can have a significant influence on the wall motion. In particular, if a crystal is allowed to "sit" with no field applied for perhaps something like a few minutes it will polarize more easily in the direction in which it was polarized while sitting, than in the opposite direction. This effect can be largely eliminated if the crystal is completely reversed several times and then measured immediately without letting it sit. This and other allied phenomena will be discussed in more detail later. With the present method of measurement, the aging effects described previously tend to give smaller velocities than "normal" for the measured wall in the low field region and therefore cannot give rise to the curvature shown by the data in Fig. 2.

The light source used for most of the optical observations was a high-pressure Hg lamp. Several filters were used to remove the near infrared and the ultra-violet. The effects of the filtered light on the wall velocity of a liquid electroded crystal[2] are illustrated in Fig. 3. The solid curve was obtained using the single domain electrical measuring technique[2] and consequently shows the field dependence of the wall velocity in a dark environment. The dotted curve was obtained by direct measurement of the same single domain with the filtered light level as low as possible consistent with the direct measurement technique. The dashed curve was obtained again by direct measurement, however, with the maximum filtered light intensity on the specimen. It is clear that the higher light intensity gives rise to larger wall velocities for the same field than the lower light intensity; however, the low intensity data are in agreement with the electrical data measured in a dark environment. The small difference between the low light

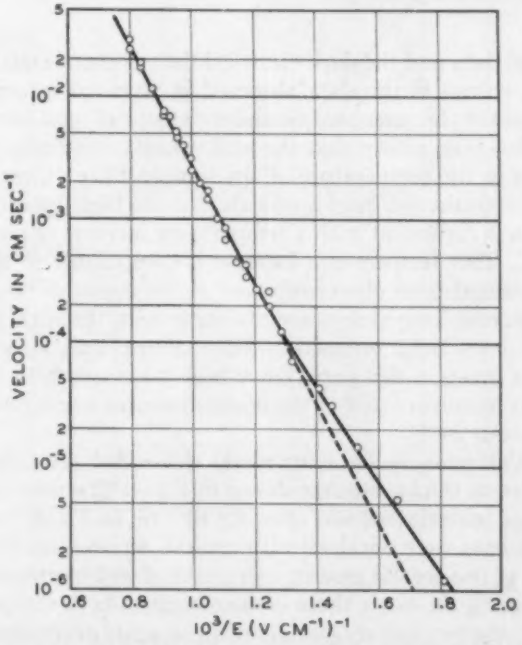

FIG. 2. Logarithm of the sidewise 180° domain-wall velocity vs the reciprocal of the applied electric field for a sample 4.0×10^{-3} cm thick. The dotted line is an extrapolation of the straight line drawn through the data for $v>10^{-4}$ cm sec^{-1}.

[9] G. G. Harman, Phys. Rev. 111, 27 (1958). Harman discusses in some detail the electroluminescence in $BaTiO_3$ which is not connected with the reversal of the direction of the spontaneous polarization. Another electroluminescent effect which is related to the "current spikes" is also mentioned. In the present paper, we are interested in this latter type of electroluminescence.

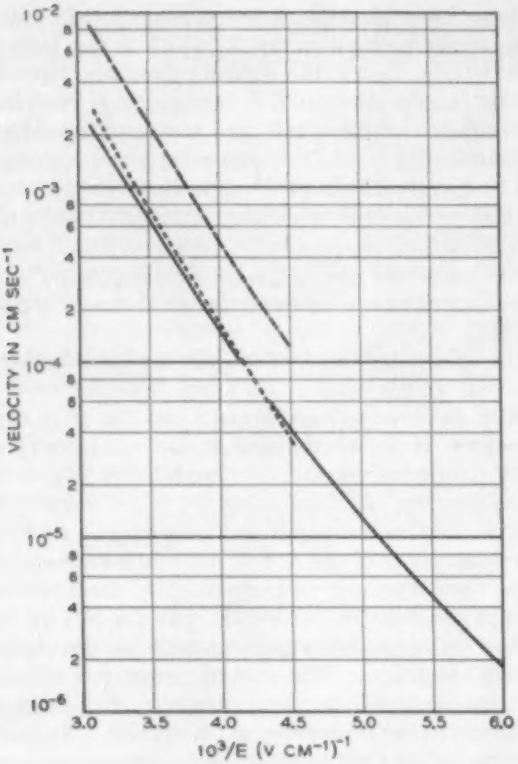

FIG. 3. Logarithm of the sidewise 180° domain-wall velocity vs the reciprocal of the applied electric field for a sample measured under several different lighting conditions. The solid line represents data obtained in the dark. The dotted and dashed lines are drawn through data taken by the direct observation technique in which the sample was exposed to minimum and maximum light intensities, respectively.

level data and the dark electrical data is about equal to the spread in the data observed in repeated measurements of the same sample under "identical" conditions. It has been shown that the wall velocity is quite sensitive to the temperature of the sample.[3] The difference between the low light level data and the high light level data is consistent with a temperature increase of about 8°C. This temperature increase is comparable to that estimated from observations of P_s by means of 60 cps hysteresis loop measurements made with the high and low level light intensities. Most of the wall velocity data given in this paper have been measured with low light intensities so that the nominal sample temperature is about 24°C.

Wall velocity data for metal electroded crystals of different thicknesses are shown in Fig. 4. The thickness range investigated was from 2×10^{-3} cm to 3×10^{-2} cm. The data were obtained with crystals which came from one of two crystal growth melts, each of which contained 0.2 at.% Fe. Since there is some suggestion in the data that the two lots are not identical, separate designations will be used for the two lots in each figure which contains data from both. Examination of the data in Fig. 4 shows that the wall velocity at a given field is very much dependent upon the crystal thickness. There is considerable spread in the values of v_∞, i.e., the extrapolated wall velocity for $E=\infty$; however, there is no indication that v_∞ depends on the crystal thickness.

This thickness dependence of v is also illustrated in Fig. 5 where the field required to give a wall velocity of 10^{-3} cm sec^{-1} is plotted vs the reciprocal of the crystal thickness. It is seen that with the data plotted as in Fig. 5, the experimental points can be fitted with a straight line.

The thickness dependence of some of the electrical characteristics of metal electroded $BaTiO_3$ crystals observed previously by Merz[6] has been considered in some detail in two papers.[6,10] Part of the data in question is the dependence of the maximum switching current i_{max} on the crystal thickness. Merz found that

$$i_{max}\sim\exp(-\alpha/E), \qquad (1)$$

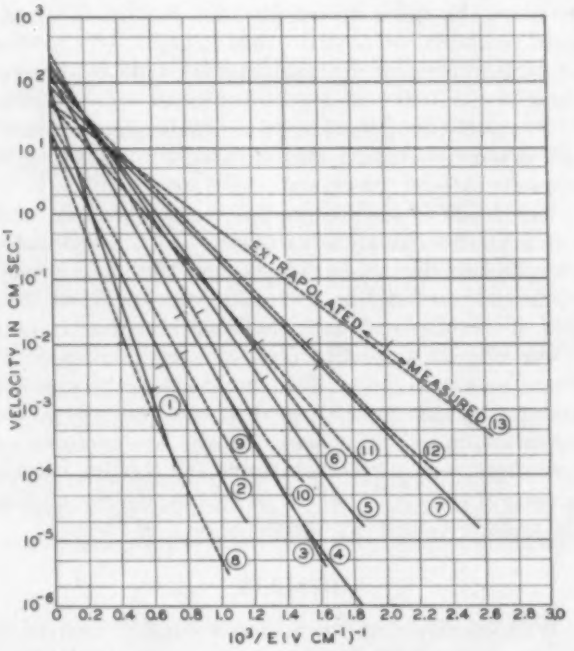

FIG. 4. Logarithm of the wall velocity vs E^{-1} for samples of various thicknesses. The region below the short line drawn normal to each plot is the range over which the data were measured. The portions of the plots which extend to velocities higher than the horizontal line are extrapolations. The crystals were obtained from one of two "identical" crystal lots. Samples numbered 1 through 7 were from lot #1 and the curves are drawn as solid lines. The remaining samples, 8 through 13 were from lot #2 and these plots are drawn as dashed lines. Thicknesses of the samples are given below.

Lot #1		Lot #2	
Sample No.	Thickness, cm	Sample No.	Thickness, cm
1	1.8×10^{-3}	8	1.5×10^{-2}
2	2.5×10^{-3}	9	2.8×10^{-2}
3	4.0×10^{-3}	10	3.8×10^{-2}
4	4.0×10^{-3}	11	7.6×10^{-2}
5	6.9×10^{-3}	12	12.1×10^{-2}
6	10.0×10^{-3}	13	32.0×10^{-2}
7	17.3×10^{-3}		

[10] M. E. Drougard and R. Landauer (referred to as DL) J. Appl. Phys. **30**, 1663 (1959).

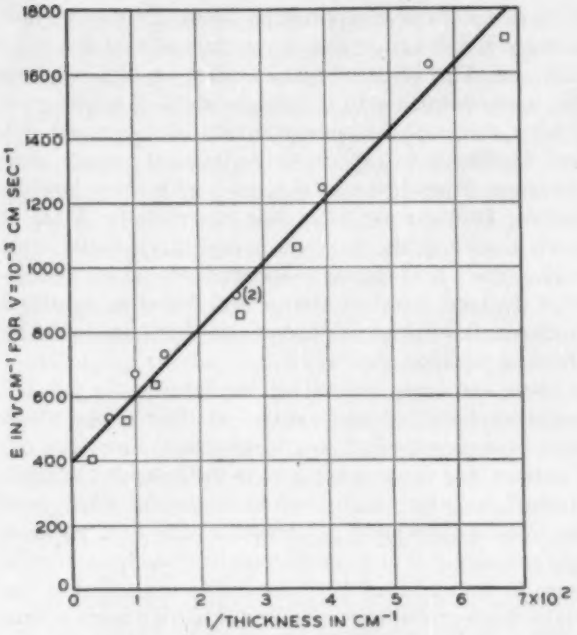

FIG. 5. Electric field required to give a velocity of 10^{-3} cm sec^{-1} vs the reciprocal of the sample thickness. Data for crystals from lots #1 and #2 are given as circles and squares, respectively.

in which E is the applied electric field. The "activation field" α was found to depend on the crystal thickness d in accordance with the relation,

$$\alpha=\alpha_\infty(1+d_0/d), \tag{2}$$

with d_0 equal to about 10^{-2} cm. The data in the present paper show that the sidewise 180° domain-wall velocity in metal electroded crystals is given by

$$v=v_\infty \exp(-\delta/E), \tag{3}$$

with v_∞ and δ independent of field for several decades of velocity. With certain assumptions regarding the rate of nucleation of reversed domains, it can be shown[2] that Eq. (1) follows from Eq. (3) and futhermore α turns out to be equal to, or nearly equal to, δ. Therefore, δ and α might be expected to exhibit approximately the same behavior. In Fig. 6, δ is plotted vs d^{-1} and a line which fits the data given by Merz[6] of α vs d^{-1} is also included. There is considerable spread in the values of δ; however, a straight line drawn "through" the experimental points gives

$$\delta=\delta_\infty(1+d_0/d), \tag{4}$$

with $d_0=5\times10^{-3}$ cm, or $\frac{1}{2}$ the value obtained from α vs d^{-1}. It should be noted that Merz made his measurements at fields considerably higher than those in the present experiments. This is illustrated by the magnitudes of the switching times in the two investigations. The longest switching times measured by Merz were about 10 msec while the shortest switching times in the present experiments were about 1 sec. The data given in Fig. 5 show that the applied field required for $v=10^{-3}$ cm sec^{-1} can be represented by

$$E=400(1+d_0/d)\text{v cm}^{-1}, \tag{5}$$

where once again, as in Eq. (4), $d_0=5\times10^{-3}$ cm. Therefore, when the wall motion data are treated in the above fashion, there is, as expected, a similarity between these data and the older data of an electrical nature given by Merz.

It has usually been assumed[6,10] that the rate of polarization reversal is proportional to $\exp(-\alpha_\infty/E_b)$ where E_b is the average field in the bulk of the crystal. Surface layers whose electrical properties are different from those of the bulk material may reduce E_b below the average value of the applied field. The wall velocity has been shown to be proportional to $\exp(-\delta/E)$ so that for a given wall velocity, if v is proportional to $\exp-(\delta_\infty/E_b)$, δ and E should both vary with the crystal thickness in the same manner, which is shown by the data in Figs. 5 and 6.

DISCUSSION

What is the origin of these thickness effects? Merz[6] assumed that the thickness dependence of α arose from the voltage dividing action of nonferroelectric surface layers estimated to be about 10^{-4} cm thick. Recently

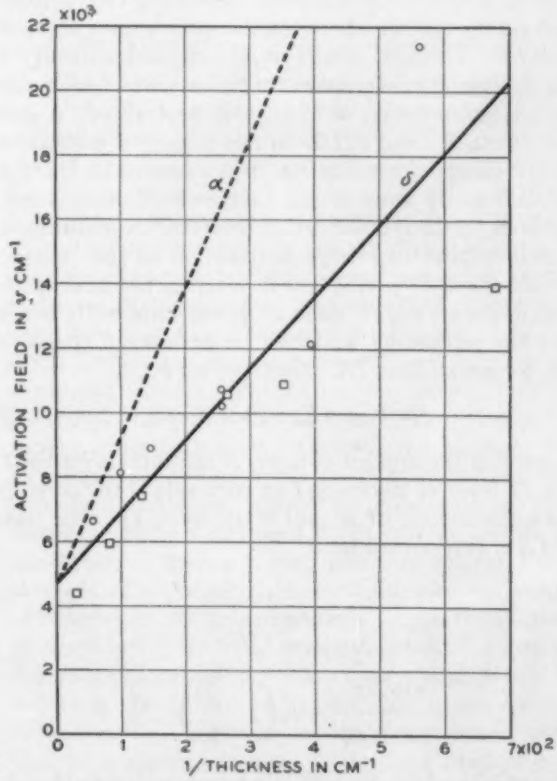

FIG. 6. Activation field vs the reciprocal of the sample thickness. The solid line applies to wall velocity data obtained in this research. The dotted line fits the switching transient data determined by Merz. Data for crystal lots #1 and #2 are plotted as circles and squares, respectively.

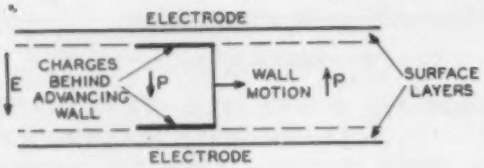

FIG. 7. Schematic drawing of the model proposed by DL to explain the thickness dependence of some of the measured electrical characteristics of $BaTiO_3$.

DL[10] have shown that the variation of α with thickness found by Merz could arise from lossy surface layers of the order of one unit cell thick. A surface layer 10^{-4} cm thick, as proposed by Merz, is considered by DL to be highly improbable. In the absence of quantitative data on the sidewise motion of 180° domain-walls in metal electroded $BaTiO_3$ crystals, DL assumed that the α's obtained by Merz in his electrical studies pertained to sidewise wall motion. From the data given in the present manuscript, it is now known that δ and α are the same within about a factor of two. The factor of two itself would not change the conclusions put forth by DL in any significant way; however, certain other aspects of the present data enable one to expand the DL surface layer model.[10]

DL consider the effects of a surface density of $2P_s$ present immediately behind an advancing 180° domain-wall, on the interface between the surface layer and bulk material. The DL model is shown schematically in Fig. 7. The layer is assumed to be lossy which allows for the charge to decay, or to become neutralized, in some characteristic time τ. DL do not suggest a mechanism for the charge neutralization. It is assumed by DL that τ is sufficiently short so that charge distributions resulting from previous polarization reversals are neutralized; therefore only the charge distribution on the interface behind the wall is effective in altering the field in the bulk of the crystal. If the wall moves sufficiently fast so that the advancing wall sees an undecayed charge of $2P_s$ behind it, then DL show that for $l \ll d$,

$$E \equiv V/d = E_b + (8\pi P_s l/\epsilon_l d), \tag{6}$$

where V is the applied voltage, $2l$ the total layer thickness (a layer of thickness l on each side of the crystal), and ϵ_l the dielectric constant of the layer. The activation field α is determined from

$$\alpha \equiv -\frac{d \ln i_{\max}}{d(1/E)},$$

or

$$\frac{d(\alpha_\infty/E_b)}{d(1/E)} = \alpha_\infty \left(1 - \frac{d_0}{2d}\right)^{-2}. \tag{7}$$

For thick crystals, Eq. (7) can be approximated by

$$\alpha = \alpha_\infty (1 + d_0/d), \tag{8}$$

where

$$d_0 = 16\pi P_s l/\epsilon_l E. \tag{9}$$

With $d_0 = 10^{-2}$ cm as reported by Merz, $E = 1000$ v cm^{-1}, and $\epsilon_l = 5$, DL arrive at a layer thickness of 4 A—one unit cell. The formulation described in, Eqs. (8) and (9), applied directly to the present data on δ, also gives a layer thickness of approximately one unit cell. DL find it difficult to explain why almost the exact same thickness dependence is observed with very low velocities, 10^{-5} cm sec^{-1}, as that observed by Merz at much higher fields, i.e., much higher velocities. One might expect that the very slow walls would see a somewhat decayed interface charge and therefore exhibit a much smaller thickness dependence than that found by Merz, or perhaps none at all.

There are some interesting implications in the DL model as described and applied in their paper which seem to shed some light on the problem. From Eq. (6) it follows that the average field in the layer of thickness l is $8\pi P_s/\epsilon_l$, which with $\epsilon_l = 5$ as assumed by DL, is of the order of 10^5 v cm^{-1}. With such a large field, electron field emission will undoubtedly occur with characteristic times of the order of 10^{-16} sec.[11] DL suggest that the relaxation is probably nonlinear due to high fields within the layer and do not give a value of τ; however, τ is considered by DL to be shorter than the Merz switching times and hence of the order of microseconds. The lateral range of the fields due to the layers is estimated[10] to be of the order of $2l$, so that with field emission processes taking place, the wall should in fact see a partially relaxed charge distribution unless $v > 10^9$ cm sec^{-1}, i.e., the wall should always see a somewhat relaxed charge distribution.

There is a way to circumvent this difficulty. It is usually assumed in discussions of surface layers in $BaTiO_3$ that the dielectric constant of the layer should be set equal to the value found in good insulators, i.e., $\epsilon_l \approx 5$. However, we believe this is not realistic. Nonferroelectric $BaTiO_3$ is in general a special insulator which exhibits large dielectric constants. This is shown by dielectric constant measurements above the Curie point. Furthermore, ceramic $BaTiO_3$ subjected to pile irradiation to the extent that it was no longer ferroelectric was found[12] to have $\epsilon = 200$. Therefore a value of 100 for the dielectric constant of a nonferroelectric $BaTiO_3$ surface layer seems more reasonable than a value of 5. With $\epsilon_l = 100$, the field within the layer is $\sim 3 \times 10^6$ v cm^{-1} and the layer thickness as calculated from Eqs. (8) and (9) becomes 20 times larger than estimated by DL,[10] or about 80 A. A field of 3×10^6 v cm^{-1} is sufficiently large so that one might still expect electron field emission.[11] With these high fields, electroluminescence might also be expected to occur during polarization reversal. Harman[9] has observed electroluminescence during polarization reversal in metal electroded single crystals of $BaTiO_3$. The electroluminescence was reported to be a function of the "current spikes." We have also observed

[11] E. Spenke, *Electronic Semiconductors* (McGraw-Hill Book Company, Inc., New York, 1958), Chap. 7.
[12] F. T. Rogers, Jr., J. Appl. Phys. 27, 1066 (1956).

electroluminescence and have found that most of the light comes from the sample during the middle and later stages of polarization reversal. This is illustrated in Fig. 8 which shows plots of: $i_s \propto dp/dt$; the output of a photomultiplier used to observe the light; and i_s plus the photomultiplier output, all as a function of time. Each pulse on the photomultiplier output indicates one photon. The sample used to obtain these data was made from the same material and electroded in the same manner as the samples used to obtain the wall velocity data given in Fig. 4.

These preliminary electroluminescent data are shown to demonstrate that field emission is indeed a possibility during polarization reversal with samples like those used in the wall velocity measurements. The presence of electroluminescence during polarization reversal does not of course prove that field emission also occurs. On the basis of these and other data of an exploratory nature it is proposed that part of the charge neutralization in the DL surface layer may arise from field emission processes. If field emission is an important process in the charge decay on the interface, then of course no well-defined relaxation time exists.

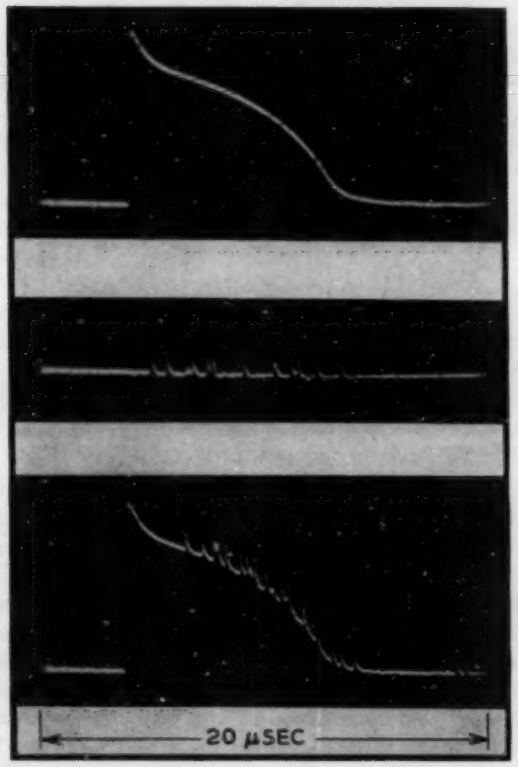

FIG. 8. Electroluminescence observed during polarization reversal in $BaTiO_3$. Curve (a) shows the switching current dp/dt as a function of time. Curve (b) shows the photomultiplier output as a function of time; each pulse represents one photon observed. In curve (c) the switching current plus photomultiplier output are shown as observed during polarization reversal. It can be seen from curves (b) and (c) that the light output is not the same for each polarization reversal.

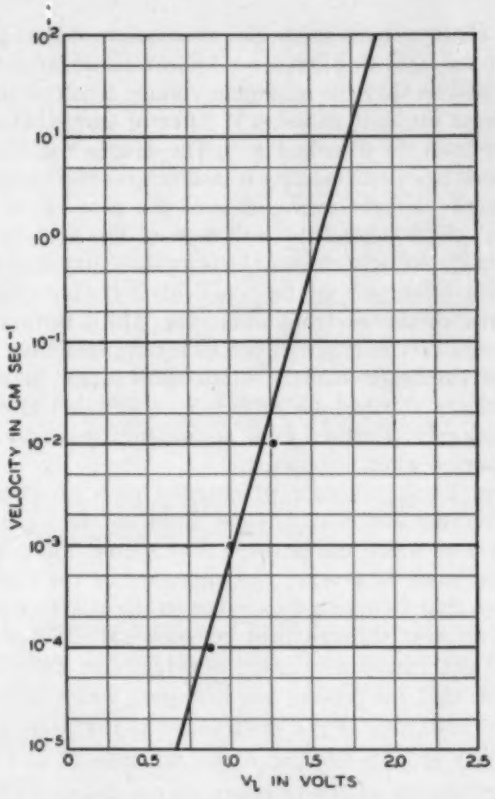

FIG. 9. Logarithm of the wall velocity vs the voltage drop across the surface layer.

Plots similar to Fig. 5 have been obtained from the data in Fig. 4 for velocities of 10^{-4} and 10^{-2} cm sec^{-1}. The analyses show that d_0 increases with increasing field. Now assume that the applied voltage can be broken up into two parts, a voltage drop V_l across each surface layer (assume a layer on each side of the sample) and a voltage drop across the bulk. Then from Eq. (5), it follows that $V_l = 200 d_0$ or 1.0 volts, for $v = 10^{-3}$ cm sec^{-1}. Similar analyses with $v = 10^{-2}$ and 10^{-4} cm sec^{-1} show that $V_l = 1.3$ and 0.9 v, respectively. These data are shown in Fig. 9. If the observed light originates from surface layers with voltages across them as given in the foregoing, then the energy of the photons emitted during polarization reversal cannot be greater than V_l ev. Experimentally it has been noted that no visible light was observed from a sample when the applied voltage was below that required to give a sidewise wall velocity of about 3 cm sec^{-1}. On making a long extrapolation of the data in Fig. 8 to this velocity, one finds V_l equal to 1.8 ev which means photons of wavelengths less than ≈ 7000 A should not be present and hence for lower velocities, i.e., lower fields, the light should not be visible. A spectral analysis of the light emitted during polarization reversal has not been made, and the intensity level is so low that we cannot use the eye to observe color effects. Therefore, there are no data to indicate whether or not the wavelength of the emitted

light changes with field. The mechanism which gives rise to the light emission is not known. However, it may very well be that the minimum voltage required across the layer for light emission is different from that estimated from the data in Fig. 9. The data in Fig. 9 were obtained from wall velocity measurements and therefore represent voltages averaged over the portions of the crystal which control the wall motion. The fields in the layer deduced from the wall velocity data may therefore be quite different from the local fields in the layer which give rise to the electroluminescence. Much further experimentation is required before a comprehensive discussion can be given of the relationship, if any, between the effects ascribed to surface layers[4,10] and electroluminescence. Further work is contemplated and will be reported when completed.

Even in the absence of detailed data on electroluminescence and field emission, there are some general conclusions which can be given at this time. The rate of field emission is a very rapid function of the electric field, so that changing the charge on the interface by a small amount through field emission can change the rate of field emission by orders of magnitude. Therefore, the fact that the present low field data which indicate a layer thickness of the same order as the Merz high field data may simply mean that in times of $2l/v$ the average charge on the interface over a distance l does not change by very much. This is consistent with the electric field dependence of field emission.

Field emission processes can be effective in reducing the field in the layer to perhaps 10^4 to 10^6 v cm^{-1} after which some other process must take over. This other process could be dielectric relaxation in the layer with a time constant $\tau_d = \rho\epsilon_l/4\pi$ where ρ is the resistivity of the layer. The value of τ_d in the bulk material is of the order of 10^2 sec.[13] Therefore, we would expect these thickness effects to be present down to very low velocities, even 1 A sec^{-1}. As mentioned earlier, there is experimental evidence that some slow relaxation processes do take place. Some of the relevant data are shown in Fig. 10. Two crystals were left for 16 hr completely polarized in one direction with $E=0$. Following this, the automatic voltage cycle was started and the time required for a 180° domain-wall to move about 10^{-3} cm was recorded for a number of consecutive cycles. These growth times vs the number of the cycle are shown in Fig. 10. The duration of each cycle was 3 min. Another related example which illustrates that slow relaxation processes are present is that, under the conditions given below, the wall velocity decreases slightly as the domain

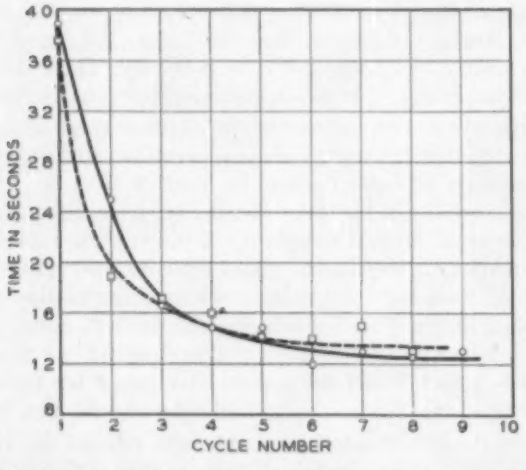

FIG. 10. Time required for a 180° domain-wall to move 10^{-3} cm vs the number of voltage cycles after the crystals were left for 16 hr polarized in a direction opposite to that of the field applied for the measurement. The data for a crystal from each lot, # 1 and # 2, are plotted as circles and squares, respectively.

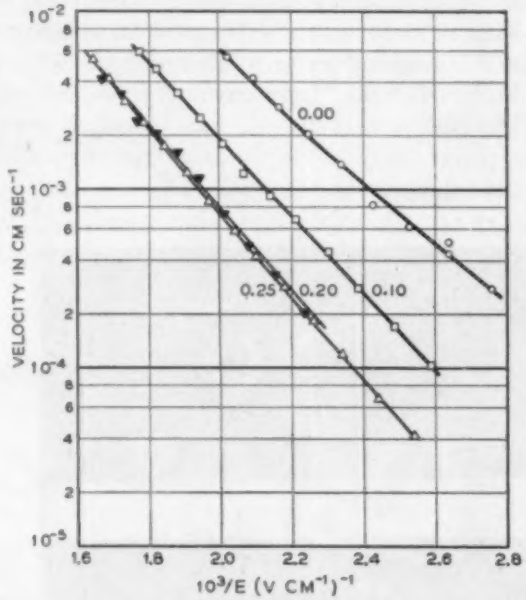

FIG. 11. Logarithm of the wall velocity vs the reciprocal of the electric field for samples with different iron concentrations. The amount of iron in atomic percent added to the growth melt is given in the figure.

size increases. This reduction in the wall velocity is observed when the growth times of the domains are a significant fraction of the voltage cycle. The areas polarized in the direction of the measuring field for the longest times are the easiest to polarize in that same direction in subsequent reversals. These phenomena demonstrate that charge distributions left from previous reversals can have an effect on the wall motion that persists for many minutes.

A layer thickness can be estimated from the present measurements using the data in Fig. 9 along with Eq. (6) for

$$l = \epsilon_l V_l / 4\pi\gamma P_s, \tag{10}$$

[13] R. C. Miller and R. D. Heidenreich, J. Appl. Phys. **29**, 957 (1958).

where γ is the effective fraction of unneutralized charge on the interface. If one assumes $\gamma=1$ for $v=10^{-2}$ cm sec^{-1}, the highest velocity for which data are available, then with $\epsilon_l=100$, $l=40$ A. When the data in Fig. 9 are extrapolated to wall velocities comparable to those characteristic of the fields employed by Merz, i.e., $v\approx 10$ to 100 cm sec^{-1}, with $\gamma=1$ and $\epsilon_l=100$, $l\approx 80$ A. This value agrees with that estimated earlier using the original data given by Merz.[6] In view of the various uncertainties involved in the above estimate, e.g., the long extrapolation of $\ln v$ vs V_l, the values of γ and ϵ_l, the only meaningful estimate is that l is of the order of 100 A.

The field emission plus dielectric relaxation model described in the foregoing seems to be capable of explaining some of the features of the data. However, the origin of the layer is still unknown. There is evidence that the characteristics of the layer might depend on several factors. Figure 11 shows plots of $\log v$ vs E^{-1} for several samples each of almost the same thickness, but obtained from crystal batches with different impurity concentrations. It is clear that the impurity additions to the growth melt, in this case iron, affects the wall velocity data and therefore perhaps the characteristics of the surface layer. The wall velocity data are also affected by the particular electrode material used. In Fig. 12 data are shown for a sample which was first measured with the standard 200 A Au electrodes on the specimen. Then the gold was dissolved off, and the same portion of the sample remeasured with aqueous LiCl electrodes applied to it. The data in Fig. 12 show that the surface layer might be less effective with the liquid electrodes than with the metal electrodes. However, preliminary data with liquid electrodes also indicate the presence of surface layer effects.

The wall velocity of metal electroded crystals is found to be affected by water vapor. Samples prepared and measured during the dry days of the winter months are found to have higher velocities for the same fields when measured under conditions of high humidity. The effects due to the humidity do not appear to be completely reversible.[14] Some of the scatter in the data shown in Fig. 4 is believed to be the result of variations in the humidity at the time the samples were measured.

It has been suggested that sidewise motion of the 180° domain wall in $BaTiO_3$ may take place through a nucleation mechanism.[2,3,7] If the nucleation mechanism is indeed the correct one, then the conditions in the region of the crystal where the nucleations occur are important. A nucleation region at or near the surface may be sensitive to the properties of the particular electrode—$BaTiO_3$ interface. Therefore, it is not certain that the effects on the wall velocity resulting from changes in the impurity content, the electrode material, and the humidity result from changes in the characteristics of the surface layers which are then reflected in the average value of the bulk field.

[14] J. R. Anderson, G. W. Brady, W. J. Merz, and J. P. Remeika, J. Appl. Phys. **26**, 1387 (1955).

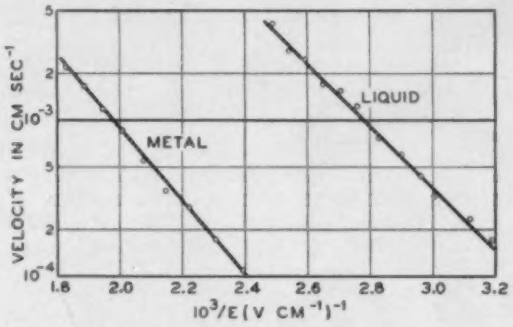

FIG. 12. Wall velocity data for a sample measured with both metal and liquid electrodes. The sample, 1.2×10^{-2} cm thick, was selected from a growth melt which contained 0.1 atomic percent Fe.

SUMMARY

The sidewise motion of 180° domain-walls in metal electroded crystals of $BaTiO_3$ has been measured as a function of several parameters. The electric field dependdence of the wall velocity is given by $v=v_\infty \exp(-\delta/E)$, where δ and v_∞ are constants for several decades of velocity. The velocity for a given field is very much dependent upon the crystal thickness. In some ways, the thickness dependence of the wall velocity at constant applied field is similar to that observed in earlier electrical studies of $BaTiO_3$ obtained under quite different experimental conditions. It is proposed that these thickness effects arise from surface layers of the order of 100 A thick. Furthermore, it is suggested that the high fields in the surface layer behind a rapidly advancing wall may be reduced initially through an electron field emission process. The field emission may in turn manifest itself in electroluminescence and therefore account for the electroluminescence which is observed during polarization reversal. For low fields in the surface layer, field emission becomes unimportant and dielectric relaxation is proposed as the mechanism which further reduces the field in the layer. The wall velocity is also a function of the impurity content in the crystal, the electrode material and the humidity, all of which could alter the properties of the surface layer.

ACKNOWLEDGMENTS

We would like to take this opportunity to thank Dr. A. G. Chynoweth for several informative discussions on the field emission aspects of the paper. Also, we wish to thank Dr. R. Landauer and Dr. M. Drougard of the I.B.M. Laboratories for a preprint of their paper on surface layers in $BaTiO_3$. The $BaTiO_3$ crystals used in this research were grown by Messrs. R. C. Linares, Jr., and J. P. Remeika.

JOURNAL OF APPLIED PHYSICS VOLUME 31, NUMBER 4 APRIL, 1960

Formation and Initial Growth of Single-Asperity Solid-State Bonds*

F. C. Holden, J. B. Melehan, H. R. Ogden, and R. I. Jaffee
Battelle Memorial Institute, Columbus, Ohio
(Received March 16, 1959)

A gold needle point in contact with a gold flat has been used to study the formation and initial growth of single-asperity solid-state bonds. In the absence of external pressure, the growth of the bonded area can be expressed analytically by a diffusion-controlled rate equation. Values for the coefficient of self-diffusion determined from these experiments are in reasonable agreement with those given in the recent literature.

INTRODUCTION

RECENTLY, a number of basic and applied research programs have included studies of solid-state bonding. These programs have been aimed at such diverse objectives as sintering of powders, cladding, pressure welding, and the fundamentals of friction and seizing in metals.

Despite the usefulness of information gained from studies of massive systems, the results frequently are not amenable to theoretical treatment. The usual measures of the degree of bonding, such as densification of a powder compact or the adhesion of a metal cladding, represent the averages of a very large number of bonds established under widely differing conditions.

In the present work, an attempt has been made to simplify the bonding system to the point where a rational expression for bond formation and growth can be determined. This has been done by choosing the material and testing conditions in such a way as to simulate the bonding of a single asperity (i.e., point of contact) under controlled conditions. The strength of the single-asperity bond then can be measured directly. The test data obtained from these experiments have been expressed in terms of a diffusion-controlled rate equation, in which the bond strength is expressed in terms of material properties and experimental variables. From these data, it also is possible to determine the coefficient of volume self-diffusion with reasonably good accuracy.

THEORETICAL MODEL

A two-stage process is visualized for the massive solid-state bonding of metals. Initially, as the two pieces are brought together, contact is made at a relatively small number of asperities. With the application of pressure, the number and total area of these asperities are increased by elastic and plastic deformation. At the same time, any adherent brittle films and surface layers present are broken up, allowing areas of the metallic surfaces to come into close contact and form metallurgical bonds. The second stage of the bonding process is the growth of these bonded areas, ultimately to include the entire interface.

In tests conducted on massive specimens, it is difficult to control those variables which are dependent on the actual surfaces of contact. Although useful empirical data have been obtained by using average apparent pressures, it is not possible to describe the bonding process in terms of a rational model. For this reason, attempts have been made in the present work to devise a simplified system that would be amenable to both theoretical and experimental treatments.

The theoretical model used here consists of a single asperity, simulated by a needle tip, bonded to a plane surface. It is assumed that adhesion takes place instantaneously over the entire area of contact, followed by radial growth of the circular bonded area. Although it is recognized that the needle tip and flat do not represent a single asperity in the true microscopic sense, the system is considered to be a reasonable approximation of a single asperity.

The total bonded area thus may be expressed as the sum of two terms, $A=A_0+A_g$, in which A_0 is the initial bonded area and A_g is the area formed by growth. The experiments described here were conducted by applying and immediately removing a load on the needle. In this way, the effects of creep on the A_g term were eliminated.

The assumption is made that the force required to break the bond is directly proportional to the bond area. Thus, the equation above may be expressed in terms of forces as: $F=F_0+F_g$, where the subscripts have the same significance as before. The necessity for determining the proportionality constant (i.e., the tensile strength at the test temperature) is eliminated by using only ratios of area or force in the calculations.

Although this experimental method has the distinct advantage that bond strengths can be measured directly, it is necessary to measure bond areas indirectly. Further, the radius of the initial contact area appears as a term in the growth rate expression. It, therefore, becomes necessary to determine the size of the contact area experimentally in order to develop the expression for bond growth.

Initial Bond Area

A $\frac{1}{16}$-in. diam steel ball, used as an indentor, was forced into a gold flat under various conditions of load and temperature. The diameter of the resulting impression then was measured directly. In using these results to determine the contact areas for the bonding

* Work performed under a U. S. Atomic Energy Commission contract.

experiments, geometric similarity was established by maintaining constant the ratio of applied load to the square of the radius. The data then were replotted as mean pressure versus reciprocal temperature, and from these values the curves of initial area and initial contact radius shown in Fig. 1 were plotted.

Bond Growth Expression

The expression for the rate of growth of the bonded area was developed following the work of Kuczynski[1] and of Dedrick and Kuczynski.[2] The final expression is written as follows:

$$Xo^5\left[\left(\frac{F}{Fo}\right)^{\frac{1}{3}}-1\right]^3=\left(\frac{81\sigma\delta^3a^2}{4k}\right)\left(\frac{Dv}{T}\right)t, \qquad (1)$$

in which F = breaking force at time t; Fo = breaking force at time zero; σ = surface tension, d/cm; δ = interatomic distance, cm; a = asperity radius, cm; k = Boltzmann's constant, d-cm/°K; Dv = coeff of self-diffusion, cm²/sec; T = temperature, °K; Xo = radius of initial contact area, cm; t = time, sec.

The terms on the left can be determined experimentally. The terms on the right have been grouped as constants, and as temperature and time dependent quantities, respectively. The values for surface tension (σ) and interatomic spacing (δ) are considered to be relatively unaffected by temperature, and are treated as constants.

EXPERIMENTAL PROCEDURES

Specimen Preparation

The majority of the tests were conducted using fine (high-purity) gold for the components of the bonding couple. Gold was selected for these studies for its oxidation resistance, and because most of its physical properties have been established. The simulated single asperity system consisted of a gold needle, with a tip radius of about 2×10^{-3} cm, in contact with a flat gold surface. The needles were prepared from 36-mil cold drawn wire by electropolishing in aqua regia. The tip radius of each needle was carefully checked, and a photographic record of each needle profile was maintained. The plane surfaces were first mechanically polished and then electropolished in aqua regia to remove the worked surface layer. All the flat specimens were prepared from annealed rod. Immediately before use, the specimens were cleaned in dichromic acid and rinsed in ethyl alcohol and distilled water. One series of tests was carried out using silver needles and flats. The methods of preparation were quite similar, except that the specimens were electropolished in a KCN solution. The silver specimens were cleaned before use in a boiling NaOH solution, and then rinsed with ethyl alcohol and distilled water.

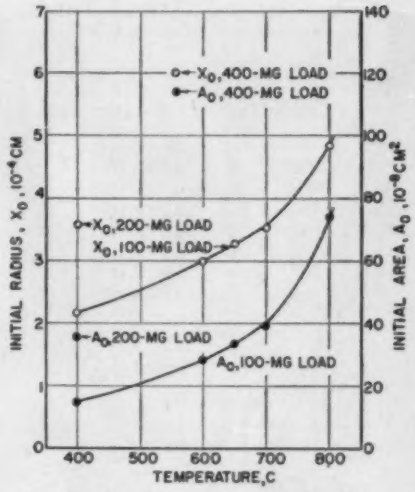

FIG. 1. Initial radius and area of Au-Au bond as functions of temperature.

Test Apparatus

The basic unit for the bonding experiments was a torsion balance, suspended on a steel piano wire. One end of the wire was fixed, and the other attached to a chuck which could be rotated in either direction. A calibrated scale was used to indicate the force exerted at the end of the beam. A sketch of the torsion-balance device is shown in Fig. 2.

The needle was fixed at one end of the torsion beam in position to make normal contact with the flat surface. An auxiliary electric circuit employing a galvanometer was used to indicate the instant that contact was made between the two sides of the bond junction. Rotation of the torsion element then could be used either to apply a known load or to measure the breaking force. The torsion balance was calibrated periodically, although no appreciable changes in calibration were observed over several months of operation. The sensitivity of the balance was found to be about ±10 mg. with a total calibrated capacity of ±3000 mg.

The flat specimen, a section of $\frac{1}{4}$-in. diam rod about

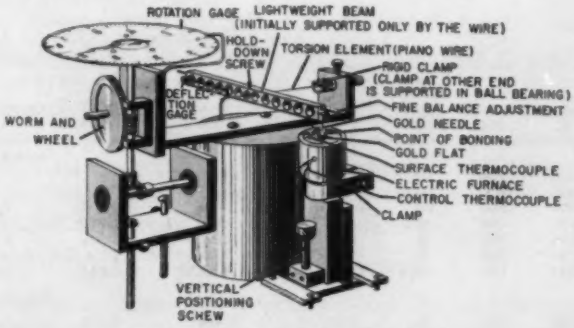

FIG. 2. Torsion balance device.

[1] G. C. Kuczynski, Trans. Am. Inst. Met. Engrs. 185, 169–178 [J. Metals (1949)].
[2] J. H. Dedrick and G. C. Kuczynski, J. Appl. Phys. 21, 1224–1225 (1950).

TABLE I. Test data for Au-Au and Ag-Ag bonding experiments.[a]

Temp, C	1000/T, $°K^{-1}$	Pre-load, mg	Bond load, mg	Xo, cm	Xo^5, cm^5	Average breaking force, mg, after indicated time, sec: 0	120	300	600	1200	1800	2400	3600
					Gold-gold bonding								
400	1.486	200	10	3.09×10^{-4}	2.80×10^{-18}	330	···	340	370	···	370	···	410
600	1.145	400	10	6.01×10^{-4}	7.90×10^{-17}	435	550	···	604	···	535	···	507
650	1.083	100	10	3.29×10^{-4}	3.80×10^{-18}	526	743	994	865	1253	···	1510	1600
700	1.028	50	0	2.51×10^{-4}	1.00×10^{-18}	405	1300	1818	1937	2190	···	2451	2318
700	1.028	100	0	3.54×10^{-4}	5.60×10^{-18}	440	723	900	1195	1405	···	1637	1534
700	1.028	200	0	5.02×10^{-4}	3.20×10^{-17}	545	1160	1330	1578	1555	···	1886	2048
800	0.932	100	0	4.86×10^{-4}	2.72×10^{-17}	700	723	1003	1280	1793	···	2333	2493
					Silver-silver bonding								
700	1.028	100	0	3.54×10^{-4}[b]	5.60×10^{-18}[b]	693	1028	1708	1938	2039	···	2228	2681

[a] Tests made by using cold-worked electropolished needles having an average tip radius of 0.002 cm against annealed electropolished flats.
[b] Value of Xo for silver taken as that for gold.

$\frac{3}{10}$ in. long, was fixed in a small platinum-wound resistance furnace. Temperatures were measured and controlled from a Pt-Pt-10 Rh thermocouple placed directly on the surface of the specimen. Not shown in the sketch is a slotted radiation shield placed over the specimen during operation. The entire unit was enclosed in a plastic dry-box and mounted on sponge rubber to minimize vibration effects. Tests using gold specimens were done in dry air; the silver specimens were tested in an atmosphere of argon to minimize oxidation effects.

In operation, the beam was lowered slowly until contact was indicated by the closing of the galvanometer circuit. An initial load was then applied, either by further rotation of the torsion element or by adding a weight directly to the beam. This load was then removed immediately to eliminate growth of the bond area through creep. At the lower temperatures, it was found necessary to maintain a slight positive load (10 mg) to prevent premature fracture caused by background vibration. After the desired time, the normal force required to break the bond was measured by rotating the torsion element until rupture occurred.

EXPERIMENTAL RESULTS

Bonding Experiments

Table I presents the results of bonding tests on Au-Au couples at 400 to 800 C, and Ag-Ag couples at 700 C. The values listed for the initial contact radius (Xo) were taken from the curves of Fig. 1.

For the purpose of comparison between theory and experiment, it is convenient to solve the bond growth equation for the diffusion coefficient, as follows:

$$Dv=\frac{4kXo^5T[(F/Fo)^{\frac{1}{3}}-1]^3}{81\sigma\delta^3a^2t}. \qquad (2)$$

In computing Dv, the following values for the physical constants were used: k = Boltzmann's constant = 1.38×10^{-16} erg-sec, σ = surface tension = 1400 d-cm, δ = interatomic spacing = 2.89×10^{-8} cm.

The average measured value for the needle tip radius was taken as: $a=2.0\times10^{-3}$ cm.

For tests carried out at constant temperature, and at a fixed preload, the value of Dv then becomes a function of F, Fo, and t, so that a value for Dv may be obtained for each nonzero time interval. Table II lists the computed values of $[(F/Fo)^{\frac{1}{3}}-1]^3$ for the experiments made on Au-Au and Ag-Ag couples, and the value of $[(F/Fo)^{\frac{1}{3}}-1]^3/t$ for each temperature, obtained by the method of least squares. From this value, the diffusion coefficient Dv was determined for each condition of temperature and preload; the values of Dv are included in Table II.

Logarithms of the self-diffusion coefficients of gold are plotted against reciprocal temperature in Fig. 3;

TABLE II. Computed values for Au-Au and Ag-Ag bonding experiments.

Temp, C	Pre-load, mg	Bond load, mg	$[(F/Fo)^{\frac{1}{3}}-1]^3$ after indicated time, sec: 120	300	600	1200	1800	2400	3600	$[(F/Fo)^{\frac{1}{3}}-1]^3/t$ least squares	Dv, cm^3/sec
					Gold-gold bonding						
400	200	10	···	3.31×10^{-6}	0.202×10^{-6}	···	0.202×10^{-6}	···	1.501×10^{-6}	3.54×10^{-7}	3.35×10^{-14}
600	400	10	1.916×10^{-6}	···	5.675×10^{-6}	···	1.2955×10^{-6}	···	0.496×10^{-6}	4.68×10^{-7}	1.62×10^{-13}
650	100	10	6.67×10^{-6}	0.053	0.0225	0.161	···	0.336	0.412	1.218×10^{-4}	2.145×10^{-11}
700	50	0	0.497	1.405	1.672	2.338	···	3.110	2.700	1.041×10^{-3}	5.09×10^{-11}
700	100	0	0.0223	0.0793	0.275	0.439	···	0.804	0.654	2.425×10^{-4}	6.65×10^{-11}
700	200	0	10.3×10^{-6}	0.8173×10^{-6}	7.02×10^{-6}	6.14×10^{-6}	···	0.0277	0.0457	1.159×10^{-5}	1.81×10^{-11}
800	100	0	4.79×10^{-6}	7.63×10^{-6}	0.044	0.216	···	0.564	0.705	2.025×10^{-4}	2.97×10^{-10}
					Silver-Silver bonding						
700	100	0	0.01035	0.185	0.306	0.367	···	0.499	0.907	2.492×10^{-4}	6.81×10^{-11}

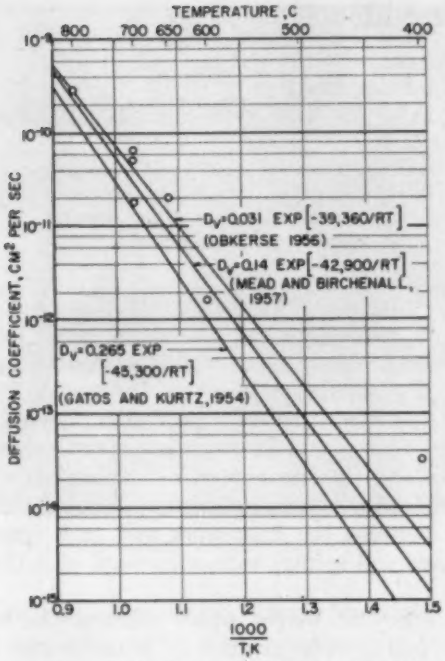

FIG. 3. Self-diffusion coefficients of gold determined from bonding experiments.

included for comparison are recent data[3–5] obtained using single crystals and radioactive tracer techniques. The agreement appears good, particularly at the higher temperatures. The single value obtained for silver at 700 C is compared below with the results of Tomizuka[6]; again, agreement appears good.

$Dv_{700C}=6.81\times10^{-11}$ cm²/sec (present work),

$Dv_{700C}=4.04\times10^{-11}$ cm²/sec

(Tomizuka, $D=0.395\exp[-44\,090/RT]$).

Metallographic Observations

A number of bonded couples were mounted and sectioned for metallographic observation. A typical photograph is shown in Fig. 4. The results of visual examination of these sections are summarized below:

(1) Measurements of the bond junction diameter and the radius of the neck agree well with the calculated values.

(2) There is no evidence that recrystallization has occurred at the interface. However, there is definite evidence that the original interface, visible as a curved line of voids in some of the sections, becomes a grain boundary. This newly-formed grain boundary migrates toward its center of curvature (i.e., toward the needle) during the diffusion anneal.

(3) The deposit of metal at the root of the bond junction is apparent, in agreement with the mechanism of sintering proposed by Kuczynski.

[3] H. C. Gatos and A. Kurtz, Trans. Am. Inst. Met. Engrs. **200**, 616–619 [J. Metals (1954)].
[4] B. Obkerse, Phys. Rev. **103**, 1246–1249 (1956).
[5] H. W. Mead and C. E. Birchenall, Trans. Am. Inst. Met. Engrs. **209**, 874–877 [J. Metals (1957)].
[6] C. T. Tomizuka and E. Souder, Phys. Rev. **103**, 1182 (1956).

FIG. 4. Section through gold needle bonded to gold flat for 60 min at 700 C. 400×.

DISCUSSION OF RESULTS

The agreement between theory and experiment shows that the formation and initial growth of a single asperity bond can be described adequately by the modified Kuczynski equation. Further growth is limited by the configuration of the experimental system.

This model of a single asperity approximates the conditions existing in a massive system during the formation and initial growth of solid-state bonds. However, the extension of this model to a massive system requires more than a simple summation. First, the asperities in a massive system include a multitude of variations in size, shape, and contact pressure. These variables are difficult to evaluate and control. Further, the completion of bonding between massive surfaces requires the elimination of voids through an outward diffusion of vacancies. This process is not described by the present model.

Despite these limitations, the factors that were found to determine the formation and initial growth of single-asperity bonds likewise apply to these stages in the bonding of massive systems. Thus, time, temperature, and diffusion rate should be direct factors in the bonding of massive surfaces, whereas the effects of applied pressure and surface finish probably can be included as indirect factors in an empirical function.

ACKNOWLEDGMENTS

The authors wish to acknowledge the contributions of Dr. J. E. Reynolds, who conducted the initial studies, and Messrs. J. B. Bergin and R. L. Kennard, who performed most of the experiments.

A Dynamic Hard Sphere Model

D. TURNBULL AND R. L. CORMIA
General Electric Research Laboratory, Schenectady, New York
(Received December 21, 1959)

A simple two-dimensional model, in which uniform hard spheres are made to move steadily and apparently nearly at random, is described. At low sphere density the model exhibits "gas-like" behavior. As the density is increased the behavior becomes more "liquid-like" and then "crystallization" occurs. Many dynamic atomic phenomena, believed to occur in the gas, liquid, or solid state, are illustrated by the model.

MODELS which simulate many atoms interacting together can be useful for giving insight on what assumptions may be satisfactory to treat multiatomic interactions and for teaching. One such model is the soap bubble raft described by Bragg and Nye.[1] As ordinarily used this model is static but Fukushima and Ookawa[2] have made the model dynamic by imparting vibrations to the solution which supports the soap bubbles. This dynamic model illustrates the behavior of many of the defects believed to exist in crystals.

Another interesting dynamic model was described recently by Moore.[3] In this, model spheres of magnetic material are made to move on a flat surface by an alternating magnetic field. The spheres act as sychronous motor rotors and move in a circular path. Apparently the motion of the spheres is not random but the model does illustrate some of the expected dynamic features of atomic behavior.

We have developed a dynamic hard sphere model which is very simple and flexible. In this model many uniform spheres are fenced in on a round horizontal glass plate and agitated by the vibrations of a wooden board, suspended from springs, on which the plate is mounted. The board is vibrated by a rotating eccentric weight which is attached to the shaft of an electric motor mounted on the underside of the board. With this excitation the spheres move continually and apparently at random. The motion of the spheres is both lateral and vertical, but a motor speed can be selected so that the vertical component is very small.

We present here the details of the model design that we have found most satisfactory. However, the design requirements are quite flexible and probably there are modified designs that would serve as well or better than the one which we have used.

MODEL DESIGN

A photograph of the model is shown in Fig. 1. The glass plate on which the spheres are placed is 9 in. in diameter and $\frac{1}{4}$ in. in thickness. It is surrounded by a fence 2 in. high made from $\frac{1}{16}$ in. aluminum sheet. Usually, a corrugated aluminum liner with a period of $\frac{1}{2}$ in. and amplitude $\frac{3}{16}$ in. was placed inside the fence; but, under most circumstances, it seemed to have little or no effect on the operation of the model. The glass plate is positioned in the center of a plywood board, 15 in. sq by $\frac{3}{4}$ in. thick, which is suspended by springs attached to each of its corners from an angle-iron framework. Leveling is accomplished by turnbuckle screws placed between the framework and each spring. We have used coil springs with a constant of 3.18×10^5 d cm^{-1}.

The eccentric weight which vibrates the board is an iron half-cylinder about 1 in. in radius and 1 in. in length. It is located under the center of the board and rotated by a universal ac-dc 1/30 hp variable speed type motor. The drive shaft is $\frac{1}{2}$ in. long and its maximum rate of rotation is about 1700 rpm. Figure 2 shows how the motor is mounted on the under side of the board. The motor is fastened in the slot of a brass crossbar and can be positioned anywhere along the bar. In turn the crossbar is attached to two slotted brass side bars located along opposite edges of the board. The crossbar can be put in any desired position parallel to one edge by sliding it along the side bars.

At the suggestion of Dr. Francis P. Bundy we also tried imparting vibrational energy to the model by means of a vibration tester (Model No. T-51-MC Type G) made by MB Manufacturing Company. To do this, the model was bolted securely to the vibration tester. This arrangement worked very satisfactorily. The vibrational frequency and amplitude could be controlled more precisely and varied over a wider range than with the simpler arrangement described above. However, excepting where otherwise noted, the observations reported in this paper were made using the simpler apparatus.

OPERATION OF MODEL

The motor speed is controlled by a variable auto transformer. In operating the model, a speed is selected which causes the board to vibrate near its resonant frequency. The amplitude of vibration and hence the energy of the spheres can be varied considerably by small changes in the motor speed.

We have used in the model: spheres of glass (diam = 3, 4, 5, or 6 mm); iron (diam = 4 mm), aluminum (diam = 4 mm), or polyethylene (diam = 4, 5 mm). All have worked satisfactorily. The aluminum spheres acquire

[1] L. Bragg and J. F. Nye, Proc. Roy. Soc. (London) **A190**, 474 (1947).
[2] E. Fukushima and A. Ookawa, J. Phys. Soc. Japan, **10**, 970 (1955).
[3] A. D. Moore, Electrical Engineering, **78**, 148, 229 (1959).

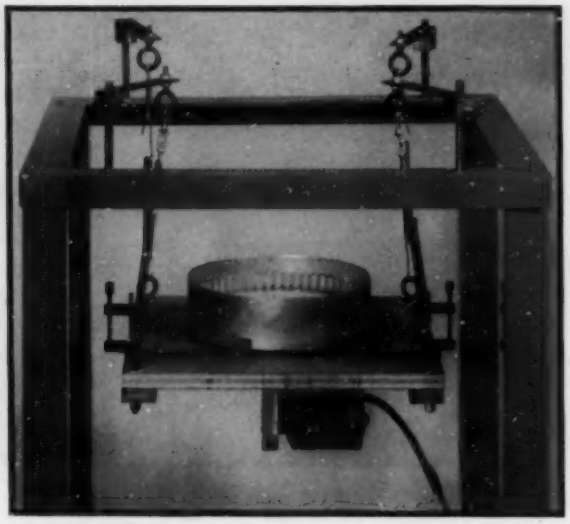

FIG. 1. Photograph of hard sphere model.

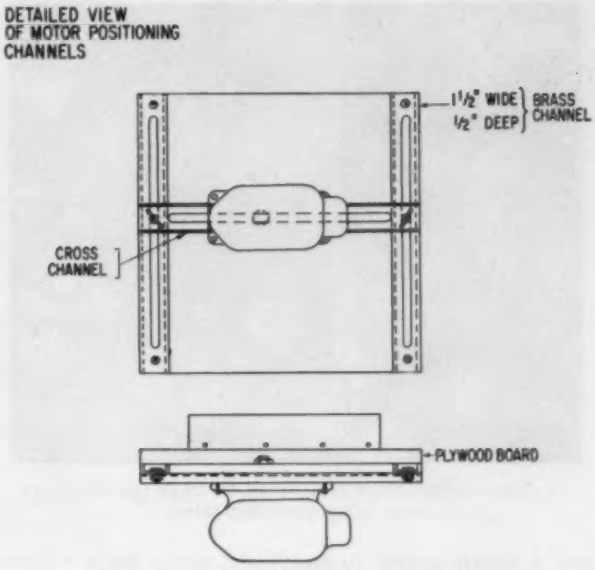

FIG. 2. Schematic diagram showing positioning of motor under plywood board.

during their motion an electric charge from the glass base and repel each other. When the humidity is very low the glass spheres behave similarly. Most of our observations were made using 4-mm diam glass spheres supplied by the Fisher Scientific Company. Thus there could be as many as 2400 spheres in the base layer of the model.

During the operation of the model the spheres appear to move randomly and marked spheres appear to become distributed at random after a time. Usually the lateral velocity of the spheres averages around 1 cm/sec, corresponding to a kinetic theory temperature of the order of 10^{16}°K. Very long paths, such as are seen at a low sphere density, appear to be curved slightly. The average energy of the spheres seemed to be uniform over most of the surface but there usually remained a small area over which the average energy was noticeably higher than elsewhere. We have been unable to eliminate these "warm spots" consistently in the simple apparatus. However no warm spots are apparent when the vibrations are imparted by the M. B. vibrational tester.

The most critical requirements for satisfactory operation of the model appeared to be that the plane of the board be kept horizontal and the eccentric weight be positioned under the center of the board.

In most of our work we have used mutually unattracting spheres. Nevertheless even without attraction the model illustrates a remarkable number of atomic interactions believed to occur in actual matter. The reason for this is that on the *inside* of dense matter the atomic attractions, to a large extent, cancel each other out.

We have found two methods whereby the spheres are made to attract each other. One method is to magnetize steel spheres. In this case, the attractive force falls off relatively slowly with distance but unfortunately the force law between spheres changes when they associate. A second method is to coat the spheres of any of the materials with a thin liquid film.[4] This results in a very short range attraction due to capillary forces.

BEHAVIOR OF MODEL

We shall now describe various interesting features of the behavior of the model. Excepting where otherwise noted, all the observations reported were made with mutually unattracting glass spheres, 4 mm in diameter, in the model. Several high-speed photographs (Figs. 3–9) were made of the glass spheres in motion. For these photographs only 5-mm spheres were used instead of of the 4-mm spheres. The principal variable governing the behavior of the model is the "free space ratio" which is defined to be the ratio of the area occupied by the spheres at rest in a perfect close-packed arrangement to the total area of the model.

Transition from Gas-Like to Liquid-Like to Solid-Like Behavior

In this experiment the density of glass spheres is gradually increased from zero while energy is supplied continually. The sequence of events is very like that which would occur in a material initially in the gaseous state if the pressure were increased gradually. At first the spheres are very far apart and move distances many times their diameter before colliding with another sphere. A photograph of the model in this "gas-like" state is shown in Fig. 3.

As the density increases, the distance between collisions becomes less and less until it is no more than the diameter of a sphere. So long as the free space ratio exceeds 0.20 to 0.25, no long-range order is apparent,

[4] This method was suggested to us independently by several conferees at the 1959 Gordon Conference on liquids. We regret that we do not recall who first made the suggestion.

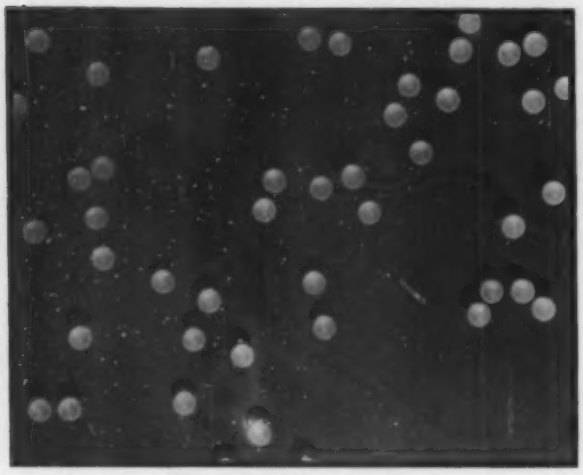

FIG. 3. Photograph of dynamic model in "gas-like" state (large free-space ratio).

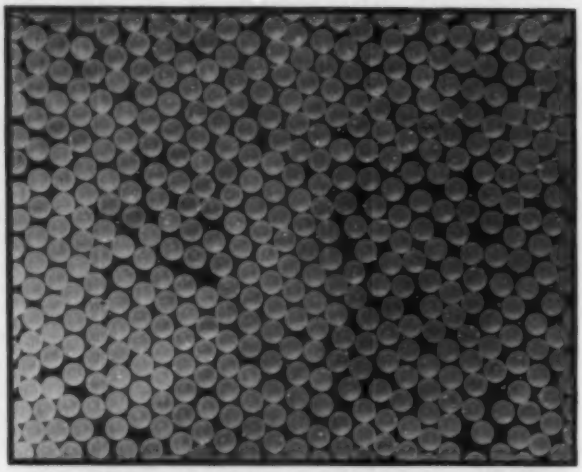

FIG. 5. Photograph of dynamic model at transition to "crystal-like" state (free-space ratio ~0.18).

and a sphere added to the model easily finds a place anywhere. We call the behavior at a free space ratio between 0.20 and 0.35 "liquid-like" though the state is, of course, more analogous to that of a highly compressed gas. Figure 4 is a photograph of the liquid-like state at free space ratio of 0.30.

As the free space ratio is decreased below 0.20, small domains exhibiting long range order seem to appear quite suddenly and grow larger as the free space ratio is decreased further. In this crystal-like state the spheres are most of the time confined to a single position and spheres added to the model flit over the surface until they encounter a defect and are there incorporated into the crystal. Figure 5 shows the model just after long range order has developed at a free space ratio of 0.18. Apparently the onset of long range order occurs at nearly the same free space ratio at all values of the average sphere energy.

When the free space ratio is less than 0.17, the crystal-like structure of the model is well defined and various crystal defects and their dynamic behavior are clearly seen.

Liquid-Like Behavior

High-speed motion pictures were made of the liquid-like state at a free space ratio of 0.26 to 0.30. From these it appeared that most diffusive displacements result from density fluctuations and ranged in magnitude from a small fraction to, in rare instances, 2- or 3-sphere diam. Quite a number of displacements were of the order of 1-sphere diam but no quantitative assessment has been made of the relative contribution of the different displacements to the diffusion constant. As yet, we have made no effort to determine the various distribution functions for the liquid like state.

Defects in the Crystal-Like State

We have observed the dynamic behavior of mono- and multivacancies, dislocations and grain boundaries

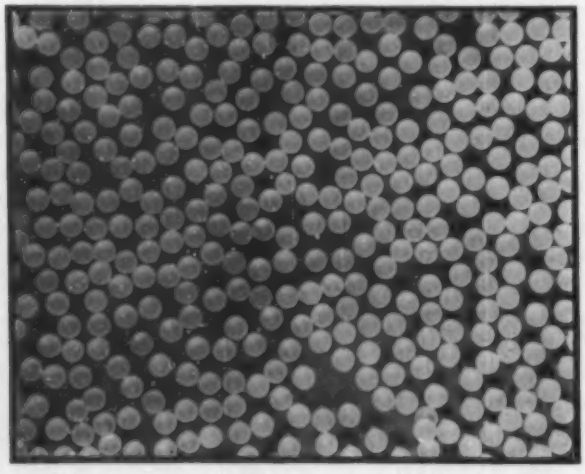

FIG. 4. Photograph of dynamic model in "liquid-like" state (free-space ratio ~0.30).

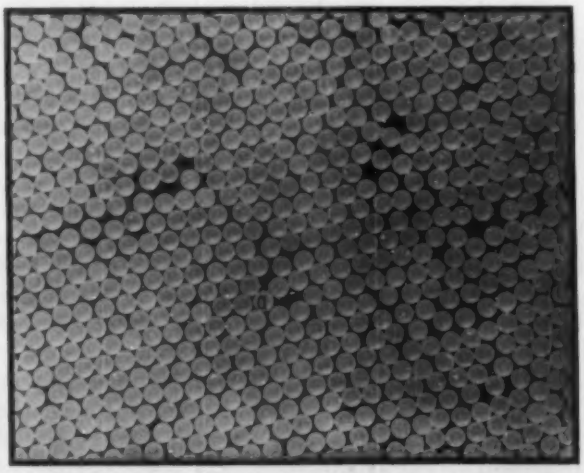

FIG. 6. Photograph of dynamic model showing monovacancy at point *a* in transition from one position to adjacent one (free-space ratio ~0.10).

in the crystal like state. At a free space ratio a little smaller than that necessary for crystallization, 0.18 to 0.13, monovacancies form spontaneously and move quite rapidly. (Occasionally divacancies are seen to dissociate into a pair of monovacancies). Figure 6 shows a monovacancy in the middle of the act of jumping from one position to an adjacent one.

When the free space ratio is decreased to about 0.07, the monovacancies become quite immobile. However di- or multivacancies injected into the model at this density are very mobile and do not dissociate. Figure 7 shows a divacancy and Fig. 8 a pentavacancy. Multivacancies have an appearance somewhat resembling the configuration of the spheres in the liquid-like state. Also we have observed that at small free space ratios divacancies in 4-mm spheres are pinned by 5-mm "impurity" spheres.

There are dislocations in the model after crystallization and they also form when the spheres are stirred.

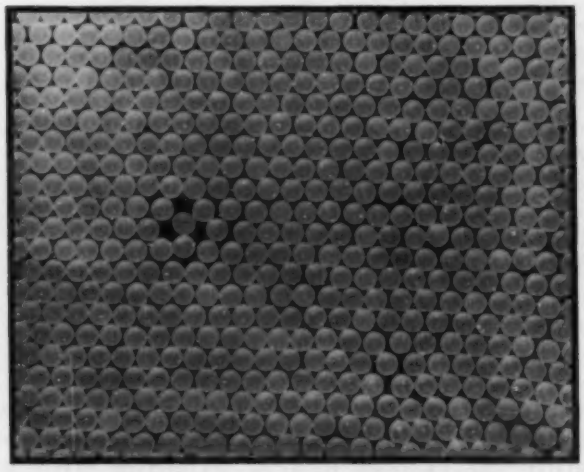

FIG. 7. Photograph of dynamic model showing a divacancy (free-space ratio ~0.06).

Mono- and multivacancies are annihilated when they encounter dislocations. This results in climb of the dislocation. Climb in the opposite direction occurs when a sphere on the crystal surface enters the crystal at the dislocation.

Grain boundaries are present immediately after crystallization. Also they can be introduced by stirring the spheres. They are seen to be sources and sinks for vacancies and surface spheres. Grain growth occurs rapidly at relatively high free space ratios and sometimes at small ratios. In time all grain boundaries and dislocations usually anneal out of the crystal excepting for small areas at the fence. Figure 9 shows grain boundaries and various other imperfections.

Surface Diffusion

Spheres added to the crystal flit over its surface in what seems to be a random path. It is seen that the mean velocity of motion is greater the lighter the sphere. High-speed motion pictures revealed that the spheres move almost always along the depressions in the surface formed by the underlying spheres.

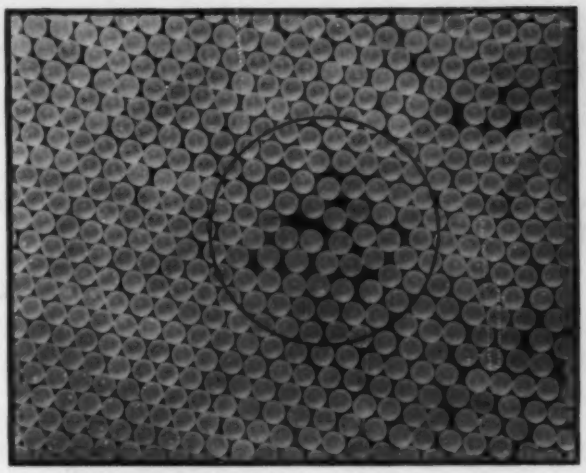

FIG. 8. Photograph of dynamic model showing pentavacancy within circled area (free-space ratio ~0.06).

Nucleation and Growth of Crystals

When the spheres were made attracting, either by magnetizing them or coating them with a thin film of liquid, (for example ethylene glycol) crystallization occurred by nucleation and growth. Generally crystallization begins at the edge of the model, proceeds very rapidly then stops abruptly; presumably when the density of the spheres in the disordered state reaches the equilibrium value for crystallization. Crystallization is promoted by decreasing either the average energy of the spheres or the free space ratio. Under most condi-

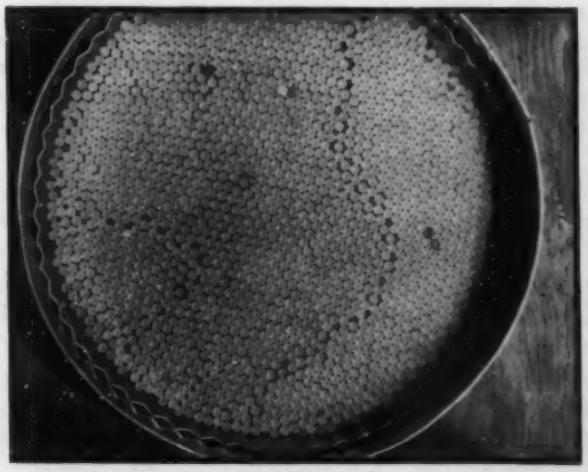

FIG. 9. Photograph of dynamic model showing grain boundaries and other imperfections. A vacancy is in its equilibrium position at point *a*. There are dislocations centering at points *b* and *c*. A surface sphere is at point *d* (free-space ratio ~0.06).

tions the "crystallites" formed by the attracting spheres drift slowly toward one side of the model. We have not been able to eliminate this drift consistently.

Motion Pictures

We have been successful in obtaining motion pictures of various features of the model behavior. Prints of these pictures are available for loan.

ACKNOWLEDGMENTS

F. P. Price and W. DeSorbo of this laboratory directed our attention to static models consisting of glass spheres. The use of a spring suspension in the dynamic model was suggested to us by Professor J. W. Mitchell of the University of Virginia. Additional useful suggestions on the design and operation of the model were made by several other of our associates.

JOURNAL OF APPLIED PHYSICS VOLUME 31, NUMBER 4 APRIL, 1960

On the Yield and Energy Distribution of Secondary Positive Ions from Metal Surfaces*

HENRY E. STANTON
Argonne National Laboratory, Lemont, Illinois
(Received May 11, 1959)

The kinetic energy distribution of secondary positive ions liberated from a solid metallic target of beryllium under bombardment by positive ions was measured in a mass spectrometer provided with an energy analyzer. In conformity with earlier investigations, it was found that an appreciable fraction of the ions was liberated with energies less than 5–10 ev, although some secondary ions of more than 200 ev were found. The distributions appeared to be at least partially Maxwellian in character. Although errors in measurement were large, there appeared to be little dependence of the yield of secondary ions on the mass of the bombarding ion.

I. INTRODUCTION

UNTIL recently, most studies of sputtering have been concerned with relatively massive transports of material under bombardment by positive ions. Other focal points of attention have dealt with secondary electron emission and the liberation of negative ions under sputtering conditions in high vacuum. Honig,[1] however, analyzed the products of sputtering in a mass spectrometer and found that ions of both signs as well as neutral atoms of the target were liberated under positive ion bombardment for the materials being investigated. He also studied the positive ions driven out of the surface when a target of Ge-Si alloy was bombarded by positive ions of the rare gases, in order to compare the yields of Ge^+ and Si^+ from the alloy.

Bradley[2] extended the work of Honig to the refractory metals Mo, Ta, and Pt, and found that secondary ions of the base metals were produced under positive ion bombardment. He found that the method had serious difficulties if used for quantitative analysis. He also included a discussion of the spread in energy of the secondary ions.

There was a possibility of using this method for microanalysis of solid materials, which led to the investigations to be described here. The difficulties of the method under the experimental conditions employed in this work were very apparent.

II. EXPERIMENTAL

1. Mass Spectrometer

The mass spectrometer used was equipped with an energy analyzer, which filtered the ions issuing from the source and, following it, a 60° sector-type magnetic analyzer with a radius of 1 ft, as shown in Fig. 1. The energy analyzer was formed by a pair of concentric cylindrical electrodes with a mean radius of 1 ft and a separation of $\frac{7}{8}$ in. They subtended an angle of 90° at the center of curvature of the analyzer, and shielding end plates were provided so that the effects of fringing fields were theoretically eliminated. The source and image slits for the analyzer were spaced along the ion path a little over $4\frac{1}{4}$ in. from the ends of the deflecting plates. Between the energy analyzer and the magnetic analyzer, a stack of slits was provided to permit additional acceleration and refocusing of the ions prior to mass analysis.

The final detector, shown at the top of Fig. 1, consisted of an adjustable defining slit, some focusing slits, various shield plates, and a 16-stage electron multiplier. The output pulses of the multiplier were fed into a counting rate system which in turn drove one channel of a strip chart recorder. The ion beam issuing from the energy analyzer was monitored by an intermediate electrode which clipped the edges of the beam, the current

* Work performed under the auspices of the U. S. Atomic Energy Commission.
[1] R. E. Honig, J. Appl. Phys. **29**, 549 (1958).
[2] Richard C. Bradley, J. Appl. Phys. **30**, 1 (1959).

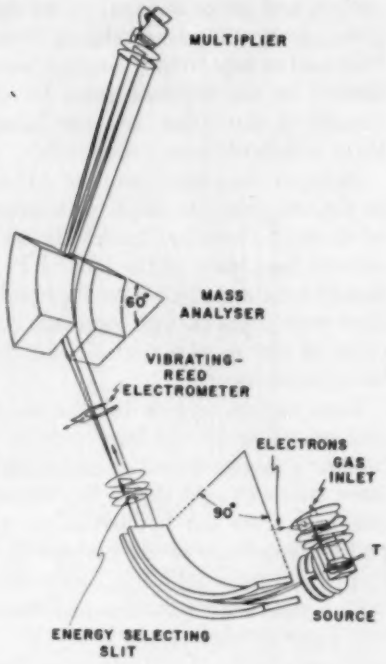

FIG. 1. A perspective drawing (semi-schematic) of the energy selecting mass spectrometer. Ions arising at the target T in the lower right hand corner are given an acceleration of a few hundred volts before entering the energy selector. The emergent ions of the proper energy pass through the final accelerating slit system and are then separated mass-wise in the magnetic field and finally enter the multiplier at the top of the figure.

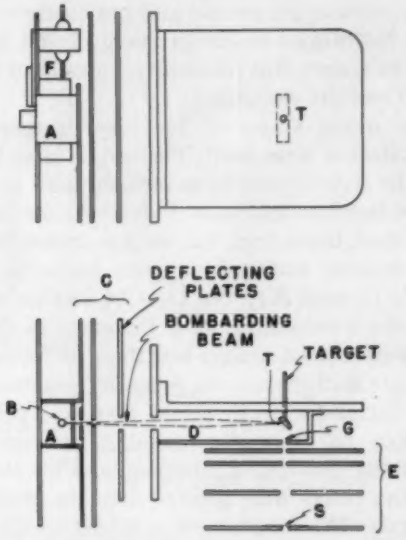

FIG. 2. Two views, one in cross section, of the source system used. The target is shown at T. Ions originating in the ion box A are focused on this target and the secondary ions produced are drawn off at right angles into the energy analyzer. The target was inclined 30° to the bombarding beam.

being measured by a vibrating-reed electrometer, whose output drove a second channel of the strip chart recorder. With this arrangement, the vibrating-reed electrometer measured the current of all masses, but of the selected energy, while the counting-rate system simultaneously measures the ion current of a particular mass and the same energy. Consequently, by varying the energy of the ions transmitted by the energy analyzer, one could determine the energy distribution of the total ion beam and compare it with the distribution in energy of a particular ion.

2. Source

The source used in these investigations is shown in cross section in Fig. 2. After an acceleration of 50–100 v, electrons originating at the filament (F) entered an ion box (A) through a $\frac{1}{16}$-in. hole (B) and there produced the ions of the bombarding beam. The ions were drawn out and focused by a set of plates (C) before entering into the target chamber (D). They travelled about an inch through this chamber before hitting the target (T). The chamber (D) formed an electric shield about the target and prevented the entrance of stray electrons and ions. A pair of deflecting plates was provided so that the beam could be adjusted to fall either onto or off the target. At right angles to the system of slit plates in the bombardment section was a similar system (E) for the spectrometer proper. By means of the latter system, the ions formed by bombardment of the target were drawn out through a slit (G) in the wall of the chamber and focused on the entrance slit (S) of the energy analyzer.

3. Operation

Ions generated at the target were first drawn out of the target chamber and accelerated initially to energies of from 100–500 ev before entering the energy analyzer. The potential difference between the curved condenser plates had to be maintained at 15.4% of the initial accelerating voltage in order to transmit ions formed "at rest." Ions transmitted at higher condenser voltages were considered to have kinetic energy of formation and the change in the condenser voltage was interpreted to be a measure of it. The zero point and energy resolution could be obtained approximately from an analysis of the energy distribution of rare gas ions produced by electron bombardment since these are formed with thermal energies.

Ions leaving the exit slit of the energy analyzer were monoenergetic within approximately ± 0.5 ev, but the beam was composed of ions of all masses. The ions were then accelerated through from 2–10 kv by the intermediate slit system which also served to refocus the beam for magnetic analysis.

The exit slit of the accelerating slit system formed the source slit of the magnetic analyzer; after a deflection of 60°, the beam was focussed on an adjustable image slit and entered an electron multiplier and pulse-counting system which formed the final detector.

The bombarding ions were formed by an electron beam which was electronically regulated and the current to the target was measured by a dc amplifier. The voltages used for the electrodes throughout the spectrometer were regulated to within ± 10 mv to prevent the entrance of ripple. This was particularly important on the initial accelerating and the energy analyzing

voltages, since ripple on one and not on the other gave spurious indications of kinetic energy in the ion beam. In order to reduce this possibility, capacitors were connected across the electrodes.

In the initial stages of the investigation, various target materials were used. The target faces measured about $\frac{3}{8}$ in.$\times\frac{3}{16}$ in. and were inclined with an angle of 30° to the bombarding beam. Polycrystalline samples of stainless steel, brass, lead, tin, and finally beryllium were used as targets, and various gases including the rare gases (He through Xe), N_2, O_2, CO, and air were used to form the bombarding ions. Pressures in the source volume were almost always less than 10^{-5} mm Hg and the machine background was generally less than 5×10^{-7} mm Hg. Except for the Be target, no special precautions were taken to clean the metallic surfaces beyond thorough degreasing and pumping, and for this reason background peaks were greater than the peaks of the base metals. The target structure was modified when the Be target was installed. Two holes parallel to the bombarded face were drilled through a solid piece of Be. A resistance heater was placed in one hole and a resistance thermometer in the other, with the thermometer closer to the face. This permitted heating the target to ~200°C above the ambient temperature. Target currents of $\sim5\times10^{-8}$ amps, corrected for secondary electron emission, represented the maximum obtainable with the source structure used. The energy of the bombarding ion could be varied between 0 and 3 kv.

Electrons could be injected directly into the target chamber to ionize residual gases and permit initial adjustments since the secondary ion beams, both total and mass analysed, were very small.

III. RESULTS

The stainless steel and brass targets were studied first. The energy analyzer was adjusted for maximum beam and the final acceleration was varied to examine the mass analysis. It became evident immediately that background peaks were quite troublesome. The hydrocarbon and other residual peaks appeared to have approximately the same relative intensities either when liberated as ions from the target under bombardment or formed in the residual gases by electron impact, although in the latter case the intensities were two or three orders of magnitude greater.

None of the constituents of either the stainless steel or the brass targets could be detected, possibly because of these background peaks. It seemed reasonable to assume that some of the ions of Fe, Ni, Cr, Cu, or Zn should have appeared from the bombardment; but if so, they were small enough to escape detection. These portions of the mass spectrum did, however, have high background peaks.

Lead and tin targets did give unambiguous ion peaks corresponding to the base metals. In the latter case indium was also found as an impurity in the tin. The mass spectra could easily be compared by alternately changing from ion bombardment to electron impact, and the existence of the metallic ions under bombardment conditions definitely established.

The yield of $^{208}Pb^+$ ions was studied using different rare gases as bombarding ions. The experimental results are shown in Fig. 3 without any corrections. It is doubtful whether the slight trend in the curve is significant, since for a given ion there were fluctuations of ~25% in the yield. The high yield for bombardment by $^4He^+$ was surprising. The yield was proportional to the ion current within the same error for all bombarding ions. Below ion energies of about 30v it was difficult to adjust the bombarding beam very well, and the ions from the base metal were difficult to detect because of their small numbers.

Na^+ and K^+ ions were easily found under bombardment conditions. The first was unmistakable because of a relatively high yield and the absence of a background peak at m/e=23, while the second stood out far enough above the background to be easily found.

Since up to this stage only ions from "soft" metals had been obtained, and the background had been troublesome, the beryllium target and heater were installed.

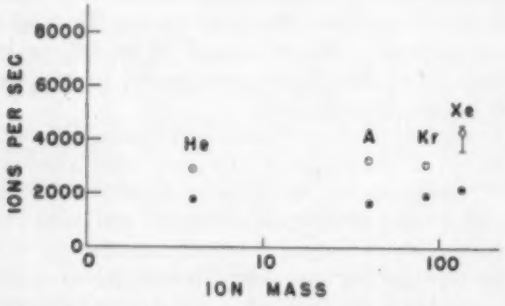

FIG. 3. The number of secondary lead ions of the isotope 208 is shown here as a function of the mass number of the bombarding beam, for two target currents. Points shown as open circles were obtained with a target current of approximately 5×10^{-9} amp, and the points shown as closed circles represent a similar set of observations with a target current of 3×10^{-9} amp, with a fixed bombarding ion energy of 1000 ev.

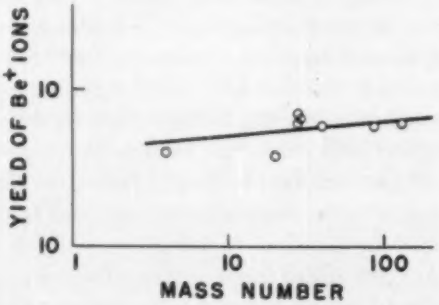

FIG. 4. The comparative yield of Be^+ ions from a target under bombardment by various gases. The cluster of 3 points close together at the middle of the curve were values found from the chemically active gases N_2, O_2, and CO. The curve is corrected for secondary emission of electrons from the target, with a fixed bombarding ion energy of 1000 ev.

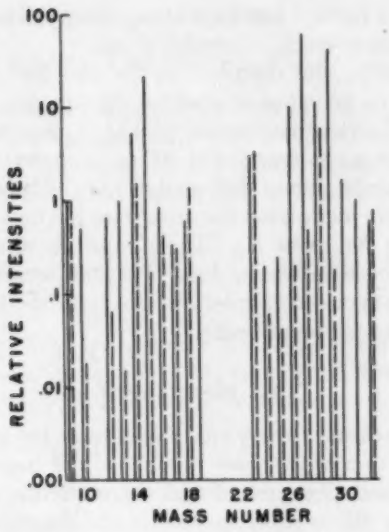

FIG. 5. Two typical mass spectra are shown schematically in a semi-log plot for beryllium under bombardment by helium ions. The intensities indicated by the solid lines show the magnitudes of all masses less than 32 normalized to a yield of one ion of Be^+ taken at room temperature after the target had sufficient time to absorb an equilibrium amount of background gases. The second mass spectrum shown with dashed lines and also normalized for a yield of one ion of Be^+ was taken after prolonged heating of the target at an estimated temperature of about 200°C.

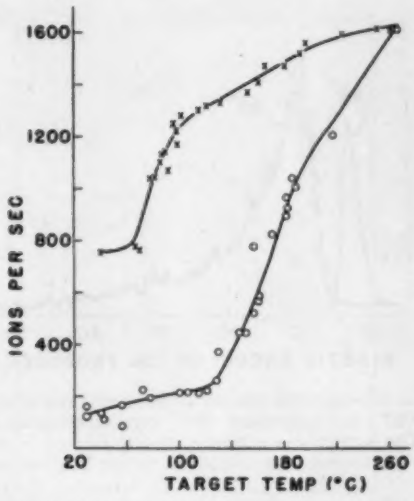

FIG. 6. The yield of ions of Be^+ when the bombarding ions were formed from air at 1000-v energy is shown as a function of the target temperature. The lower curve was obtained by measuring the intensity of the ions at mass 9 for a bombardment current of 10^{-8} amp, as the target temperature was increased from about 30° to 270°C. The target was then permitted to cool, giving the upper curve. After cooling to room temperature, the yield of ions of Be^+ was about 5 times larger than at the beginning as a result of the cleaning of the target.

Experimentally, the generation of ions from the beryllium target seemed to depend little if at all on the mass of bombarding ions when correction was made for the secondary emission of electrons. This is shown in Fig. 4 for bombarding ions of 1000-ev energy, approximate corrections for secondary emission having been made.

These corrections for secondary emission were made empirically by changing the voltage between the target (T) and the chamber (D) from $+50$ v to -50 v approximately and measuring the target current while the bombarding ion beam was held constant. During the analysis of kinetic energy distributions, the potential between the target and target chamber had to be kept at such a value as to give optimum focusing for the secondary ions ($\sim+10$ v).

The curve in Fig. 4 for beryllium is very similar to the yield curve for lead shown in Fig. 3. In the latter case, no correction was applied for secondary emission, but this correction is believed to be approximately the same for all the rare gas ions and would not change the form of the curve in Fig. 3 within the experimental uncertainties encountered. This similarity between the two metals is still less certain because target heating was not used with lead and background effects had to be estimated by electron impact measurements in the residual gases. The relationship found in Fig. 4 was determined with a heated target and background effects were less important.

The heater, it was hoped, would permit at least a partial cleaning of the surface. This turned out to be the case as shown in Figs. 5 and 6. In Fig. 5 two mass spectra from masses 9^+ to 32^+ are shown with intensities plotted on a log scale for two different target temperatures. Both spectra were normalized to the same ionic yield at $m/e=9$, although at 200°C the intensity of Be^+ ions was several times the value at 25°C. The behavior of masses 14, 16, 28, and 32 was probably caused by a leak in the vacuum system. The peaks at $23(Na^+)$, $18(H_2O^+)$, and $17(OH^+)$ changed anomalously or very little but most of the remaining peaks were diminished relative to the intensity of Be^+ by at least an order of magnitude, and some were eliminated.

The effect of target temperature on the yield of beryllium ions is shown in Fig. 6. Actually, of course, the curves shown there represent only one set of experimental conditions and procedures. Much depended on timing. If a high target temperature were used, cleaning of the target would take place in a few minutes, but with lower temperatures (150°C) cleaning might take hours. Most of the work on beryllium was done with the target as clean as it could be made. As nearly as could be determined from the studies of kinetic energy, the background peaks were, in all cases, ions driven from the target by the bombarding ions and did not arise from reactions in the residual gases in the target chamber. All kinetic energy analyses were made with the Be target.

The studies of kinetic energy showed there was a difference in the distribution in kinetic energy for ions formed in the gas and those driven from the target. This is shown in Fig. 7. The bombarding gas used was argon, the mass analyzer was adjusted to $m/e=39^+$ (mostly potassium) and 40^+ (argon) successively, and

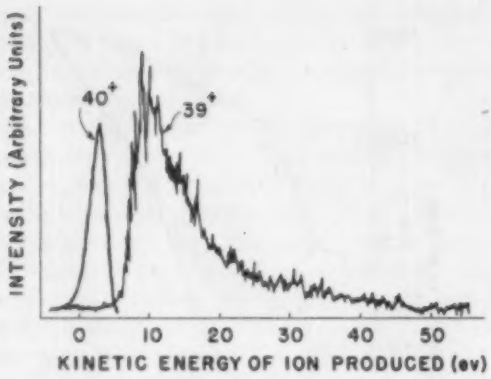

FIG. 7. In this figure two traces of the kinetic energy distribution of argon (40^+) and potassium (39^+) were superimposed for comparison. The former was evidently largely formed in the gas and the latter was driven from the target by ion bombardment.

the potential between the curved plates in the energy analyzer was swept across the peak for each ion. The recorder traces were superimposed and redrawn in the figure. Abscissas represent the energy with which the ion was formed and ordinates the number of ions within an energy band represented by the resolution of the energy analyzer ($\sim$0.8 ev). The potassium peak arose from impurities on the surface of the Be target.

The K^+ peak has a width at half-maximum more than three times that of the Ar^+ peak. The former appears to have been driven from the target by bombardment, while the latter was formed in the residual gas close to the target, perhaps by charge exchange. The potassium peak, like the target current, increased linearly with the pressure of argon in the source box for the bombarding ions, whereas the peak at mass 40 increased very closely to quadratically with the argon pressure. The relative displacement of the two peaks indicates that the Ar^+ ions may have been formed in the target chamber at a lower potential than the ions emitted by the target. One notes further that K^+ ions are detected with energies of 30 ev or more, whereas on the high-energy side of the Ar^+ peak, there is a rapid decrease into the noise at about 5 ev. The low-energy sides of both peaks appear to be quite similar in shape. The intensity of the Ar^+ peak was several times that of K^+. The type of energy distribution found for $m/e=39^+$ was characteristic of all the background peaks, including the hydrocarbons arising from the target, under ion bombardment. When these same peaks were generated by electron impact, on the other hand, they showed kinetic energy distributions like the one for $m/e=40^+$ in Fig. 7. This unambiguously indicated that the background peaks shown in Fig. 5 actually arose by ion impact with the target and were not generated in the background gas in the target chamber (except for the exchange peak of the bombarding gas).

The kinetic energy distribution for a base metal of the target was studied only for Be^+. A typical distribution is shown in Fig. 8 for ions of Be^+ produced under bombardment by Ne^+ ions of 1000-ev energy. The distribution is not a simple Maxwellian one.

Generally, the distribution for the Be^+ in Fig. 8 appears to be quite similar to the one for $m/e=39^+$ in Fig. 7. The distribution in Fig. 8 continued to be detectable up to energies of 300 ev or more (with 1000-ev bombarding ions). Be^+ analyses of the type shown in Fig. 8 were made with the other rare gas ions up to and including Xe. Also N_2, CO, O_2, and air were used to supply the bombarding ions. They all seemed to give the same types of distributions for both the base metal and the background peaks.

IV. DISCUSSION

The flatness of the yield of ions from the base metal as a function of the mass number of the impinging ion (Figs. 3 and 4) suggested that the mechanism for ionic liberation differs from the one for the liberation of neutral atoms. Whereas Wehner[3] found that the sputtering of macroscopic amounts of material depended on the momentum of the bombarding particles, the generation of secondary ions by primary ion impact appears to depend on the energy rather than the momentum. This is implied in Figs. 3 and 4 since the momentum of the bombarding ion beam changes widely with the mass in going from He to Xe for fixed ion energy.

Because of this energy dependence, the analyses of the distributions in kinetic energy shown in Figs. 7 and 8 have been based on Maxwell-Boltzmann distributions. The distributions for K^+ in Fig. 7 appears to be similar in shape to a simple distribution of that type, but the curve for Be^+ in Fig. 8 clearly cannot be Maxwellian with a single temperature. It can, however, be fit by a summation of several Maxwellian distributions of different temperatures.

If $f(E)dE$ denotes the number of ions in the interval dE about the energy E, the Maxwell-Boltzmann dis-

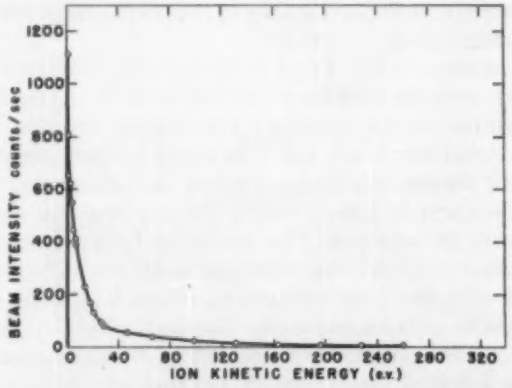

FIG. 8. The distribution of kinetic energy of Be^+ ions driven from the target under bombardment by neon ions of 1000-ev energy.

[3] G. K. Wehner, Phys. Rev. **102**, 690 (1956).

tribution for a given temperature T is

$$f(E)=g(T)E^{\frac{1}{2}}\exp(-E/kT). \quad (1)$$

The distribution function $g(T)$, which is a measure of the number of ions associated with temperature T, is independent of the energy E. If $F(E)dE$ represents the corresponding measured distribution of Fig. 8, then we have

$$F(E)=\int_0^\infty g(T)E^{\frac{1}{2}}\exp(-E/kT)dT. \quad (2)$$

The function $\lambda^{-2}g(1/\lambda)$, where $\lambda\propto T^{-1}$, is clearly the inverse Laplace transform of the function $E^{-\frac{1}{2}}F(E)$. If the distribution $g(T)$ is discrete, i.e., if we assume

$$g(T)=\sum_i g_i\delta(T-T_i),$$

Eq. (2) may be written in the simpler form,

$$E^{-\frac{1}{2}}F(E)=\sum_i g_i\exp(-E/kT_i). \quad (3)$$

The determination of the discrete coefficients g_i corresponding to a measured distribution $F(E)$ by means of Eq. (3) allows a simple approximation of the inversion of Eq. (2).

Figure 9 is a semilog graph of $E^{-\frac{1}{2}}F(E)$ vs E for the two ions. The generally lower curve for K^+ seems to correspond to a single Maxwell distribution with an absolute temperature of 7.1×10^4 °K. The accuracy of the data does not seem to warrant a more refined analysis.

The curve for Be^+, however, is clearly complex. Four different distributions could be "peeled" from the curve in Fig. 9. This, of course, represents a simple way of inverting Eq. (2) and serves only to give an approximate idea of the form of the curve for $g(T)$ as a function of temperature. It seems probable, however, that the temperatures of the Maxwell distributions necessary to synthesize the kinetic energy distribution of the Be^+ ions lie between the limits of 3000° to 10 000°K and approximately 600 000°K, even though there is a continuous variation in these temperatures and the coefficients of the distributions.

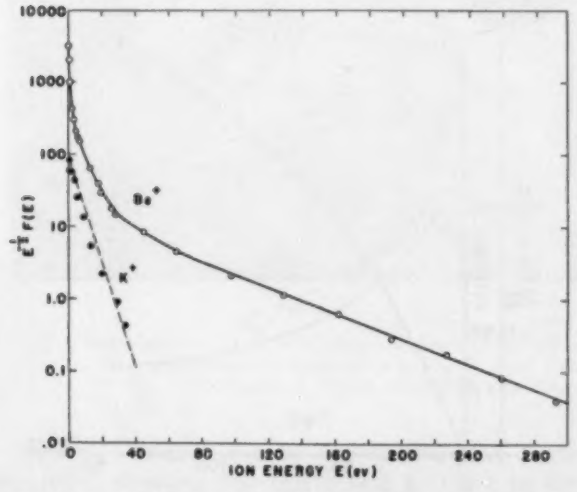

FIG. 9. In this figure, the function $E^{-\frac{1}{2}}F(E)$ of Eq. 3 is shown in semi-log plot vs the ion energy E as derived from the experimental curves for K^+ in Fig. 7 and Be^+ of Fig. 8.

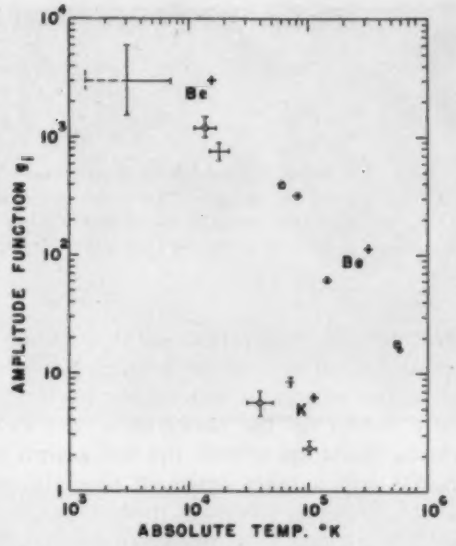

FIG. 10. The various coefficients g_i in Eq. 3 derived from the previous figure are shown at the values of the absolute temperature T_i, to which they correspond. The estimated errors are quite large for the lower temperatures because of the indefiniteness in the zero point of the energy scale. The points shown for Be^+ represent two possible analyses for slightly different values of this zero energy point. In the case of K^+, two possible analyses for the same curve are shown. Points characterized by solid dots are to be grouped together, and those by open circles similarly, representing two possible analyses of the same distribution curve.

One of the chief sources of error in the analysis lies in (see p. 5) determining the precise point of zero kinetic energy. The zero point of kinetic energy was calculated by assuming a Maxwellian distribution near the peak maximum, and in all cases it agreed within approximately a half volt with the spectrometer calibration using a gas source. The inversion is further complicated by the effects of the spectrometer on the distribution curve. The non-vanishing energy width (0.8 ev) transmitted by the energy analyzer becomes more important at low ion energies than at high energies, tending to broaden the peak and depressing the value of energy at which ions begin to appear. Furthermore, the electrodes which draw out the secondary ions, have important effects at low ion energies by more effectively focusing them into the beam, and thereby tending to increase the relative intensity at low energies.

ACKNOWLEDGMENTS

The writer wishes to express his appreciation to Dr. Louis A. Turner and Dr. Mark G. Inghram for helpful discussions during the experiments and in their interpretation. He is also indebted to Dr. James E. Monahan for carefully checking the manuscript from a theoretical standpoint.

JOURNAL OF APPLIED PHYSICS VOLUME 31, NUMBER 4 APRIL, 1960

Origin of the "First-Order Structure" of CP4-Etched Ge Surfaces*

G. Bonfiglioli, A. Ferro, and A. Mojoni
Istituto Elettrotecnico Nazionale, Torino, Italy

(Received November 9, 1959)

The present paper briefly reports about the results of examinations of surfaces of CP4-etched Ge. The origin of the so called "1st-order structure" observed on the micrographs is discussed. It is shown that while etching proceeds, the ending points of some dislocations are reached, or some of them become passivated. In both cases, the etch pits no longer grow and their traces give origin to the 1st-order structure.

IN the course of observations of semiconductor surfaces at optical microscope magnification, it often occured to the writers to look at the peculiar aspect frequently shown by the background of CP4-etched Ge surfaces. Quite apart from the well-known pattern of etch pits which takes place on properly oriented crystals,[1] a network structure delimitating halos or rounded hills, looking very much like a polycrystalline structure, can often be seen. A clear example is shown in Fig. 1. This feature of Ge micrographs has already been observed by other investigators, although no satisfactory explanation of it can be found in the literature as far as we know. As a matter of fact, Rhodes et al.[2] have remarked about the existence of such a structure, noting that networks of three different sizes are sometimes present: one about 100 μ diam (called 1st-order structure); a smaller one about 10 μ size (called 2nd-order) within the 1st-order one; and a 3rd-order structure, approximately 0.5 μ, visible as faint dots within the former. Noggle and Stiegler[3] have carried on further studies with optical and electron microscopes on Ge (irradiated and unirradiated), complementing the observations cited previously as follows:

(*a*) The aforementioned structures are only observed when the etched surface is very near to (111) orientation.

(*b*) On unirradiated crystals, Br enriched CP4 is necessary to reveal 2nd- and 3rd-order structures, while the 1st-order one is revealed by the normal CP4 etchant.

(*c*) The 1st-order structure is readily reproduced but is dependent on the specimen preparation, as for example, preliminary grinding or the deformation caused by cutting the crystal.

(*d*) The 1st-order network marks the boundary between areas of slightly different elevation.

(*e*) About 2nd- and 3rd-order structures, no definite conclusions are presented.

We believe that all these remarks suggest the same conclusion, namely, that the so called "first-order structure" is due to nothing else than the memory of the dislocations previously present on the area considered which have become passivated at a certain moment, or whose ending points have been surpassed while the etching action proceeds.

This paper briefly deals with the results of some examinations performed with the scope of ascertaining whether this idea was correct.

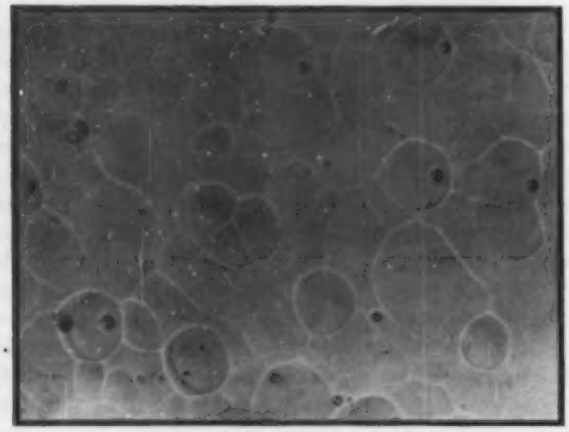

FIG. 1. Example of well developed 1st-order structure; (112.5×)

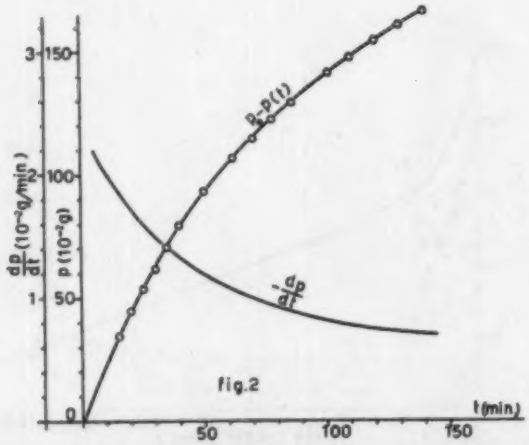

FIG. 2. (a) Loss of weight vs total etching time $[p_0-p(t)]$. (b) Derivative of the curve (a), i.e., loss of weight per unit time vs time.

* The research reported in this document has been sponsored by the Air Force Office of Scientific Research of the Air Research and Development Command, U. S. Air Force, through its European Office, under contract.

[1] R. G. Rhodes et al., J. Electronics and Control, 3, 403 (1957).

[2] R. Chang, J. Appl. Phys. 28, 385 (1957).

[3] T. S. Noggle and J. O. Stiegler, Ann. Progress Rept. ending August 31, 1958, Solid State Div., Oak Ridge National Laboratory; ORNL-2614, Phys. and Math., TID 4500, p. 11 ff. cfr. also T. S. Noggle and J. O. Stiegler, J. Appl. Phys. 30, 1279 (1959).

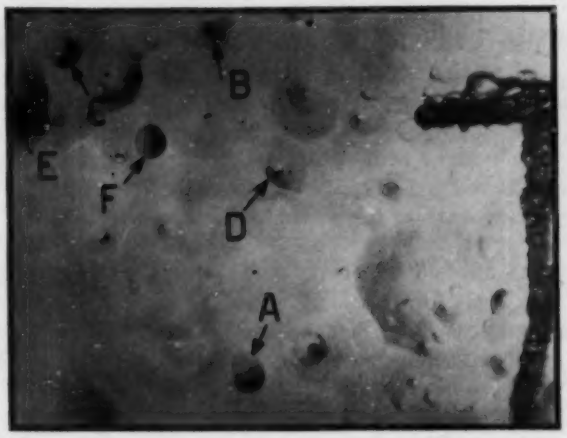

FIG. 3.

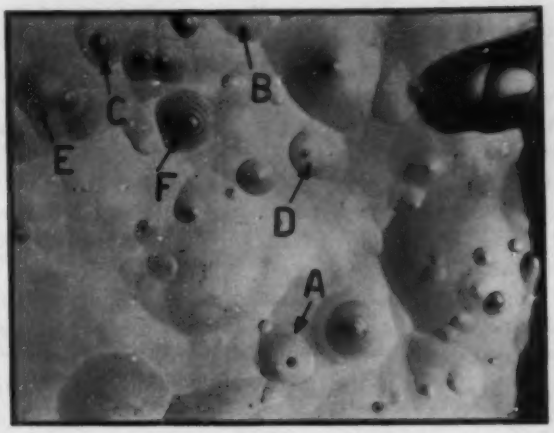

FIG. 6.

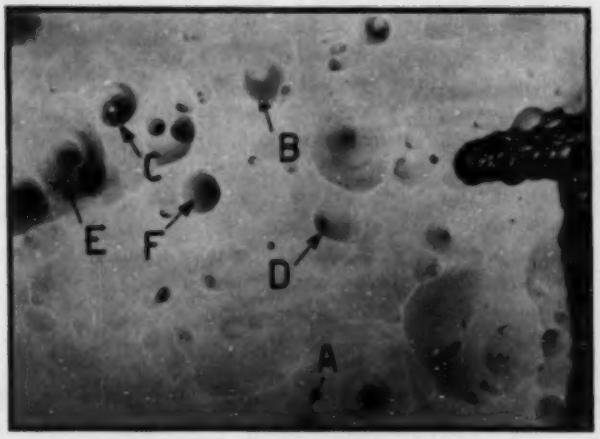

FIG. 4.

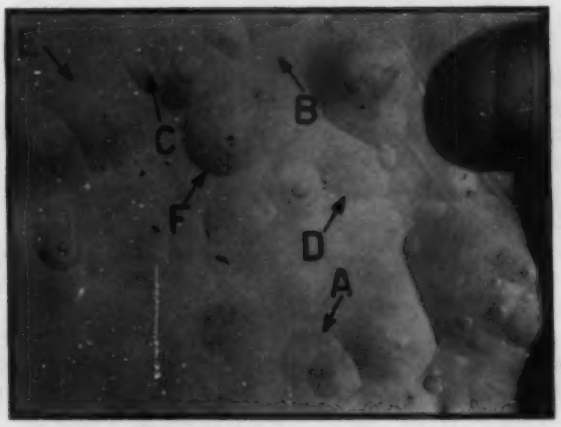

FIG. 7.

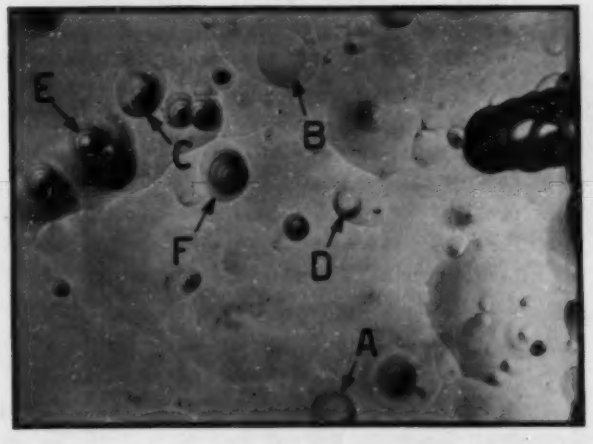

FIG. 5.

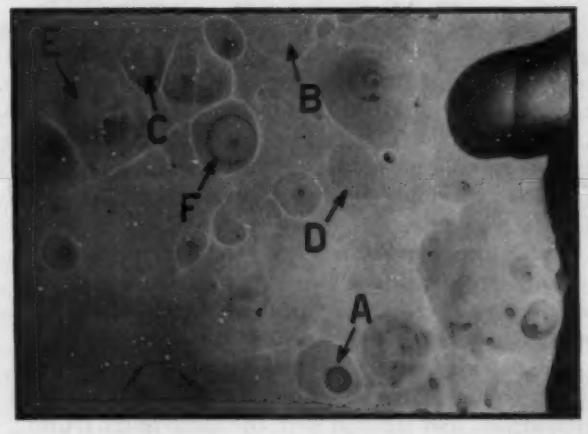

FIG. 8.

FIGS. 3–8. Show how the 1st-order structure originate from etch pits. Arrows point to some selected etch pits, whose behavior is followed during etching. The same letter labels the same etch pit in successive micrographs, taken, respectively, after etching 1, 6, 16, 24, 36, and 60 min from the initial moment. The magnification is 75×.

Figures 3 through 8 show the development of the first-order structure and of the etch pits due to dislocations after successive etching times, respectively 1, 6, 16, 24, 36, and 60 min from the beginning.

With regard to such experiments, some points are to be carefully considered to obtain results well reproducible and free from criticism. As a matter of fact, it has been shown[3] that the etching characteristics of Ge

are much affected by changes in composition of the etchant. By consequence, a strictly standardized procedure must be adopted and a full description of the experimental details is to be given.

A specimen was prepared from a single crystal of intrinsic Ge, cut along (111) with an accuracy better than 2°, polished with Al_2O_3 and treated 20 min at room-temperature with an etcher of HF and HNO_3 (10 p. HF 38% and 1 p. HNO_3 65%), to dissolve the cold worked layer.

This operation is necessary to avoid dealing with a structure which has the great amount of dislocations introduced by cold working. Such a structure is in fact subject to change in the progress of etching, as the cold worked surface layers are successively removed.

The specimen was then etched with freshly prepared CP4, for increasing times, and examined after rinsing in deionized water and methyl alcohol.

The etching is carried on by putting the specimen (etched area about 1 cm^2) in a small polyethylene vessel, with 10 cm^3 of freshly prepared CP4, starting at room-temperature and without stirring. Gas development and temperature rise are sensible. Each attack of the whole series was carried on following strictly the same procedure.

In Fig. 2 the loss of weight of the specimen vs the etching time $[p_0 - p\ (t)]$ and its derivative $|dp/dt|$ are shown.

It is evident that the surface is becoming passivated, since the velocity of the weight loss is sensibly lower after long etching times than it is at the initial moment.

A region of the crystal was marked with a scratch, to identify the position of the etch pits, whose average density turned out to be around $10^4/cm^2$; from the Figs. 3 through 8, it appears clearly that the etching gives origin to hollow conoids with an etch pit at their bottom. During the progress of etching, some pits disappear and some new ones form. When a conoid loses its etch pit, it takes the aspect of a more or less rounded hill, whose contour is still visible after a long etching.

It is to be emphasized that such an effect does not happen simultaneously on all the etch pits present at a certain time—only on a few. This circumstance can be considered sufficient to exlude that changes in composition of the etchant are responsible for the observed behavior of the surface.

The process just described can be followed unambigously, looking at the evolution of the etch pits marked with arrows and labelled with the same letter (A,B,C, D,E,F).

In this way, the network corresponding to the 1st-order structure originates and, after sufficiently long etching times, develops such that its relation to the etch pits is completely lost or masked.

A further confirmation of the above statements, which can be verified by simple inspection, can be found in the fact that the average size of the 1st-order network is very near to the value of the distance between the etch pits.

Finally, an important point which must be stressed (cf. Fig. 2) is that after very long etching periods (60 min or more), the attack performs quite differently than for shorter times. Actually, the reactivity of the material seems to be strongly lowered, so that only a faint 1st-order structure is observed, while new etch pits hardly originate. This circumstance proves that a passivation tendency is present and is likely due to accumulation of impurities on the surface, which must on the other hand be primarily sensible on the centers of attack.

It is extremely probable, therefore, that when a conoid loses its etch pit, it happens sometimes because the dislocation terminated, and other times because it has become passivated. These possibilities may also be inferred from what is now known about the length of dislocations in semiconductor crystals.[4]

The present observations allow no distinction between these two possibilities. We intended to carry on further examinations to clear this point. One simple way would be to alternate CP4 etching with a different etching reagent. However, a more accurate way would be to complement the observations of the surface with infrared observations of the transverse section of decorated crystals. It would also be useful to examine the behavior of highly perfect, nearly etch-pit free specimens.

At any rate, the sole point we wish to emphasize is that, should it be due to the fact that the end of a dislocation has been reached, or that accumulation of surface impurities has rendered the dislocation "passive" toward the etchant, the halos of the "1st-order structure" surely originate on a dislocation etch pit, when the latter has become incapable of further deepening into the crystal. The two possibilities pointed out previously actually appear to be (if not the unique) at least, the most straightforward explanations as to why the etch pits stop growing.

---

[4] W. C. Dash, *Growth and Perfection of Crystals*, (Proceedings, Cooperstown Conference, Wiley & Sons, N. Y. 1958), pp. 361 and ff.

JOURNAL OF APPLIED PHYSICS VOLUME 31, NUMBER 4 APRIL, 1960

Behavior of Individual Dislocations in Strain-Hardened LiF Crystals

J. J. Gilman and W. G. Johnston
General Electric Research Laboratory, Schenectady, New York
(Received December 21, 1959)

The velocities of dislocations have been measured as a function of stress for both undeformed and deformed crystals. The motion is slower at a given stress in a strained crystal, and extra stress is needed to give the same velocity in a strained crystal as in one that is unstrained. It has been found that the extra stress is just equal to the difference in macroscopic flow stresses for the two states of a crystal.

Existing theories of strain-hardening do not correctly predict the behavior of LiF. Barrier-type theories are ruled out because the distance that a dislocation can move in a strain-hardened crystal does not seem to be limited. Theories of Taylor hardening or of cutting of a dislocation forest do not give the observed dependence of strain-hardening on dislocation density. It is observed that the strain-hardening increment is proportional to the dislocation density (also to the plastic strain), and the proportionality constant is 3-5 dynes/disl. The data are consistent with the idea that the hardening is due to defects left in the wakes of moving dislocations. These defects would interfere with the movement of subsequent dislocations on the same or nearby glide planes.

INTRODUCTION

It is usually difficult to study the behavior of individual dislocations in strain-hardened crystals because so many dislocations are present that no one of them can be readily singled out for observation. However, in the case of LiF crystals, a procedure has been devised which allows observations to be made of individual dislocations moving in strain-hardened crystals. By taking advantage of the fact that "aged" dislocations etch differently than "fresh" dislocations,[1] it is possible to strain a crystal, age the dislocations in it, introduce some fresh dislocations, and etch the crystal so that the aged and fresh dislocations can be distinguished from each other. Then stresses can be applied to the crystal in order to produce motion of the fresh dislocations, and their velocities can be measured. The aged dislocations are pinned so they do not move during these later stress applications.

The purpose of this study was to compare dislocation mobilities in undeformed crystals with those in strain-hardened crystals, and to relate these mobilities to the macroscopic flow curves of the crystal. A quantitative correlation was found, demonstrating directly that more stress is needed to move dislocations at a certain velocity in a strained crystal than in an undeformed one. The extra stress is approximately equal to the observed increase in flow stress of a hardened crystal.

Previously,[2] it was observed that both strain-hardening and dislocation density vary linearly with plastic strain. This, together with the observations of dislocation mobilities, is difficult to account for with theories of strain-hardening that are based on the mutual interactions of independent dislocations. Therefore, it is suggested instead that hardening is caused by "debris" left along glide planes behind moving dislocations.

[1] J. J. Gilman and W. G. Johnston, in *Dislocations and Mechanical Properties of Crystals* (John Wiley & Sons, New York, 1957) p. 116.
[2] W. G. Johnston and J. J. Gilman, J. Appl. Phys. **30**, 129 (1959).

EXPERIMENTAL

The crystals that were used in this work were purchased from the Harshaw Chemical Company. Techniques that have been described previously[2] were used to handle and etch specimens that were cleaved from the crystals. Compression tests were made with an Instron testing machine, and a four-point bending jig was used to apply stresses to the crystals for the measurements of dislocation velocities.

In order to study dislocation mobility in a strain-hardened crystal, the crystal was first strained (either in compression, or by bending and straightening). Then the crystal was reloaded in compression and its stress-strain curve was determined. The deformed crystal was next heated to 300°C and cooled at a rate of 5°C/hr, together with a control specimen of undeformed crystal. The aged dislocations in such crystals do not produce sharp etch-pits when etched with a dilute aqueous solution of FeF_3, whereas fresh dislocations form sharply-defined pyramidal etch-pits. Therefore, one can place fresh dislocations in a strained and aged crystal without having them become lost among the numerous dislocations of the background. This is illustrated in Fig. 1 (b). The indistinct pits in the background of this figure were caused by the dislocations put into the crystal by the prestrain treatment. Two pits due to a dislocation that was introduced after the aging treatment stand out quite clearly against the background. They mark successive positions of the dislocation. This makes it easy to measure the distances that dislocations move when a stress is applied to them, and hence to determine their average velocities. Figure 1(a) is presented for comparison; it shows successive positions of a dislocation in an undeformed crystal.

In order to determine the dislocation density in a crystal such as in Fig. 1 (b), the crystal can be etched with an acid etch (1 part HF, 1 part acetic acid, plus about 10^{-5} parts of FeF_3) that clearly reveals *all* the dislocations.[1]

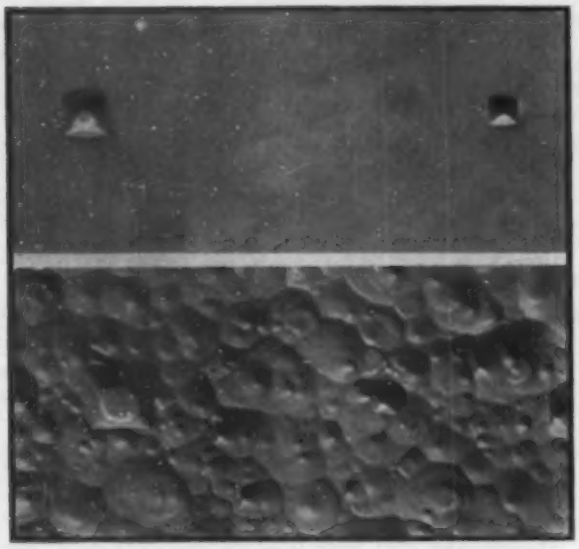

FIG. 1. Screw dislocations moving in LiF crystals. Initial positions are indicated by flat-bottomed pits; positions after stress was applied by pyramidal pits. 600× (a) Undeformed crystal, (b) Strained crystal containing $\sim 5\times10^6$ disl/cm^2.

RESULTS

Observations of dislocation behavior in a strain-hardened and aged crystal indicate that it is qualitatively the same as in undeformed crystals, but that higher stresses are required to produce the various phenomena in the strain-hardened crystal. In both types of crystals, a single dislocation can be moved large distances (across the entire crystal if necessary); and also, a single fresh dislocation can multiply so as to form an entire glide band. Figure 2 shows a glide band that formed when a strain-hardened and aged crystal containing an isolated *fresh* dislocation loop was bent. This same phenomenon has previously been demonstrated in undeformed crystals.[1]

In order to compare dislocation velocities in undeformed and strain-hardened crystals, two sets of crystals were treated as follows:

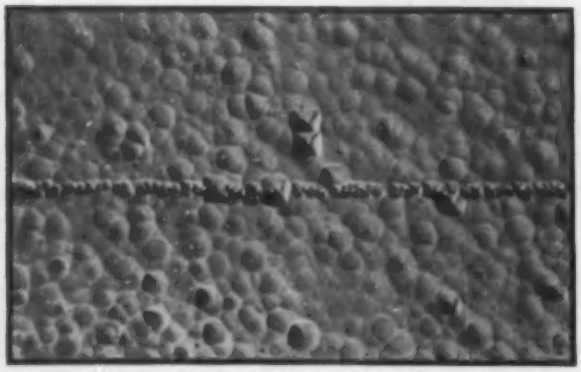

FIG. 2. Glide band that was formed by expanding a single dislocation loop in a strain-hardened and aged crystal. The pair of large pits near the center of the band show the initial position of the loop. ~560×.

Set (1)—as-grown; annealed at 300°C for 1 hr and then cooled at rate of 5°C/hr; a steel ball was rolled over the surface to make dislocation rosettes[1]; chemically polished to dissolve away all but the deepest loops of the rosettes so as to isolate individual dislocation loops; measured screw dislocation velocities as a function of stress.

Set (2)—strained by bending and then straightened to produce uniform dislocation density of about 4.7×10^6 disl/cm;[2] annealed at 300°C for 1 hr and then cooled at rate of 5°C/hr to age the dislocations due to the pre-strain; introduced fresh dislocations by rolling a steel ball over the surface and thereby making rosettes of dislocations; chemically polished to isolate individual fresh dislocations of the rosettes; measured screw dislocation velocities as a function of the applied shear stress.

It may be noted that both sets of crystals were given the annealing treatment. This is important because it is known that heat treatments strongly affect the hardness of LiF.[2]

The dislocation velocity vs stress data were collected by: etching the surfaces of the crystals to locate the initial dislocation positions; applying stresses for several seconds by means of a four-point bending jig, reetching to locate the final dislocation positions; measuring the distances moved by at least 20 dislocations with a microscope.

The velocity measurement data are shown in Fig. 3. For both undeformed and strain-hardened crystals, the

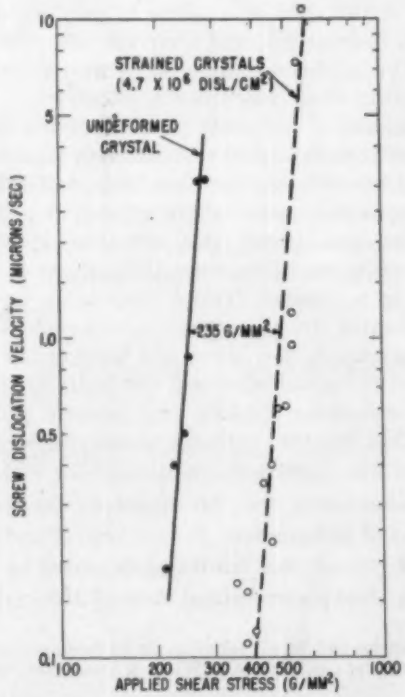

FIG. 3. Effect of strain-hardening on mobility of dislocations in lithium fluoride crystals.

dislocation velocities are very sensitive to applied stress, and to about the same extent, as shown by the parallelism of the two curves. The major effect of the prestrain is thus to shift the velocity curve upwards on the stress axis. The shift varies from 195 to 260 g/mm² along the two parallel lines.

To see how the change of dislocation velocity is reflected in the macroscopic behavior, compression stress-strain curves were made on specimens of the same crystal that was used for the measurements of Fig. 3. Figure 4 shows the results. Curve I is for an as-grown piece of the crystal that was strained enough (~0.01 strain) to produce a dislocation density of about 5 $\times 10^6$ disl/cm². After this strain, the flow stress was 514 g/mm², and this was still the flow stress after the ageing treatment (Curve II). On the other hand, a piece that was not prestrained had a flow stress of about 280 g/mm² after the ageing treatment. The difference between these two stresses is 235 g/mm² which is the average difference in stress level of the two curves in Fig. 3. Thus the effect of prestrain on dislocation velocities is reflected very clearly in a change of macroscopic behavior.

No claim of precision is made in the above comparison of the stress differences, but regradless of the exact numbers that are chosen from the measurements, it seems clear that there is a simple correlation between

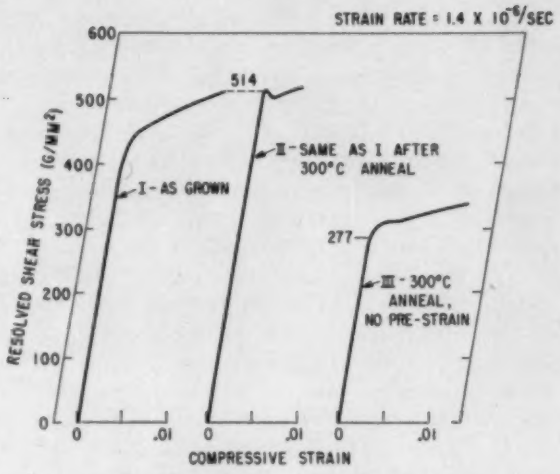

FIG. 4. Compression stress-strain curves.

dislocation behavior in strained LiF crystals and the macroscopic stress-strain curves. Furthermore, this proportionality between macroscopic flow stress and the stress needed to move dislocations is just what was found previously for a variety of other conditions.[2]

Another aspect of strain-hardening that can be observed directly in LiF is the interactions of glide bands. Some photographs of interactions have been shown previously,[2] and others are shown in Fig. 5. In Fig.

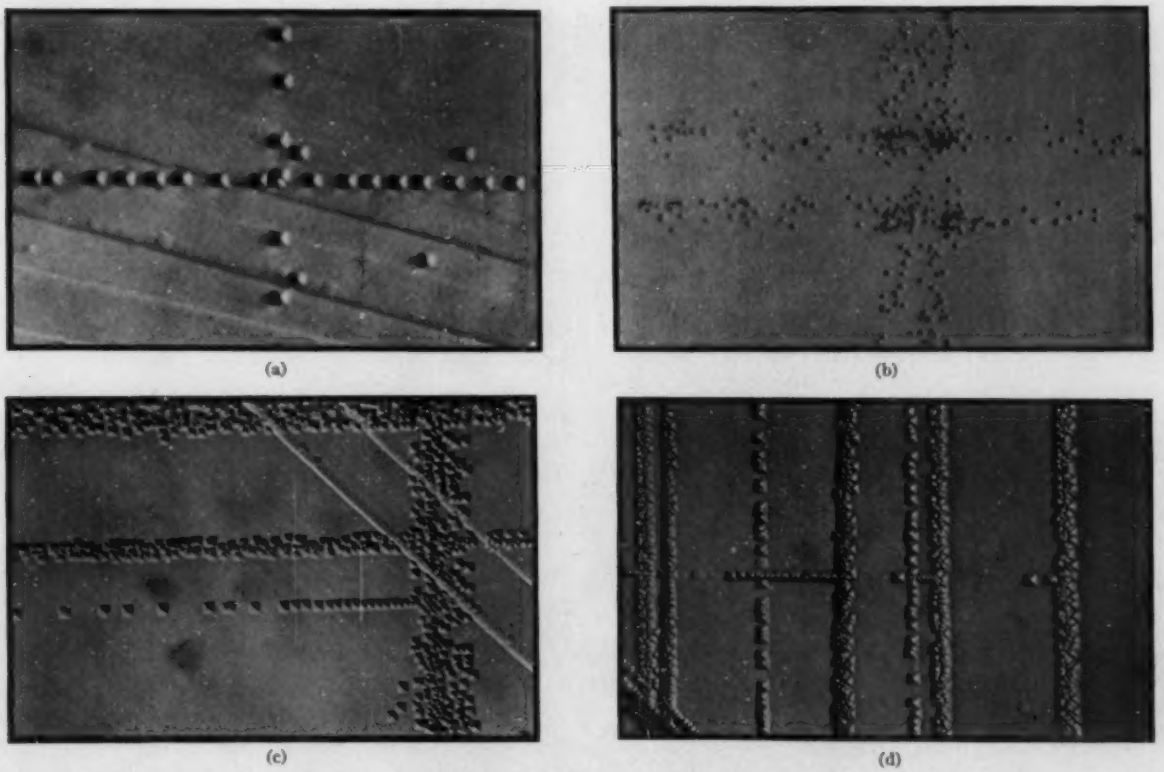

FIG. 5. Interactions of glide bands in LiF crystals. (a) two edge bands that formed a "pair" at their intersection—800×. (b) many "pairs" at the intersections of edge bands—800×. (c) blocking of one edge dislocation band by another—400×. (d) blocking of one screw dislocation band by another—400×.

5 (a) two lightly populated bands of edge dislocations may be seen, and where they cross two of the dislocations have formed a pair. Since the dislocations have glided into a bent crystal from the surface, their signs are known. Their extra half-planes lie in the upper left-hand quadrant of the photograph. Thus the dislocations of the pair have the configuration that would be expected[3] if they were bound together by an interaction of their elastic fields. Figure 5 (b) shows how two edge dislocation bands have interacted at their intersection to form many pairs like the one shown in Fig. 5 (a). Note that this has not caused any substantial impediment to the other dislocations. However, when the density of dislocations at such an intersection becomes somewhat greater, impediment does occur as shown in Fig. 5 (c). In this photograph many blocked edge dislocations may be seen that were moving horizontally from left to right when they encountered the vertical band of edge dislocations. Note that many of the blocked dislocations have become grouped into short vertical walls.

The blocking of screw dislocations by bands of other screw dislocations is illustrated in Fig. 5 (d). It is also commonly observed that edge bands and screw bands block each other. All of these interactions: edge-edge, screw-screw, edge-screw, and screw-edge block approximately equal numbers of dislocations at a given stress level. Thus, there does not seem to be a specific dislocation reaction that makes any one type of band a more effective block than other types. This leads one to believe that specific dislocation reactions do not play an important role in the strain-hardening of LiF (and perhaps other crystals).

The effectiveness of a glide band as a block to other bands increases rapidly with thickness until the band is about 20μ thick, and then remains constant. This demonstrates, directly, the origin of the phenomenon called "overshooting," or latent glide-plane hardening. Once a set of glide planes becomes active and established, it becomes difficult for intersecting planes to become active because they are blocked by the established planes. At the same time the already active planes may be quite hard near their centers, but at their edges they can broaden by extending into virgin crystal. Therefore, in effect, they are not hardened as much as the latent glide-planes, and they continue to operate even though the shear stress on the latent planes may be greater.

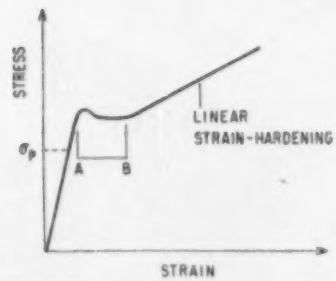

FIG. 6. Schematic stress-strain curve.

[3] W. T. Read, *Dislocations in Crystals* (McGraw-Hill Book Company, New York, 1953), p. 132.

DISCUSSION

A schematic stress-strain curve for LiF is shown in Fig. 6. This is the type of curve that is obtained from a "hard" testing machine when the crosshead moves at constant speed. It consists of a linear elastic portion up to the stress σ_p at which dislocation motion begins (the plastic limit). Next comes a portion of rapidly rising stress until enough dislocation multiplication has occurred to allow rapid plastic flow. The stress must rise until flow in the crystal is rapid enough to match the speed of the testing machine. This is followed by a portion where the stress drops somewhat and then remains relatively constant (region AB). During this stage of the deformation, the glide bands that began to form at σ_p are continually widening, but the dislocation density within them remains constant.[2] At the end of the "easy-glide" region the glide bands have widened sufficiently that they impinge on one another, and the entire surface of the crystal is covered with a uniform density of dislocations. The final portion of the curve is a region of linear strain-hardening (Stage II hardening in the fcc metal nomenclature). No region of "parabolic" hardening is observed; probably because fracture intervenes.

During the AB region it is often observed that many glide band intersections occur and cause some impediment of dislocation motion as shown in Fig. 5. However, this does not seem to be the most important source of strain-hardening because rapid hardening begins after the glide bands are so wide as to cover the total surface area of the crystal. Therefore, a more important source of strain-hardening is the impediment to dislocation motion that is found within glide bands. This is also indicated by the data of Figs. 3 and 4 which show that this type of hardening accounts for virtually the entire amount of hardening.

The data presented in Fig. 7 show that the stress increment, $\Delta\tau$, due to strain-hardening; and the overall dislocation density, ρ, are both proportional to the plastic strain. Therefore:

$$\Delta\tau \propto \rho.$$

The reason why the over-all dislocation density is proportional to strain is that the glide bands grow in thickness in proportion to the strain, ϵ, as was shown previously.[2] Hence, since the dislocation density within the bands remains constant as they grow, $\rho \propto \epsilon$.

The linear relation between stress and dislocation density is also observed during the growth of glide bands. During the widening of bands, the dislocation density within the bands remains roughly constant, and the bands may be said to be "saturated" with

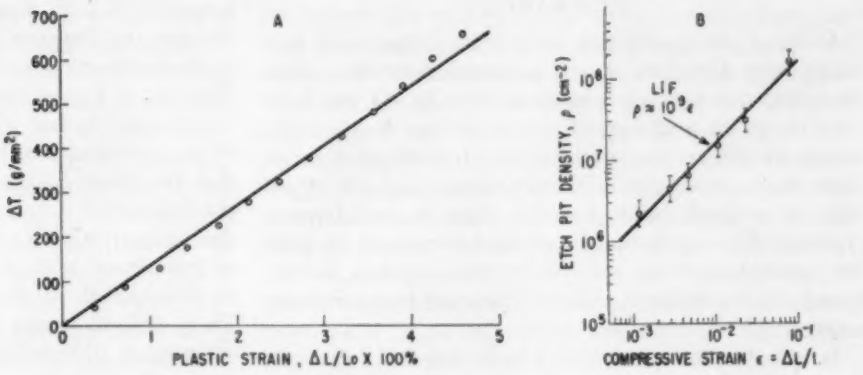

FIG. 7. Linear relations between stress, strain, and dislocation density in strain-hardened lithium fluoride.

dislocations. The saturation density depends on the applied stress as shown in Fig. 8 for crystals of various hardnesses. It may be seen that the relationship is linear. The proportionality constant between stress increment and dislocation density may be calculated in two ways. From Fig. 3 we get $\Delta\tau/\rho \simeq 5$ d/disl, and from Fig. 8, we get $\Delta\tau/\rho = 3.7$ d/disl. Since completely different crystals and measurements are involved, this seems to be consistent agreement.

The present experiments have shown that the strain-hardening in LiF is due to the increased stress required to move a dislocation, and that this increased stress is proportional to the dislocation density. Also, it has been shown that the individual dislocations in a strain-hardened crystal are able to move very large distances if necessary, so the strain-hardening mechanism is not one that strongly limits the distance that a dislocation can move by setting up strong barriers.

Most current discussions of strain-hardening center around the idea that it results from dislocations having to cut through a "forest" of other dislocations which impede their motion.[4] Another type of interaction is that considered by Taylor, where a moving dislocation interacts with the stress fields of other parallel dislocations. In neither case is the stress required to move a dislocation proportional to the dislocation density. In the case of Taylor hardening the stress varies as $\rho^{\frac{1}{2}}$, and in the case of the forest theory the stress may vary in a more complicated manner with dislocation density, but in the simplest case it varies as $\rho^{\frac{1}{2}}$. It therefore appears that current theories of strain-hardening cannot explain the linear variation of flow stress with dislocation density that is observed in LiF.

The fact that strain-hardening in LiF is proportional to ρ, suggests that the hardening may be caused by defects that are left behind by expanding dislocation loops. The number of such defects would be proportional to the area swept out by moving loops, and would therefore be proportional to the plastic strain.

The multiple cross-glide mechanism of dislocation multiplication which has been proposed for LiF, provides a natural way for defects to be left in the wakes of moving dislocations.[5] Double cross-glide forms jogs in moving screw dislocations. These jogs retard the motion of the screw dislocations and cause them to leave trails of defects behind them (direct evidence of these trails has been observed[5]). In the case of very small jogs the trails may consist of point defects left by the moving jog, but in the case of larger jogs the trials probably consist of pairs of dislocations (dislocation dipoles). If these defects act like impurity atoms or small precipitate particles, so the stress increment that they cause is proportional to the density of defects, then they could account for the linear strain-hardening.

There is no reason why this same mechanism of strain-hardening should not operate in other crystals. For example, since strain-hardening in fcc metals is often linear in the plastic strain, the hardening mechanism for them may be quite similar to that in LiF. At the present time, however, direct measurements of dislocation densities as a function of plastic strain do not exist for fcc metals, so this model of strain-hardening cannot be tested for them.

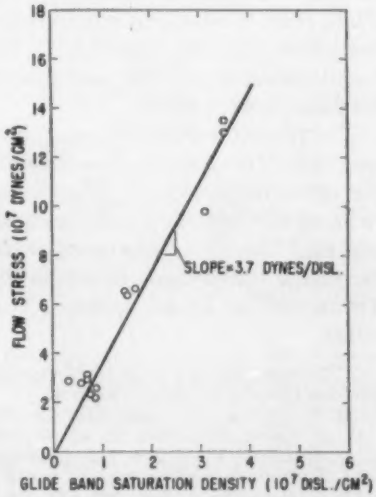

FIG. 8. Effect of flow stress on glide band dislocation densities.

[4] A. Seeger, in *Dislocations and Mechanical Properties of Crystals* (1957), p. 243. (John Wiley & Sons, New York, 1957.)

[5] W. G. Johnston and J. J. Gilman, J. Appl. Phys. **31**, 626 (1960).

SUMMARY

It has been shown that individual dislocations can move long distances in strain-hardened crystals, and that they can multiply and form glide bands, much as they do in an undeformed crystal. It has been established by direct observations that individual dislocations move more slowly in strain-hardened LiF crystals, at a given applied stress, than in undeformed crystals. The stress increment that is needed to give the same dislocation velocity in both crystals, corresponds to the difference that is observed between their macroscopic flow stresses.

It has also been shown that both individual dislocations and glide bands interact and impede one another's motions. However, this is not believed to be the most important source of strain-hardening.

The usual treatments of dislocation interactions leading to strain-hardening do not correctly predict the behavior of LiF. Barrier-type theories are ruled out because the distance that a dislocation can move in a strain-hardened crystal does not seem to be limited. Theories of Taylor hardening or of cutting of a dislocation forest do not give the observed dependence of strain-hardening on dislocation density. It is observed that the strain-hardening increment is proportional to the dislocation density (also to the plastic strain), and the proportionality constant is 3–5 d/disl. The data are consistent with the idea that the hardening is due to defects left in the wakes of moving dislocations. These defects would interfere with the movement of subsequent dislocations on the same or nearby glide planes.

ACKNOWLEDGMENTS

The authors are indebted to Dr. J. D. Livingston and Dr. J. R. Low of the General Electric Research Laboratory for helpful comments on the manuscript.

JOURNAL OF APPLIED PHYSICS VOLUME 31, NUMBER 4 APRIL, 1960

Piezoresistive Effect in p Type PbTe*

LEWIS E. HOLLANDER AND T. J. DIESEL
Lockheed Aircraft Corporation, Missiles and Space Division, Sunnyvale, California

(Received December 7, 1959)

A large positive piezoresistive effect has been observed in p type PbTe. The following room temperature coefficients were determined: $\pi_{\text{Hydrostatic}} = +150 \pm 50$; $\pi_{11} = 80 \pm 30$; $\pi_{l[111]} = +220 \pm 50$, all in 10^{-12}/d. The shear coefficient π_{44} is estimated to be $+255 \times 10^{-12}$ cm²/d. The calculated value of π_{12} was $+35 \pm 40 \times 10^{-12}$ cm²/d. These measurements were performed on single-crystal, p type PbTe with a mobility of approximately 700 cm²/v sec and a carrier concentration of about 10^{18} per cm³. Consideration of the coefficients indicates the major axes of the energy ellipsoids are oriented in the [111] direction, which is in agreement with magnetoresistance measurements.

LEAD telluride, PbTe, is a semiconductor which crystallizes in the cubic NaCl structure.[1] The magnitude of the piezoresistive effect seems to be greater in PbTe than in silicon or any of the other semiconductor materials thus far reported.[2–5] Measurements of the longitudinal, transverse, and hydrostatic piezoresistive coefficients were made.

The piezoresistive coeff, π_{ijkl}, is a fourth-rank tensor quantity. The matrix arrangement of the fourth-rank piezoresistive tensor for cubic crystal symmetry can be reduced to yield the three piezoresistive coeff, π_{11}, π_{12}, and π_{44}.[6] These coefficients are considered positive when increasing compression results in decreasing resistivity. The π coeff is $\Delta\rho/\rho T$, where ρ is resistivity and T is stress.

The majority of the samples were cut from a single p type polycrystalline ingot, which was grown from the melt. Samples $2 \times 2 \times 5$ to 10 mm were cut in the [100] and [111] crystal directions. The crystal axis was determined by inspection of the predominant cleavage planes, which generally form along the planes formed by the cubic crystal axes.[1] These PbTe crystals had a carrier concentration in the order of 10^{18} per cm³, a mobility of 700 cm²/v sec, and a resistivity of 0.01 ohm-cm at 300°K.

All resistivity measurements were made by the four-contact method with indium soldered wires for current leads and 90% platinum, 10% iridium sparked wires for voltage leads. A K-2 potentiometer was used to measure the potential drop across the sample. A force of about 2.5×10^7 d/cm² was applied in compression for measurements of π_{11}, π_{12}, and $\pi_{l[111]}$. Resulting from the structural weakness of the material, tension measurements are difficult. No corrections were made for dimensional changes.[2] This correction is comparatively small and is well within the experimental error.

The hydrostatic coefficient was measured at pressures

* This work was supported by the Lockheed Missiles and Space Division General Research Program.

[1] R. S. Allgaier, Phys. Rev. **112**, 828 (1958).
[2] C. S. Smith, Phys. Rev. **94**, 42–49 (1954).
[3] H. Fritzsche, Phys. Rev. **115**, 336–346 (1959).
[4] L. E. Hollander, Phys. Rev. L. 1, 370–371 (1958).
[5] R. F. Potter Phys. Rev. **108**, 652–658 (1957).
[6] W. P. Mason and R. N. Thurston, J. Acoust. Soc. **29**, 1096–1101 (1959).

up to 3000 psi in a bomb containing mercury to reduce the compressional heating in the pressure-transmitting fluid. The samples were coated with a thin plastic film for electrical insulation. The hydrostatic piezoresistive coefficient was $+150\pm50\times10^{-12}$ cm²/d. The longitudinal coefficient measured along the crystal axis, π_{11}, was $+80\pm30\times10^{-12}$ cm²/d. The longitudinal coefficient measured in the [111] direction, $\pi_{l[111]}$, is $+220\pm50\times10^{-12}$ cm²/d. Measurements of the transverse coefficient, π_{12}, stress along [100] axis and resistivity measured along [010] axis, yielded a value of $+150\pm120\times10^{-12}$ cm²/d. This is inconsistent with the values of π_H and π_{11}. There appears to be, however, a large positive shear coefficient, π_{44}, which may obscure the π_{11} and π_{12} measurements if the sample is slightly misaligned. This is particularly true for the π_{12} coeff where alignment is most difficult; therefore, the measured value of π_{12} is probably erroneously large. During measurements of π_{11}, a minimum was observed along the crystal axis. By applying force at an angle off the axis, larger values are obtained. By considering the relation for the hydrostatic coeff,

$$\pi_{H[100]}=\pi_{H[111]}=\pi_{11}+2\pi_{12},$$

and using the values $\pi_{11}=+80$ and $\pi_H=+150$, a value for $\pi_{12}=+35\times10^{-12}$ cm²/d may be computed. This may be a more realistic value for π_{12}. The shear coefficient π_{44} may be computed from the longitudinal measurement,

$$\pi_{l[111]}=\tfrac{1}{3}\pi_{11}+\tfrac{2}{3}(\pi_{12}+\pi_{44}).$$

If we assume $\pi_{11}=+80$, $\pi_{l[111]}=+220$, and $\pi_{12}=+35$, then π_{44} will equal $+255\times10^{-12}$ cm²/d.

The above-reported values for the piezoresistive coefficients in p type PbTe are only approximations, but they do indicate that there is a very large positive effect exhibited by this material. The electron transfer mechanism of C. Herring[2,7] predicts a large π_{44} contribution and a zero $\frac{1}{2}(\pi_{11}-\pi_{12})$ contribution for the case, where the major axes of the energy ellipsoids are oriented in the [111] direction, and predicts both these shear constants be finite of the same sign and that $\pi_{44}>\frac{1}{2}(\pi_{11}-\pi_{12})$ for the case where the major axes of the energy ellipsoids are oriented in the [110] direction. Within the experimental limits $\frac{1}{2}(\pi_{11}-\pi_{12})$ can equal zero, and π_{44} is very large, both facts suggesting the axes of the energy ellipsoids are oriented in the [111] direction, which is in agreement with magnetoresistance measurements.[1,8] However, $\frac{1}{2}(\pi_{11}-\pi_{12})$ may be finite, leaving the possibility of a [110] orientation. Only the piezoresistive constants were considered, since the elastic moduli for PbTe were unavailable. The use of the elastoresistive coefficients may clarify this problem. It may be concluded from the data that the ellipsoids are not oriented along the crystal axes and are most likely oriented in the [111] direction.

ACKNOWLEDGMENTS

The authors would like to express their appreciation to Mr. Gerald Vick and Dr. Kermit Cuff for helpful discussions, to Mr. Mont Ellett for measurements of the carrier concentration and mobility, to Mr. J. R. Field for mounting the samples, and to Dr. Thomas Perls for his advice and support in this work.

[7] C. Herring and E. Vogt, Phys. Rev. **101**, 944–961 (1956).
[8] H. N. Leifer, R. Ellett, K. F. Cuff, and R. S. Krogstad, Bull. Am. Phys. Soc. Ser. II, **4**, 6, 362 (1959).

JOURNAL OF APPLIED PHYSICS VOLUME 31, NUMBER 4 APRIL, 1960

Molecular Trajectories in Electric Fields and State Selection in a Beam of Sodium Chloride*

M. Peter,† H. G. R. Venkates,‡ and M. W. P. Strandberg
Department of Physics and Research Laboratory of Electronics, Massachusetts Institute of Technology, Cambridge, Massachusetts

(Received November 16, 1959)

A molecular beam of sodium chloride can be partially sorted with respect to the rotational levels of the molecule when it is passed through an inhomogeneous electric field. The possibility of state selection of the beam in one of the lower rotational states of the molecule ($J=2$; $|M|=0, 1, 2$) has been investigated by studying the molecular trajectories for the rotational states $J=1$; $|M|=1, 0$ and $J=2$; $|M|=2, 1, 0$. A typical calculation for a state selector is given.

I. INTRODUCTION

THE quadrupole structure of magnetic poles for focusing atomic beams has been investigated by Bennewitz and Paul.[1] The state-selecting properties of an inhomogeneous electric field (that is, the transparency of the field for a given quantum state) produced by a similar structure of electrodes was demonstrated

* This work was supported in part by the U. S. Army (Signal Corps), the U. S. Air Force (Office of Scientific Research, Air Research and Development Command), and the U. S. Navy (Office of Naval Research).

† Present address: Bell Telephone Laboratories, Inc., Murray Hill, New Jersey.
‡ Present address: Indian Institute of Technology, Kharagpur, India.
[1] H. G. Bennewitz and W. Paul, Z. Physik **139**, 489 (1954).

by Gordon, Zeiger, and Townes[2] in the device called the maser, which employs a beam of ammonia molecules. By state selection of a molecular beam we mean that the molecules are sorted with respect to their quantum states, so that a nearly collimated or convergent beam of molecules that are predominantly in a single quantum state can be obtained. If the state-selected beam is in a quantum state higher than its lowest energy state, it can be induced to make a transition to a state of lower energy by the rf electric field in a microwave cavity tuned to the transition frequency. An emission line of extremely narrow spectral width (a few kilocycles) results because the Doppler effect is negligible, and collisions between molecules in the cavity are rare. Such an arrangement is very desirable for studying the hyperfine structure of spectral lines. It also serves as a frequency standard of high precision. The study of molecular trajectories is important for investigating the possibility of obtaining a nearly collimated state-selected beam. The investigation of trajectories depends on an understanding of the Stark effect of the molecule for a wide range of electric fields. A typical calculation of sodium-chloride trajectories in an inhomogeneous electric field arising from a lattice structure of charged rods is outlined in this paper. Our investigation shows the possibility of obtaining a molecular beam with a greater number of molecules in the state $J=2$, $|M|=0, 1, 2$ than in the state $J=1$, $|M|=1, 0$. The rotational energy levels for a given vibrational state are

$$W_R=BhJ(J+1),$$

($B=6.54\times10^9$ cycles). The frequency for the transition $J=2\rightarrow J=1$ for sodium chloride lies in the K-band of microwave frequencies ($\nu=2.61\times10^{10}$ cycles). Furthermore, the rotational levels are split into hyperfine levels because of nuclear quadrupole and magnetic interactions. If we assume that the quadrupole interactions are the most important ones for the molecule we are studying, we obtain the energy levels from certain determinantal equations. The detailed spectral scheme has been presented elsewhere.[3]

II. STATE SELECTOR

Figure 1 shows the state-selecting structure[3] of our apparatus. Alternate rods, arranged in a periodic lattice, are charged to equal positive and negative potentials. There are four columns of rods, each column being considered virtually infinite in length (from mirror-image theory) because of the metal surfaces A, B that are parallel to the rows. The distance between successive rods is normalized to π and written

$$x'\pi/L=x; \quad y'\pi/L=y,$$

where L is the distance between the successive rods, and x', y' are the position coordinates measured from any given column. The potential of each column is given by

$$\phi_i=\phi_0\log\frac{\cosh x_i+\cos y_i}{\cosh x_i-\cos y_i}. \tag{1}$$

The total potential at any point arising from the four columns is given by

$$\phi=\phi_1+\phi_2+\phi_3+\phi_4.$$

The equipotential surfaces of the rods are approximately cylindrical. The required derivatives are calculated to be

$$\frac{\partial\phi}{\partial x}=-2A_1\cos y; \quad \frac{\partial\phi}{\partial y}=-2B_1\sin y$$

$$\frac{\partial^2\phi}{\partial x^2}=-\frac{\partial^2\phi}{\partial y^2}=2D_2\cos y-2B_2\cos y\sin^2 y \tag{2}$$

$$\frac{\partial^2\phi}{\partial x\partial y}=2C_2\sin y+2A_2\sin y\cos^2 y.$$

The magnitude of the total field at any point is given by

$$|F|=2(A_1^2\cos^2 y+B_1^2\sin^2 y)^{\frac{1}{2}}. \tag{3}$$

The reduced field defined by $\lambda=F\mu/hB$, where μ is the electric dipole moment, is given by

$$|\lambda|=(\pi/L)(\mu/hB)(A_1^2\sin^2\Delta y+B_1^2\cos^2\Delta y)^{\frac{1}{2}}$$

with the x axis shifted to $y=\pi/2$. The functions A, B, C, D in (2) are given by

$$A_1=\sum\phi_0\frac{\sinh x}{\cosh^2 x-\sin^2\Delta y};$$

$$A_2=\sum\phi_0\frac{\sinh x}{(\cosh^2 x-\sin^2\Delta y)^2};$$

$$B_1=\sum\phi_0\frac{\cosh x}{\cosh^2 x-\sin^2\Delta y}; \tag{4}$$

$$B_2=\sum\phi_0\frac{\cosh x}{(\cosh^2 x-\sin^2\Delta y)^2};$$

$$C_2=\sum\phi_0\frac{\sinh x\cosh^2 x}{(\cosh^2 x-\sin^2\Delta y)^2};$$

$$D_2=\sum\phi_0\frac{\cosh x\sinh^2 x}{(\cosh^2 x-\sin^2\Delta y)^2}.$$

A molecular beam effuses from the source in the direction of the arrows in Fig. 1, the cross-section width of the beam being $\pi/2$. At the other end of the structure we have an aperture of width a. We are interested in the transition $J=2\rightarrow J=1$. We shall find that our struc-

[2] J. P. Gordon, H. J. Zeiger, and C. H. Townes, Phys. Rev. **99**, 264 (1955).

[3] M. Peter and M. W. P. Strandberg, "Theoretical and experimental study of molecular-beam microwave spectroscopy," Technical Report 336, Research Laboratory of Electronics, Massachusetts Institute of Technology, August 26, 1957.

ture nearly collimates the molecules in the states $J=2$, $|M|=2$; $J=2$, $|M|=1$; $J=2$, $|M|=0$, and makes those in states $J=1$, $|M|=1, 0$ divergent for the fields used in the state selector. The problem now is to adjust L, ϕ_0, and a, so that the flux in the $J=2$ state will exceed that in the $J=1$ state by a maximum amount.

III. STARK EFFECT

In order to plot the acceleration field, we need to find the Stark energy E as a function of the electrostatic field F. The ordinary perturbation methods for the calculation of the energy E fail because of the large electric fields involved. Hence a complete calculation of the Stark effect must be carried out. This problem has been investigated by Peter and Strandberg.[4] The Stark energy is given by the following expansion in terms of the field:

$$\begin{aligned} W_{J,M} = &-\lambda^1+\sqrt{2}[2J-|M|+1]\lambda^{\frac{1}{2}} \\ &+\tfrac{1}{4}[M^2+2|M|J-2J^2+|M|-2J-2]\lambda^0 \\ &+(\sqrt{2}/64)[-4|M^3|+6M^2J+6|M|J^2 \\ &-4J^3+3M^2+6|M|J-6J^2 \\ &+3|M|-6J-2]\lambda^{-1}+\cdots, \quad (5) \end{aligned}$$

where $W=E/hB$.

Curves showing the reduced Stark energy W as a function of the reduced field λ are shown in Fig. 2. These curves are applicable to the whole class of diatomic molecules with electric dipole moments. Note that for each quantum state there is a critical field for which the force on the molecules vanishes. Below these critical fields, the forces on the molecules in the corresponding quantum states act in the direction of the beam axis; above these fields, the forces act away from the beam axis. As far as the lower rotational states are concerned, the critical fields are clearly resolved. This resolution of critical fields is the basis for the expectation that state selection is feasible, and hence that by choosing the focusing fields properly, we may be able to obtain a state-selected beam. The critical fields for the various quantum states are:

$$\begin{aligned} J=2 \quad &|M|=0, \quad \lambda_c=14 \\ &|M|=1, \quad \lambda_c=6.15 \\ &|M|=2, \quad \lambda_c<6 \end{aligned}$$

$$\begin{aligned} J=1 \quad &|M|=0, \quad \lambda_c=2.64 \\ &|M|=1, \quad \lambda_c<2. \end{aligned}$$

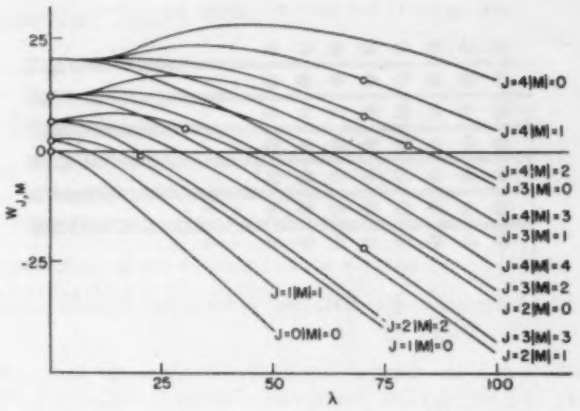

FIG. 2. Reduced Stark energy vs reduced field.

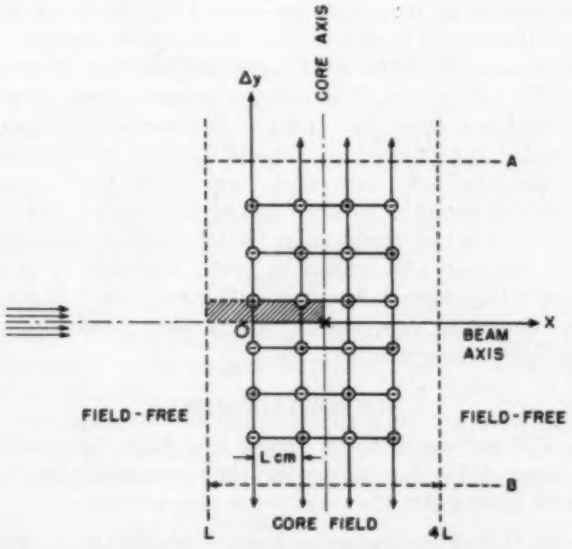

FIG. 1. Structure of a state selector used in a molecular-beam experiment.

[4] M. Peter and M. W. P. Strandberg, J. Chem. Phys. **26**, 1657 (1957).

IV. ACCELERATIONS AND TRAJECTORIES

The forces $P_{x'}$, $P_{y'}$ acting on the molecule at any point x', y' are given by

$$P_{x'}=-\frac{\partial E}{\partial\lambda}\frac{1}{2\lambda}\left(2\lambda_{x'}\frac{\partial\lambda_{x'}}{\partial x'}+2\lambda_{y'}\frac{\partial\lambda_{y'}}{\partial x'}\right)$$

$$P_{y'}=-\frac{\partial E}{\partial\lambda}\frac{1}{2\lambda}\left(2\lambda_{x'}\frac{\partial\lambda_{x'}}{\partial y'}+2\lambda_{y'}\frac{\partial\lambda_{y'}}{\partial y'}\right).$$

If we introduce the reduced energy W, then we have the following expressions for the accelerations:

$$\begin{aligned} a_{x'}=&\left(\frac{\pi}{L}\right)^3\frac{\mu^2}{hB}\frac{1}{m}\frac{1}{|\lambda|}\frac{dW}{d|\lambda|}\sin^2 2\Delta y(B_1A_2-A_1B_2+B_1C_2 \\ &\times\operatorname{cosec}^2\Delta y+A_1D_2\sec^2\Delta y) \\ a_{y'}=&-\left(\frac{\pi}{L}\right)^3\frac{\mu^2}{hB}\frac{1}{m}\frac{1}{|\lambda|}\frac{dW}{d|\lambda|} \\ &\times 2\sin^2\Delta y(A_1C_2-B_1D_2+A_1A_2 \\ &\times\sec^2\Delta y+B_1B_2\cos^2\Delta y), \end{aligned} \quad (6)$$

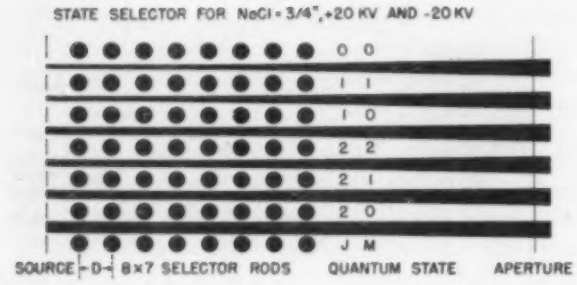

FIG. 3. Performance of state selector for sodium-chloride beam.

where m is the mass of the molecule. Since the functions A_1, A_2, etc. do not change sign when the sign of Δy is changed, the acceleration vector is symmetrical about the beam axis. Hence the trajectories of two molecules in the same quantum state, which start from symmetrical positions about the beam axis and have the same initial velocities along x and y, are symmetrical about the beam axis. Also, at points x, Δy and $3\pi-x$, Δy that are equidistant from the core axis, a_x has opposite signs, but not a_y. Hence the acceleration vector is symmetrical about the core axis. In view of this symmetry, and also because the field falls off exponentially on both sides of the field core, we need only map one quadrant (shaded region in Fig. 1) for the accelerations between $x=-\pi$ and $x=5\pi$. In view of the reversing of the sign of a_x at two points equidistant from the core axis, and because $\sin^2\Delta y$ varies within narrow limits, additional velocity acquired along x from acceleration in the field can be averaged to zero, and the x velocity can be treated as essentially constant and equal to the initial velocity of projection into the field core.

If we let the subscript i refer to initial states, then the new positions and velocities are found to be

$$x=x_i+\frac{\pi}{L}\delta t u_i^x+\frac{\pi}{2L}a_i^x(\delta t)^2;$$

$$\Delta y=\Delta y_i+\frac{\pi}{L}\delta t u_i^y+\frac{\pi}{2L}a_i^y(\delta t)^2;$$

and

$$u_x=u_i^x+a_i^x\delta t;$$
$$u_y=u_i^y+a_i^y\delta t.$$

The most probable velocity at $T=800°$K for NaCl is approximately 5×10^4 cm/sec. If the length of the field core is 10 cm, the time of flight is 2×10^{-4} sec. If we divide this length into 20 steps, the time of flight in each step is 10^{-5} second. With the choice of these short intervals of time, we have for $L=1.905$ cm,

$$x=x_i+1.649\times10^{-5}u_i^x+0.8245\times10^{-10}a_i^x;$$
$$\Delta y=\Delta y_i+1.649\times10^{-5}k_iu_i^x+0.8245\times10^{-10}a_i^y;$$

and

$$u_x=u_i^x+10^{-5}a_i^x;$$
$$u_y=k_iu_i^x+10^{-5}a_i^y,$$

where

$$\tan\theta_i=u_i^y/u_i^x=k_i. \tag{7}$$

If we take k_i at the left fringe to be $1/10, 1/20, \cdots$, and the three positions at the left fringe $x=-\pi$, $\Delta y=0, 25°$, $45°$, the trajectories can be calculated for the various quantum states. The values of the quantities involved in the calculations are:

$$m=58.85\times1.67\times10^{-24}\text{ g}$$
$$B=6.536\times10^9\text{ cps}$$
$$\mu=8.5\times10^{-18}\text{ esu}$$
$$L=1.905\text{ cm}$$
$$\phi_0=80\text{ esu}.$$

Figure 3 shows the effective areas of the source on the left (for the quantum states indicated), from which the molecules emerge and then pass through the aperture on the right after they have traversed the electrostatic field of the state selector. The effective area of the source for each quantum state is a measure of the transparency of the state selector for an aperture of given dimension.

V. CONCLUSION

If we assume that the molecular flux associated with the individual quantum states is measured by the effective area of the source, we find that the beam is state-selected with respect to state $J=2$, $|M|=0, 1$. If the beam is passed through a microwave cavity tuned to the resonant frequency of the $J=2\rightarrow J=1$ position, power is emitted by the beam when it makes an induced transition in the cavity to state $J=1$. However, the emitted power is proportional to the excess number of molecules in state $J=2$ over the number in state $J=1$, $|M|=1, 0$. (The other quantum states are not considered, since they are not in resonance.) Experiments,[3] in which hot sources and the state selector that is described here were used, have shown that a more effective potential barrier (that is, with respect to state $J=2$) than that produced by the lattice structure would be necessary for sufficient state selection to give perceptible signals. A multipole focuser of the type used in ammonia experiments[5] offers the possibility of sufficient state selection.

ACKNOWLEDGMENT

The authors wish to thank the Joint Computing Group, MIT, for calculating the acceleration by the field, from which the trajectories were plotted.

[5] F. O. Vonbun, Engineering Report NRE-1203, U. S. Army Signal Engineering Laboratories, Fort Monmouth, New Jersey, April 1957.

Polyhedral Holes in Evaporated AuCu Films

VICTOR A. PHILLIPS
General Electric Research Laboratory, Schenectady, New York
(Received September 23, 1959)

A transmission electron microscope study of ordered (001) films of Au-50 at. % Cu made by evaporation in vacuo onto cleaved rocksalt at 400°C showed (a) the presence of a 6 sided roughly hexagonal single crystal area in the film about 2 μ across apparently surrounded by polycrystals, the 3 pairs of sides being nearly parallel to $[\bar{1}00]$, $[\bar{1}20]$, and $[\bar{1}\bar{1}0]$, respectively, (b) streaks within this crystal interpretable as twins on (111), (c) holes through the film tended within this crystal to be polyhedral, developing sides parallel to ⟨100⟩ and ⟨110⟩. The latter observation indicates that the effective supersaturation during evaporation is relatively low.

I. INTRODUCTION

ALTHOUGH polyhedral cavities have been reported previously in sintered rocksalt by Muller,[1] and in lithium fluoride crystals annealed after neutron irradiation by Gilman and Johnston,[2] they do not appear to have been observed in evaporated films. This report describes the occurrence of somewhat analogous faceted holes in an oriented evaporated film of AuCu within a single polyhedral crystal.

II. EXPERIMENTAL

The films, which were about 300 A in thickness, were made by direct evaporation of an accurately synthesized copper-50 at. % gold alloy onto a freshly cleaved rocksalt surface 5½ in. distant. A thermo-couple inserted into a hole in the rocksalt crystal enabled it to be kept at 400°C during evaporation. The hotplate was then switched off and the vacuum maintained until the film and substrate reached room temperature which took 15 to 20 min. The films were floated off on water and collected on 200-mesh grids for examination in a Siemens Elmiskop I microscope operated at 100 kv.

III. RESULTS AND DISCUSSION

Examination by means of selected area electron diffraction showed that the greater part of the area of the films consisted of single crystal with (001) parallel to the surface; however, some areas were composed of randomly oriented polycrystals. Analysis of transmission electron diffraction patterns from oriented regions showed that the films were ordered and interpretable in terms of a mixture of AuCu I and AuCu II. The features of such patterns have been described in detail previously by Ogawa and Watanabe[3,4] and by Glossop and Pashley.[5]

Transmission electron micrographs occasionally showed geometrically shaped areas some 0.1–3 μ in maximum dimension such as rectangles, parallelograms, and hexagons, although the latter were often incomplete. Such areas do not appear to have been reported previously. Figure 1 is an example of a hexagon which had a diameter of about 2½ μ. Selected area diffraction on a region of 2 μ diam inside the hexagon, and inspection of patterns from similar areas just outside the hexagon indicated that it was a single (001) crystal surrounded by randomly oriented material. Analysis of the pattern showed that the hexagon edges (Fig. 1) were oriented as follows; *CB* and *EF* were within 8° of $[\bar{1}00]$, *BA* and *DE* were within 3° of $[\bar{1}20]$, while *FA* and *DC* fell between $[\bar{1}\bar{1}0]$ and $[\bar{2}\bar{3}0]$, *FA* being 7° from $[\bar{1}\bar{1}0]$ and 4° from $[\bar{2}\bar{3}0]$, *CD* 10° from $[\bar{1}\bar{1}0]$ and 1° from $[\bar{2}\bar{3}0]$. These deviations are probably within the experimental errors involved in measuring the direction of the edges from Fig. 1 due mainly to slight curvature in the edges. These observations do not appear compatible with any description of the six side planes of the hexagonal area in terms of a common low indices type plane.

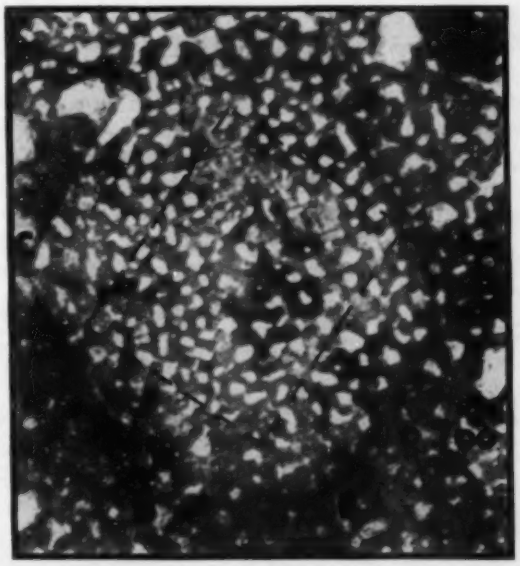

FIG. 1. AuCu slowly cooled from 400°C on cleaved rocksalt. *ABCDEF* is a parallel oriented crystal. Note streaks *GH* and *GI*. 14 000×.

[1] H. G. Muller, Z. Physik **96**, 307 (1935).
[2] J. J. Gilman and W. G. Johnston, J. Appl. Phys. **29**, 877 (1958).
[3] S. Ogawa and D. Watanabe, Acta Cryst. **7**, 377 (1954).
[4] S. Ogawa and D. Wantanabe, J. Phys. Soc. Japan **9**, 475 (1954).
[5] Ann B. Glossop and D. W. Pashley, Proc. Roy. Soc. (London) **A250**, 132 (1959).

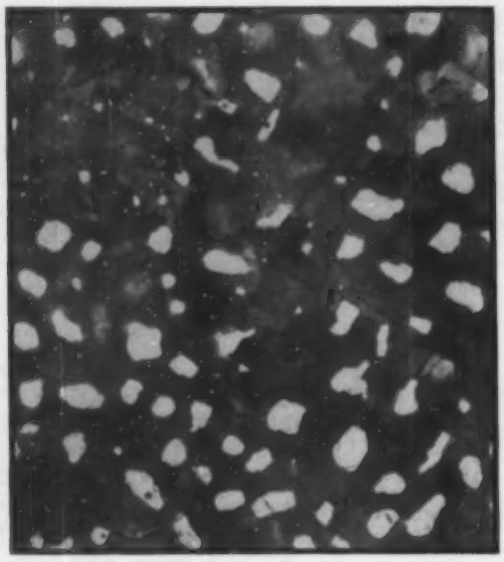

FIG. 2. Higher magnification view of area enclosed by dashes in Fig. 1. Note matrix streaks, for example, *GH* and *GI*. The holes in the foil tend to be polyhedral in form. 80 000×.

A further feature of Fig. 1, seen more clearly at higher power in Fig. 2 (taken from region enclosed by dashes in Fig. 1), is the presence of two sets of streaks at right angles, for example, *GH* and *IG*, approximately parallel and perpendicular, respectively, to the hexagon sides *AF* and *CD*. *GH* and *IG* have directions within 3° of $[\bar{1}10]$ and $[1\bar{1}0]$, respectively, which is consistent with their being growth twins on {111} which have been observed previously in silver, gold, copper, nickel, and palladium films made by a similar method (Ogawa et al.[6]). The angle between (001), which is the plane of the foil, and the appropriate {111} twinning plane is 55°. The measured projected width of the streaks is 160–250 A which gives a reasonable calculated film thickness of 225–350 A.

Figure 2 shows the typical appearance of holes through the 'hexagonal' crystal. It will be seen that many of the holes show a marked tendency to be polyhedral, whereas the holes in the randomly oriented material surrounding the hexagon do not. The holes in fact tend to develop 8 side faces intersecting the 100 plane of the crystal in 4 characteristic directions. Analyses made on a number of the holes in Fig. 2 showed that these directions were in general either within 11° of ⟨100⟩ or within 5° of ⟨110⟩ directions. Light borders seen inside the holes shown in Fig. 2 are probably caused by deposits building up during examination in the microscope.

Although it would be of great interest to study the effect of annealing on these phenomena, this was not possible since the behavior of such films on annealing off the substrate is somewhat uncontrollable and as reported previously on gold films (Pashley[7]) they tend to fragment and agglomerate in the corners of the supporting grid.

To sum up, the observations are consistent with the idea that the hexagonal area is a single crystal with sides parallel to $[\bar{1}00]$, $[\bar{1}20]$ or between $[\bar{2}30]$ and $[\bar{1}10]$, containing twins on {111}, and containing holes with sides parallel to ⟨100⟩ and ⟨110⟩.

It is believed that the holes get smaller as the film is made thicker by further evaporation, that is, that the film grows laterally into the holes as well as growing thicker. The facets on the holes are particularly interesting in that they indicate that at least at this stage in the growth of the film the atoms know that they can save energy by forming crystalline faces of low indices, that is, the facets indicate that the supersaturation is relatively low. Unlike processes for the growth of whiskers having crystalline faces from vapor (Sears[8]), where a very small supersaturation is necessary, in vacuum evaporation, it is normally expected that one has a very high supersaturation since atoms from a very hot source are being condensed on a relatively cool surface. The apparent low supersaturation suggests that the evaporated atoms on hitting the rocksalt dissipate their high kinetic energy as heat locally raising the effective surface temperature of the rocksalt higher than the measured bulk temperature (400°C in the present experiments) so that the supersaturation is lowered.

ACKNOWLEDGMENTS

I am indebted to Miss E. Alessandrini for preparing the evaporated films, to Mr. J. A. Hugo for general assistance and to my colleagues, Dr. G. Sears and Dr. J. B. Newkirk for helpful discussions.

[6] S. Ogawa, D. Watanabe, and F. E. Fujita, J. Phys. Soc. Japan **10**, 429 (1955).

[7] D. W. Pashley, Phil. Mag. **4**, 324 (1959).

[8] G. W. Sears, Acta. Met. **1**, 457 (1953).

JOURNAL OF APPLIED PHYSICS VOLUME 31, NUMBER 4 APRIL, 1960

Analysis of Composite X-Ray Diffraction Profiles*

J. J. SLADE, JR.,† AND L. F. NANNI‡
Bureau of Engineering Research, College of Engineering, Rutgers, The State University, New Brunswick, New Jersey
(Received September 17, 1959)

The irregular line profiles associated with crystals that have a random structure which is coarse relative to the irradiated area are regarded as the result of the composition of a characteristic distribution and a set of broadening and translating processes.

The inversion of this composition is expressed operationally. A differential operator associated with the transform of the intrinsic distribution is introduced. This operator reduces the line profile to the set of broadening and translating elements. The operations are such as may be performed by an analogue computer. Preliminary experiments show that it may be possible to obtain the desired resolution. The effects of "noise" and distortion are investigated.

INTRODUCTION

THE line profile obtained from an (*hkl*) reflection with a double-crystal diffractometer is the resultant of the compositions of various distributions, of which the following may be explicitly recognized:

(1) the intrinsic distribution of x-ray intensities ("rocking curves") associated with the two crystals of the diffractometer in their most perfect state;

(2) the distribution of wavelengths of the irradiating beam;

(3) the distribution due to scattering associated with lattice errors;

(4) the distribution of orientation of the fine substructure of the crystal;

(5) the distribution of the orientation of coarse substructure.

These distributions combine linearly to yield the observed rocking curves. The deduction of the third requires special and complex analysis,[1] while combinations with the second require special treatment. The fourth and fifth are not essentially distinct categories; one is separated from the other principally through the magnitude of the cross-sectional area of the irradiating beam. A single crystal, in which the point and line defects are distributed with statistical uniformity, or in which the scattering effects of these are masked by those of the statistically uniform mosaic-like structure, will be said to have fine substructure for a given beam, if the shape of the rocking curve is sufficiently independent of the location of the irradiated area. Otherwise, the substructure will be said to be coarse. The rocking curves from crystals with sufficiently coarse substructure will result in a composite rocking curve exhibiting multiple peaks.

It is our purpose in this paper to analyze the composite x-ray profile of the rocking curve so as to reconstruct or "unfold" the distribution of the substructure from the x-ray data. Although the method presented in this paper has been specifically applied to the analysis of the distribution of substructure of metal specimens, it may be applied to the study of composite x-ray profiles resulting from a variety of physical processes or instrumental aberrations.

We shall now define the following concepts. A distribution obtained conceptually by the composition of only the first four distributions listed above will be called a characteristic distribution. Each reflecting subregion may have its own characteristic distribution. These distributions are characteristic with respect both to the substructure and the experimental complex. The observed distribution of x-ray intensities will be considered as the resultant of a characteristic distribution and a distribution of reflecting sub-regions each with its own areal distribution of misalignments about an average tilt.

Figure 1 is a schematic representation of the irradiated area of the crystal surface, which we suppose to coincide in the mean with an (*hkl*) plane. The coarse substructure is represented by the three regions A, B, C, each with its own fine substructure and separated from its neighbors by low-angle boundaries. The points A,

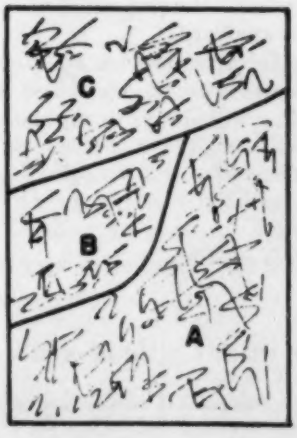

FIG. 1. Coarse substructure irradiated by beam.

* This research was supported by the U. S. Air Force through the Air Force Office of Scientific Research and by the U. S. Atomic Energy Commission.

† Professor of Engineering Mechanics and Research Director, Bureau of Engineering Research.

‡ Associate Professor of Engineering Mechanics, College of Engineering, Rutgers, The State University, New Brunswick, New Jersey.

[1] J. J. Slade, Jr., "Early detection of microcracks," Progress Rept. No. 3, AF49(638)17 (July 30, 1957).

B, C in Fig. 2(a) are the piercing points on the surface of a sphere of lines drawn through its center parallel to the normals of the reflecting planes A, B, C, Fig. 1. The contours around these points represent the intensities of reflection of x-rays. RR' is the trace on the sphere of the cone, the elements of which bisect the angles between the mid-line of the direct beam and the elements of the mid-cone of the scattered beam. As the crystal is turned, the intensity configuration advances as shown by the arrow.

For any setting of the crystal the reflected light is the integral of the product of the intensities in the arc RR' and the intensity distribution on the sphere that coincides with it.[2] This gives rise to the ordinate R of the observed rocking curve, Fig. 2(b). In the proper scale this is the marginal intensity distribution, at any rate when the reflecting power is uniform in RR'. In this figure the rocking curve is also shown as the resultant of the superposition of the three overlapping, weighted characteristic distributions for the regions A, B, C. It will be noted that the angular separation ξ_1 of A, B, is the component in the direction of rotation of the true separation ξ. Only the components of the angular misalignments in the direction of rotation of the crystal will be observed, of course.

Given the composite curve, Fig. 2(b), our problem is to resolve it into its component parts. The complete solution of this problem would include the determination of the orientation components of the areas A, B, C, the magnitude of these areas, and the parameters of their characteristic rocking curves. This paper presents a promising start in the solution of this problem

LINEAR COMPOSITION AND RESOLUTION OF DISTRIBUTIONS

The observed distributions of reflected x-ray intensities are taken as the raw materials of our investigation. These distributions, as well as their resolutes, are necessarily positive functions, though it will turn out that certain derived distributions may have negative ranges. The Fourier transforms of these distributions will be considered here merely as auxiliary functionals through the properties of which the distributions may be analyzed.

In what follows all intensity distributions will be represented by lower case letters, such as f, g, h, and they will always be normalized to unity,

$$\int_{-\infty}^{\infty} f(x)dx=1. \tag{1}$$

The corresponding rocking curves will then be given by

$$y=If(x), \tag{2}$$

in which I is the integrated intensity of the radiation.

[2] This point of view is developed in detail by J. J. Slade and S. Weissmann, J. Appl. Phys. **23**, 323 (1952).

The composition of two distributions, that is,

$$h(x)=\int_{-\infty}^{\infty} f(x-\lambda)g(\lambda)d\lambda=\int_{-\infty}^{\infty} f(\lambda)g(x-\lambda)d\lambda, \tag{3}$$

will be represented by the abbreviated notation,

$$h=f*g=g*f. \tag{4}$$

The Fourier transform of a distribution will be represented by the corresponding capital letter. The transform and its inverse will be taken in the unsymmetrical form,

$$F(u)=\int_{-\infty}^{\infty} f(x)e^{iux}dx,$$
$$f(x)=\frac{1}{2\pi}\int_{-\infty}^{\infty} F(u)e^{-iux}du. \tag{5}$$

For brevity, these relations will be written in the notation,

$$F=Tf$$
$$f=T^{-1}F. \tag{6}$$

It is known that the transforms of the distributions in the convolution, Eq. (4), are related thus[3]:

$$H=FG, \tag{7}$$

from which it follows at once that if h and g are known functions in Eq. (4), then f is determined by the inversion

$$f=T^{-1}(H/G). \tag{8}$$

A composite rocking curve, such as that represented in Fig. 2(b), may be expressed in terms of its component rocking curves by the equation,

$$y(x)=\sum y_r(x-x_r), \tag{9}$$

in which y_r, $r=1, 2, 3, \cdots$ are the characteristic rocking curves of the subregions and x_r are the angular deviations at which these are centered. The origin of x is arbitrary, but will usually be at or near the mean Bragg setting. In terms of the normalized distributions this equation may be written,

$$Ih=\sum I_r h_r(x-x_r), \tag{10}$$

where

$$I=\sum I_r \tag{11}$$

and I_r is the integrated reflecting power of the rth subregion, thus roughly proportional to its area.

We shall now consider the characteristic distribution h_r as a convolution of a basic distribution g associated with the distributions (1), (2), and (3) mentioned above, and a "broadening" process represented by a distribution f_r associated with the rth subregion of the

[3] Bochner and Chandrasekharan, *Fourier Transforms* (Princeton University Press, Princeton, New Jersey, 1949).

crystal. Thus, we have

$$\left.\begin{aligned} h_r &= f_r * g, \\ H_r &= F_r G. \end{aligned}\right\} \tag{12}$$

The solution of the first of these equations for f_r in terms of h_r and g exists and is unique for a very large class of functions.[3]

The second central moments associated with the three distributions represented in Eq. (12) are related as follows,[4]

$$\sigma_h^2 = \sigma_{f_r}^2 + \sigma_g^2. \tag{13}$$

These moments are positive if $f_r \geq 0$, $g \geq 0$, and, necessarily, $h \geq 0$. However, if merely $g \geq 0$, $h \geq 0$, it is quite possible for f_r to be negative for some values of x. If the three functions are everywhere positive, then the widths of the three distributions are proportional to the square roots of the moments. For such cases, w_{f_r}, the width of f_r, will be small whenever that of the basic g is close to that of the characteristic distribution h_r. In our approach, we shall make several assumptions about the nature of g. Possibly, this function g may be poorly chosen, perhaps through necessity. Thus, it may happen that for a function g that we are obliged to use, f_r is not everywhere positive, and its width will then not be proportional to σ_f.[5] However, for any reasonable choice of g one will find $w_{f_r} < w_g$.

If we substitute the value of h_r from Eq. (12) in Eq. (10) we have

$$Ih = g * \sum I_r f_r(x - x_r), \tag{14}$$

and, from Eq. (5), it follows that

$$IH = G \sum I_r F_r e^{iux_r}. \tag{15}$$

The distribution f, obtained through the inversion

$$y_s = If = T^{-1} \sum I_r F_r e^{iux_r} = \sum I_r f_r(x - x_r) \tag{16}$$

may now be considered as a sharpened version of h, as shown in Fig. 2(c).

Before proceeding to develop a practical method for performing the inversion, Eq. (16), we shall give three illustrations.

First we suppose that the characteristic distributions are identical and that $h_r = g$, $(H_r = G)$, $r = 1, 2, 3, \cdots$. Eq. (12) then gives the solution[6]

$$f_r = \delta, \quad (F_r = 1). \tag{17}$$

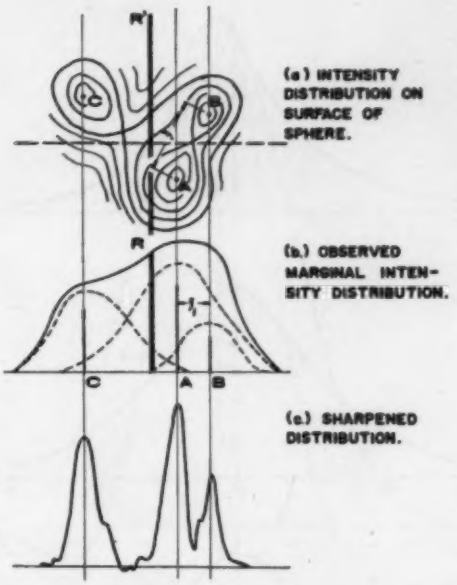

FIG. 2. Intensity of reflection from crystal surface. (a) Intensity distribution on surface of sphere. (b) Observed marginal intensity distribution. (c) Sharpened distribution.

From either of these results we obtain

$$y_s = T^{-1} \sum I_r e^{-iux_r} = \sum I_r \delta(x - x_r). \tag{18}$$

In this case the function y_s is infinitely sharp, being a set of δ's on the abscissas x_r with content I_r. This configuration would be schematically represented by the three ordinates in A, B, C, Fig. 2(b).

Next, we suppose that the characteristic distributions are gaussian, and that their widths, $w_r = 2.36\sigma_r$, vary over the reflecting subregions. For this case,

$$\left.\begin{aligned} h_r &= \frac{1}{(2\pi\sigma_r)^{\frac{1}{2}}} \exp\left[-\frac{(x - x_r)^2}{2\sigma_r^2}\right], \\ H_r &= \exp(-\tfrac{1}{2}\sigma_r^2 u^2 + iux_r), \quad r = 1, 2, 3; \cdots. \end{aligned}\right\} \tag{19}$$

We may now take g to be gaussian with $\sigma \leq \sigma_r$, $r = 1, 2, 3, \cdots$. On substituting in Eq. (16), with $F_r = H_r/G$, and $G = \exp(-\frac{1}{2}\sigma^2 u^2)$,

$$\begin{aligned} y_s &= T^{-1} \sum I_r \exp[-\tfrac{1}{2}(\sigma_r^2 - \sigma^2)u^2 + iux_r] \\ &= \frac{1}{(2\pi)^{\frac{1}{2}}} \sum \frac{I_r}{(\sigma_r^2 - \sigma^2)^{\frac{1}{2}}} \exp\left[-\frac{(x - x_r)^2}{2(\sigma_r^2 - \sigma^2)}\right]. \end{aligned} \tag{20}$$

The sharpened version of h appears as a sum of gaussians with reduced spread. When the resolution is sufficiently great we can reconstruct the parameters associated with the coarse substructure. The observed peaks of f are $f(x_r) \approx f_r(0)$ and their widths are $w_r' = 2.36(\sigma_r^2 - \sigma^2)^{\frac{1}{2}}$. From these, we can compute

$$\left.\begin{aligned} I_r &= \frac{(2\pi)^{\frac{1}{2}}}{2.36} w_r' f_r(0) \approx w_r' f_r(0), \\ w_r &= (w_r'^2 + w_g'^2)^{\frac{1}{2}}. \end{aligned}\right\} \tag{21}$$

[4] H. Cramer, *Mathematical Methods of Statistics* (Princeton University Press, Princeton, New Jersey, 1946), pp. 188–192.

[5] If the mean value of a distribution is at $x = 0$, the second central moment is $\sigma^2 = \int_{-\infty}^{\infty} x^2 f(x)dx$. If $f(x) \geq 0$, then σ measures the "spread" of x and may be taken as a measure of "width." But if $f(x) < 0$ for some range of x, then σ^2 may have small or even negative values even for "wide" functions f. For example, if $f > 0$ and is wide near $x = 0$ and $f < 0$ in a range of large values of x, then σ^2 may be negative even when the negative amplitudes of f are very small.

[6] For a rigorous treatment of generalized functions such as $\delta(x)$, see M. J. Lighthill, *Fourier Analysis and Generalized Functions* (Cambridge University Press, New York, 1958).

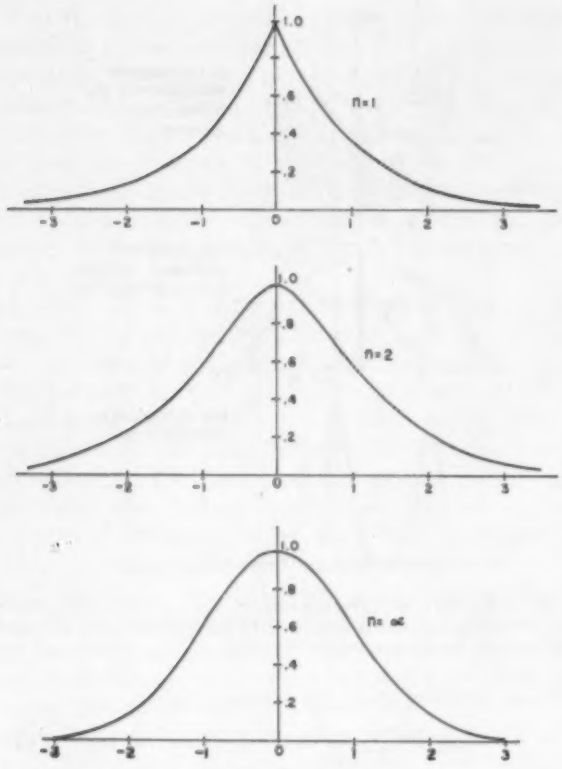

FIG. 3. Graph of g_n.

We thus have the set of numbers I_r, w_r, x_r, $r=1, 2, 3 \cdots$, which are reflecting power proportional to the area of the subregion, width of its characteristic curve, and tilt component.

For a third illustration, which will be shown to be of importance for the practical solution of the inversion problem, we take

$$G_n=(1+\sigma^2u^2/2n)^{-n}. \tag{22}$$

This sequence of symmetric rational functions is suitable because

$$G_n \to G=\exp(-\tfrac{1}{2}\sigma^2u^2), \quad n\to\infty \tag{23}$$

and, as will be shown later, the inversions with these functions can be performed by an electronic analogue computer.

The corresponding functions g_n are readily found to be[7]

$$g_n=\frac{(n)^{\frac{1}{2}}\exp[-(n)^{\frac{1}{2}}/\sigma]|x|}{2^{2n-1}(n-1)!\sigma}\sum_{0}^{n-1}\frac{(2n-2-r)!2^r}{(n-1-r)!r!}\times\left[\frac{(n)^{\frac{1}{2}}}{\sigma}|x|\right]^r. \tag{24}$$

The functions g_n are shown in Fig. 3 for $n=1, 2, \infty$.

Explicitly, the first two are

$$\left.\begin{aligned} g_1&=\frac{1}{\sigma}\exp-\left(\frac{1}{\sigma}|x|\right)\\ g_2&=\frac{\sqrt{2}}{4\sigma}\left(1+\frac{\sqrt{2}}{\sigma}|x|\right)\exp-\left(\frac{\sqrt{2}}{\sigma}|x|\right)\end{aligned}\right\}. \tag{25}$$

The second moment of x is σ^2 for all values of n. This can most easily be seen by expanding G_n in a Maclaurin series,

$$G_n=1-\tfrac{1}{2}\sigma^2u^2+0(u^4), \tag{26}$$

from which it follows that[8]

$$m_0=1, \quad m_1=0, \quad m_2=\sigma^2=m_2-m_1^2.$$

COMPUTATION OF THE INVERTED INTEGRAL

An arithmetic algorithm for performing the inversion, Eq. (8), has been developed by Stokes and Wilson,[9] but this method is very awkward in our problem because of the exponentials in Eq. (15), which arise from the distribution of peak positions, x_r, Eq. (14). In Eq. (18), Ty_s is an almost periodic function and even in less idealized cases, if the peaks $f(x_r)$ of f are sharp, Ty_s has those characteristics of almost periodic functions which make it difficult to separate the components.[10]

The results obtained by the use of an electronic analogue computer show promise. The basic operational relation that permits the use of the computer is the following:

$$\frac{d}{dx}f=\frac{d}{dx}T^{-1}F=T^{-1}(-iuF). \tag{27}$$

This follows at once from the second of Eq. (5). Since the computer operates in the time-frequency domain we shall, in what follows, replace the reciprocal variables (x,u) by (t,ω). The relation, Eq. (27), then says that ω inside the integral is equivalent to $i(d/dt)$ outside.

Similarly,

$$(d^n/dt^n)f=T^{-1}[(-1)^ni^n\omega^nF]. \tag{28}$$

If $G(\omega)$ is such that it can be expanded in a power series, we have

$$\left.\begin{aligned} h(t)&=T^{-1}G(\omega)F(\omega)=T^{-1}\sum a_n\omega^nF(\omega)\\ &=\sum a_nT^{-1}\omega^nF(\omega)=\sum a_n[i(d/dt)]^nT^{-1}F(\omega)\\ &=G[i(d/dt)]T^{-1}F(\omega)\\ &=G[i(d/dt)]f(t).\end{aligned}\right\} \tag{29}$$

[7] G. A. Campbell and R. M. Foster, *Fourier Integrals for Practical Applications*, D. Van Nostrand Company, Inc., Princeton, New Jersey, 1948); J. J. Slade, Jr., Progress Rept. #3.

[8] These relations can be established by using the properties of the moment generating function; see also footnote 4.

[9] A. R. Stokes and A. J. C. Wilson, Proc. Cambridge Phil. Soc. **38**, 313 (1942); Proc. Phys. Soc. (London) **56**, 174 (1944).

[10] J. J. Slade, Jr., "Sinusoidal surface waves in stratified soil," ASTM Spec. Tech. Publ. No. 232, 312.

Hence,

$$f(t)=\frac{1}{G[i(d/dt)]}\cdot h(t). \tag{30}$$

By introducing the notation

$$G_{(op)}=G[i(d/dt)] \tag{31}$$

we have, from Eq. (30),

$$f=G_{op}^{-1}\cdot h. \tag{32}$$

Consequently, if the graphical record of the distribution, $h(t)$, of reflection intensities is converted into a continuous proportional voltage variation and fed to the computer, the output will be $f(t)$ when the computer is set to perform the sequence of operations G_{op}^{-1}.

Let us take for $g(t)$ a gaussian, whose Fourier transform is

$$G=\exp(-\tfrac{1}{2}\sigma^2\omega^2).$$

As stated previously, G can be approximated by the sequence given in Eq. (22). By taking

$$G_1=[1+(\sigma^2/2)(\omega^2/n)]^{-1} \tag{33}$$

we have, using the notation given in Eq. (31),

$$G_1^{-1}{}_{(op)}=[1-(\sigma^2/2n)(d^2/dt^2)]=[(1-a^2(d^2/dt^2))], \tag{34}$$

where

$$a^2=\sigma^2/2n \tag{35}$$

and

$$f_1=G_1^{-1}(op)\cdot h=[(1-a^2(d^2/dt^2))]h. \tag{36}$$

Thus, as a first approximation to obtain $f(t)$, knowing $h(t)$, the analogue computer will take the second derivative of h, multiply it by a constant a^2 and subtract the result from h.

On applying n times the operator given in Eq. (34), i.e., applying the operator,

$$G_{n(op)}^{-1}=G_{1(op)}^{-n}=[1-a^2(d^2/dt^2)]^n, \tag{37}$$

we will get an nth approximation of $f(t)$.

If the characteristic distributions are approximations to the gaussian of the form (25), then

$$G_{n(op)}^{-1}g_m=\delta, \quad m=n, \tag{38}$$

but if $m\neq n$, the resulting function has zero second moment, but is not infinitely narrow, consequently it must have negative ordinates. The graphical sharpening of the gaussian, $m=\infty$, when $n=2$ is shown in Fig. 4.

Since the second moment of the characteristic functions is not known the parameter, $a=\sigma/(n)^{\frac{1}{2}}$, of G_n will be adjusted to give the best resolution of the peaks.

DESCRIPTION OF COMPUTER OPERATION

The experimental setup consists of a curve tracer (variplotter), a low pass filter to reduce noise and spurious oscillations from the tracer, operational amplifiers whose outputs are the derivatives of the inputs, amplifiers that reverse the phase of the signals and summing amplifiers. Thus, the signal from the curve tracer is differentiated twice, inverted and added to the original signal. This output is fed into an identical arrangement so that the over-all result is

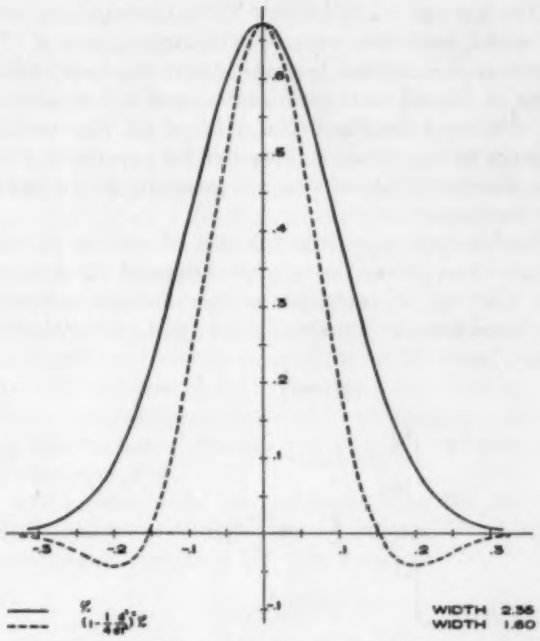

FIG. 4. Second order sharpening of the gaussian.

$$f_2=G_1^{-2}{}_{(op)}h=[1-a^2(d^2/dt^2)]^2h. \tag{39}$$

This operation can be repeated any number of times so as to obtain as close an approximation to $G_{1(op)}^{-n}$ as desired.

Aside from the original function generator noise there is noise within the computer which is exaggerated with every application of the operator $G_{1(op)}^{-1}$.

A low pass wide band filter reduces the noise of the curve tracer. A time limited filter of this sort is equivalent to the averaging distribution,

$$\left.\begin{aligned} k_\alpha&=\frac{1}{2\alpha}, \quad |t|\leq\alpha \\ &=0 \quad\ |t|>\alpha \\ K_\alpha&=\frac{\sin\alpha\omega}{\alpha\omega} \end{aligned}\right\}. \tag{40}$$

If

$$f_n=G_{n(op)}^{-1}h, \tag{41}$$

then, by using the filter before each operation $G_{1(op)}^{-1}$ we have

$$\tilde{f}_n=(G_{1(op)}^{-1}k_\alpha*)^n h=T^{-1}\frac{K_\alpha{}^n H}{G_n}\begin{aligned}&\to f_n, \quad \alpha\to 0 \\ &\to 0 \quad\ \alpha\to\infty \\ &\to \quad\ n\to\infty\end{aligned} \tag{42}$$

almost everywhere.

The last two follow because K_α^n is bounded and tends to zero almost everywhere with large α and n. The function $\hat{f}_n$ is leveled to nothing with too many repetitions of the operator with a filter, and it is masked by noise without the filter. The width of the filter and the number of repetitions is a matter for experimentation. The number of repetitions will generally be limited by the computer.

To determine the distortion of the functions $f(t)$ that occurs through successive applications of the operator Eq. (34), as an operation of the analogue computer, we introduce a function $\varphi_1(x)$ with the following properties[11]:

$$\varphi_1(x) \to 0, \quad |x| \to \infty \tag{43}$$

$$\int_{-\infty}^{\infty} \varphi_1(x)dx = 0 \tag{44}$$

$$\varphi_0(x) = \int_{-\infty}^{x} \varphi_1(\xi)d\xi \geq 0 \tag{45}$$

$$\int_{-\infty}^{\infty} \varphi_0(x)dx = 1 \tag{46}$$

$$T\varphi_0(x) = \Phi(u). \tag{47}$$

Let $R^2\varphi_1(Rt)$ be the output of a computer circuit when the input is a voltage impulse of unit content. In this expression R is an adjustable circuit parameter. Now

$$R\int_{-\infty}^{\infty} \varphi_0(Rt)dt = \int_{-\infty}^{\infty} \varphi_0(x)dx = 1 \quad \text{for all } R. \tag{48}$$

It will be seen that

$$R\varphi_0(Rt) \to \delta(t), \quad R \to \infty. \tag{49}$$

If the input is $h(t)$, then the output is

$$h_1 = R^2\varphi_1(Rt) * h = R\varphi_0(Rt) * h', \tag{50}$$

as one integration by parts of the convolution integral Eq. (3) shows. Also,

$$h_1 \to h', \quad R \to \infty, \tag{51}$$

showing that the circuit is a differentiator in the limit and an approximation to one when the circuit parameter has finite values. All differentiating circuits approximate the operation, more or less sharply.

Differentiating Eq. (3) yields the relation,

$$(f * g)' = f' * g = f * g', \tag{52}$$

from which it follows that

$$h_n = (R^2\varphi_1(Rt) *)^n h = (R\varphi_0(Rt) *)^n h^{(n)} = T^{-1}\Phi^n(w/R)(iw)^n H(w). \tag{53}$$

[11] S. Bochner, *Harmonic Analysis and the Theory of Probability* (University of California Press, 1955). (In Chap. 1 there is a development of a theory of approximations pertinent to the present investigation.)

We also see that

$$\Phi^n(w/R) \to 1, \; n \text{ fixed}, \; R \to \infty \to 0 \text{ almost everywhere}, \; R \text{ fixed}, \; n \to \infty. \tag{54}$$

The approximation

$$f^+ = T^{-1}G^{-1}(w\Phi(w/R))H(w) \sim G_{op}^{-1}h = f \tag{55}$$

is the output of the computer.

A number of conclusions follow from this result principal of which is that successive applications of the operator Eq. (34) do not indefinitely distort $f(t)$. Because of Eq. (54) little change is produced by the operation beyond a certain number $n = N$ of repetitions. The degradation of $f(t)$ beyond the distortion produced by the approximation resulting from the finiteness of R will be caused by noise and filtering which require the number of repetitions to be limited, as shown by Eq. (42). The experimental results to be shown below correspond to the application of the operator described in Eq. (39).

The constant a^2 can be experimentally determined in terms of the circuit components. In fact, if an exponential curve of the type,

$$f(t) = e^{(t/a)} \tag{56}$$

is fed to the computer which is operating with

$$G_{1(op)}^{-1} = [1 - b^2(d^2/dt^2)], \tag{57}$$

we shall have

$$[1 - b^2(d^2/dt^2)]e^{t/a} = [1 - (b^2/a^2)]e^{t/a} = 0 \quad \text{if} \quad b = a. \tag{58}$$

By adjusting these constants so that the operation (58) produces a zero result and by changing the values of a in the function (56) it will be possible to determine a one-to-one relation between the circuit components and the values of a.

The value of b^2 depends on the circuit constants and the time it takes the tracer to sweep a curve. All curves are traced with magnetic ink in a paper of standard size. The tracer moves horizontally at a constant rate of 15 in. in 33 sec.

The reliability of the computer operations can be checked in various ways. By differentiating a step function fed through the variplotter a function δ will be generated. Some inertia due to circuit components may be expected in which case the width of the response to a step function will give a measure of this inertia. The ability of the computer to separate peaks in a multimodal curve can be checked by feeding it with a curve obtained by adding two or more normal curves with known means and standard deviations. Finally, the effect of "personal noise" in tracing from the original record or from another tracing can be checked by obtaining independent tracings and observing the response of the computer.

EXPERIMENTAL RESULTS

Figures 5 and 6 show two rocking curves of a silver single crystal grown from the melt. Figures 5(b) and 6(b) show the corresponding sharpened versions obtained through the use of $G_1^{-2}(o\dot{p})$. The obvious existence of several modes in Fig. 5 is clearly exhibited in Fig. 5(b). Besides the two main peaks, there appear other secondary peaks that explain the plateau between the two main peaks and the asymmetric tail observed to the right of the second peak. The sharpened version of Fig. 6 indicates the existence of several minor peaks that explain the asymmetry observed to the left of the main peak.

It appears that the values of x_r, or tilt components in the direction of rotation of the crystal, can be determined accurately enough by the use of the operator $G_1^{-2}(o\dot{p})$. Improvements are needed in the computer operation in order to obtain a resolution sufficiently great that will allow the computation of the reflecting power and width of each reflecting region.

The curves (*b*) of Figs. 5 and 6 are perfectly reproducible from fixed curves (*a*), and no notable variations in detail occur even when the curves (*a*) are redrawn, thus introducing personal noise.

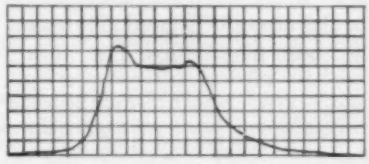

(a)

FIG. 5. Sharpening of a multimodal rocking curve.

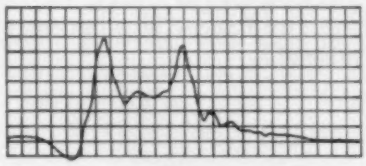

(b)

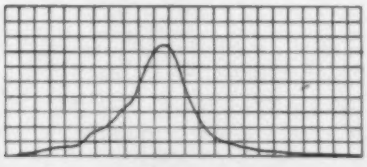

(a)

FIG. 6. Sharpening of a unimodal rocking curve.

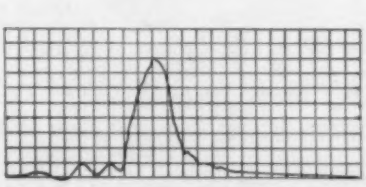

(b)

CONCLUSIONS

A sharpened version of the inverted x-ray diffraction profile is obtained by means of differential operations performed by an analogue computer. Ideally, a multipeaked rocking curve is resolved into several single-peaked curves. Each curve is associated with a subgrain. The integrated intensity as well as the width of these curves are a measure of the reflecting power and lattice defects within the corresponding subgrains, whereas the separation of adjacent peaks gives information of the tilt of neighboring subgrains.

The method is applicable to any configuration resulting from the convolution $g*f$, in which $g*=\prod g_r*$ is constant and $f*=\prod f_r*$ is variable. Instead of fine and course substructures this could equally well apply to the distribution of variation in lattice parameters in a powdered crystal.

The success of the method depends on the ability of of the computer to represent $G_{(o\dot{p})}{}^{-1}$ and the function generator to transduce $h(t)$ into a voltage.

APPENDIX

The basic operation, Eq. (34), is associated with gaussian distributions, but the distributions that characterize very perfect crystals are more closely represented by a Cauchy curve. A rational operator that may be used in connection with such distributions will now be deduced.

The two-parameter family[7]

$$G(\omega;\beta,\lambda)=\frac{\cosh(\lambda-1)\beta\omega}{\cosh\lambda\beta\omega}$$

$$=T\frac{(1/\beta\lambda)\sin(\pi/2\lambda)\cosh(\pi t/2\beta\lambda)}{\cosh(\pi t/\lambda)-\cos(\pi/\lambda)}=Tg \quad \text{(A1)}$$

is suitable for the present investigation since its members lie between the distributions

$$\begin{cases} G(\omega;\beta,\lambda)\to e^{-\beta|\omega|}=T\dfrac{1}{\pi}\dfrac{\beta}{\beta^2+t^2}, & \lambda\to\infty, \\ =\operatorname{sech}\beta\omega=T\dfrac{1}{2\beta}\operatorname{sech}\dfrac{\pi t}{2\beta}, & \lambda=1. \end{cases} \quad \text{(A2)}$$

The first of these is obtained through the relation $\tanh\lambda\beta\omega\to\operatorname{sgn}\omega$, $\lambda\to\infty$. It is possible to include $1\geq\lambda\geq\frac{1}{2}$, but the distributions for this range merely repeat those for the range $1\leq\lambda\leq\infty$.

The functions G has the infinite product, representation,

$$G(\omega;\beta,\lambda)=\prod_{r=1}^{\infty}\left(\frac{1+k_r(\lambda-1)^2\beta^2\omega^2}{1+k_r\lambda^2\beta^2\omega^2}\right), \quad \text{(A3)}$$

$$k_r=\frac{4}{(2r-1)^2\pi^2}.$$

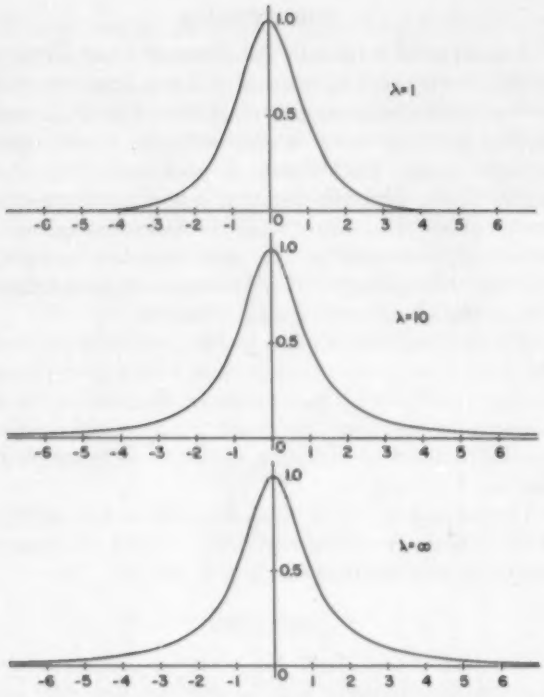

FIG. 7. Graph of $g_\lambda(t)$.

By expanding this product in a power series and by using the relation $\sum_1^\infty k_r=\frac{1}{2}$, or expanding the expression in (A1), we obtain

$$G=1-\tfrac{1}{2}(2\lambda-1)\beta^2\omega^2+0(\omega^4),$$

so that

$$(2\lambda-1)\beta^2=\sigma^2. \tag{A4}$$

Now,

$$G_n=\prod_1^n\left(\frac{1+k_r(\lambda-1)^2\beta^2\omega^2}{1+k_r\lambda^2\beta^2\omega^2}\right)=\prod_1^n G_{nr}\to G \tag{A5}$$

with

$$2p_n(2\lambda-1)\beta^2=\sigma^2,\quad p_n=\sum_1 k_r. \tag{A6}$$

The basic operator associated with these distributions is, therefore,

$$G_{nrop}{}^{-1}=\frac{1-k_r\lambda^2\beta^2(d^2/dt^2)}{1-k_r(\lambda-1)^2\beta^2(d^2/dt^2)}. \tag{A7}$$

The distribution $g(t)$, Eq. (A1), may be written

$$g_\lambda(t)=\frac{K\sin(\pi/2\lambda)\cosh\frac{1}{2}K\pi t}{\cosh K\pi t-\cos(\pi/\lambda)} \tag{A8}$$

with

$$K=\frac{1}{\beta\lambda}=\frac{(2\lambda-1)^{\frac{1}{2}}}{\sigma\lambda}$$

$$=\frac{4}{\pi W}\cosh^{-1}\left[\sin^2\frac{\pi}{2\lambda}+\left(1-\tfrac{1}{4}\sin^2\frac{\pi}{\lambda}\right)^{\frac{1}{2}}\right], \tag{A9}$$

depending on whether the parameter β, σ or W, the width, is used. The last expression is obtained by solving the equation $g(W/2)=\frac{1}{2}g(0)$ for W. The parameter K_n corresponding to the approximation $g_n=T^{-1}G_n$ is $K_n=2p_nK$ when σ is used, and it should be very close to this when W is used. The exact value of W for g_n has not been determined. The variation in p_n is small,

$$4/\pi^2\le p_n\le\tfrac{1}{2},\quad 1\le n\le\infty.$$

The three curves of Fig. 7 have a common width, being plotted in terms of $\tau=2t/W$, and show the shape variation for $\lambda=1,\ 10,\ \infty$.

The curve for $\lambda=10$ does not vary significantly from that for $\lambda=\infty$, so that Eq. (A3) may be used in connection with Cauchy distributions with a relatively small value of λ.

JOURNAL OF APPLIED PHYSICS VOLUME 31, NUMBER 4 APRIL, 1960

Precipitation in Silicon Crystals Containing Aluminum

R. BULLOUGH, R. C. NEWMAN, J. WAKEFIELD, AND J. B. WILLIS
Research Laboratory, Associated Electrical Industries, Aldermaston Court, Aldermaston, Berkshire
(Received October 1, 1959)

Silicon crystals containing aluminum have been annealed at various temperatures within the range 700° to 1350°C, particular emphasis being given to the range 1200° to 1300°C. Precipitation, which occurs during the heat treatment in the bulk crystal and on various structural defects, has been detected by transmission optical microscopy. A lowering of the aluminum concentration in the neighborhood of the precipitate particles after heating at 1250°C has been revealed at the surface by a novel technique involving the etching of crystals which also contain phosphorus, where internal cylindrical and planar p-n junctions are formed round individual dislocations and grain boundaries, respectively. At this temperature, no precipitation is observed on dislocations in plastically deformed crystals. The precipitation of aluminum is interpreted in terms of a chemical reaction involving the coprecipitation of oxygen and possibly carbon.

1. INTRODUCTION

PRECIPITATION of a second phase within a crystal is to be expected on annealing, if the crystal initially contains two or more types of impurity which have a strong chemical affinity for each other. Initially, the impurity atoms will preferentially migrate to the neighborhood of any internal lattice defects; nucleation is most likely to occur in such regions of enhanced concentration.[1] Subsequently, growth of these nuclei will be controlled by a combination of both drift and diffusion flow.[2,3]

In the present paper we shall consider the precipitation behavior of aluminum in silicon crystals which are known to contain oxygen and carbon.[4] Lederhandler and Patel[5] have previously demonstrated the precipitation of oxygen on dislocations in silicon and since there is a strong affinity between oxygen and aluminum,[6,7] the formation of an aluminum-oxygen complex at these sites is to be expected.

Such precipitation has been observed on various internal defects including dislocations, twin boundaries and tilt boundaries in the temperature range 1200° to 1300°C, and detailed results are given in Sec. 3. The precipitate particles have been revealed by transmission infrared microscopy.[8]

The size of these precipitates and the resulting spatial distribution of the aluminum have been estimated theoretically. A comparison of the former with observation requires a correlation of the size of an optical image with that of the object: this is discussed in Sec. 2. The spatial distribution has been revealed by a novel technique involving the delineation of p-n junctions by etching doubly-doped silicon containing a slight excess of aluminum over an n type impurity such as phosphorus. A survey of the precipitation effects over the wider temperature range 700° to 1350°C is then given in Sec. 4. Finally, a discussion of the results with special reference to the importance of oxygen is given in Sec. 5.

2. SPECIMEN PREPARATION AND EXPERIMENTAL TECHNIQUES

The crystals used in this investigation were grown by the Czochralski technique from a quartz crucible in an argon atmosphere.[9] Crystals of the following types have been grown: single crystals with [111] and [100] growth directions, crystals with a [112] growth direction containing a single [11$\bar{1}$] twin boundary, and crystals with a growth direction close to [$\bar{2}$21] containing a single "semicoherent" (313) boundary. Some of these crystals contained low angle tilt boundaries and other regular configurations of dislocations: the average dislocation density varied from zero up to 10^5 cm^{-2} as revealed by standard etching techniques.

Metallic aluminum was introduced into the melt during growth to give a concentration near the top of the ingot of 10^{16}–10^{18} atoms/cc. In the majority of crystals, phosphorus was also added to the melt so that the phosphorus to aluminum ratio varied between 0.3 and unity. The ratio was estimated from the measured segregation coefficient of each impurity appropriate to the particular equipment used, and from the resistivity profile along the length of the ingot. The accuracy of estimation of this ratio was limited to about $\pm 5\%$ because of the formation of resistivity striations down the ingot.[10] For the purpose of comparison, several ingots were also prepared containing other group III and V impurities. The oxygen content of these crystals was estimated to be 10^{18} atoms/cc from the measured absorption coefficient in the infrared at 9.1 μ, as previously described by Kaiser and Keck.[11]

The crystals were cut into slices 1 mm thick to within $\pm 1°$ from the relevant crystallographic direction. These

[1] J. W. Cahn, Acta Met. **5**, 169 (1957).
[2] F. S. Ham, J. Appl. Phys. **30**, 915 (1959).
[3] R. Bullough, R. C. Newman, J. Wakefield, and J. B. Willis, Nature **183**, 34 (1959).
[4] H. A. Papazian and S. P. Wolsky, J. Appl. Phys. **27**, 1561 (1956).
[5] S. Lederhandler and J. R. Patel, Phys. Rev. **108**, 239 (1957).
[6] C. S. Fuller, Chem. Revs. **59**, 65 (1959).
[7] R. Bullough, R. C. Newman, and J. Wakefield, Proc. Inst. Elec. Engrs. (London) **106B** (Suppl. 15), 277 (1959).
[8] W. C. Dash, J. Appl. Phys. **27**, 1193 (1956).
[9] E. Billig and D. B. Gasson, J. Sci. Instr. **35**, 360 (1958).
[10] P. J. Holmes, Proc. Inst. Elec. Engrs. (London) **106B** (1959) (to be published).
[11] W. Kaiser and P. H. Keck, J. Appl. Phys. **28**, 882 (1957).

slices were ground and etched in a mixture of 50% nitric acid and 50% hydrofluoric acid ("Analar" grade reagents); they were then placed in a carefully cleaned quartz tube which was evacuated to a pressure of 10^{-5} mm Hg and sealed off. The heat treatment was carried out in a resistance furnace.

After heat treatment, the specimens were polished on fine grade diamond paste for examination by transmission infrared microscopy. Subsequently, the double-doped specimens were again etched in the 50/50 HNO_3, HF mixture to remove the surface damage caused by polishing; this etching also produced steps which delineate any p-n junctions present round defects. These samples were then further etched for a short time in the Dash etch,[8] until small dislocation etch pits were produced. These specimens were re-examined by transmission infrared microscopy to correlate surface and internal structure. Fine details of the surface structure were determined by shadowed carbon replicas in the electron microscope. A few samples were thinned down by etching in a mixture of 15% hydrofluoric acid and 85% nitric acid or by polishing techniques so that they were suitable for examination by transmission microscopy with both electrons and visible light.

The optical examination of the specimens was carried out on a Reichert MeF projection microscope. With infrared illumination, an image converter was used to focus the image, which was then recorded directly on Kodak type Z plates. All the microscope objectives up to a numerical aperture of 0.75 were found to be suitable for the infrared work. No increased resolution was obtained by using an oil-immersion lens with a numerical aperture of 1.3, presumably because of the uncorrected spherical aberration at this wavelength. Thus a considerable improvement in resolution was obtained with visible light on thinned specimens.

The smallest opaque object that can be detected with an optical microscope is considerably smaller than the limit of resolution, S. The distribution of intensity in the image plane of an opaque strip of width $2X_0$ is

$$i(x)=\{1-1/\pi[Si(x_0+x)+Si(x_0-x)]\}^2, \quad (1)$$

where $x_0=(2\pi X_0/\lambda)N\sin\alpha$; $N\sin\alpha$ is the numerical aperture and λ is the wavelength. It can be shown from Eq. (1) that if X_0 is less than S, the width of the image is comparable with S. Under this condition the contrast C_x at the middle of the image ($X=0$) is approximately

$$C_x=4x_0/\pi. \quad (2)$$

The corresponding expression for an opaque disk of radius R_0 is

$$C_r=r_0^2/2. \quad (3)$$

A detailed derivation of these expressions has been given by Canals-Frau and Rousseau.[12]

We have found that a variation of 5% in intensity produces a detectable contrast on the photographic plates used. Hence, it is reasonable to set $C_x=C_r=0.1$, to estimate the minimum values of X_0 and R_0; these are given in Table I.

TABLE I. Limit of resolution and detection for opaque strips and disks.

Wavelength $\lambda(\mu)$	Numerical aperture $N\sin\alpha$	Limit of resolution S (A)	Width of opaque strip $2X_0$ (A)	Diameter of opaque disk $2R_0$ (A)
0.65	1.3	3100	130	720
1.1	0.75	8900	370	2100

The values quoted in Table I are the theoretical lower limit and are rather optimistic since no allowance has been made for aberrations in the microscope, or for spurious refraction effects at the surface of the silicon specimen which has been assumed to be optically flat.

3. PRECIPITATION IN THE TEMPERATURE RANGE 1200°–1300°C

Single Crystals

After heat treatment of silicon crystals containing aluminum, precipitation is observed along the dislocation lines as shown in Fig. 1. The amount of precipitation is independent of the rate of cooling, and thus the precipitation must occur during the heat treatment; this is in contrast to copper precipitation which occurs entirely within the period of cooling. To check that the observed precipitation is a consequence of the presence of aluminum, silicon samples containing other group III and V elements were heated together with the aluminum-doped samples in the same silica tube. Although in the former samples light precipitation was sometimes observed, the amount of precipitation in the latter aluminum-doped samples was in all cases very much greater, and furthermore increased with increasing periods of heat treatment. The slight precipitation observed in crystals not deliberately doped with aluminum may, however, be a consequence of the presence of a small concentration of aluminum originating from the quartz crucible.[9]

The number of aluminum atoms which precipitate on an isolated dislocation after a given time of heat treatment together with the resulting spatial distribution are now estimated. The dislocation line is considered to be surrounded by a cylindrical region of radius r_0 in which impurity atoms have very high mobility. It is difficult to allocate a precise value to r_0, but we expect its value to lie in the range 10–60 A. Precipitate particles can then nucleate in this region at certain favorable sites, such as jogs, and do in fact appear as discrete particles strung out along the dislocation line as shown in Fig. 1. Subsequent growth of the precipitates occurs by the diffusion of impurities to the dislocation followed by rapid migration along the core to the nucleated particles. If an infinite reaction rate at the surface of the

[12] D. Canals-Frau and M. Rousseau, Optica Acta 5, 15 (1958).

precipitates is assumed,[13] the concentration within the region $r \leqslant r_0$ will be maintained at a constant value C_s. It is shown below that at least one other impurity element must be involved in the growth of the precipitates and the adoption of this boundary condition implies that there is an adequate supply of this impurity.

The differential equation for the concentration $C(r,t)$ governing migration of aluminum atoms to the dislocation is[14]

$$\frac{1}{D}\frac{\partial C(r,t)}{\partial t}=\frac{\partial^2 C(r,t)}{\partial r^2}+\left(\frac{1}{r}+\frac{L}{r^2}\right)\frac{\partial C}{\partial r}(r,t)-\frac{L}{r^3}C(r,t), \quad (4)$$

where we have assumed a radially symmetric potential field of the form

$$U=-A/r \quad (5)$$

and $L=A/kT$.

With the boundary condition

$$C(r_0,t)=C_s, \quad (6)$$

there will be a net diffusion flow across any internal surface, and hence to a first approximation, drift flow may be neglected.[3,15] We thus set $L=0$ in the governing Eq. (4) and the required solution subject to the boundary condition (6) and the initial condition,

$$C(r,0)=C_0 \quad (7)$$

is,[16] for $\rho>1$,

$$\frac{C(r,t)-C_s}{C_0-C_s}=\frac{2}{\pi}\int_0^\infty \frac{e^{-mu^2}}{u} \times\frac{J_0(u)Y_0(u\rho)-J_0(u\rho)Y_0(u)}{J_0^2(u)+Y_0^2(u)}du, \quad (8)$$

where $m=Dt/r_0^2$ and $\rho=r/r_0$.

The number $N(t)$ of aluminum atoms that cross unit length of the surface $r=r_0$ is given by

$$N(t)=2\pi r_0 D\int_0^t \frac{\partial C(r_0,t)}{\partial r}dt, \quad (9)$$

that is,

$$N(t)=\frac{8r_0^2}{\pi}[C_0-C_s]\int_0^\infty \frac{[1-\exp(-mu^2)]du}{u^3[J_0^2(u)+Y_0^2(u)]}. \quad (10)$$

The diffusion length appropriate to aluminum in silicon after heating at 1250°C for 16 hrs is $(Dt)^{\frac{1}{2}}=1.3\times10^{-3}$ cm, and is considerably larger than both r_0 and the maximum observed size of the precipitate particles. Thus, for such large values of m, equation (10) may be replaced by its asymptotic form[16]

$$N(t)=4\pi(C_0-C_s) \times Dt\left\{\frac{1}{[\ln 4m-2\gamma]}+\frac{1-\gamma}{[\ln 4m-2\gamma]^2}-\cdots\right\}, \quad (11)$$

where $\gamma=0.577$ is Euler's constant. Although the size of the precipitate particles exceeds r_0, this will not affect the rate of precipitation significantly since the boundary condition $C=C_s$ will still apply at the precipitate matrix interface, and the expression for $N(t)$ given in Eq. (11) is seen to be insensitive to variations in r_0. With $m=5\times10^6$ (appropriate to $r_0=60$ A), $C_0=10^{17}$ atoms/cc, and $C_s=0$, we find $N(t)=1.36\times10^{11}$ atoms/unit length of the dislocation. This value of $N(t)$ is nearly two orders of magnitude smaller than the number estimated from micrographs such as shown in Fig. 1, if an aluminum density in the precipitates of 5×10^{22} atoms/cc is assumed. Furthermore, the amount of precipitation observed was not proportional to the initial aluminum concentration within the range 10^{16}–10^{18} atoms/cc. It is therefore concluded that the density of aluminum in the precipitate particles is considerably lower than the above estimate and hence the particles must consist primarily of other impurities; the only impurities known to be present in sufficient con-

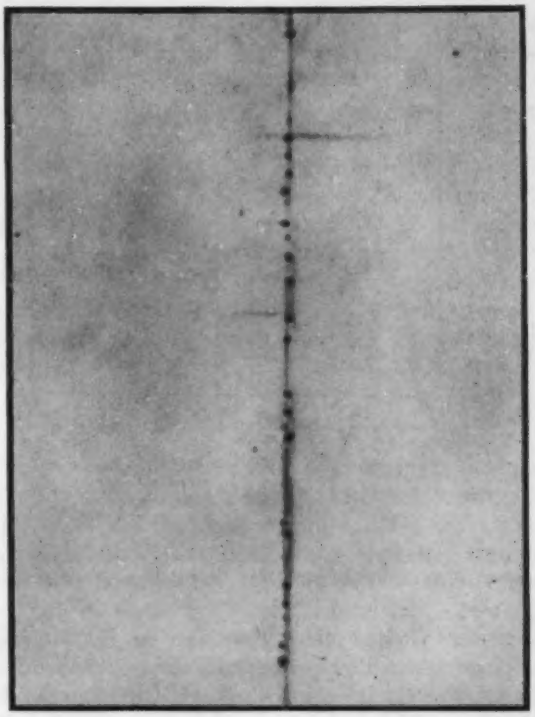

FIG. 1. Precipitate particles on an isolated dislocation after annealing at 1250°C for 18 hrs. Visible transmission: ×1800.

[13] D. Turnbull, Acta Met. **1**, 764 (1953).

[14] R. Bullough and R. C. Newman, Proc. Roy. Soc. (London) **A249**, 427 (1959).

[15] This is in contrast to our previous treatment[14] for the growth of a Cottrell atmosphere, where the nature of the boundary condition was such as to produce zero initial net diffusion flow and the migration was caused by the small drift perturbation only. Ham[3] also has shown that with a boundary condition similar to Eq. (6), the effect of drift is quite small.

[16] H. S. Carslaw and J. C. Jaeger, *Conduction of Heat in Solids* (Clarendon Press, Oxford, England, 1959), 2nd ed.

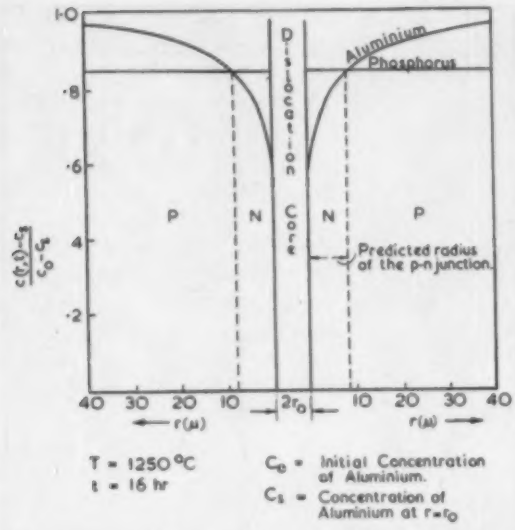

FIG. 2. The concentration distribution of aluminum round a dislocation, illustrating the formation of cylindrical *p-n* junctions.

centrations which could give rise to the observed precipitation are oxygen and carbon.

Equation (11) is nevertheless still valid for the flow of aluminum if it can be shown that the spatial distribution agrees with that given by Eq. (8), which is illustrated in Fig. 2. This figure indicates that if the crystal contains an *n*-type impurity, which does not precipitate, at a slightly lower concentration than that of the aluminum, then a *p-n* junction should be formed round each dislocation. Such effects have been observed using the technique described in Sec. 2. (Figure 6 illustrates the correlation between the internal precipitation and the surface features revealed by etching.) If the dislocation meets the surface normally the *p-n* junction delineated at the surface is circular, some examples of which can be seen in Fig. 3. In general, however, the dislocations are not normal to the surface and elliptical traces are often observed. The radial symmetry of these *p-n* junctions provides justification for the assumption of radially symmetric diffusion flow to the dislocation. On any individual specimen there is a range of values for the radii of the *p-n* junctions; we attribute this to the impurity fluctuations previously referred to, since a small change in the ratio of aluminum to the *n*-type impurity causes a comparatively large change in the radius expected from the distribution given in Fig. 2. If the ratio of the two impurity levels is very close to unity, it is difficult, by this method, to delineate the *p-n* junction because the circular step now occupies a wide annular region as a result of the small concentration gradient. The measured radii agree within experimental error with the value expected from Fig. 2 provided a value of C_s approximately equal to 10^{16} atoms/cc is adopted. (It is interesting to note that this value is comparable to the surface concentration found at external surfaces for the diffusion of aluminum either into or out of silicon in the presence of oxygen.)[7,17] In crystals containing an aluminum concentration less than this value, no *p-n* junctions have been found. Precipitation is, however, still observed on the dislocations, although under these circumstances the solution (8) is not applicable, since a different boundary condition is required as previously discussed by Bullough et al.[7] These results indicate that when $C_0 > C_s$ the actual spatial distribution is in agreement with that predicted by Eq. (8), and hence the amount of aluminum present

FIG. 3. *P-n* junctions round isolated and groups of dislocations as revealed by etching. ×330.

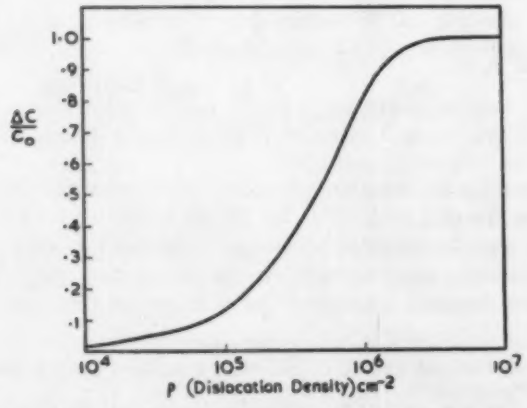

FIG. 4. The variation of degree of depletion with dislocation density for $(Dt)^{\frac{1}{2}} = 1.3 \times 10^{-3}$ cm and $r_0 = 60$ A.

[17] C. S. Fuller and J. A. Ditzenberger, J. Appl. Phys. **27**, 544 (1956).

in the precipitate particles is given fairly accurately by Eq. (11).

So far we have considered precipitation on an isolated dislocation. In regions of high dislocation density the n-type zones overlap and sometimes assume interesting shapes as shown in Fig. 3, where the "neck" has been produced by a dislocation line lying almost parallel to the surface. When the over-all dislocation density is very high, crystals have been observed to convert completely from p type to n type. The degree of conversion as a function of dislocation density has been computed by assuming the dislocations are all parallel and uniformly distributed within the crystal. Each dislocation is surrounded by an outer cylindrical surface of radius R across which there is zero flow: R and the dislocation density ρ are related by $R=[\pi\rho]^{-\frac{1}{2}}$. The drop in the concentration ΔC from the initial value C_0, at the outer radius, is then given by

$$\frac{\Delta C}{C_0}=1-\frac{2}{R}\sum_{n=0}^{\infty}\frac{\exp(-Dt\alpha_n^2)J_1(R\alpha_n)J_0(r_0\alpha_n)}{\alpha_n[J_0^2(r_0\alpha_n)-J_1^2(R\alpha_n)]}, \quad (12)$$

where $\alpha_n(n=0, 1, 2, \cdots)$ are the positive roots of

$$J_0(\alpha r_0)Y_1(\alpha R)=J_1(\alpha R)Y_0(\alpha r_0), \quad (13)$$

and we have assumed that C_s is small compared with C_0; this is valid for aluminum levels exceeding 10^{17} atoms/cc. $\Delta C/C_0$ is plotted in Fig. 4 against the dislocation density ρ. The experimental results are in agreement with this curve provided the dislocations are introduced into the crystals during growth. Dislocations in plastically deformed crystals were not observed to act as sites for aluminum precipitation; this observation is discussed in Sec. 5.

In dislocation-free crystals, and in regions of very low dislocation density in the normal crystals, needle-shaped precipitates, oriented with their major axis parallel to the ⟨110⟩ directions, are observed (Fig. 7). The sites of such random precipitates may well be small dislocation loops created as a result of the aggregation and collapse of vacancies during the growth of the crystal.

Crystals Containing Internal Boundaries

The effect of various internal boundaries on the mode of precipitation has also been examined. In very low angle tilt boundaries, the individual edge dislocations are easily resolved, and are decorated to the same extent as the isolated dislocations in the same crystals (see Fig. 5). As the angle of tilt increases, the n-type regions round each dislocation eventually overlap to produce a continuous planar region of n-type material. Such a planar region is observed adjacent to the {331} boundary. This interface has considerable misfit and provides ideal sites for the the precipitation of a second phase, and in fact infrared micrographs show a planar sheet of precipitate on this boundary; it is seen in Fig. 6 that small deviations from planar symmetry are pro-

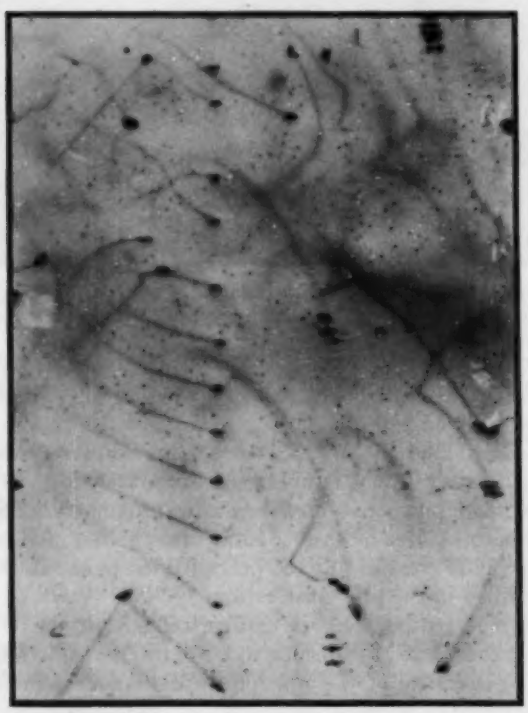

FIG. 5. Precipitation on the dislocations in a low angle tilt boundary, showing correlation with surface features produced by etching. Transmission infrared: ×150.

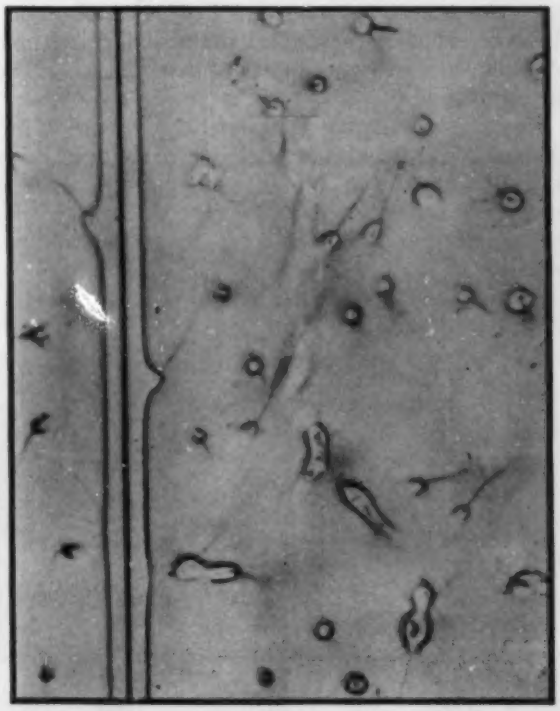

FIG. 6. Depletion of aluminum in the neighborhood of a semi-coherent boundary and around isolated dislocations as revealed by etching. Transmission infrared: ×320.

FIG. 7. Precipitation on isolated dislocations and on dislocations lying against a coherent twin boundary. Also random precipitates in dislocation-free regions. Transmission infrared: ×160.

duced by the extra depletion occurring round isolated dislocations which run into the boundary. In regions very close to the boundary, little precipitation is observed, which suggests that the boundary is a more favorable site for precipitation than the individual dislocations.

Figure 7 shows what is apparently decoration on a coherent {111} twin boundary. Higher resolution micrographs taken with visible light on thinned specimens, however, indicate that the decoration is caused entirely by precipitation on dislocations lying against the twin boundary. This is confirmed by the geometry of the *p-n* junctions observed along the boundary (see Figs. 8 and 9). Dislocations impinging against twin boundaries have also been reported by Dash[18] who used the copper decoration technique.

TABLE II. Time of heat treatment at various temperatures.[a]

Temperature (°C)	Time (hr)	Diffusion length $(Dt)^{\frac{1}{2}}(\mu)$
700	950	0.05
800	300	0.20
900	300	0.97
950	470	2.5
1000	170	2.9
1050	110	4.1
1100	88	6.5
1150	16	4.6
1200	43	12.5
1250	16	11.8
1300	7	12.6
1350	16	27.0

[a] Values of the diffusion coefficient D have been extrapolated from the results of Fuller and Ditzenberger.[17]

4. SURVEY OF PRECIPITATION IN THE TEMPERATURE RANGE 700°–1350°C

Considerable variation in the type of precipitation is observed over the temperature range examined. To make strict comparison between observations at different temperatures, it would be desirable to vary the time of heat treatment so as to maintain a constant diffusion length $(Dt)^{\frac{1}{2}}$. At the lower temperatures this is not practicable, although as can be seen from Table II, the time of heat treatment has been increased substantially compared with the higher temperatures. Results have been obtained for crystals containing aluminum and phosphorus over the temperature range 700° to 1350°C.

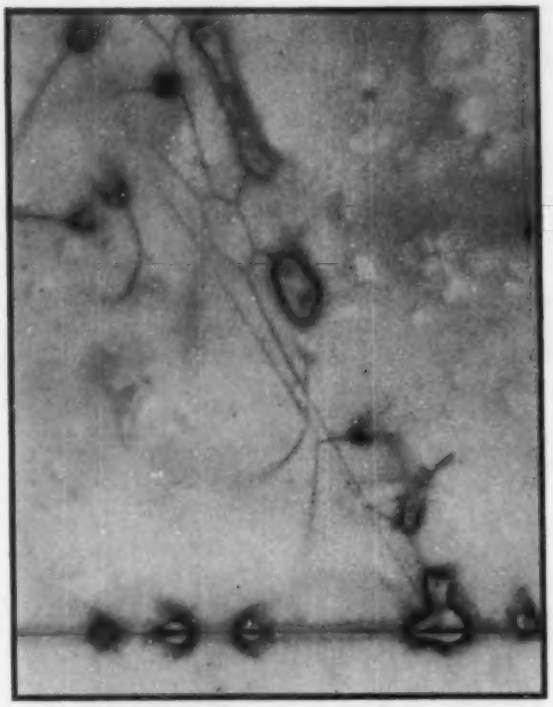

FIG. 8. *P-n* junctions round dislocations lying against a twin boundary and precipitation on a hexagonal network. Transmission infrared: ×400.

No precipitation is observed after prolonged heating at temperatures above 1350°C. In the temperature range 1200° to 1300°C, the precipitation behavior is as described in the previous section.

As the temperature is further reduced from 1200° down to 1100°C, the dislocations are still decorated, but the appearance of the precipitate undergoes a radical

[18] W. C. Dash, *The Growth and Perfection of Crystals*, edited by R. H. Doremus, B. W. Roberts, and D. Turnbull (John Wiley & Sons, Inc., New York, 1958).

change as shown in Fig. 10. The precipitation along the dislocation line is now continuous and, in addition, the line is surrounded by a cloud of globular precipitate particles. The estimated number of impurity atoms along the dislocation line shown in Fig. 10 is about four times greater than that shown in Fig. 1, even though the diffusion length in the former is about half of that in the latter. *P-n* junctions are again observed round individual dislocations.

At about 1000°C, precipitation on the dislocations is considerably reduced although there is still heavy precipitation on semi-coherent boundaries. There is also precipitation at random sites throughout the bulk crystal; this consists of two types: (a) needle-shaped as found at the higher temperatures in dislocation-free

FIG. 9. Electron micrograph of a *p-n* junction around a group of dislocations lying along a coherent twin boundary. ×5700.

regions, and (b) globular-shaped particles. Some of these crystals showed large areas of complete conversion from *p*-type to *n*-type conductivity, as determined by the hot probe method and etching. Between 900° and 950°C, the results are similar apart from the absence of detectable precipitation on the dislocations. At the lowest temperatures, 700° to 800°C, only very slight precipitation was observed, and this occurred entirely on the dislocations; all these crystals had completely converted to *n* type. Similar conversion in aluminum-doped silicon at these lowest temperatures has been previously observed and interpreted as a molecular reaction.[19]

[19] C. S. Fuller and F. H. Doleiden, J. Appl. Phys. **29**, 1264 (1958).

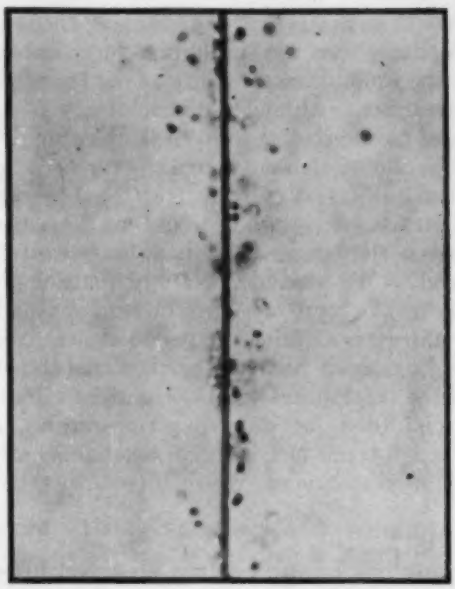

FIG. 10. Precipitation on and around an isolated dislocation after annealing at 1100°C for 88 hrs. Visible transmission: ×2500.

Electron micrographs of globular and needle-shaped precipitates produced by heat treatment at 1000°C are shown in Fig. 11. No diffraction pattern could be obtained from these particles, suggesting a highly disordered structure, and hence it was not possible to obtain any information concerning their composition by this means.

5. DISCUSSION

The solubility of aluminum in silicon has been previously determined as 10^{19} and 5.10^{17} atoms/cc at 1250°

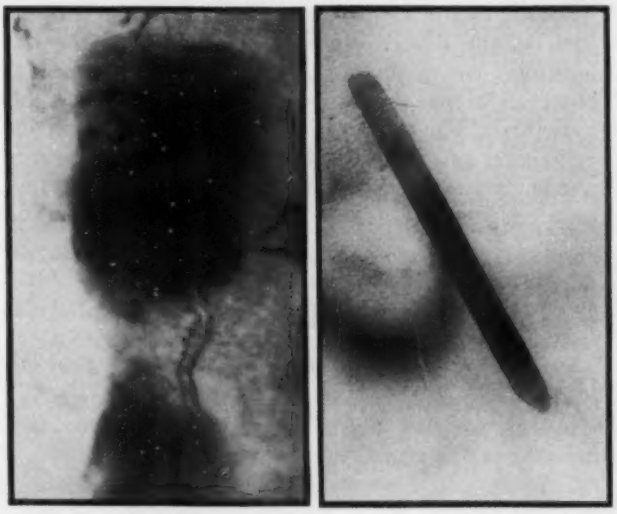

(a) (b)

FIG. 11. Examples of (a) globular, (b) needle-shaped random precipitates. Transmission electron micrographs: (a) ×72 000, (b) ×100 000.

and 700°C, respectively.[20–22] It is clear, therefore, that the aluminum level used in the present experiments was below the equilibrium solubility at the temperatures of heat treatment. Although this solubility is probably exceeded during cooling to room temperature, virtually no migration of aluminum could occur because of the very small diffusion coefficient at these low temperatures. Hence, precipitation would not be expected on the basis of retrograde solubility as in the case of copper in silicon.[8,23] We conclude, therefore, that the precipitation occurs as a result of a chemical reaction and that the precipitates grow during the period of heat treatment.

The discrepancy between the calculated and observed size of the precipitates and the transitions in the mode of precipitation, at different temperatures, can be explained in terms of a chemical reaction involving the precipitation of oxygen. We shall consider the reaction

$$\mathrm{Si}+x\mathrm{O} \rightleftharpoons \mathrm{SiO}_x \qquad \text{(I)}$$

where any precipitated oxide is presumed to be stabilized by the relatively small concentration of aluminum; the strength of the aluminum-oxygen bond is known to be greater than the corresponding bond strengths between silicon-oxygen and other group III or V elements and oxygen.[6,7] Our observations of a high density of random precipitates at 1000°C and complete absence of precipitates at 1350°C are in agreement with the known temperature dependence of reaction I.[24] To correlate the observed precipitation behavior at intermediate temperatures with *I*, we invoke a pressure dependence of the free energy of the reaction. It has been shown, in fact, that oxygen occupies interstitial sites in silicon,[25,26] and hence an increase in volume is to be expected on the formation of the oxide complex. As the temperature is increased above 1000°C, the equilibrium will be displaced gradually towards the left-hand side of *I* except in regions of reduced pressure such as the dilated regions associated with the dislocations. Heavy uniform precipitation at 1100°C was observed along the dislocations in support of this hypothesis. The compressive stresses set up round the cylindrical precipitate will facilitate the collapse into sessile dislocation loops of any vacancy aggregates that form in this region as a result of random diffusion processes. The dilated regions associated with such loops can then act in the same way as the original dislocation; this provides a possible explanation for the cloud of globular precipitates found in such regions. At the higher temperature of 1250°C the pressure effect should be relatively smaller, and only discrete precipitates distributed along the dislocation are observed. At this higher temperature, the glissile motion of dislocations is more favorable and therefore any local stresses may be relieved by prismatic punching.[27] This is a probable explanation of the ⟨110⟩ spikes associated with some of the precipitate particles.

The observation that dislocations introduced into the crystal by deformation do not act as sites for precipitation at 1250°C suggests that the cores of ingrown dislocations contain impurities picked up from the melt, which act as nuclei for subsequent growth of the precipitates; evidence for this has also been given previously by Dash.[28]

Although the precipitation results appear to follow the behavior of oxygen rather well, some preliminary results, using oxygen-free crystals grown without a silica crucible,[29] indicate that precipitation still occurs when aluminum is present. The interpretation of these results must involve some other impurity such as carbon, which may also be involved in the precipitation in crystals containing oxygen.

Finally, the formation of the *p-n* junctions around crystal defects by a controlled process suggests a method for the practical realisation of various types of analogue transistors as originally proposed by Shockley[30] and others. In particular, a planar *p-n-p* structure formed about the semicoherent boundary may be used as a field effect device and an array of cylindrical *p-n* junctions about dislocations forming a low angle tilt boundary may be used to make an analogue triode.

6. ACKNOWLEDGMENTS

The authors wish to thank Mr. D. P. R. Petrie and Mr. R. L. Rouse for their encouragement, and particularly the latter for his valuable comments throughout the course of the work. We are also indebted to Mr. D. B. Gasson for growing the crystals, and various other colleagues for their assistance. Thanks are also due to Dr. T. E. Allibone, F.R.S., Director of the Laboratory, and to the Admiralty for permission to publish this paper.

[20] R. N. Hall, Phys. Chem. Solids **3**, 63 (1957).
[21] D. Navon and V. Chernyshov, J. Appl. Phys. **28**, 823 (1957).
[22] R. C. Miller and A. Savage, J. Appl. Phys. **27**, 1430 (1956).
[23] J. D. Struthers, J. Appl. Phys. **27**, 1560 (1956).
[24] W. Kaiser, Phys. Rev. **105**, 1751 (1957).
[25] W. Kaiser, P. H. Keck, and C. F. Lange, Phys. Rev. **101**, 1264 (1956).
[26] H. J. Hrostowski and R. H. Kaiser, Phys. Rev. **107**, 966 (1957).
[27] A. S. Parasnis and J. W. Mitchell, Phil. Mag. **4**, 171 (1959).
[28] W. C. Dash, J. Appl. Phys. **29**, 705 (1958).
[29] D. B. Gasson, Proc. Inst. Elec. Engrs. (London) **106B** (1959) (to be published).
[30] W. Shockley, Proc. Inst. Radio Engrs. **40**, 1365 (1952).

JOURNAL OF APPLIED PHYSICS VOLUME 31, NUMBER 4 APRIL, 1960

Production and Demonstration of Atomically Clean Metal Surfaces

H. D. HAGSTRUM AND C. D'AMICO
Bell Telephone Laboratories, Murray Hill, New Jersey

(Received November 6, 1959)

Ion bombardment as a means of cleaning solid surfaces has been tested by applying it to the metal tungsten. The test, which showed the resulting surface to be clean, is a sensitive one because atomically clean tungsten is very reactive to the common gases. The test is definitive since it is performed on a material for which there is overwhelming evidence that another means, namely heating, does produce an atomically clean surface. The phenomenon used in this work to observe surface conditions during the cleaning procedures is the Auger-type ejection of electrons by slowly moving positive ions. This is again shown to be a sensitive means of detecting surface contamination. Data on the electron release by ions from heavily contaminated metal surfaces are reported.

I. INTRODUCTION

IN the field of surface phenomena, considerable attention is being paid to the production and demonstration of atomically clean solid surfaces in vacuum. Certainly, this is an extremely important step in the achievement of the kind of surface control which is essential to the proper study of many surface effects. Means used to achieve the atomically clean surface have been heating, ion bombardment, and cleavage.

The atomically clean surface is in many cases extremely reactive to minute traces of adsorbable gases and vapors. It is for this reason that the demonstration of atomic cleanliness and the careful documentation of the experimental methods used can hardly be overdone. It is a primary purpose of this paper to present work in which ion bombardment, as a means of surface cleaning, has been tested in the case of tungsten. This method has been used largely to clean semiconductor surfaces, which when clean appear not to be as reactive as are clean metal surfaces.[1,2] For this reason, a test of the method on a refractory metal which is highly reactive to ambient gas should be a particularly sensitive one. Furthermore, there is decisive evidence that the tungsten surface produced by heating is atomically clean. Thus, if one possesses a sensitive means of detecting surface contamination, it is possible to decide for this solid whether the ion bombardment technique is successful or not. The success of this test will perhaps increase the confidence with which sputtering can be relied upon to clean surfaces in which such a direct comparison with another cleaning method is not possible. The present work also documents further the care required in the use of the sputtering technique.

The surface sensitive phenomenon used in this work is the ejection of electrons in the Auger-type neutralization of slowly moving positive ions at the surface. The present work, as well as work already published (Sec. IV), demonstrates this effect to be capable of detecting changes in surface concentration of foreign atoms which amount to a few percent of a monolayer. The present experiment demonstrates that ion bombardment produces the same surface as is produced by high temperature flashing. Data on the release of electrons by the neutralization of ions at heavily contaminated metal surfaces, previously unpublished, also are presented (Sec. VII).

In this work, we accept as atomically clean the surface of tungsten, which has been thoroughly outgassed and heated to above 2200°K for a few seconds in vacuum in the absence of soluble impurities. This position has been taken by a number of investigators over a period of many years. There are many arguments and much experimental work bearing on the question. Several review papers have brought together the evidence from specific fields. A brief, yet comprehensive statement of the reasons for believing that the tungsten surface can be cleaned by heating alone is attempted here in Sec. III.

Farnsworth and others[3] have tested the ion bombardment method of cleaning for metals and semiconductors by using low-energy electron diffraction as the means of detecting surface contamination. This technique depends upon the low penetration of surface layers and the consequent sensitivity of the diffracted beams to their constitution. This sensitivity was demonstrated by Farnsworth[4] using the deposition of small quantities of one metal upon the surface of another. Even when the structure of the surface contamination is identical with the supporting lattice, it can be detected by slight changes in the inner potential or in the spacing of the layer with respect to the underlying lattice.[3] The direct comparison of diffracted beams from a tungsten surface cleaned by sputtering with such beams from the same surface cleaned by heating to high temperatures has not been made.

Kingdon and Langmuir[5] studied the effect of ion bombardment in removing thorium from the surface of a thoriated tungsten filament. Langmuir[6] had shown earlier that the thermionic emission of tungsten at

[1] J. A. Dillon, Jr., and H. E. Farnsworth, J. Appl. Phys. **28**, 174 (1957); **29**, 1195 (1958).
[2] R. E. Schlier and H. E. Farnsworth, J. Appl. Phys. **30**, 917 (1959).
[3] H. E. Farnsworth, R. E. Schlier, T. H. George, and R. M. Burger, J. Appl. Phys. **29**, 1150 (1958).
[4] H. E. Farnsworth, Phys. Rev. **49**, 605 (1936).
[5] K. H. Kingdon and I. Langmuir, Phys. Rev. **22**, 148 (1923).
[6] I. Langmuir, Phys. Rev. **20**, 107 (1922).

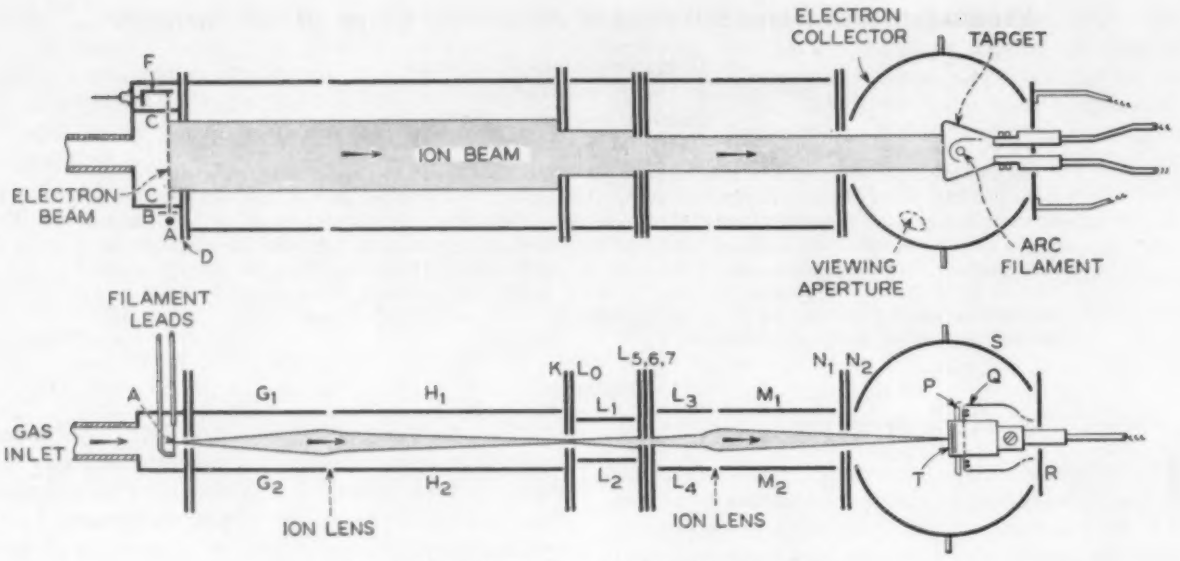

FIG. 1. Schematic diagram of experimental apparatus.

1500°K was increased by 10^5 when a monolayer of thorium was deposited on its surface and studied the relationship of this emission increase to surface concentration of thorium. By using the emission at 1500°K as a measure of the amount of thorium present, Kingdon and Langmuir evaluated ion bombardment at room temperature as a means of removing the surface thorium. They showed that bombardment with any one of several gaseous ions did, in fact, remove the thorium. Emphasis in this work was placed on the rate of removal of thorium by different ions of differing velocities, and essentially no attention was paid to the question of ultimately achieving the atomically clean condition.

Considerable work has been done in studying the phenomenon of sputtering and recent work has been carried out under rigorously controlled conditions.[7] High density sputtering has been relied upon to keep the surface clean while the sputtering proceeds but no attempt made to demonstrate that the surface thus produced is atomically clean.

II. EXPERIMENT AND APPARATUS

Release of electrons in an Auger-type process when positive ions are neutralized at a metal surface is the surface sensitive phenomenon used in this work. One measures both total yield of ejected electrons and the kinetic energy distribution of such electrons for a given ion of known incident kinetic energy. The phenomenon has been discussed theoretically elsewhere[8] and it has been studied experimentally for tungsten[9] and molybdenum[10] in the atomically clean condition.

The data reported in this work were obtained with an instrument like that shown schematically in Fig. 1. The measurements reported in Sec. IV were made on the linear tube (Instrument III) already described.[11] The work on sputtering (Sec. V) was performed with a rebuilt version of the apparatus used in the study of the effect of monolayer adsorption on the ejection phenomenon.[12]

An electron beam from the filament A is used to bombard a noble gas. Ions formed are drawn out and focussed into a beam in the G-H and L-M lenses. The ion beam impinges on the surface on a tungsten ribbon target T situated at the center of the spherical electron collector S. Measurements of the currents to electrodes S and T as functions of the voltage V_{ST} between them, enables one to determine total yield γ_i of electrons ejected per incident ion and $N_0(E_k)$, the kinetic energy distribution of these electrons.[9,11] Both γ_i and $N_0(E_k)$ are very sensitive to the conditions prevailing at the metal surface.

Heating of the target is accomplished by passing ac current directly through the ribbon. Sputtering is accomplished by means similar to those employed by Wehner.[7] The arrangements for sputtering are shown in Fig. 1 at P and Q and in more detail in Fig. 2. An arc is run between the filament Q and the sphere S at a pressure of neon near 10^{-2} mm Hg (not accurately measured). This arc discharge commonly runs at 60 v and 120 ma. A magnetic field of about 100 oe is used to confine the arc plasma inside the sphere S. The target is protected by the shield plate P from possible small amounts of material evaporated from the arc filament. When the target is put at a negative potential of 100 v relative to the arc plasma, it is bombarded

[7] G. K. Wehner, Advances in Electronics and Electron Phys. **7**, 239 (1955); Phys. Rev. **108**, 35 (1957).
[8] H. D. Hagstrum, Phys. Rev. **96**, 336 (1954).
[9] H. D. Hagstrum, Phys. Rev. **96**, 325 (1954); **104**, 317 (1956).
[10] H. D. Hagstrum, Phys. Rev. **104**, 672 (1956).
[11] H. D. Hagstrum, Rev. Sci. Instr. **24**, 1122 (1953).
[12] H. D. Hagstrum, Phys. Rev. **104**, 1516 (1956).

uniformly with a current of positive ions of density 3–5 ma/cm². By use of Wehner's sputtering yield of 0.01 atom per ion for 100 ev Hg^+ on tungsten,[7] one calculates a sputtering rate of approximately a monolayer per second for the current densities used here. This is undoubtedly greater than the rate for neon, but not by as much as proportionality in rate to atomic weight would predict.[7] In this work, except as noted, each sputtering was carried out for one minute, thus removing between 6 and 60 monolayers.

In Wehner's work, a large density of sputtering ions was maintained in order to overcome possible formation of chemisorbed layers on the surface during the sputtering experiment. In the present work, conditions are more stringent since we want to look at the tungsten surface with a surface sensitive phenomenon after sputtering has been completed and the sputtering gas pumped out or its pressure reduced. The fastest Auger measurement could be made with Ne^+ ions since, in this case, the pressure of the sputtering gas in the target region need only be reduced rapidly from the pressure (ca 10^{-2} mm Hg) used in sputtering to that (10^{-6} to 10^{-7} mm Hg) appropriate to the Auger measurements. The first measurement of γ_i was normally made about two minutes after the conclusion of the sputtering period. In order to prevent adsorption on the highly reactive clean tungsten target during this period, it was necessary to reduce the background pressure to very low values (ca 10^{-10} mm Hg), to outgas thoroughly the region of the arc filament and the filament shield, and to admit the sputtering gas over a renewable molybdenum getter. Achieving clean conditions during sputtering was particularly difficult because one wanted to test the procedure on a target which had *not* been heated to high temperature and thus contained dissolved gas. The target used in the sputtering experiments had been heated no hotter than 600°K during baking of the apparatus before sputtering began. This target and the one used in the heating experiments had been degreased in a trichloroethylene vapor bath, heated in wet hydrogen for 15 min at 1500°K, and exposed to room air before being installed in the experimental apparatus.

In this work, ions are used to sputter the surface and also to eject electrons from the surface in the Auger ejection measurements. In the latter, the ion bombardment density is less than 10^{-6} that used in sputtering. Because of this and also because ions of low kinetic energy (10 ev) are employed for the most part, no detectable sputtering of the surface occurs during the Auger measurements.

III. EVIDENCE THAT HEATING ALONE WILL CLEAN THE TUNGSTEN SURFACE

As indicated in the Introduction, cleaning of tungsten by heating is the standard with which the sputtering results are compared. In this section we shall review the evidence that heating under proper conditions will produce an atomically clean tungsten surface.

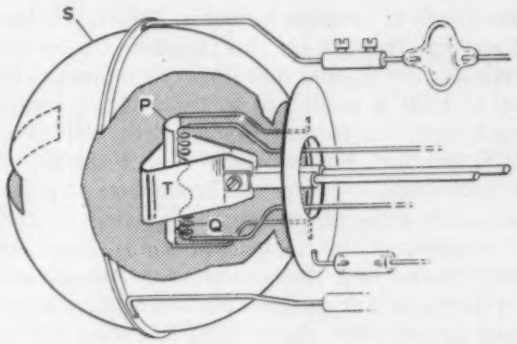

FIG. 2. Cutaway view of the electron collector *S*, showing target *T*, arc filament *Q*, and shield *P*.

Based on the work of many people extending over a period of many years, one can make two definitive statements concerning the cleaning of tungsten by heating. These are:

(1) *In the absence of contaminating impurity atoms which are soluble in the tungsten lattice, the atomically clean surface can be produced by heating for times of the order of seconds to temperatures in excess of 2200°K.*

(2) *Surface contamination by soluble impurities of an amount as small as a few percent of a monolayer can be detected and means of removing such contamination devised, in every case yielding the same surface condition as obtained by the procedure of statement (1).*

It is clear that one must distinguish possible contaminants on the basis of whether they are soluble in the tungsten lattice or not. We shall discuss the case of insoluble impurities in the first six numbered items below, that for soluble atoms in items 7 and 8.

1. Because tungsten, as pointed out by Langmuir,[13] can be heated to 3000°K, at which temperature "all other substances vaporize," one should expect to be able to break the surface bond with any insoluble atom.

2. In observing the tungsten surface with any of a number of surface sensitive phenomena, it is found that heating to 2200°K is sufficient to produce a reproducible surface in a matter of seconds, heating to higher temperatures making no further change.

3. The behavior described in item 2 is observed in extensive experiments with the adsorption of oxygen which one would expect to make strong bonds to the surface tungsten atoms. Langmuir and Villars[14] found that cesium on oxygenated tungsten had a lower work function than cesium on tungsten alone. They used this phenomenon to study the adsorbed oxygen and found that at 2070°K one half of the oxygen disappeared in 20 sec. Müller,[15] using the field electron microscope he had invented, first recognized the emission pattern

[13] I. Langmuir, J. Chem. Soc. (London) 511 (1940).
[14] I. Langmuir and D. S. Villars, J. Am. Chem. Soc. **53**, 486 (1931).
[15] E. W. Müller, Z. Physik **106**, 541 (1937).

characteristic of tungsten heated to 2200°K. He found[16] that oxygen remains on the tungsten tip for a few seconds at 2100°K, and that the oxygen film can be reduced at 1500°K in 10^{-5} to 10^{-3} mm Hg of hydrogen. In each case, the pattern characteristic of heating to 2200°K returned. Further work[17,18] with the field electron microscope confirms the production of a stable, reproducible emission pattern by heating to 2200°K after exposure of the tip to a variety of gases, which themselves and their dissociation fragments are insoluble in tungsten. The emission pattern is independent of heating temperature above 2200°K except for small changes in relative sizes of dark areas associated with surface diffusion of tungsten itself. Work with photoelectric emission[19,20] confirms these conclusions, as do studies by Roberts[21] using accommodation coefficient measurements to study the presence of oxygen films on tungsten.

4. Heavy evaporation of tungsten which can be observed using pulsed field emission techniques[22] produces no different surface from the 2200°K heating.

5. A very important piece of evidence comes from the field desorption work of Müller. After showing[23] that Ba can be pulled off tungsten yielding the "clean" condition at 1.2×10^{8} v/cm, he went on to demonstrate that tungsten itself desorbs at 800–900°K at fields of $2\text{–}3\times10^{8}$ v/cm,[24] and at room temperature at fields of 5×10^{8} v/cm.[25] After annealing, the emitter point to produce the proper geometry by surface migration, it was shown that the same "clean "pattern was obtained after these drastic field desorption techniques.

6. The adsorption characteristics for tungsten after heating to 2200°K are what one would expect for the atomically clean condition.[26–28] The surface is highly reactive for a time necessary to adsorb a number of molecules which is reasonably related to the surface structure of the tungsten.

7. Concerning the removal of soluble atoms (principally the electropositive atoms and carbon) from the tungsten surface, the evidence is equally strong. Langmuir[29] found that at temperatures greater than 2200°K, thorium evaporates faster than it comes to the surface from the interior and can be removed completely when the internal reservoir is depleted. Similarly, Becker[30] found all surface barium to leave tungsten in 5 min at 1600°K, and Langmuir and Taylor[31] found that all cesium could be kept off a tungsten surface at 1800°K even when cesium atoms were arriving at a rate of 10^{15} atoms/cm²/sec.

8. By using the field electron microscope, Müller[17] studied the migration, solution, and evaporation of carbon which had been deposited on tungsten by the decomposition of organic vapors. Klein[32] showed that carbon can be oxidized on tungsten changing the field emission pattern from that of carbon on tungsten to that of oxygen on tungsten. More recently, carbon on tungsten has been studied by its formation of CO and CO_2 when oxygen is introduced and the metal heated.[33,34] This work and the earlier field emission studies enable one to conclude the following. Carbon from inside the tungsten lattice comes to the surface over a range of temperatures, say 1400° to 2800°K. At the high temperature end of this range, the surface carbon evaporates faster than it arrives from the inside and the surface is clean as evidenced by its condition immediately upon cooling. This is similar to the results for thorium (item 7) where the absence of thorium on the surface at the high temperature is demonstrated by the thermionic emission characteristics. At lower temperatures carbon can accumulate on the surface. However, it can be shown that the internal reservoir can be depleted and the surface freed of carbon even though the process is lengthier and the temperatures required higher than for other impurities.

One may conclude from the evidence given above that either the tungsten surface produced by heating is reproducibly the same or the methods of looking at it are insensitive, which latter statement is amply disproved. Reproduciblity under such a great variety of conditions and in so many different experiments would appear to preclude the possibility of some constant contaminant appearing in all. One is reduced to the impossible task of finding what atoms could possibly have remained on surface through such varied and vigorous treatments.

IV. EFFECTS OF HEATING UPON THE AUGER EJECTION RESULTS

We turn now to discuss how the sequence of surface conditions during cleaning by heating appears through the "eyes" of the Auger ejection phenomenon. The experimental measurements of total yield γ_i and kinetic energy distribution, $N_0(E_k)$ are plotted in Figs. 3 and 4, respectively. Experimental conditions for the curves in each of these figures are as follows: curve 1 is for the heavily contaminated surface of the target after instal-

[16] E. W. Müller, Z. Elektroch. **59**, 372 (1955).
[17] E. W. Müller, Ergeb. exakt. Naturwiss. 27, 290 (1953); R. H. Good, Jr., and E. W. Müller, *Handbuch der Physik* (Springer Verlag, Berlin, 1956) Vol. XXI, pp. 206–214.
[18] J. A. Becker and R. G. Brandes, J. Chem. Phys. **23**, 1323 (1955).
[19] L. Apker, E. Taft, and J. Dickey, Phys. Rev. **73**, 46 (1948).
[20] J. Eisinger, J. Chem. Phys. **27**, 1206 (1957); **28**, 165 (1958); **29**, 1154 (1958).
[21] J. K. Roberts, Proc. Roy. Soc. (London) **A152**, 464 (1935).
[22] J. K. Trolan, J. P. Barbour, E. E. Martin, and W. P. Dyke, Phys. Rev. **100**, 1646 (1955).
[23] E. W. Müller, Naturwiss. **29**, 533 (1941).
[24] E. W. Müller, Z. Physik. **131**, 136 (1951).
[25] E. W. Müller, Phys. Rev. **102**, 618 (1956).
[26] J. A. Becker and C. D. Hartman, J. Phys. Chem. **57**, 153 (1953).
[27] J. A. Becker, Advances in Catalysis **7**, 135 (1955).
[28] G. Ehrlich, J. Phys. Chem. **60**, 1388 (1956).
[29] I. Langmuir, Phys. Rev. **22**, 357 (1923).
[30] J. A. Becker, Bell System Tech. J. **30**, 907 (1951).
[31] I. Langmuir and J. B. Taylor, Phys. Rev. **44**, 423 (1933).
[32] R. Klein, J. Chem. Phys. **21**, 1177 (1953).
[33] R. E. Schlier, J. Appl. Phys. **29**, 1162 (1958).
[34] J. A. Becker, E. J. Becker, and R. G. Brandes (to be published, private communication).

lation in the experimental tube and before any baking; curve 2 was taken after heating to 800°K; curve 3, after heating to 1330°K; and curve 4, after further outgassing at 1500°K and flashing to 2200°K. It is clear that heating has produced drastic changes in the Auger data. Curves 4 of Figs. 3 and 4 are the same as the characteristics for clean tungsten published earlier.[9] Curves like 1 and 4 of Figs. 3 and 4 have also been obtained for He^+ ions on molybdenum and for Ne^+ ions on tungsten. They are qualitatively similar to the results shown here for He^+ on tungsten. Evidence presented elsewhere[12] shows that contamination of the tungsten surface by the adsorption of a monlayer of gas can be monitored by its effect on the Auger characteristics. The method is sensitive enough to detect changes in surface concentration of less than 5% of a monolayer.

It was found that heating to temperatures greater than 2200°K produced no further change in the Auger measurements. The above results also show that heating to appreciably lower temperatures for long periods of time does not produce the final condition. These conclusions are in excellent agreement with the many other evidences of cleaning tungsten by heating listed above. Thus we take the γ_i and $N_0(E_k)$ data of curves 4 of Figs. 3 and 4, respectively, to be characteristic of the atomically clean surface.

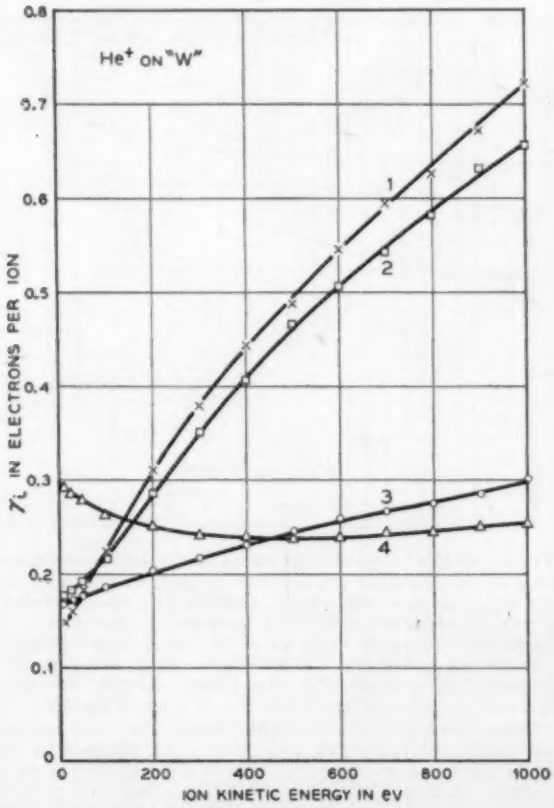

FIG. 3. Yield γ_i of electrons ejected by He^+ ions from tungsten in various surface conditions during cleaning by heating. Experimental conditions corresponding to these curves are specified in the text.

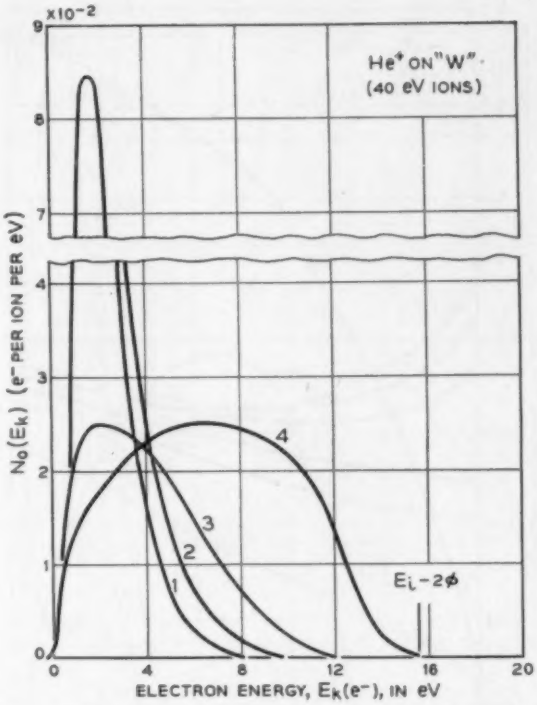

FIG. 4. Kinetic energy distributions $N_0(E_k)$ of electrons ejected by 40-ev He^+ ions from tungsten. The surface conditions for curves 1–4 are the same as those for the corresponding curves of Fig. 3. The energy E_i-2φ indicated on the E_k scale is the maximum possible kinetic energy the electrons can attain in the Auger ejection process.

V. CLEANING OF TUNGSTEN BY ION BOMBARDMENT

The data presented in Fig. 3 show that the procedure of cleaning by heating takes the γ_i dependence on ion energy through a recognizable sequence. It starts for the dirty surface with a curve which rises sharply with incident ion energy and proceeds to the dished curve for the clean surface. During the ion bombardment experiments in a different apparatus and with a different target, considerably more data of this kind were obtained. These are shown in Fig. 5. Here are shown a number of γ_i curves obtained with the surface in a variety of conditions. Each curve fits into the sequence from contaminated (curve 1) to clean (curve 7) in a position which seems appropriate as judged from the experimental conditions. These conditions for the data of Fig. 5 are as follows:

Curve 1: The target has had no other treatment after installation than heating to 570°K for several days. In this condition, the target was undoubtedly also contaminated with some Nichrome *V* metal. This resulted from inadvertant overheating and vaporization of a small section of the electron collector sphere (*S* in Fig. 1) during bombardment of it by electrons from the outside during outgassing procedures.

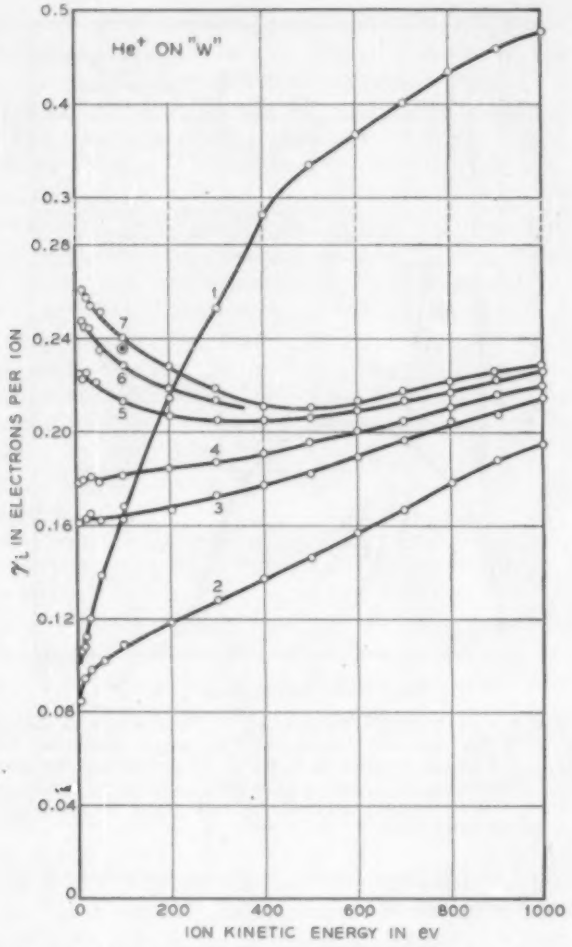

FIG. 5. Sequence of γ_i characteristics taken before, during, and after the sputtering experiments. These show a continuous variation from the contaminated (curve 1) to the atomically clean condition (curve 7). The special point below curve 7 at $E_k = 100$ ev is the highest γ_i reading taken as soon after the sputtering procedure as is experimentally possible (see Fig. 6).

Curve 2: After 26 sputterings of the surface (see Fig. 6), followed by exposure to background gases in the instrument for 64 days.

Curve 3: After four sputterings, followed by heating overnight at 670°K and a period of 1.5 hr at room temperature.

Curve 4: After sputter #7, followed by 4.5 hr at room temperature. Between sputter #6 and #7 the target was heated to 960°K overnight. This apparently degraded the vacuum conditions to such an extent that a single 1-min sputter (#7) did not clean the surfaces. This is most likely due to the release during the sputtering of gas from surrounding parts which was subsequently readsorbed rather than to failure of the sputtering to clean the surface. Curve 1 of Fig. 7 gives further evidence bearing on this.

Curve 5: After sputter #9 followed by 4 hr at room temperature. The target has now been heated more and background vacuum conditions have improved.

Curve 6: After sputter #20, followed by 4.5 hr at room temperature.

Curve 7: After sputter #26, followed by heating to 1500°K and 2000°K for extended periods and flashing to 2350°K. This curve represents the atomically clean condition. It lies a little lower on the γ_i scale than curve 4 of Fig. 3 which is attributed to a small change in amplifier calibration brought about by the acquisition of vibrating reed amplifiers between the two experiments.

The point indicated just below curve 7 at 100-ev ion energy is the highest γ_i reading taken immediately after sputtering (see Fig. 6). The fact that it lies below curve 7 is not taken to mean that sputtering does not clean the surface but that some adsorption has taken place in the interval between the conclusion of sputtering and the reading of γ_i. A sequence of γ_i characteristics similar to that for He^+ in Fig. 5 has also been obtained for Ne^+.

The trend of the $N_0(E_k)$ characteristic during the sputtering experiments is shown in Fig. 8. Here, the experimental conditions are:

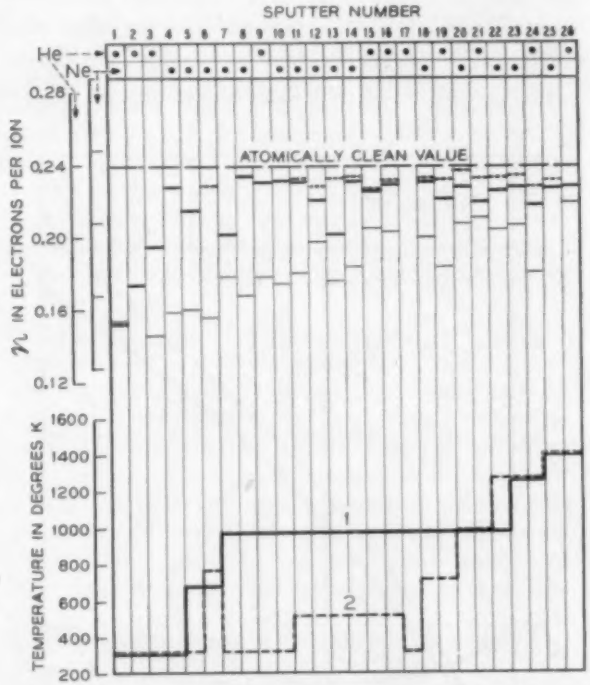

FIG. 6. Graph of γ_i measurements and target temperatures during 26 sputterings of the tungsten surface. At the top is indicated the sputter number. Below this are plotted γ_i values for He^+ and Ne^+ ions to scales which have been adjusted vertically to make the atomically clean value for 100-ev ions coincide on the horizontal dashed line. The ion used in the γ_i measurement is indicated by the position of the dot either in the "He" row or the "Ne" row immediately below the row of sputter numbers. The light bars (which generally lie lower) indicate the γ_i measurement made before the sputtering took place. The heavy solid bars indicate the γ_i values measured as soon after sputtering as the experiment permits. The heavy dashed bars indicate the γ_i values measured after a subsequent anneal of the target at the temperature indicated in curve 2. The annealing duration for various temperature ranges is indicated in the text. Curve 1 indicates the maximum temperature to which the target has been heated at any time in the experiment up to that point.

Curve 1: Raw target at the start of the experiment.

Curve 2: After 26 sputterings, followed by exposure to background gases for 64 days (corresponds to curve 2 of Fig. 5).

Curve 3: Taken during the interval 12–45 min after the second sputter used to remove adsorbed gas (see Fig. 9 and discussion in Sec. VI). Note that sputtering here has produced the distribution characteristic of the atomically clean surface.

The data of Figs. 5 and 8 have been presented first to establish the fact that cleaning of the tungsten surface, whether by heating or sputtering or both, can be monitored by observing the Auger ejection characteristics. These characteristics can differentiate surface conditions such as heavy initial contamination and monolayer adsorption. When properly calibrated,[12] γ_i for 10-ev ions can provide a quantitative measure of surface concentration of foreign atoms in the range zero to one monolayer.

We shall now discuss the series of sputtering experiments in more detail. Twenty-six sputterings of the surface were carried out in the manner described in Sec. II. The first five were for time durations of 2, 10, 10, 12, and 5 min, respectively, the others for 1 min each. Data on γ_i measurements for 100-ev ions of $^4He^+$

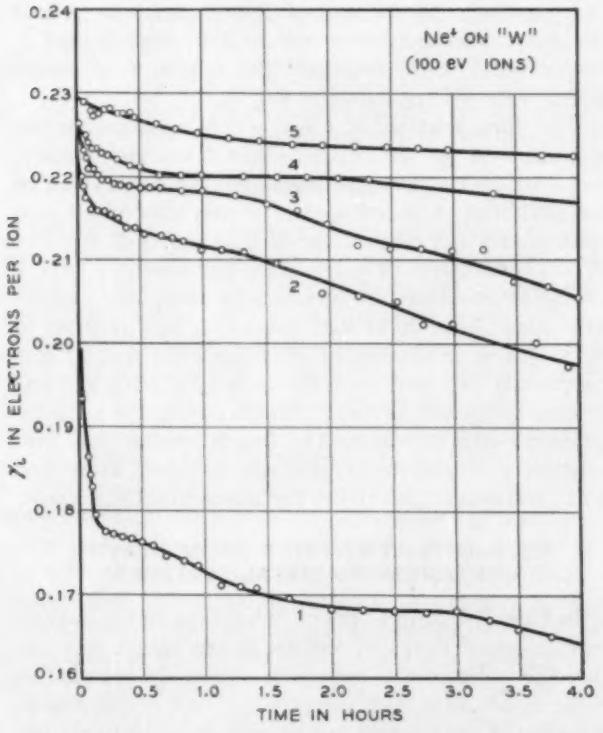

FIG. 7. Curves showing the variation of γ_i with time after annealing on exposure to background gases in the experimental apparatus. Curve 1: after sputter #7 when the vacuum conditions were poorer than normal (see text re: curve 4 of Fig. 5). Curve 2: after sputter #6 and anneal to 760°K for 10 min. Curve 3: after sputter #8 (no anneal). Curve 4: after sputter #13 and anneal to 500°K for 10 min. Curve 5: after sputter #20 and anneal to 960°K.

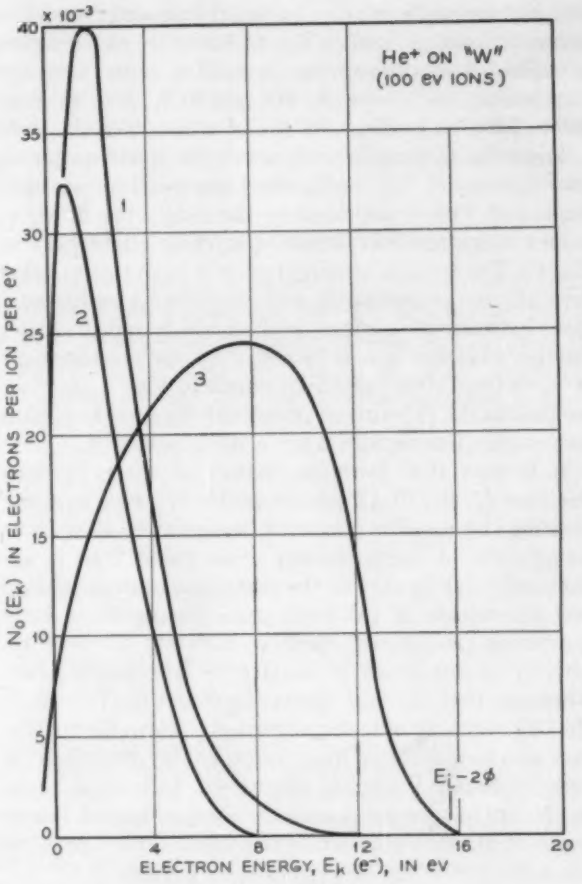

FIG. 8. $N_0(E_k)$ characteristics taken during the sputtering experiments.

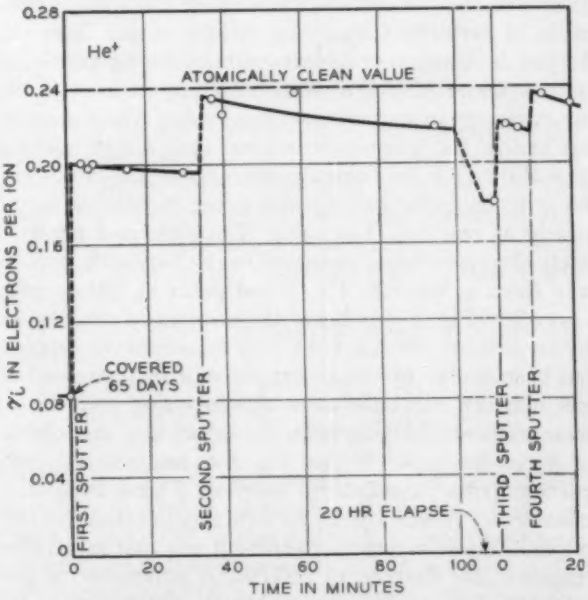

FIG. 9. γ_i values measured during an experiment designed to test the removal by sputtering of gas adsorbed on the atomically clean surface.

and Ne^+ and data relative to target annealing temperatures, etc., are plotted in Fig. 6. Structure of the figure is explained in the caption. Annealing times were approximately as follows. At 500 to 750°K, 5 to 15 min; 960 to 1250°K, 3 min; 1250°K and above, 10-sec flashes.

From Fig. 6, the following trends are apparent during the experiment. The background gas condition steadily improved. This is indicated by the steady rise in the γ_i values measured just before sputtering (light bars in Fig. 6). The trend is apparent even though this γ_i value depends on the processing and exposure to background gases between sputterings, both of which varied widely. Further evidence is also provided by the measurement of γ_i vs time after annealing shown in Fig. 7. Here we see that as the experiment progresses the drop in γ_i with time occurs less rapidly later in the experiment.

It is seen that four sputterings of relatively long duration (2, 10, 10, 12 min, respectively) were required to bring the γ_i value measured immediately after sputtering close to the atomically clean value. This is undoubtedly due in part to the poorer vacuum conditions and the release of gas from parts during these early sputtering procedures. Here we note the extreme reactivity of the clean W surface to adsorbable gases. Note also that the first sputtering didn't improve γ_i at all. The necessity of four sputterings to clean the surface may also have resulted from the probable contamination with Nichrome V already mentioned. In general, these results are in agreement with the observations of Farnsworth et al.[3] that production of a clean surface requires not only sputtering, but rigorous outgassing.

The general conclusion to be drawn from this experiment appears to be the following. Sputtering alone will clean the surface of a refractory metal like tungsten. However, the specific conditions under which the experiment is performed involving release of gas from the heated arc filament or its surroundings during sputtering and/or the admission of adsorbable impurities with the sputtering gas are of extreme importance. These matters are crucial for tungsten which has such a high sticking probability for the common gases. It is less important for semiconductor experiments where the surface is not nearly as reactive. The value of γ_i measured immediately after sputtering (compare heavy bars with atomically clean γ_i value in Fig. 6 and point at 100 ev with curve 7 in Fig. 5) lies below the atomically clean value by an amount which it is entirely reasonable to suppose has been caused by the adsorption of a small amount of gas between the conclusion of sputtering and the γ_i measurement. Judging from the effect of a monolayer of N_2 on the γ_i for W (see Fig. 8 of footnote 12), this contamination amounts to between 5 and 10% of a monolayer. This points up the difficulty in using sputtering as the sole means of cleaning a reactive metal like tungsten. By flashing to 2200°K, it is possible to get readings of γ_i which correspond to about 1% of a monolayer as judged from released gas on repeated flashing.

The results of the present experiment would appear to answer the objection of Tel'kovskii[35a] to the author's previously published work on tungsten.[9] Tel'kovskii has claimed that the tungsten surfaces used were not atomically clean because such surfaces can be obtained only by sputtering. The present work shows sputtered and heated tungsten surfaces to be equivalent as far as the Auger ejection process is concerned. Whereas it is in all probability true that many metals cannot be cleaned by heating alone Tel'kovskii's apparent inclusion of tungsten in the list of such metals also neglects the overpowering evidence listed in Sec. III.

Finally, the question arises as to whether annealing of the tungsten after sputtering has any effect on the Auger characteristics. The evidence appears to be that there was little or no such effect. Apparently the Auger ejection process is not particularly sensitive to possible disarrangement of the surface atoms of a clean surface.

VI. REMOVAL OF ADSORBED GAS BY ION BOMBARDMENT

After the sputtering sequence of Fig. 6 was completed, an experiment was performed to test the effectiveness of sputtering in the removal of gas layers adsorbed on the previously clean surface. The target was allowed to remain unheated for 64 days in an average background gas pressure of 8×10^{-10} mm Hg (equivalent N_2 pressure). At the end of this period, the γ_i and $N_0(E_k)$ characteristics of curves 2 in Figs. 5 and 8, respectively, were obtained.[35] The sequence of events which followed are shown in Fig. 9.

The "first sputter" of Fig. 9 was in neon gas for one minute with 100 ev ions of about 5 ma/cm² density. γ_i for 100 ev He^+ ions rose from 0.082 before this sputter to 0.202 after. A second sputter 35 min later raised γ_i to very nearly the clean value of 0.24 (see Fig. 9). The $N_0(E_k)$ characteristic taken after this sputter (curve 3 of Fig. 8) also shows the surface to be essentially atomically clean. After 20 hr had elapsed, γ_i had dropped to 0.18. The γ_i measurement after the third sputter was incorrectly executed since the neon sputtering gas was inadvertantly left in the apparatus during the γ_i measurement with He^+ ions. The fourth sputter and subsequent γ_i measurement, properly executed, showed γ_i to be restored to essentially the atomically clean value.

VII. ELECTRON EJECTION FROM HEAVILY CONTAMINATED METAL SURFACES[35]

In Figs. 3, 4, 5, and 8 are included data for the heavily contaminated tungsten surface as the target was put into the experimental apparatus. Attention is called to these results here from the point of view of our understanding of the ejection mechanism. It is clear that the γ_i and $N_0(E_k)$ characteristics are far from those for the clean surface and cannot be explained on the basis of the

[35a] V. G. Tel'kovskii, Akad. Nauk SSSR Isvest. Ser. Fiz. **20**, 1179 (1956); Bull. Acad. Sci. USSR **20**, 1070 (1956).

[35] Results reported earlier at the Gaseous Electronics Conference (October, 1954); Phys. Rev. **98**, 56 (1955).

theory of the Auger ejection mechanism.[8] γ_i vs ion kinetic energy is seen to rise rapidly for the contaminated surface in contradistinction to the theoretically predicted fall in γ_i with increasing ion energy for the Auger process at the clean surface. Similarly, the $N_0(E_k)$ distribution for the contaminated surface is very narrow whereas the pure Auger process for the clean surface should yield electrons of energies as high as $E_i-2\varphi$ (ionization energy minus twice the work function). These results are undoubtedly due in part to the difference in distribution over electron energy in the contaminant surface atoms from that in the surface atoms of the clean metal. Even though the ejection process may well be purely Auger in character at the lowest ion energies, the onset of kinetic ejection processes must occur sooner on the ion energy scale for the contaminated surface than for the clean in order to account for the rapid rise in γ_i.[36] Very similar results have been obtained for Ne^+ ions also and for molybdenum targets. These data appear to join on well to data taken at higher ion energies by other investigators, for example, Higatsberger, Demorest, and Nier.[37]

ACKNOWLEDGMENTS

The authors wish to thank J. A. Becker for critical reading of the manuscript and G. K. Wehner for a helpful discussion of sputtering technique.

[36] See the work of P. M. Waters, Phys. Rev. **109**, 1466 (1958).
[37] M. J. Higatsberger, H. L. Demorest, and A. O. Nier, J. Appl. Phys. **25**, 883 (1954).

JOURNAL OF APPLIED PHYSICS VOLUME 31, NUMBER 4 APRIL, 1960

Efficiency of the Plasma Thermocouple*

H. W. Lewis† and J. R. Reitz‡
Los Alamos Scientific Laboratory, Los Alamos, New Mexico
(Received September 10, 1959)

The efficiency of a thermionic converter containing cesium ions is calculated for the regime, in which the plasma density is sufficiently high so that the random current density, $nev/4$, is large compared to the actual current density. Under these circumstances, positive space charge barriers are set up at the electrodes, and the plasma region is many free paths in length. The output voltage V is determined for various currents by a consistent solution of the electrical and thermal conduction problems. The efficiency of the thermocouple is then deduced from the calculated current-voltage characteristic and the appropriate electron temperature distribution. Overall efficiencies up to 32% are predicted for a typical thermocouple circuit.

1. INTRODUCTION

In a previous note,[1] we have discussed the open-circuit voltage obtainable from the plasma thermocouple under conditions in which the space charge is completely neutralized, and a very small current is drawn for the purpose of measurement. We treat here, in the same spirit, the behavior of the thermocouple under load, and will see that the behavior falls naturally into two regimes: in the first, the joule heating of the electrons is not important, and in the second it is. We will also have to treat the barrier heating of the electrons. We refer the reader to the previously cited reference for a preliminary discussion of the space charge barriers that prevail at the cathode and anode of the thermocouple; we will not repeat that discussion. For moderate currents, the electrons that carry the current will not experience any great joule or barrier heating, and we will assume that they are at the temperature of the cathode, which we call T. Then, for a current density j_c at the cathode, the cathode barrier B_c will be increased above the value given in footnote 1 and will be given by

$$B_c=kT\ln\left[\frac{pe}{(j_c(T)-j_c)(2\pi mkT)^{\frac{1}{2}}}\right], \qquad (1)$$

where p is the *electron* pressure in the cell outside the space charge sheath, $j_c(T)$ is the *saturation* emission current density of the cathode in amp/cm², e is the charge of the electron in coulombs, and everything else is in cgs units. This differs from the formula given in footnote 1 only in the appearance of j_c, which was neglected there.

The anode barrier is still given by the previous expression,[1]

$$B_a=kT\ln\left[\frac{pe}{j_a(2\pi mkT)^{\frac{1}{2}}}\right], \qquad (2)$$

where j_a is the current density at the anode, not necessarily the same as j_c because of possible differences in area between the two. In addition, we must take into account the resistive drop in the cell IR, where I is the total current, and R is the resistance, discussed in another previous note.[2]

* Work performed under the auspices of the U. S. Atomic Energy Commission.
† Permanent address: University of Wisconsin, Madison, Wisconsin.
‡ Permanent address: Case Institute of Technology, Cleveland, Ohio.
[1] H. W. Lewis and J. R. Reitz, J. Appl. Phys. **30**, 1838 (1959).
[2] H. W. Lewis and J. R. Reitz, J. Appl. Phys. **30**, 1439 (1959).

Then the net voltage in this simple case is given by

$$V=B_a-B_c+W_c-W_a-IR \tag{3a}$$

$$=kT\ln\left[\frac{j_c(T)-j_c}{j_a}\right]+W_c-W_a-IR. \tag{3b}$$

The appearance of W_c, the work function of the cathode, is deceptive, since it also appears implicitly in $j_c(T)$, through Richardson's equation, but W_a, the anode work function, is uncompensated by any such effect, and it is always good to have that as low as possible. If the variation of j_c and j_a under the logarithm, in the first term, can be neglected, then the first three terms of (3) can be lumped together and called the EMF of the cell. This is the case treated in reference 2. If, on the other hand, the resistive drop can be neglected, one can notice that W_c-W_a is usually much bigger than kT, so that the limiting current is determined by $j_c(T)$. The cell is then emission limited, for all practical purposes.

In the domain $j_c \ll j_c(T)$, well below the point of emission limiting, (3) can be simplified, and becomes

$$V\approx kT\ln(j_a(T)/j_a)-IR, \quad j_c\ll j_c(T), \tag{4}$$

where $j_a(T)$ is the saturation current density the anode would emit *if* it were at the temperature of the cathode. Apart from the IR drop, this is the expression given in (1) for the "open-circuit" voltage. For large $j_c(T)$, joule heating becomes important before j_a becomes comparable with $j_c(T)$, so that (4) is relevant. We now discuss the inclusion of joule heating, first, in an approximate way which emphasizes the fundamental physics involved, and secondly, by solution of the appropriate heat conduction equation.

2. APPROXIMATE TREATMENT OF THE TEMPERATURE DISTRIBUTION IN THE PLASMA

For large current density j, a power density $j^2\rho$ is dumped into the plasma by joule heating, where ρ is the resistivity of the plasma. For a current density of 50 amp/cm², and a resistivity of 0.2 ohm-cm (both of which are reasonable, if not typical, numbers), this amounts to 500 w/cm³. We estimate that the plasma is totally incapable of disposing of such large quantities of heat, so that this heat must go into heating the electrons, while they are in transit between cathode and anode. More elegantly stated, we expect the joule heat to go into Thomson heat, producing a temperature gradient in the cell, with *increasing* temperatures as we leave the cathode. This gradient will be given by

$$j\mu\nabla T=j^2\rho, \tag{5}$$

where μ is the Thomson coefficient. For an ideal gas at constant pressure, μ (which is nothing more than the specific heat of the electron gas, per electron) is given by $\frac{5}{2}k$, where k is Boltzmann's constant. Thus

$$\tfrac{5}{2}k\nabla T=\rho j=\mathcal{E} \tag{6}$$

where $\mathcal{E}$ is the resistive electric field in the cell. Or

$$k(T_0-T)=\tfrac{2}{5}V_R, \tag{7}$$

where V_R is the resistive voltage drop in the cell, T is the temperature of the cathode, as before, and T_0 is the electron temperature achieved at the hottest point, in the cell, just outside the anode in this model. Our estimates indicate that the electrons do not normally have time to transfer any appreciable energy to the ions, so that we are treating the electrons as a closed system.

Again for a current density of 50 amp/cm², and a resistivity of 0.2 ohm-cm, we find from (7) that the temperature will rise about 4000°K/mm, so that this is in fact a dominant effect. Of course, the variation of ρ with temperature and j with position have to be taken into account for a detailed integration of (6), but (7) is correct in any case.

Apart from details, which we will come to in a moment, the important point of (7) is that the electrons at the anode can be hotter than the cathode temperature, so that the anode barrier and the output voltage can be increased. Thus, not all the joule heat is lost, and the efficiency is greatly improved over what one would naively have supposed.

For the integration of (6), we will consider successively two simple geometries, plane and cylindrical, the latter with the cathode on the inside.

For the plane case, j is constant, and ρ is given approximately by[2]

$$\rho(T)\approx 0.16(3000/T)^{\frac{1}{2}}, \tag{8}$$

so that

$$\frac{kT_0}{e\rho(T_0)}=\frac{kT}{e\rho(T)}+jd, \quad \text{plane}, \tag{9}$$

where d is the distance from the cathode to the anode. This enables us to find T_0, and to determine B_a from (2). Then again V is given by (3a). Note that for a combination of parameters in (2) such that the logarithm is greater than $\frac{5}{2}$, it would appear that we actually gain more than we lose from joule heating. We'll return to the discussion of this interesting point after we have treated the energy balance in the barrier.

For the cylindrical case, with cathode radius a and anode radius b, the current density varies as $1/r$, so that T_0 is determined by

$$\frac{kT_0}{e\rho(T_0)}=\frac{kT}{e\rho(T)}+j_c a\ln\left(\frac{b}{a}\right), \quad \text{cylinder}, \tag{10}$$

which differs only in detail from (9). Again, B_a is obtained by substituting T_0 into (2), and V is given by (3a), by using T in (1) for B_c.

At this point, it is important to note that the presence of space charge barriers at the cathode and anode induce additional heating and cooling, respectively, of the electron gas. We will call these barrier thermal effects. First consider the cathode, at which the emitted current

runs down a barrier B_c. The potential energy is converted into heat, and it is easy to see that the temperature T' of the electron gas just outside the cathode is related to the cathode temperature T, by[3]

$$\frac{k}{e}(T'-T)=\frac{j_e}{j_e(T)}\left[B_c-\frac{1}{2}\frac{k}{e}T'\right], \tag{11}$$

or

$$1-\frac{T}{T'}=\frac{1}{2}\frac{j_e}{j_e(T)}\left\{\ln\left[\frac{pe}{(2\pi mkT')^{\frac{1}{2}}(j_e(T)-j_e)}\right]-\frac{1}{2}\right\}, \tag{12}$$

which is obtained after proper account is taken of the Peltier cooling of the cathode. Thus, the electron gas starts its joule heating from a temperature T', rather than T, and the maximum temperature near the anode is obtained from (9) or (10), by using T' from (12), instead of T.

A similar situation prevails at the anode. Denote by T_a the temperature of the electrons in contact with the anode, which we have tacitly identified, up to now, with T_0. The potential barrier that forms at the anode now has the property of draining from the electron cloud near it only the energetic electrons, that have enough energy to surmount the barrier. These have to be replaced through collisions between slower electrons, which replenish the supply of energetic ones. In other words, this is a cooling effect on the electron gas (indeed, it is the only cooling effect we take into account in this model and therefore must be adequate to drain off all the accumulated energy that is being brought downstream by the electrons). This, however, is $\frac{5}{2}kT_0$ per electron, since it is the enthalpy that counts in this constant pressure situation. (Note, incidentally, that we have consistently ignored the kinetic energy associated with the drift velocity of the electrons. If this should matter, it should simply be added to the enthalpy.)

The cooling effect, per electron, is given by B_a+2kT_a, where B_a is given by (2), with $T=T_a$. Thus, T_a is determined by

$$kT_a\left[\ln\left(\frac{pe}{j_a(2\pi mkT_a)^{\frac{1}{2}}}\right)+2\right]=(5/2)kT_0 \tag{13}$$

or analogously to (12),

$$(T_0/T_a-4/5)=(2/5)\ln\left[\frac{pe}{j_a(2\pi mkT_a)^{\frac{1}{2}}}\right]. \tag{14}$$

It should be noted that the anode heating, per electron, is given by W_a+2kT_a, and that this is the only inevitable anode heating. This point is relevant to a discussion of the efficiency.

The anode barrier is, then, given by (2), with $T=T_a$, or, alternatively, by $(5/2)kT_0-2kT_a$.

[3] The derivation of this expression is given in detail in Eq. (15). Note that when a saturation current is drawn from a surface the average kinetic energy flux is $2(k/e)T_{\text{local}}$.

3. SOLUTION OF THE HEAT CONDUCTION PROBLEM IN THE PLASMA

Let us now solve the barrier problem taking into account heat conduction. We restrict the derivation to plane geometry. Let T denote the temperature of the cathode, T' the temperature of the electron gas just outside the cathode, T_0 the maximum electron temperature in the plasma, and T_a the temperature of plasma electrons in the vicinity of the anode. The anode temperature, itself, is not relevant so long as it is low enough that back emission is negligible. At the cathode, the emitted current $j_e(T)$ runs down a barrier B_c, its potential energy being converted into heat in the plasma, and the return current, $j_e(T)-j$, has to go up the barrier. We assume the barrier is so thin that no collisions are made in the barrier, an assumption which is approximately fulfilled. Thermal balance requires that

$$j_e(T)[B_c+2(k/e)T]-[j_e(T)-j][B_c+2(k/e)T']=j\tfrac{5}{2}(k/e)T'-\kappa_e\frac{dT}{dx}\bigg|_c, \tag{15}$$

where κ_e is the thermal conductivity of the electrons. Here $\frac{5}{2}(k/e)T'$ is the enthalpy flux per unit current in the plasma, and $2(k/e)T'$ is transport heat flux when a saturation current is drawn. Regrouping the terms yields (with $A\equiv j_e(T)/j$),

$$2Ak(T'-T)+\tfrac{1}{2}kT'=eB_c+\frac{e}{j}\kappa_e\frac{dT}{dx}\bigg|_c. \tag{16}$$

At the anode a similar situation prevails,

$$j[B_a+2(k/e)T_a]=j\tfrac{5}{2}(k/e)T_a-\kappa_e\frac{dT}{dx}\bigg|_a. \tag{17}$$

In the region between cathode and anode, the heat conduction equation must be satisfied,

$$\frac{d}{dx}\left(\kappa_e\frac{dT}{dx}\right)=-j^2\rho+\tfrac{5}{2}(k/e)j\frac{dT}{dx}, \tag{18}$$

which when integrated once yields

$$\kappa_e\frac{dT}{dx}\bigg|_a-\kappa_e\frac{dT}{dx}\bigg|_c=j[-IR+\tfrac{5}{2}(k/e)(T_a-T')]. \tag{19}$$

Equations (16), (17), and (19) may be combined conveniently to eliminate the thermal conduction fluxes. The resulting equation is

$$B_a-B_c-IR=2(k/e)[AT-(A-1)T'-T_a], \tag{20}$$

where $A=j_e(T)/j$. Substitution of Eq. (20) into (3a) gives[4]

$$V=W_c-W_a+2(k/e)[AT-(A-1)T'-T_a]. \tag{21}$$

[4] Equation (21) is valid also in cylindrical and spherical geometries. Here $A=j_e(T)/j_c$, where j_c is the actual current density at the cathode.

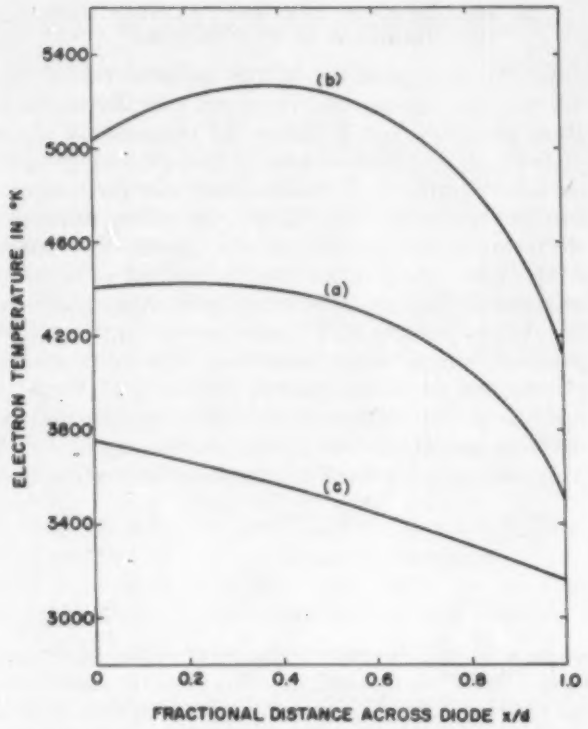

FIG. 1. Electron temperature distribution in the plasma thermocouple. Anode temperature <1000°K, electron pressure of 0.06 mm Hg. (a) Cathode temperature $T=2900$°K, $j=50$ amp/cm², 1 mm cathode-anode spacing. (b) $T=2900$°K, $j=50$ amp/cm², 2 mm spacing. (c) $T=2550$°K, 5 amp/cm², 1 mm spacing.

An essential part of the problem is the solution of Eq. (18). This equation is somewhat complicated because both κ_e and ρ are functions of temperature; in most cases of interest (plasma ionization >1%), the temperature dependence is given by[2]

$$\kappa_e \propto T^{\frac{1}{2}}; \quad \rho \propto T^{-\frac{1}{2}}. \tag{22}$$

The current may be eliminated from Eq. (18) by the substitution: $\xi = jx$, and the resulting equation has been integrated numerically. It is worth while noting that because the equation scales ($T \to aT$, $\xi \to a^{\frac{1}{2}}\xi$), only one master equation need be integrated. This equation was joined to the boundary conditions: (16), (17), (1) and (2), where in Eq. (1) the temperature T', and in Eq. (2) the temperature T_a must be used. Several examples of the electron temperature distribution in the plasma thermocouple are given in Fig. 1.

If the plasma path is not too thick (<200 mean free paths for cesium ions) the electrons will not be able to transfer an appreciable fraction of their energy to the ions. Hence, the ion and neutral gas temperature will be completely different from that of the electrons and in first approximation will be a uniform gradient.

4. EFFICIENCY OF THE PLASMA THERMOCOUPLE

After having found the temperature distribution, and hence V [from Eq. (21)], we turn to the efficiency. It is convenient to define a quantity η_i, the *intrinsic efficiency*, which takes into account only thermodynamic losses; this, of course, contains the effects of electronic heat conduction in the plasma element. The efficiency may be written as the ratio of load power to the heat flux extracted from the cathode, or as the ratio of load power to the sum of load power and heat flux delivered to the anode,

$$\eta_i = \frac{jV}{j_c(T)[W_c+2(k/e)T]-[j_c(T)-j][W_c+2(k/e)T']}, \tag{23a}$$

or

$$\eta_i = \frac{jV}{jV+j[W_a+2(k/e)T_a]}. \tag{23b}$$

Table I. Output voltage and efficiency of a plasma thermocouple under various conditions of operation. The results are for plane geometry, and an electron pressure of 0.06 mm Hg corresponding to a density of 2×10^{14}/cm³ at 2900°K. $W_c=4v$, $W_a=2v$. Case 1: $T=2900$°K, $j_c(T)=100$ amp/cm², 1 mm plate spacing. Case 2: $T=2900$°K $j_c(T)=100$ amp/cm², 2 mm plate spacing. Case 3: $T=2550$°K $j_c(T)=10$ amp/cm², 1 mm plate spacing. The efficiencies η and η' refer to the complete thermocouple circuit.

j (amp/cm²)	V (volts)	η_i	η	η'
Case 1:				
5	2.28	0.504	0.065	0.268
10	2.14	0.488	0.103	0.309
25	1.91	0.448	0.168	0.321
50	1.64	0.386	0.193	0.287
75	1.24	0.289	0.160	0.213
Case 2:				
10	1.94	0.461	0.099	0.286
25	1.64	0.399	0.145	0.280
50	1.41	0.342	0.168	0.250
75	0.95	0.226	0.121	0.159
Case 3:				
2.5	2.22	0.502	0.054	0.243
5.0	1.81	0.415	0.078	0.248
7.5	1.45	0.339	0.083	0.215

Now, we must consider the other losses. The most important of these is radiation which transfers

$$P_r = 5.66(T/1000)^4[\epsilon_1\epsilon_2/(\epsilon_1+\epsilon_2-\epsilon_1\epsilon_2)]\text{w/cm}^2 \tag{24}$$

directly to the anode, where T is the cathode temperature in °K, and ϵ_1 and ϵ_2 are cathode and anode emissivities, respectively. Thermal conduction by ions and neutral particles has been estimated[2]; it is quite small and can probably be neglected in most cases. A third power loss is in the lead wire, which connects the load to the cathode (or which connects anode to successive cathode if several thermocouples are joined together). Since this lead wire conducts heat as well as electricity, its power loss cannot be made zero but it can be minimized. Consider, for example, a plasma thermocouple of unit area, so that the current I in the external

circuit $= j$; the power loss through the lead wire is

$$P_l = \tfrac{1}{2} I^2 R_0 + K_0 \Delta T, \tag{25}$$

where R_0 is the resistance of the lead wire and K_0 its thermal conductance. Now the lead wire is presumably made of metal, for which the Wiedemann-Franz law applies: $K_0 R_0 = LT$, where L is the Lorentz number, and T the absolute temperature. It is easily seen that (25) is minimized by

$$(R_0)_{\min} = (1/I)(2LT_h \Delta T)^{\frac{1}{2}}, \tag{26}$$

giving

$$(P_l)_{\min} = I(2LT_h \Delta T)^{\frac{1}{2}}. \tag{27}$$

Unfortunately, this choice gives a rather large IR_0 drop in the lead (amounting to about 0.42 v for a $\Delta T = 2300°\text{K}$), and this must be subtracted from V. The actual efficiency of the thermocouple circuit

$$\eta = \frac{V - IR_0}{V + W_a + 2(k/e)T_a + (P_r + P_l)/I} \tag{28}$$

is maximized by taking R_0 smaller than (26) (by a factor 3 or 4 for the cases listed in the table).

In Table I the output voltage V and the efficiencies η_i and η are listed for a typical thermocouple under various conditions of operation. No attempt has been made to optimize the parameters, but as has been previously noted, the efficiency can always be improved by reducing the anode work function. The emissivities of cathode and anode have been taken to be 0.35 and 1.0, respectively.

It is evident from the table that η is far below the intrinsic efficiency η_i, and this is due mostly to the radiation transfer term. There are many steps which can be taken to reduce the relative importance of this term, and thus η, as computed from Eq. (28), does not represent the ultimate efficiency of the device. In the last column of Table I, we have listed a quantity η' which has been calculated from Eq. (28) with the radiation term P_r reduced by a factor of ten. We believe that this sort of reduction can be achieved through a suitable combination of radiation shields, use of perforated cathodes to increase electron emission relative to radiative loss, changes in geometry, and changes in anode emissivity.

It should be emphasized that the efficiencies η and η' refer to the complete circuit. A substantial part of the difference between η' and η_i is due to losses in the lead wire.

JOURNAL OF APPLIED PHYSICS VOLUME 31, NUMBER 4 APRIL, 1960

Effect of Viscosity on the Splash Caused by a Drop of Water Falling into a Mixture of Glycerol and Water*

A. G. Davis Philip†
Department of Physics, New Mexico State University, Las Cruces, New Mexico
(Received December 5, 1959)

The effect of viscosity and velocity on splashes produced by low-velocity water drops was investigated by means of high-speed photography. Graphs have been constructed showing the effects on the time of duration of the various stages of the splash and a dimensional analysis in terms of the Reynold's number and Froude's number has been made.

INTRODUCTION

THE first and definitive investigation of splashes was made by Worthington in the early 1900's. His work was published by the Royal Society in 1900[1] and in a book, in 1908.[2] He discussed qualitatively how the splash developed and what factors influenced its growth.

In 1918, Mallock investigated the shape of the cavity formed by a spherical ball.[3] Bell criticized this report and reported his investigations of the effects of surface layers on the liquid and the object dropped.[4]

The first work with high speed cameras was done by E. G. Richardson of King's College. He investigated the pressure in the cavity during the various stages of the splash.[5] More recent reports have come from the Naval Ordnance Laboratory in Maryland, [6–8] where investigations have been made on the entry of high speed missiles into water.

* This paper contains material from a Masters Thesis for New Mexico State University.

† Present Address, Case Institute of Technology, Cleveland, Ohio.

[1] A. M. Worthington and R. S. Cole, Trans. Roy. Soc. (London) **A194**, 175 (1900).

[2] A. M. Worthington, *A Study of Splashes* (Longmans, Green and Company, Inc., New York, 1908).

[3] A. Mallock, Proc. Roy. Soc. (London) **95**, 138–43 (1916).

[4] G. E. Bell, Phil. Mag. Ser. VI, (November, 1924).

[5] E. G. Richardson, Proc. Roy. Soc. (London) **A61**, 352–67 (1948).

[6] Gilbarg and Anderson, J. Appl. Phys. **19**, 127 (1951).

[7] A. May, J. Appl. Phys. **22**, 1219 (1951).

[8] A. May, J. Appl. Phys. **23**, 1363–72 (1952).

DESCRIPTION OF THE PRESENT EXPERIMENT

A diagram of the apparatus is shown in Fig. 1. A Wollensak Fastax camera, borrowed from the White Sands Missile Range, was used to photograph water drops as they fell into varying mixtures of glycerol and water. Free fall in a vacuum was used as a basis for scaling the velocities. A 20% variation in the drop velocity was noted on the film. No correction was made for air resistance as these corrections were smaller than other statistical fluctuations. The water level in the dropper tube was maintained at a predetermined level in order to keep the sizes of the drops constant. The splash time sequence was obtained from a flashing neon light. Viscosities were calculated from the percentage mixture of water and glycerol and tables in the Handbook of Chemistry and Physics,[9] corrected for temperature changes. The viscosity range from 1 to 1500 centipoises was investigated.

The physical dimensions of the splashes showed great random fluctuations, the times at which the various stages occurred did not. For this reason, it was decided to study the splashes in terms of the time duration of the splash stages.

DESCRIPTION OF SOME TYPICAL SPLASH CONFIGURATIONS

Figure 2 shows an idealized cutaway drawing of a typical splash configuration observed for drops falling into a low viscosity mixture. The velocity was 650 cm/sec. Individual splash configurations may vary from these profiles by 10% in time and by as much as 50% in size. These splash configurations were smoothed by combining the photographic results of several like runs, so that the essential features of the ring splash could be studied. Dotted lines indicate the inferred boundary lines where the profiles were obscured by the miniscus at the container wall.

The ring splash (Fig. 2) built up extremely fast. For the highest impact velocities into pure water, the ring closed over to form a dome or what is called a "bubble splash". For lower impact speeds or more viscous liquid mixtures, the ring sank back to the surface without closing over. At the same time the first jet formed in the cavity beneath the surface, as the lining of the inside walls of the cavity flowed to the center, producing a thin column of rising liquid. This jet acted somewhat like a second drop falling into the mixture, forming a smaller cavity which in turn produced a second jet. The second jet segmented into a series of drops except for high viscosity mixtures or low impact speeds.

The ring splash was considered over when the walls no longer could be distinguished from the water level. The duration of the first or second jet was measured from the time that it first appeared above the water level until it disappeared below the surface. The time of deep closure was taken as the time at which the mass of water, at the bottom of the air cavity, separated into two parts.

EXPERIMENTAL RESULTS

For analysis, the splash profiles were traced from an image projected onto a ground glass plate, and the splash event time sequence was measured relative to the time of impact for the following splash events: ring splash, first jet, deep closure, and the second jet. In some of these measurements, the times were in error since the event started below the surface of the liquid, but could not be observed until it appeared above the surface. This error was well under the 20% error in other parts of the experiment, for the splash was moving fastest at these times. The error was less than ± 0.02 sec.

The first jet (Fig. 3), one of the most important phases of the splash, showed a uniform decrease in duration as the viscosity increased to about 70 centipoises. Then this rate of decrease in the duration increased until finally the first jet no longer occurred, at a viscosity of 1800 centipoises.

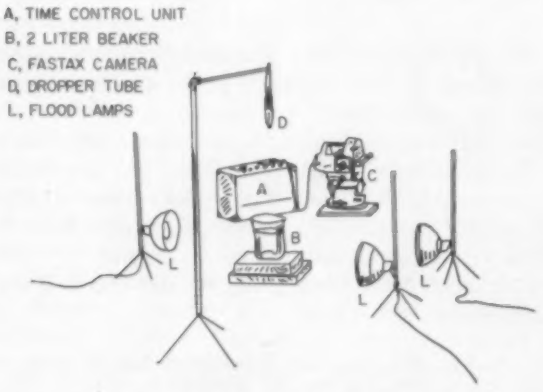

FIG. 1. Setup of the apparatus.

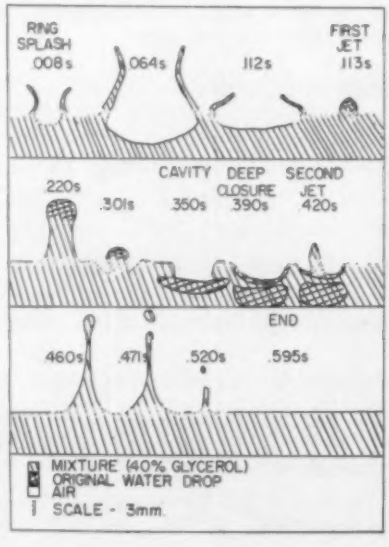

FIG. 2. Idealized splash profiles. These cutaway drawings illustrate important stages in the splash configurations. The times of occurrence are noted above each diagram.

[9] "Viscosity of aqueous glycerol solutions," *The Handbook of Chemistry and Physics* (Chemical Rubber Publishing Company, Cleveland, Ohio, 1948), p. 1742.

The time of deep closure, the most reproducible phase investigated, showed a regular decrease with viscosity until a value of about 70 centipoises was reached, when it no longer occurred.

The duration of the ring splash was very nearly constant. The second jet showed the most variation, decreasing, then increasing, and then decreasing in time duration as the viscosity increased.

For a given viscosity (Fig. 4) all events but the second jet, which was anomolous, showed a decrease in duration as the velocity increased.

It was noted that when the time durations of the splash phases were divided by $V^{0.3}$, the ratio was nearly constant for all phases, but the second jet. From this information, an empirical formula is formed,

$$T=KV^{0.3}, \tag{1}$$

which gives the relationship between the time and the impact velocity for constant viscosity. Curves computed from this empirical formula are plotted on Fig. 4.

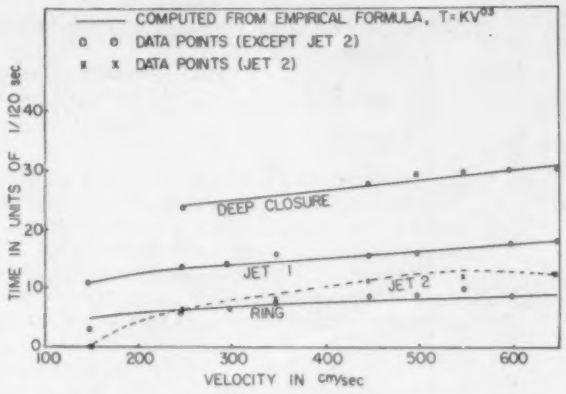

FIG. 4. Duration of four stages of the splash plotted vs velocity for drops of water falling into a 50% glycerine solution. The solid lines were computed from the formula $T=KV^{0.3}$.

ANALYSIS

The two main phases studied in the experiment were the first jet, a surface feature, and deep closure, a cavity feature. An examination of the first jet was made since it seemed to be the single most important configuration in the splash. Deep closure was examined because it showed the smallest random error.

The time duration of the splash is expected to depend upon the following variables:

Symbol		Dimensions
r	Radius of the drop	L
V	Impact velocity of the drop	L/T
ρ	Density of the mixture	M/L^3
η	Viscosity of the mixture	M/LT
γ	Surface tension of the mixture	M/T^2
g	Acceleration of gravity	L/T^2

The time of duration of the splash phases can be set up in an equation involving these parameters,

$$T=f(r,V,\rho,\eta,\gamma,g). \tag{2}$$

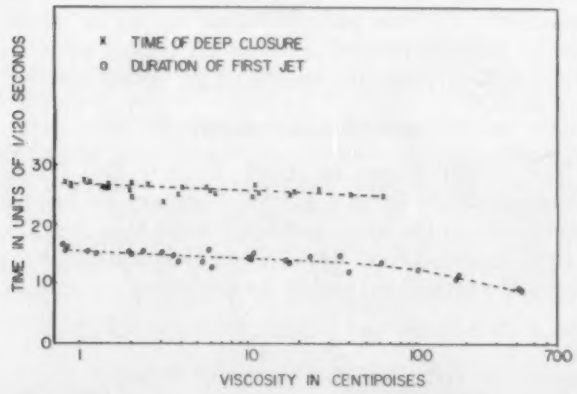

FIG. 3. Duration of two stages of the splash plotted vs viscosity.

The surface tension was not measured directly in this experiment and since it varied by only 16%, γ was assumed constant for this analysis. The equation for the time duration can be written as follows in terms of the above variables together with Reynold's number, $R=2r\rho V/\eta$, and Froude's number, $F=V^2/rg$,

$$T=(r/V)f(R)h(F). \tag{3}$$

Dimensional analysis gives no insight into the nature of the functions $f(R)$ and $h(F)$. However, it is possible to construct them empirically from the data.

The product VT/r was plotted vs $\ln R$ (V = velocity at impact in cm/sec, T = time in msec, r = radius in cm) in Fig. 5. The most obvious feature about the plots for deep closure is that the data points fall on straight lines. The slopes vary slightly with velocity, so that on extension, the lines intercept at a common point on the horizontal axis.

These features of the curve can be described by the following equation:

$$f(R)h(F)=m(V/V_0)(\ln R+b). \tag{4}$$

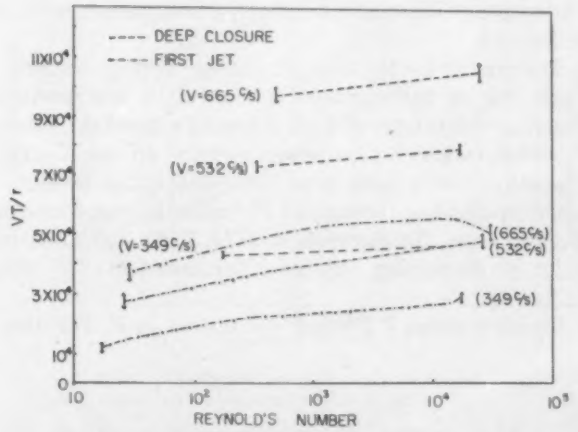

FIG. 5. Plot of VT/r vs the Reynold's number. Three velocities are shown for two of the splash stages.

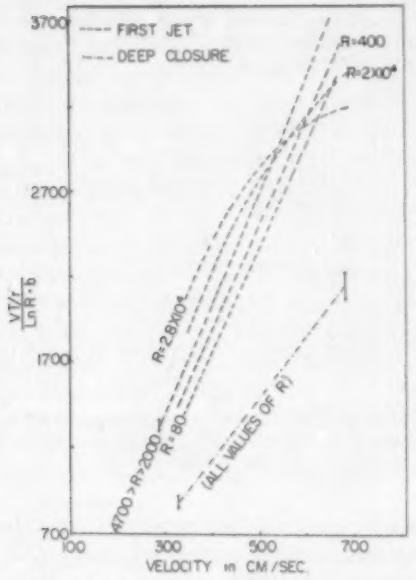

FIG. 6. Plot of $h(F)$ vs velocity for two of the splash stages.

The slopes, m, are 1884, 1461, and 856, in order of decreasing velocity. For all cases, "b" was found to be $44.3\pm1.4\%$. The equation can be separated, one part depending on the velocity only, the other on the Reynold's number. The separated equations are,

$$f(R)=\ln(R+b) \tag{5}$$

$$h(F)=m(V/V_0) \tag{6}$$

It was found that if the curves for each velocity were scaled by dividing equation (4) by $V^{1.3}$, a single curve would result and, therefore, a single slope. Hence,

$$m(V/V_0)/V^{1.3}=K, \tag{7}$$

or

$$h(F)=KV^{1.3} \tag{8}$$

and Eq. (3) becomes

$$T=Kr(\ln R+b)V^{0.3}. \tag{9}$$

For constant Reynold's numbers, this equation reduces to Eq. (1).

The curves for the first jet can be treated similarly. Each one of the curves has a straight line portion covering the ranges of high Reynold's numbers, when extended intersect at a common point on the X axis. The difference in both slope and position can be eliminated by dividing through by $V^{1.3}$ as in the case for deep closure. Here, the slopes were 2721, 2240, and 1260, in order of decreasing velocity. The constant "b" was $12.1\pm3\%$.

Figure 6 shows $VT/r/\ln R+b$ plotted vs V. For deep

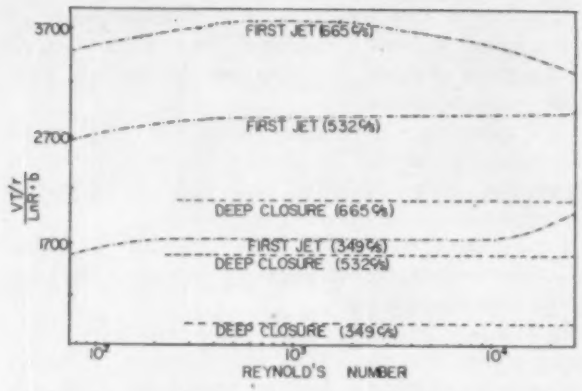

FIG. 7. Plot of $h(F)$ vs the Reynold's number. Deviations from the straight lines indicate where the empirical equations fail.

closure, a straight line occurred for all values of R. For the first jet, a series of lines resulted, showing some variation in R. Here, the representation by Eqs. (5) and (6) is not as good, but it holds well in the region $R=400$ to 2000.

The region for which Eq. (5) is valid may be determined from Fig. 7. Ideally, $VT/r/\ln R+b$ should be independent of R. This is true for deep closure. For the first jet, there is a straight line portion in the middle of each curve for which one can suppose that the separation in Eq. (5) is valid. At the extremes in Reynold's numbers, the curves break away from the horizontal lines.

EVALUATIONS AND COMMENTS

This paper has pointed the way to a more thorough investigation of splash effects, and indicated some of the main problems that stand in the way of obtaining accurate data. It showed in graphical form, the manner in which increasing viscosity decreased the time of duration of the various splash stages. The dimensional analysis gave empirical formulas applicable to the middle range of the viscosity, from 1 to 70 centipoises. For velocity effects, the experiment and the empirical equation obtained for velocity dependence was in good agreement. The two main problems still to be solved are, an accurate determination of the impact velocity, and the effect of surface tension on the splash effects.

ACKNOWLEDGMENTS

The author wishes to thank the late Dr. Irving Langmuir of the General Electric Company for helpful discussions on the work, and Dr. Harold Daw and Dr. Ralph Dressel of New Mexico State University for help during the experiment and in the analysis of the results.

JOURNAL OF APPLIED PHYSICS VOLUME 31, NUMBER 4 APRIL, 1960

Temperature-Dependence of the Electrical Resistivity of bcc Cr-Fe Alloys

N. S. RAJAN, R. M. WATERSTRAT, AND PAUL A. BECK
Department of Mining and Metallurgical Engineering, University of Illinois, Urbana, Illinois
(Received September 21, 1959)

The electrical resistivity vs temperature was determined for a bcc Cr+20 at.% Fe alloy from 4.2° to 300°K. The absence of any discontinuity in this curve indicates that the very high temperature-coefficient of the linear term of the specific heat previously found at that composition is not associated with a phase transformation between room temperature and 4.2°K. For bcc Cr-alloys with Fe contents increasing from 0 to 16 at.% Fe the resistivity vs temperature anomaly shifts from approximately 308°K to progressively lower temperatures, and the anomalous resistivity increase with decreasing temperature becomes progressively larger. It is quite possible that these anomalies are connected with antiferromagnetic-paramagnetic transition in the alloys considered.

IN the course of an investigation of the low-temperature specific heat of bcc Cr-Fe solid solution alloys, a large peak in the temperature-coefficient of the term of the specific heat linear in temperature has been noted at 19 at.% Fe.[1] In order to ascertain whether or not this large effect is associated with a phase transformation on cooling between room temperature, where the alloys have the bcc structure, and liquid helium temperatures, where the specific heat measurements were made, the electrical resistivity of the alloys has been measured in the temperature range between 4.2° and 300°K.

The measurements were carried out by means of the potentiometer method, and thermal emf contributions were eliminated by simultaneously reversing the current and the potentiometer leads between duplicate measurements at the same temperature. Because of the unfavorable length:diameter ratio of the specimens (prepared by induction melting, homogenized by annealing for 3 days at 1170°C, quenched in cold water, and machined to rods approximately 20-mm long and 3-mm diam) and because of the uncertainty of the exact distance between the potential leads, the absolute value of the resistivity could be determined only to an estimated accuracy of ±5%. In comparison with the uncertainties just mentioned, that arising from the small amount of oxide-inclusions metallographically observed should be negligible. The relative accuracy of the resistivity measurements for a given specimen as a function of the temperature was considerably better, approximately ±1%, except for the first run made between 4° and 78°K (Cr+9.96 at.wt Fe alloy), where it may have been about ±2%. The temperature measurements were made by means of Cu-constantan thermocouples soldered to both ends of each specimen. These were calibrated by means of a Cu resistance thermometer which was, in turn, calibrated using the boiling points of liquid He, and N_2.[2] Resistivity measurements were made with most specimens at 4.2°K and 78°K by dipping them directly into liquid helium and nitrogen. The resulting data points fit the data points for other temperatures, determined in a cryostat, within the estimated relative accuracy.

The results obtained for Cr alloys with 20.3, 29.1, 37.4, and 77.6 at.% Fe are given in Fig. 1. It is noteworthy that the resistivity vs temperature curve for the Cr+20.3 at.wt Fe alloy, which has a high-temperature coefficient of the linear term of the specific heat near the highest value at the peak, is quite normal with no discontinuity. This fact indicates that the high value of the temperature coefficient of the linear term of the specific heat of this alloy is not likely to be a result of a phase transformation in the temperature range 4°–300°K.

The resistivity vs temperature for Cr alloys with 2, 4.7, 9.96, and 16.1 at.% Fe, together with the data for Cr and for a Cr+1 at.% Fe alloy obtained by deVries[3] is plotted in Fig. 2. It is seen that the anomaly, which in the case of Cr occurs at about 308°K,[4] is shifted to progressively lower temperatures with increasing Fe-contents; at 16.1 at.% Fe the minimum of the resistivity

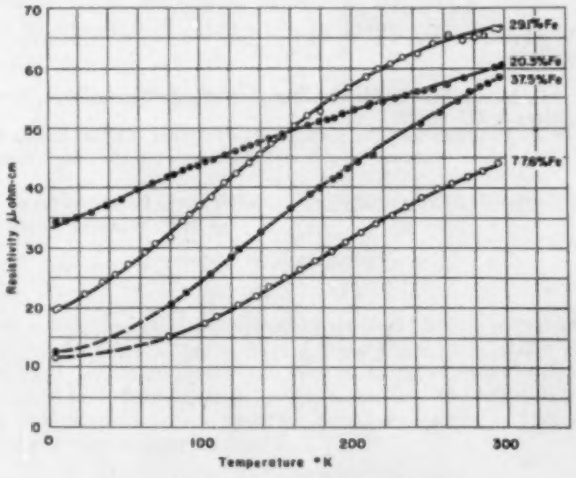

FIG. 1. Electrical resistivity vs temperature for Cr-Fe alloys with 29 to 78 at.% Fe.

[1] C. T. Wei, C. H. Cheng, and P. A. Beck, Phys. Rev. Letters **2**, 95 (1959).
[2] T. M. Dauphinee and H. Preston-Thomas, Rev. Sci. Instr. **25**, 884 (1954).
[3] G. deVries, J. Phys. radium **20**, 438 (1959).
[4] M. E. Fine, E. S. Greiner, and W. C. Ellis, Trans. Am. Inst. Mining, Met., Petrol., Engrs. **189**, 56 (1951).

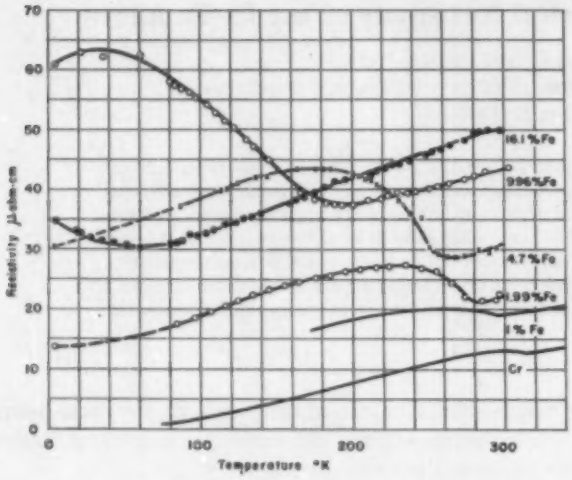

FIG. 2. Electrical resistivity vs temperature for Cr-Fe alloys with 0 to 16 at.% Fe.

is at approximately 60°K. Also, with increasing Fe-content the extent of the anomalous resistivity increase with decreasing temperature becomes very much larger; at 9.96 at.% Fe the resistivity rises to a maximum of about 63 μohm-cm at 30°K.

Recent single crystal neutron diffraction work by L. Corliss, J. Hastings, and R. Weiss[5] shows that the anomaly in Cr at 308°K corresponds to the Néel temperature. It seems reasonable to assume that the Néel temperature decreases with increasing Fe-content. Thus, the observed anomaly in the Cr-Fe alloys may well be connected with the antiferromagnetic transition in these alloys, although, by analogy with other systems,[6] the magnetic contribution to the resistivity might have been expected to decrease rather than to increase as the magnetic order becomes more perfect, when the temperature is lowered. The large magnitude of the anomalous resistivity effect at 5–10 at.% Fe remains to be explained.

[5] L. M. Corliss, J. M. Hastings, and R. J. Weiss, Phys. Rev. Letters **3**, 211 (1959).
[6] R. J. Weiss and A. S. Marotta, J. Phys. Chem. Solids **9**, (1959).

Similar resistivity vs temperature data were obtained independently by Newmann and Stevens[7] in the more limited range of approximately 90° to above 300°K for Cr alloys with 1.05, 2.06, 5.76, and 16.88% Fe. The authors became aware of this unpublished work through the courtesy of Professor K. W. H. Stevens, after the present investigation had been almost completed. For the alloys of similar composition the results of the two investigations are in good agreement. In order to explain some of their results, Newmann and Stevens propose a model involving two different antiferromagnetically ordered arrangements of the atomic magnetic moments in Cr-Fe alloys.

SUMMARY

It was found that in bcc Cr-alloys with Fe-contents increasing from 0 to 16 at.% Fe, the resistivity vs temperature anomaly shifts to progressively lower temperatures and that the anomalous resistivity increase with decreasing temperature becomes progressively larger. It appears quite possible that these anomalies are in some way connected with the antiferromagnetic-paramagnetic transition in the alloys considered, since extrapolation to 0% Fe leads to the Néel temperature of Cr.

The lack of any discontinuity in the resistivity vs temperature curve for the Cr+20 at.% Fe alloy indicates that the very high temperature-coefficient of the linear term of the specific heat previously found at that composition is not associated with a phase transformation between room temperature and 4.2°K.

ACKNOWLEDGMENT

The authors wish to thank Dr. R. J. Weiss for fruitful discussions and advice, and Dr. C. T. Wei for making available to them the alloy specimens prepared by him for low-temperature specific-heat measurements. This investigation was supported by the U. S. Air Force, WADC.

[7] M. M. Newmann and K. W. H. Stevens, *Magnetic susceptibilities of iron-chromium alloys* (to be published).

Letters to the Editor

Heating in Liquid Helium Resulting from Neutron and Gamma Bombardment by a Fission Source

M. G. CHASANOV
International Business Machines Corporation, Military Products Division, Owego, New York
(Received August 6, 1959)

INTEREST in utilization of solid state devices operable only at low temperatures raises the question of the effects of a radiation environment on a coolant such as liquid helium. In the following such effects have been considered for optimum conditions—namely, a single neutron collision with a helium atom as the major energy dissipation process. It would appear that the effects predicted would occur to a greater extent when a less optimistic approach is employed. However, the conclusions reached would not be materially changed.

Mechanism of heat dissipation. Neutrons and gamma rays passing through liquid helium dissipate a portion of their energies as heat. The extent of heating of helium resulting from these dissipation processes will help determine the utility of low-temperatured evices depending on liquid helium as a coolant. The estimates of this heating effect are based upon the following postulates:

(1) Elastic scattering of neutrons is the primary collision process for the helium nucleus.
(2) Neutron absorption (n,γ) does not occur for helium.
(3) Energy absorption from gamma rays is proportional to the energies absorbed from gammas in the ORNL graphite pile by water.

Postulates (1) and (2) are experimentally and theoretically valid. Postulate (3) is subject to error on several bases, secondary electrons produced may possess sufficient energy to escape from the sample—admittedly, however, for samples of reasonable thickness (ca 1 cm) this does not produce a great error. Postulate (3) may lead to an overestimation of the gamma heating[1]; though this may not be the case for water moderated reactors whose gamma fluxes are an order of magnitude greater per neutron.

Energy from neutron scattering. The energy absorbed by the helium is the mean energy lost by the neutrons,

$$\text{absorbed energy } \frac{2A}{(A+1)^2}N\int_0^\infty E\varphi_E\sigma_s dE, \qquad (1)$$

where A = atomic mass of helium divided by mass of the neutron, N = number of helium atoms considered, $\varphi_E dE$ = flux of neutrons of energy E from the source with energies between E and $E+dE$, and σ_s = microscopic scattering cross section in barns (one barn $=10^{-24}$ cm^2).

Postulate (1) allows us to use the total microscopic cross section σ_T in place of $\sigma_s \cdot \sigma_T$ is given in BNL325.[2]

If we assume Watt's fission spectrum[3] for the neutron source, we may use

$$\varphi_E = 0.484\ \varphi_0 e^{-E}\sinh(2E)^{\frac{1}{2}},$$

where φ_0 is the source neutron flux (neutrons per square centimeter per second) and E = neutron energy in Mev. For our calculations, we shall assume a negligible number of neutrons with energies less than 0.01 Mev; thus, our integration will be from the limits 0.01 Mev to effectively 20 Mev.

For a cubic centimeter of liquid helium, the following constants are pertinent:

$A=3.97$,
ρ (density of liquid helium) $=0.125$ at 4.2°K,[4]
c (specific heat) $\cong 1$ cal/g °K at 4°K,[5]
L_v (latent heat of vaporization) $=6$ cal/g,[6]
T_B (boiling temperature at one atmos pressure) $=4.2$°K,[6] and
$N=\rho N_0/4=1.88\times10^{22}$ (atoms/cm^3),

where N_0 is Avagadro's number $=6.03\times10^{23}$. The equation for absorbed energy thus becomes

$$\text{absorbed energy } 2.92\times10^{-3}\ \varphi_0\int_{0.01}^{20}\sigma_T e^{-E}\sinh(2E)^{\frac{1}{2}}dE, \qquad (2)$$

where σ_T is in barns (10^{-24} cm^2) and E is in Mev.

This integral was evaluated between 0.01 Mev and 20 Mev by using an IBM 704. The results obtained were

$$\begin{aligned}\text{absorbed energy} &= 3.86\times10^{-2} && \varphi_0(\text{Mev/cm}^3\text{ sec}),\\ &= 6.18\times10^{-3} && \varphi_0(\text{ergs/cm}^3\text{ sec}),\\ &= 1.48\times10^{-14} && \varphi_0(\text{calories/cm}^3\text{ sec}).\end{aligned}$$

For a reactor spectrum with $1/E$ neutron distribution the absorption may be 300 times less than that for a fission spectrum.

Energy from neutron absorption processes. The absence of (n,γ) reactions for helium eliminates a large possible source of heat. However, there is one other reaction we should consider,

$$_2\text{He}^3(n,p)1^H3.$$

The energy release of this reaction is of the order 2.373×10^{-3} mass units per absorption or about 8.45×10^{-14} calories. Although the thermal cross section for the process is rather large (5400 barns), the cross sections for larger energies are considerably smaller and the fractional abundance of $_2$He^3 is 1.3×10^{-6}. The combination of small absorption probability, low abundance, and low energy resulting allows us to neglect the heating effects of this reaction.

Gamma heating. We assume that the energy lost in the liquid helium is proportional to the gamma energy absorbed by a mole of water as previously stated in postulate (3).

$$\text{energy absorption from gammas} \cong \frac{M_{\text{He}}}{M_{\text{H}_2\text{O}}}\times\frac{\mu\text{He}}{\mu\text{H}_2\text{O}}\times E_{\text{H}_2\text{O}},$$

where M = atomic or molecular weight, μ = mass absorption coefficient (cm^2/g), $E_{\text{H}_2\text{O}}$ = energy absorbed from gamma photons by one mole in the ORNL graphite pile at 3500 kw -7.4516×10^{-8} cal/mole sec.

By using data for the ORNL graphite pile, one can estimate the gamma energy absorption by Richardson's method to be approximately 3.9×10^{-17} (cal cm^3/n) for a cubic centimeter of helium. Hence,

$$\text{absorbed } \gamma \text{ energy} \cong 3.9\times10^{-17}\ \varphi_0 \text{ cal/cm}^3\text{ sec}.$$

However, as noted before, this value may be an order of magnitude smaller than for the case of an MTR type reactor.

Vaporization of liquid helium. The heat required to vaporize of liquid helium is given by

$$\begin{aligned}q\ (\text{calories}) &= [(T_B-T_i)c+L_v]\rho\\ &\cong 1.3[1-(T_i/10)],\end{aligned}$$

where T_i is the initial temperature of the liquid helium in degrees Kelvin. If $T_i \cong 4$°K (an operating temperature for a maser or cryotron) we obtain $q=0.78$ cal. We can readily express the time required for helium vaporization t as a function of neutron flux, φ_0 from a fission source, based on a cubic centimeter of helium and assuming no heat conduction

$$t=\frac{q}{1.48\times10^{-14}\varphi_0}=\frac{8.8\times10^{13}(10-T_i)}{\varphi_0}. \qquad (3)$$

Some devices, of course, could cease to function before the helium boiled. The time required to raise the helium from the

initial temperature T_i to the temperature of transition (e.g., where superconductivity disappears) T_t is given by

$$t=\frac{(T_t-T_i)c\rho}{1.48\times10^{-14}\varphi_0}=\frac{8.5\times10^{13}(T_t-T_i)}{\varphi_0}. \quad (4)$$

Superconducting transition temperatures are given below for some metals

Metal	T_0 °K
Lead	7.22
Mercury	4.1
Niobium	8.7–8.9
Tantalum	4.38

In general, since cryostats are large and immobile, most applications involving liquid helium would use liquid helium at the boiling point. Of course, once the helium has vaproized it does not recondense.

It would appear that careful consideration should be given to possible nuclear radiation environments when considering the utilization of devices operable only at liquid helium temperatures.

The author gratefully wishes to acknowledge the advice and comments of Dr. N. H. Kramer.

[1] D. M. Richardson, ORNL 129 (December 23, 1948).
[2] D. J. Hughes and J. A. Harvey, "Neutron cross sections," Brookhaven Natl. Lab. 325 (July 1, 1955), U. S. Atomic Energy Commission.
[3] S. Glasstone and M. C. Edlund, *Elements of Nuclear Reactor Theory* (D. Van Nostrand, Inc., Princeton, New Jersey, 1952).
[4] *American Institute of Physics Handbook*, edited by D. E. Gray (McGraw-Hill Book Company, Inc., New York, 1957).
[5] W. H. Keesom and A. Keesom, Physica 2, 557 (1933).
[6] *Handbook of Chemistry and Physics* (Chemical Rubber Publishing Company, Sandusky, Ohio, 1948), 30th ed.

Gamma-Ray Induced Conductivity in Polyethylene Coaxial Cable

KICHINOSUKE YAHAGI* AND AKIBUMI DANNO
Japan Atomic Energy Research Institute, Tokai-mura, Naka-gun, Ibaraki-ken, Japan
(Received December 16, 1959)

IN this communication is reported the electrical conductivity changes in polyethylene coaxial cable during Co^{60} gamma-ray irradiation, which was measured at comparatively high dose rate. The radiation source was a 10 kc Co^{60} at Japan Atomic Energy Research Institute that consists of a cylindrical form (diam, 134 mm; height, 400 mm).[1]

The sample is a 3C-2V-type high-frequency coaxial cable (central wire diam, 0.5 mm single conductor; outer diam of polyethylene cylinder, 3.1 mm; outer diam of copper sheath, 3.8 mm; outer diam of the sheath, 5.8 mm) and is formed in a flat spiral, of which the diameter is 25.4 cm and the lead wire length is 358 cm. For the range of the dose rate, the distance between the radiation source and the sample was varied from 180 cm to 10 cm that corresponded to the dose rate from 4.2×10^3 r/hr to 1×10^5 r/hr, but the experimental plot of induced conductivity was limited up to 1.4×10^5 r/hr because nonuniformity of irradiation would appear at the shorter distance.

The dose rate was measured by the Fricke dosimeter as well as Victoreen ionisation chamber and the total dose of irradiations under the experiments was limited to less than 10^6r. An electronic micro-micro ammeter was used which had a maximum sensitivity of 1×10^{-14} A and an accuracy of readings of $\pm3\%$ for the larger currents, down to $\pm10\%$ for the smallest. The measured current range was about 10^{-11} A to 10^{-9} A.

The measurements were carried out in a Co^{60} 10 kc irradiation cave, in which the flat spiral cable was fixed on the inner surface of the cave wall and the central conductor of the cable was connected with the meter through the shielded wall. The copper sheath was charged with the voltages from 200 to 1000 v. The induced currents were almost at equilibrium about 2 min after application of voltage at the constant dose rate. The stabilization

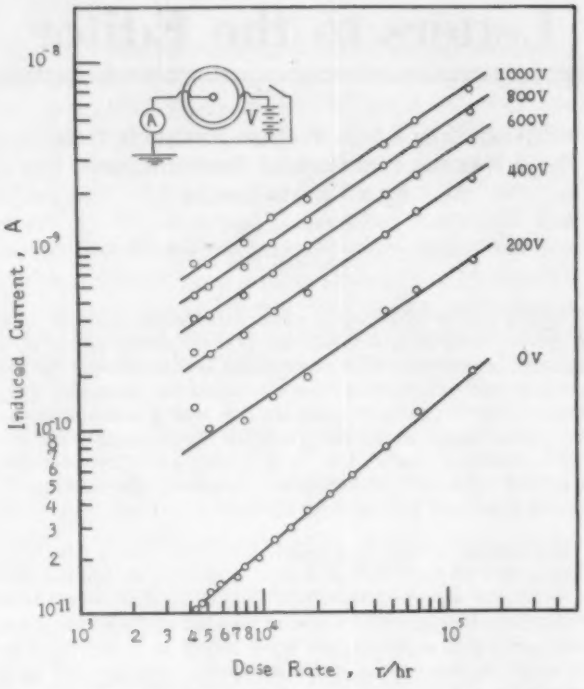

FIG. 1. Plots of $\log_{10}$ (induced currents, I) vs $\log_{10}$ (dose rate, R) for polyethylene, showing straight lines of slope $\Delta\doteqdot0.68$; each line at a different applied voltage except the case of $V=0$. The direction of the current in the case of $V=0$ is reversed to that in the case of the voltage supply.

time used was about 20 min. The current at zero voltage was also measured. In this case the decrease of the current was about 1% of the initially measured value at 1.2×10^4 r/hr dose rate during the irradiation of 30 min. The dark currents without irradiation need not be taken into account because the intensities of the source were sufficiently high.

Figure 1 shows the relation between the induced current and the dose rate at room temperature that $\log I$ is proportional to $\log R$; i.e., $I\propto R\Delta$ even at such a high dose rate, where I is the induced current and R is the dose rate. In addition to this, the ohmic character will be found in the relation between induced currents vs applied voltages by replotting this figure.

The coefficient Δ can take on values between $\frac{1}{2}$ to 1, depending on trap depth, distribution, temperature, and dose rate. The value of Δ in Fig. 1 is about 0.68 and is not dependent on the applied voltage. This experimental value is smaller than the reported one, 0.75, by Mayburg and Laurence[2] that was measured under the condition up to about 4×10^3 r/hr. If we use the electron band model in this case,[3] it may be conveniently supposed that the smaller value of Δ will be due to the effects of the predominance of the bimolecular recombination between free electrons and positive ions over the trapping of electrons by trapping centers.

In the absence of applied voltages, the direction of the induced current was reversed to that in the case of the voltage supply. As to the mechanism of current generation in this case, it may be considered that the current carriers are not holes but electrons, because the direction of the induced current can be explained by the photovoltic effect in the vicinity of the metal insulator barrier of the coaxial cable. This effect in the case of the coaxial cable was also suggested by J. C. Pigg et al.[4]

* Formally in Department of Electrical Engineering, Faculty of Science and Engineering, Waseda University, Tokyo, Japan.
[1] K. Kimura *et al.*, *Proceedings of the International Conference on the Peaceful Uses of Atomic Energy, Geneva, 1958* (United Nations, New York), Vol. 29, p. 1328 (Japan).
[2] S. Mayburg and W. L. Laurence, J. Appl. Phys. 23, 1006 (1952).
[3] R. W. Smith, RCA Rev. 12, 350 (1951).
[4] J. C. Pigg, C. D. Bopp, O. Sisman, and C. C. Robinson, Commun. and Electronics 22, 717 (1956).

Microwave Noise from Low-Pressure Arcs*

R. M. Hill and S. K. Ichiki
Sylvania Electric Products Inc., Microwave Physics Laboratory, Mountain View, California
(Received August 28, 1959)

THE microwave noise from low-pressure arc discharges has been studied with the tube shown in Fig. 1. An oxide-coated, hot tungsten cathode and a copper anode are separated

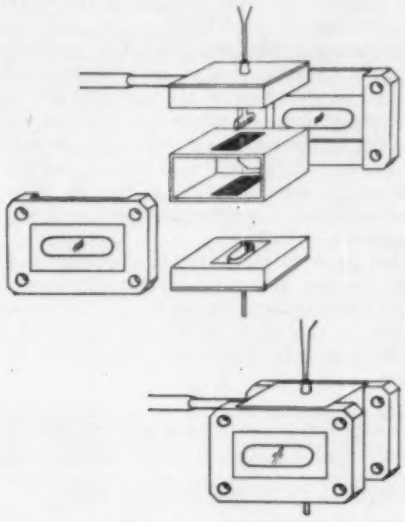

Fig. 1. Detail of microwave arc tube.

from a rectangular waveguide transmission system by wire mesh grids. The waveguide is sealed by vacuum windows. The power supply consisted of a condenser connected to a dc charging supply and a pulse-forming network which limited the arc discharge to 5 μsec or less. The discharge was triggered by the application of a short, low-voltage pulse to the waveguide grid. The noise was detected by a superheterodyne receiver using a balanced mixer which had an i.f. bandwidth of 10 Mc. A variable attenuator was placed between the tube and the receiver. A commercial 16-db/Mc noise tube was used as a reference.

After processing the cathode and filling with 200 μ of neon, the only detectable noise contributed by the arc discharge occurred in a very short spike at the beginning of the current pulse. This noise appeared throughout the waveguide range, 8–12 kMc, and within the limits of our measurements was of constant amplitude. The output of the commercial noise tube and this spike noise were compared by changing the variable attenuator until equal outputs at the receiver were achieved. This indicated a noise level during this spike of 45 db above thermal.

As the tube aged, noise became discernible in other parts of the pulse and increased monitonically with time until the cathode ceased functioning. This type of noise generation appears to be caused by deposition of cathode material around the tube and consequent secondary emission and possible unstable cathode emission.

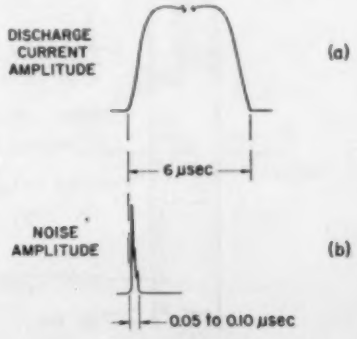

Fig. 2. (a) Current pulse. (b) Microwave noise spike.

The short spike of noise occurs just as the current through the tube starts to rise (Fig. 2). Since the level at the detector could be changed by the waveguide attenuator, it must be microwave noise propagating in the waveguide. By use of a 10-Mc bandwidth scope, the current pulse was observed to rise to a peak of approximately 5 amp in 6×10^{-7} sec. The initial rise was at a rate of 50 amp/μsec. This spike occurs at the very leading edge of the current rise and its duration is less than 10^{-7} sec. Observations of time shorter than this were not possible with our oscilloscope. The time at which it occurs and the shortness of duration indicates a generation mechanism which operates during or before the establishment of the arc discharge. Westberg[1] has shown that large traveling potential waves accompany a glow to arc transition. Our results indicate that the ignition of an arc discharge is accompanied by considerable microwave noise. It seems likely that the *generating* mechanism is provided by the potential waves discussed by Westberg. Similar noise has been observed by Moll *et al.*[2] emanating from an avalanching semiconductor diode.

* Work performed under contract with Rome Air Development Center, Griffiss Air Force Base, New York.
[1] R. G. Westberg, Phys. Rev. 114, 1 (1959).
[2] Moll, Uhlir, and Senityky, Proc. Inst. Radio Engrs. 46, 1306 (1958).

Experimental Magnetohydrodynamic Power Generator*

Richard J. Rosa
Avco-Everett Research Laboratory, Everett, Massachusetts
(Received November 30, 1959)

PERSONNEL of the Avco-Everett Research Laboratory have been working for some time on magnetohydrodynamic (MHD) power generation. This work has led to its consideration for military and space applications and, in particular, for the large scale generation of commercial power.[1] It has also led to the construction of an experimental facility for studying MHD generators. Some basic results of this study are presented here. More complete results will be presented in a subsequent paper.

The experimental facility is shown in the photograph on the cover of this issue. It consists of an arc wind tunnel or "plasma jet"[2] mounted above a magnet. The magnet with the MHD generator channel between its poles is supported by a tank which confines the exhaust and is vented to the roof. The arc heater performs for laboratory purposes the function of the thermal energy source in a power plant.

To facilitate easy modification of equipment, neither the arc tunnel or the MHD generator are cooled. This limits the maximum length of a run to about 10 sec. Actually, since steady state conditions are usually reached very rapidly, the facility has seldom been run for more than 5 sec. Both argon and helium have been used as the working gas. In either case, powdered potassium carbonate is introduced into the stream to enhance the electrical conductivity, the amount introduced representing generally about one atomic percent of the total gas flow. Gas conductivities of from 80 to 150 mho's per meter have been obtained depending upon the seeding rate and heating power used.

The generator itself consists of an insulated channel containing electrodes, placed between the poles of the magnet. A great many runs have been made using a variety of channel and electrode designs and under differing gas conditions. The points plotted on Fig. 1 summarize the basic data obtained from a series of six runs, all made with the same channel (1 in.×3 in. ×20 in. long), the same magnetic field strength (14 000 gauss), and as nearly constant as possible arc power, mass flow, and seeding rate. In this figure is shown voltage, power output, and upstream stagnation pressure as a function of the current drawn

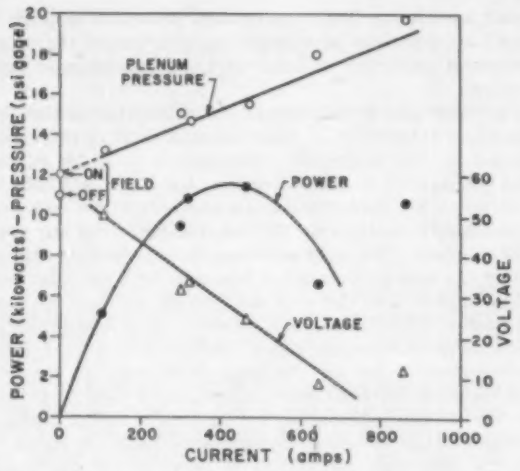

FIG. 1. MHD generator characteristics; 1 in. ×3 in. ×20 in. channel, 14 000 gauss field. The working fluid is argon plus approximately 1% K_2CO_3. The total flow rate is about 300 g/sec. The gas temperature in the channel is estimated to be about 2800°K and the Mach number of the flow equal to about 0.7.

from the generator, which, in turn, is a function of the load resistance presented to it. The solid lines give the theoretically expected variation. The data are representative in that good reproducibility is usually obtained except in about 20% of the runs. However, these occasional fluctuations in generator performance seem to correlate well with fluctuations in the performance of the arc tunnel. It seems likely that unintended variations in seeding rate are the primary source.

It is worth remarking that the overall variation in voltage, power output, and pressure drop shown in Fig. 1 does not differ basically from what one would expect from a turbogenerator and indeed, in theory, it should not.

As in a conventional generator (excluding those which have special features designed to improve voltage regulation), the output voltage decreases linearly as the output current increases, the slope of the line being proportional to the generator's internal impedance. Strictly speaking, the change in gas velocity with current drawn should also be considered. However, the relative change, which is about 15% at the high current end of the scale, is less than the experimental scatter of the data.

Power output rises to a maximum when load impedance equals generator impedance; however, the highest "electrical" efficiency is obtained for higher values of load impedance. "Electrical" efficiency η_e is defined here as

$$\eta_e = \frac{\text{power delivered to the load}}{\text{power generated}}.$$

Neglecting for the moment other losses such as those caused by electrode drops, the electrical efficiency is given simply by

$$\eta_e = \frac{\text{load impedance}}{\text{load}+\text{generator impedance}} = \frac{\text{output voltage}}{\text{open circuit voltage}}.$$

It is an important quantity in conventional generators since the power dissipated in its internal impedance represents waste heate which must be removed, and this not without difficulty. In an MHD generator this heat remains within the working gas. The electrical efficiency is then of importance only indirectly in that it partly determines how isentropic or reversible the process is. That is, it partly determines the effective "turbine" efficiency η_t defined by

$$\eta_t = \frac{(h_i - h_f)\ \text{actual}}{(h_i - h_f)\ \text{ideal}},$$

where h_i and h_f are the initial and final gas enthalpies obtained in both cases after expansion through the same pressure ratio. If internal dissipation were the only source of pressure loss in a generator designed for constant flow velocity, the turbine and electrical efficiency would be related by

$$\eta_t = \left[1-\left(\frac{P_f}{P_i}\right)^{(\gamma-1/\gamma)\eta_e}\right] \Big/ \left[1-\left(\frac{P_f}{P_i}\right)^{(\gamma-1)/\gamma}\right],$$

where P_i and P_f are the initial and final pressures and γ is the ratio of specific heats.

Another source of pressure loss in an MHD generator is that resulting from circulating eddy currents as the gas enters and leaves the magnetic field. On the basis of theoretical work done by Dr. F. Fishman of this laboratory, the eddy current loss in the experimental generator was estimated to be about one psi. Experimentally, the upstream pressure for zero output current was measured by switching off the magnetic field during a run. This measurement and a theoretical point one psi higher are both plotted on Fig. 1. The theoretical point now corresponds to what would be expected if the field were left on and the load made infinite. It can be seen that it is, in fact, in better agreement with the other measured pressure points and with the theoretically expected pressure variation.

The author is grateful for the technical assistance of H. Resnick. In addition, he must acknowledge his indebtedness to the prior work of many people, in particular to Dr. A. Kantrowitz and to T. R. Brogan, S. C. Lin, R. M. Patrick, and H. Petschek who, under the direction of Dr. Kantrowitz, laid the foundations for the present work.

* This work was partially supported by the Ballistic Missile Division, Air Research and Development Command, U. S. Air Force, under contract.

[1] P. Sporn and A. Kantrowitz, "Large-scale generation of electric power by application of the magnetohydrodynamic concept," Power (November, 1959).

[2] T. Brogan, ARS J. **29**, 648–653 (September, 1959).

Improvements on the Pedestal Method of Growing Silicon and Germanium Crystals

W. C. DASH

General Electric Research Laboratory, Schenectady, New York

(Received December 28, 1959)

THE pedestal method was developed to facilitate the growth of dislocation-free silicon crystals without a crucible.[1,2] The purpose of this note is to describe some modifications which permit the growth of large crystals of similar perfection. The new arrangement is shown schematically in Fig. 1.

The main feature of both the previously described and present methods is the withdrawal of a crystal from an inductively heated molten mound on top of a pedestal of the same material. In the earlier method the pedestal was cut into sectors to limit the power

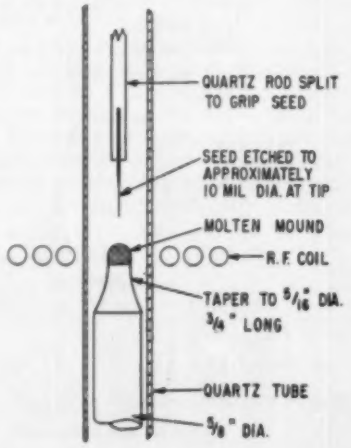

FIG. 1.

dissipated there and thus maintain a stable melt. Surface tension and electromagnetic levitation help to support the melt. As the diameter of the pedestal is decreased, the effect of the surface tension in supporting the mound becomes relatively more important. It has been found that a stable melt can be held in good thermal contact with the top of an unslotted rod if the diameter is about $\frac{5}{16}$ in. for silicon. The same can be done with the top of a $\frac{5}{8}$-in. diam bar which tapers down to $\frac{5}{16}$ in. as shown in Fig. 1. For germanium, a bar diameter of $\frac{1}{2}$ in. tapered to $\frac{1}{4}$ in. at the top behaves similarly. The dimensions quoted are not critical; a study of the limits over which they can be varied has not been made at the time of this writing.

With the tapered pedestal, it is possible to insert a small diameter seed and withdraw a crystal in much the same way as with a slotted pedestal. For about 1 cm, the growth rate is kept at about 5 to 7 mm/min in order to maintain a small diameter and facilitate the removal of dislocations.[2] The growth rate is then gradually reduced and the coil slowly lowered to melt fresh material. When the melt has reached the full diameter of the pedestal, further growth in some respects resembles that of a floating zone, except that continuous withdrawal of the growing crystal is necessary for stability. Whereas the crystals grown by the earlier method weighed only a few grams, a bar of any convenient length can be converted into a single crystal free from dislocations by the present technique. A number of silicon crystals up to about 12-mm diam and weighing approximately 20 g have been grown. Several germanium crystals weighing 10 to 12 g with diameters of about 6 mm also have been grown. A chemically polished seed can easily support the grown crystal despite its seemingly small size, since the tensile stress is less than 1 kg/mm².

The method here described resembles in some respects the one developed by Raymond and Sterling[3] for growing silicon crystals. The present method has the advantage of simplicity and also of relative ease of controlling the initial stages of growth so that a dislocation-free crystal can be grown.

[1] W. C. Dash, J. Appl. Phys. **29**, 736 (1958).
[2] W. C. Dash, J. Appl. Phys. **30**, 459 (1959).
[3] Described by M. Tanenbaum in *Semiconductors*, edited by N. B. Hannay (Reinhold Publishing Corporation, New York, 1959), p. 115.

Method for Determining the Thermal Conductivity of Incandescent Solids*

B. B. Brenden and H. W. Newkirk†
Hanford Research Operation, Richland, Washington
(Received September 22, 1959)

THIS letter reports a method for determining the thermal conductivity of solids above 1000°C. The work uses an approach similar to that reported by Nancarrow[1] in which the sample can be either a conductor or a nonconductor of electricity. Figure 1 illustrates the experimental arrangement in which a cylindrical sample is supported with one end contacting a hot

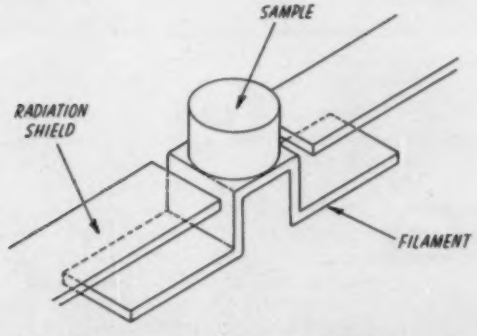

FIG. 1. Experimental arrangement for heating the sample.

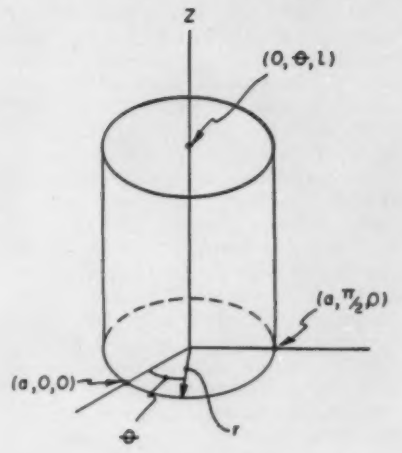

FIG. 2. Geometry used in deriving Eq. (4).

tungsten filament. Heat flows by conduction into one end of the sample and flows out of the sample by radiation from exposed surfaces. As will be shown, the thermal conductivity of the sample can be calculated from a knowledge of the bottom, middle, and top surface true temperatures and the total emissivity.

In making an analysis of the heat flow through the sample it is assumed that (1) back radiation to the sample from the walls of the furnace, (2) the effect of radiation to the sample from regions of the filament not completely eclipsed by the radiation shields, and (3) the variation of temperature with the cylindrical coordinate θ are negligible. The steady state heat flow equation consistent with these assumptions is[2]

$$\frac{\partial^2 U}{\partial r^2}+\frac{1}{r}\frac{\partial U}{\partial r}+\frac{\partial^2 U}{\partial z^2}=0, \tag{1}$$

where U is the temperature (°K) and r and z are cylindrical coordinates. An approximate solution to Eq. (1) is

$$U(r,z)=A+Bz+C(r^2-2z^2)+D(3r^2z-2z^3)+E(3r^4-24r^2z^2+8z^4). \tag{2}$$

Figure 2 shows the sample superimposed on a cylindrical coordinate system. The rate of heat loss from the sample surface per unit area is given by the equation

$$-K\frac{\partial U}{\partial r}\bigg|_{r=a}=\epsilon\sigma U^4(a,z), \tag{3}$$

where ϵ is the total hemispherical emissivity, σ is the Stefan-Boltzman constant (5.67×10^{-12} w cm^{-2} deg^{-4}), and K is the thermal conductivity (w cm^{-2} per °K cm^{-1}).

The five constants, A, B, C, D, and E and the ratio K/ϵ are determined from the temperatures, $U_1=U(a,0)$, $U_2=U(a,l/2)$, and $U_3=U(a,l)$, where "a" is the radius and "l" is the length of the sample. These temperatures substituted into Eqs. (4) and (5) can be solved to yield

$$\frac{K}{\epsilon}=\frac{\sigma l^3}{24a}\frac{U_1^4+U_3^4+10U_2^4}{U_1+U_3-2U_2}-\frac{\sigma a}{4}\frac{U_1^4+U_3^4-2U_2^4}{U_1+U_3-2U_2}. \tag{4}$$

The more simple expression

$$\frac{K}{\epsilon}=\frac{\sigma l^3}{2a}\frac{U_2^4}{U_1+U_3-2U_2} \tag{5}$$

differs from Eq. (4) by less than 2% in most cases and probably gives values as accurate as the temperature measurements permit.

In summary, the method requires the measurement of three temperatures U_1, U_2, and U_3 and the total hemispherical emissivity of the sample. Since the temperatures are true temperatures, data must be obtained on the transmission of the optical system and the normal spectral emissivity of the sample.

The method was tested by making the necessary measurements on samples of graphite and uranium dioxide and comparing the calculated thermal conductivity values with published values obtained from similar samples by other methods. Graphite samples of 0.635-cm diam and 0.953 cm long, cut from spectroscopic electrodes, and uranium dioxide samples, 0.625 cm long, cut from extruded rods, were heated in the tungsten-filament furnace previously described.[3] The samples used to determine thermal conductivity and total hemispherical emissivity were heated *in vacuo*. The samples used to determine normal total emissivity were heated in a helium atmosphere using a pinhole aperture in place of the furnace window. Temperatures were measured using a calibrated disappearing filament pyrometer. Sample radiant energy was detected by using a circular thermopile in conjunction with a Type K-2 potentiometer-Rubicon galvanometer. Normal spectral emissivity and total hemispherical emissivity were calculated from the known radiation laws.[4]

Figure 3(a) shows a comparison of the thermal conductivity of graphite as determined by the method discussed in this paper

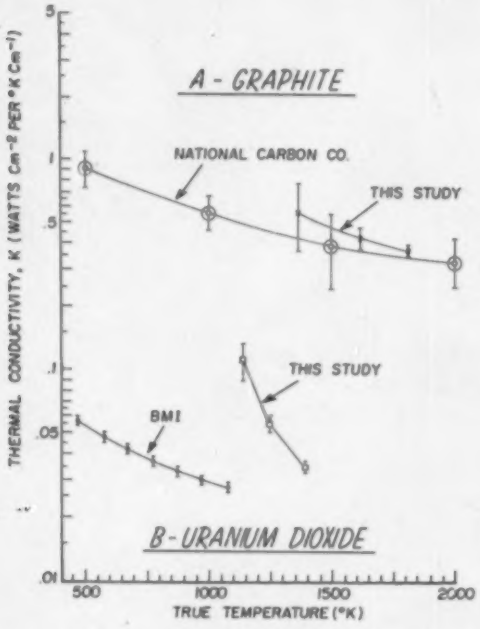

FIG. 3. Comparison of thermal conductivity values.

with the values quoted by the National Carbon Company.[5] Figure 3(b) shows a comparison of the thermal conductivity of uranium dioxide as determined by our method with the values quoted by the Battelle Memorial Institute.[6] The values determined for graphite compare well with published values, whereas a factor of five difference exists for the uranium dioxide samples. These findings suggest that our method determines the thermal conductivity at the surface of the sample, whereas the method used by Battelle yields an average value for the bulk material. Further studies should verify or refute this hypothesis.

The difference may also be due in part to the failure of the experiment to comply with the three assumptions made in the analysis. The first assumption is consistent with the design of the furnace which had blackened, watercooled walls. The validity of the other two assumptions was somewhat affected by radiation from the corners of the stepped portion of the filament which were not completely covered by the cylindrical sample or by the shields.

Refinements in the experimental technique promise greater accuracy than realized in these preliminary experiments. In particular, it is expected that the method could be improved by using a two-color pyrometer. The pyrometer would be mounted so as to permit micrometer adjustment to the desired points on the sample to within a few thousandths of an inch. The relative insensitivity of the two-color temperature to emissivity could eliminate the need of determining the spectral emissivity; the reproducibility of the temperature readings could be expected to reduce the uncertainty of the term, $U_1+U_3-2U_2$.

Details of our method and our experimental observations have been described in a document which is available on request.[7]

* This work was performed under contract between the U. S. Atomic Energy Commission and the General Electric Company, Richland, Washington.

† Mr. Newkirk is now at the David Sarnoff Research Center, RCA Laboratories, Princeton, New Jersey.

[1] H. A. Nancarrow, Proc. Phys. Soc. (London) **A45**, 447 (1933).
[2] H. W. Reddick and F. H. Miller, *Advanced Mathematics for Engineers* (John Wiley & Sons, Inc., New York, 1947), p. 269.
[3] H. W. Newkirk and J. L. Bates, Rev. Sci. Instr. **30**, 622 (1959).
[4] W. E. Forsythe, editor, *Measurement of Radiant Energy* (McGraw-Hill Book Company, New York, 1937).
[5] D. E. Muir (private communication).
[6] H. W. Deem (private communication).
[7] B. B. Brenden and H. W. Newkirk, Jr., HW-59574 (March, 9 1959).

Generation of Dislocations by an Electric Field in MgO

E. MENDEL AND S. WEINIG
Materials Research Corporation, Yonkers, New York
(Received November 23, 1959)

THE effect of an electric field on the morphology of ceramic crystals was investigated. It was observed that dislocation arrays were produced on the crystals surface. MgO crystal which were cleaved along (100) planes were used. They were etched in a solution of 5 parts saturated NH_4Cl, 1 part concentrated H_2SO_4 and 1 part distilled H_2O subsequent to cleaving. The specimens were immersed in solution for approximately 10 min. Microscopic examination revealed a random distribution of dislocation etch-pits superimposed on a fine network of substructure. This may be seen in the background of Fig. 1.

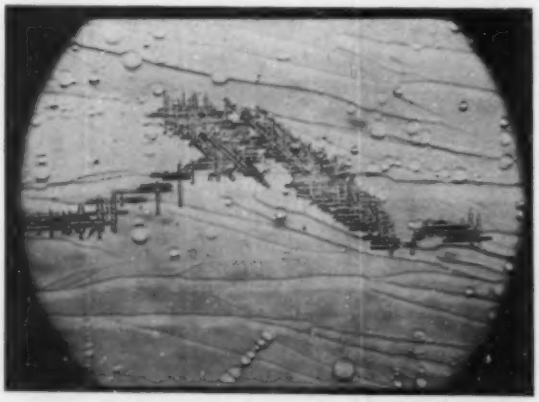

FIG. 1. Resulting dislocation pattern in MgO after application of 7.5 kv with probe in contact with the specimen (350×).

Electric fields were applied to the specimens with a 7.5-kv-dc source utilizing sharp metal probes as contacts. Two experimental procedures were used. In one case, the probes were brought in contact with the surface and voltage was applied. There was no visible spark; i.e., corona discharge. Only one probe was in contact with the specimen in the second case and the other probe was maintained approximately 1–2 mm away from the surface of the MgO. When the field was applied, a visible spark moved rapidly along the crystal surface completing the circuit. The first technique resulted in the dislocation pattern seen in Fig. 1 and the latter produced the configuration shown in Fig. 2.

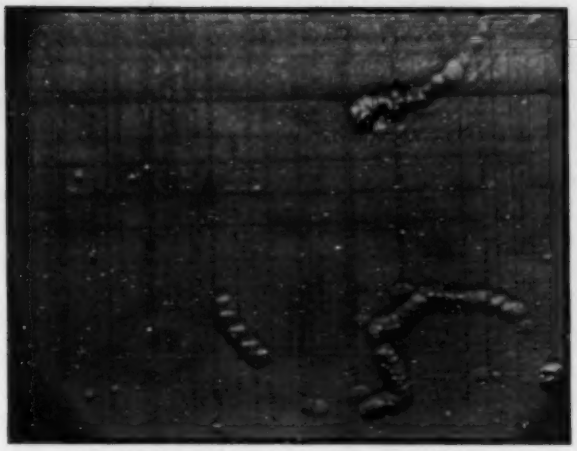

FIG. 2. Dislocation configuration resulting from 7.5 kv corona discharge across the crystal surface (300×).

The pattern shown in Fig. 1 is similar to the "Dislocation Lichtenberg" figures observed by Gilman *et al.* in LiF crystals.[1] It was thought that this array might be caused by the mechanical distortion of the contact probe and hence the following experiment was performed. A clean crystal was brought into pressure contact with the probe and then the specimen was polished, etched, and microscopically examined. Although the depression caused by the probe was clearly evident, no visible pattern of dislocations was observed. The specimen was again brought in contact with the probe and a field of 7.5 kv applied. After polishing and etching, Fig. 3 was obtained. The probe depression is clearly evident below the resulting pattern. It is interesting to note that the dislocation pattern is not isotropic relative to the electric field. Further, it is seen that the large dislocation etch pits which were present in the as-cleaved crystals are on the same crystallographic traces as the dislocations generated by the electric field. However, they do not appear to interact with each other.

When the specimens were cleaved subsequent to the application of the field, it was found that the dislocation configuration generated by the direct contact of the probes (Fig. 1) existed throughout the crystal, but the array developed by the corona discharge (Fig. 2) did not penetrate into the specimen. Although in both cases, the dislocations are on the same crystallographic traces, it must be assumed that only surface sources were activated by the corona discharge; whereas, the dislocations were generated throughout the specimen by the electric field.

FIG. 3. Pattern of dislocations corresponding to the probe contact shown as a depression on the specimen surface (7.5 kv) (350×).

Another possibility that must be considered is the effect of local heating causing the generation of dislocations. A metal probe of the same physical dimensions as the electric probe was heated and brought into contact with an MgO cleaved crystal surface. Dislocation patterns were observed, but of an entirely different morphology. The dislocation patterns were extremely widespread as compared to the electrically generated imperfections and were restricted to fewer crystallographic planes. The heat generated by the electrical probe was a very small fraction of that used in the heat experiment. It appears that heat alone could not explain the observed dislocation patterns after applying an electrical charge.

These results suggest many new experiments for the study of dislocation motion and generation in ceramic type crystals. For example, preliminary internal friction results of a 9-in. rod specimen, reveal that the decrement increased as a function of the electric field. These data corroborate the previous results; i.e., it is expected that the energy dissipated will increase as a function of the number of free dislocations present in the crystal.

[1] J. J. Gilman and D. W. Stauff, J. Appl. Phys. **29**, 120 (1958).

Total Electromagnetic Cross Sections of Imperfectly Conducting Cylinders

E. S. CASSEDY AND J. FAINBERG
Radiation Laboratory, The Johns Hopkins University, Baltimore, Maryland
(Received November 23, 1959)

IT is well known in collision theory that the total cross section (elastic+inelastic and absorption) in a scattering process is proportional to the imaginary part of the elastic scattering amplitude in the forward direction.[1]

The analogous result in electromagnetic theory for scattering of monochromatic plane waves by perfectly conducting bodies is as follows[2]:

$$\sigma_T = (4\pi/k^2)\,\mathrm{Im}[\hat{e}''\cdot\mathbf{A}(\hat{r}'',\hat{r})], \tag{1}$$

where

σ_T = total cross section
$= \sigma_a + \sigma_s$,
σ_s = scattering cross section,
σ_a = absorption cross section
$= 0$, for perfect conductors,
$\hat{e}''$ = unit polarization vector of incident electric field,
$\mathbf{A}(\hat{r}'',\hat{r})$ = scattering amplitude vector[3] in the direction of $\hat{r}$ for wave incident in the direction of $\hat{r}''$,
$= \mathbf{A}_0(\hat{r}'',\hat{r})$ for perfectly conducting bodies, and
$k = 2\pi/\lambda$.

The same result holds when scattering bodies of finite conductivity are considered, in which case $\sigma_a \neq 0$ and $\mathbf{A}(\hat{r}'',\hat{r})$ will include effects of loss.

For bodies of perfect conductivity, a solution for $\mathbf{A}(\hat{r}'',\hat{r})$ exists in terms of the induced currents on the scatterer. By a variational procedure it may be shown that $\mathbf{A}(\hat{r}'',\hat{r})$ is stationary with respect to changes in the induced current distributions from their (unknown) exact value.[2] This allows $\mathbf{A}(\hat{r}'',\hat{r})$ to be estimated by a judicious guess of the current distribution. This variational procedure has been applied to the case of imperfectly conducting cylinders.[4,5]

A case of interest is that of scattering from cylinders with length comparable to and with diameter small compared to the wavelength of the illumination. The incident radiation is considered to be plane waves with propagation normal to and polarization parallel to the axis of the cylinder. For this case an expression has been derived[4,5] for the scattered amplitude in an

azimuthal plane (x,y) normal to the axis (z) of the cylinder and containing its midpoint (0,0,0).

$$\hat{r}''\cdot\mathbf{A}(\hat{r}'',\hat{r})=f^2/(g+g'), \tag{2}$$

where[4,5]

$$g=Si(4kl)+jCi(4kl)-j\ln(\gamma 4kl)+4[\cos kl][kl\cos kl-\sin kl]$$
$$\left[\times ZCi(2kl)-jSi(2kl)-\ln(\gamma 2kl)+\ln\frac{4l}{a}\right]-j2[\cos^2 kl]$$
$$\times[\exp(-2jkl)-1]-\frac{4ka}{\pi}\sin^2 kl,$$

$$g'=-j\frac{4\pi}{k\eta}Z_i[kl(2+\cos 2kl)-\tfrac{3}{2}\sin 2kl],$$

$f=2(\sin kl-kl\cos kl)$,
$\gamma=1.781072$,
Z_i = skin impedance per unit length[6] of cylinder,
$l=\frac{1}{2}$ length of cylinder,
$k=2\pi/\lambda$ for incident wave,
a = radius of cylinder $\ll\lambda$,
$\eta=\mu^{\frac{1}{2}}\epsilon^{-\frac{1}{2}}$ = impedance of free space.

It should be noted that this expression is independent of the azimuthal angle $[\phi=\cos^{-1}(\hat{r}''\cdot\hat{r})]$, since the shadow remanant becomes isotropic for bodies of very small thickness.[7] The back scattering cross section is proportional to $|\mathbf{A}|^2$, and this result has been checked with experimental back scattering measurements[4] on fine wires for lengths less than λ. The experimental results agree with the theoretical to within 4% for cases where losses cause as much as a 75% reduction in scattering.[4] This indicates that the result given in Eq. (2) may be used in Eq. (1) to give the total cross section to about the accuracy quoted above.

A partial check on this may be made from the measurements quoted in reference 4. The absorption cross section σ_a of the cylinder may be computed by integration of the current squared times the skin resistance over the cylinder, where current is taken to be the same function as was used in deriving Eq. (2), with the constants determined by the variational method. This yields

$$\sigma_a/\lambda^2=(4\pi R_i g/k\eta f^2)|\mathbf{A}|^2, \tag{3}$$

where

$$R_i=\mathrm{Re}(Z_i).$$

The scattering cross section computed from Eqs. (1) and (2) is given by

$$(\sigma_s/\lambda^2)_{\mathrm{th}}=(\sigma_T-\sigma_a)/\lambda^2. \tag{4}$$

The scattering cross section may be obtained from the experimental measurements by integrating the differential cross section over the total solid angle. The ϕ dependence is constant, and the θ dependence of a half-wave dipole is known from antenna theory. Therefore,

$$(\sigma_s/\lambda^2)_{\mathrm{ex}}=(1/1.64)\frac{\sigma_B}{\lambda^2}, \tag{5}$$

where σ_B = scattering cross section in azimuthal plane and 1.64 = gain of half-wave dipole in azimuthal plane.

Measurements of back scattering from a 0.001-in. diam bismuth wire illuminated by 10 cm radiation[4] yield the following value at first resonance,

$$(\sigma_s/\lambda^2)_{\mathrm{ex}}=0.121\pm 0.005.$$

The calculated value for this case is

$$(\sigma_s/\lambda^2)_{\mathrm{th}}=0.127,$$

yielding a discrepancy of 5.1%, similar to those obtained in the back scattering results.[4] The scattering cross section of a wire with the same dimensions as above but of perfect conductivity is

$$\sigma_s/\lambda^2=0.515,$$

indicating the correction offered by the variational expression for the scattered amplitude.

The work described in this letter was supported by the Wright Air Development Center. The authors wish to thank Dr. J. M. Kopper for review of the manuscript.

[1] L. I. Schiff, *Quantum Mechanics* (McGraw-Hill Book Company, Inc., New York, 1955) 2nd ed., pp. 105–106; E. Feenberg, Phys. Rev. **40**, 40 (1932).
[2] R. D. Kodis, J. Soc. Ind. Appl. Math. **2**, 89 (1954).
[3] This scattering amplitude is dimensionless, differing from that of reference 2 by the factor k.
[4] E. S. Cassedy and J. Fainberg, Trans. Inst. Radio Engrs. **AP-8**, 1960 (scheduled for publication).
[5] R. C. Kouyoumjian, The Ohio State University, Antenna Laboratory, Tech. Rept. 44-13 (1953).
[6] S. Ramo and J. R. Whinnery, *Fields and Waves in Modern Radio* (John Wiley & Sons, Inc., New York, 1949).
[7] L. I. Schiff, Progr. Theoret. Phys. (Kyoto) **11**, 288 (1954).

Spontaneous Emission from an Inverted Spin System

AMNON YARIV
Bell Telephone Laboratories, Incorporated, Murray Hill, New Jersey
(Received December 16, 1959)

THIS paper summarizes the results of calculations made in an attempt to explain the origin of the observed modulation effects in two-level maser experiments.[1,2]

In a spontaneously oscillating spin system any transverse magnetization, which couples rf power out of the spin system, is due to the presence of a transverse rf field, which is in turn induced by the transverse magnetization. Any consideration of the dynamics of the spin system or the build-up of the radiation field must consequently treat the two systems simultaneously.

Our analysis uses a model first formulated by Bloembergen and Pound,[3] except that our problem is inherently nonlinear[4] and we cannot make the simplifying assumption $Mz=\mathrm{const}$, which linearizes the equations of motion, and are forced to have recourse to an IBM 704.

The physical situation is that of an inverted, homogeneously broadened, magnetization of amplitude M_0 placed inside a microwave cavity which can support a circularly polarized transverse magnetic field. If we take the spin precession frequency γH_0 to be equal to the cavity resonant frequency $(LC)^{-\frac{1}{2}}$, assume that no external power is fed into the cavity, and that the spin lattice relaxation time T_1 is infinite, we can write a set of three nonlinear simultaneous differential equations.

$$\frac{2j\omega}{T_R|M_0\gamma|}M_1+\frac{2}{T_R|M_0\gamma|}\frac{dM_1}{dt}+Q\frac{dH_1}{dt}+\omega H_1=0, \tag{1}$$

$$\frac{dM_1}{dt}-j\gamma M_z H_1+\frac{M_1}{T_2}=0, \tag{2}$$

$$\frac{dM_z}{dt}=\mathrm{Im}[\gamma M_1^* H_1]. \tag{3}$$

Equations (1)–(3) appear in a slightly different form in footnote 3. M_1 and H_1 are complex and are defined by

$$M_x+jM_y=M_1e^{j\omega t} \tag{4}$$

and

$$H_x+jH_y=H_1e^{j\omega t}, \tag{5}$$

where M_x, M_y, H_x, and H_y are the transverse components of the magnetization and magnetic field, respectively. γ is the magnetrogyric ratio. T_R is the radiation damping time defined by

$$T_R=(2\pi\eta|\gamma M_0|Q)^{-1}.$$

η is the sample filling factor, Q is the loaded "Q" of the cavity. T_2 is the spin-spin relaxation time which for a homogenous Lorentizian line is given by

$$T_2=2/\gamma\Delta H=2/\Delta\omega,$$

where ΔH is the separation in gauss between the half power points. M_1^* is the complex conjugate of M_1. Since M_z, H_1, and M_1 are functions of time. Equations (1)–(3) constitute a set of nonlinear differential equations. The solution was carried out with the aid of an IBM 704. For numerical purposes it was necessary to consider the following set of equations which are the real and imaginary parts of Eqs. (1)–(3)

$$aM_r+b\frac{dM_i}{dt}+Q\frac{dH_i}{dt}+\omega H_i=0, \tag{6}$$

$$-aM_i+b\frac{dM_r}{dt}+Q\frac{dH_r}{dt}+\omega H_r=0, \tag{7}$$

$$\frac{dM_i}{dt}+|\gamma|M_zH_r+CM_i=0, \tag{8}$$

$$\frac{dM_r}{dt}-|\gamma|M_zH_i+CM_r=0, \tag{9}$$

and

$$\frac{dM_z}{dt}+|\gamma|M_rH_i-|\gamma|M_iH_r=0, \tag{10}$$

where

$$M_1=M_r+jM_i,$$

$$H_1=H_r+jH_i,$$

$$a=\frac{2\omega}{T_R|M_0\gamma|}=4\pi\omega\eta Q,$$

$$b=\frac{2}{T_R|M_0\gamma|}=4\pi\eta Q,$$

and

$$c=1/T_2.$$

Since we are dealing with an inverted magnetization, our first boundary condition is $M_z(0)=-M_0$. This constitutes an unstable equilibrium and some mechanism is necessary to trigger the spontaneous emission. This could be either some residual transverse magnetization or some cavity current present at $t=0$. We used the residual current for a trigger and put $H_r(0)=0.1M_0$. The magnitude of $H_r(0)$ was found to have little effect on the subsequent behavior of the magnetization.

The values of ω, Q, and M_0 were chosen to approximate the experimental conditions prevailing at the two-level maser experiment performed by Chester, Wagner, and Castle of Westinghouse.[2] These are

$$M_0=5\times10^{-4} \text{ gauss } (10^{18} \text{ spins at } 4.20\text{K}),$$

$$Q=10\,000,$$

and

$$\omega=2\pi\times10^{10} \ (f=10 \text{ kMc}).$$

The resulting behavior of H_1^2, which is equal to $H_r^2+H_i^2$, is shown in the lower trace of Fig. 1. H_1^2 is proportional to the power coupled out of the cavity and is to be compared with the experimental observations in which the spontaneous emission power following inversion was monitored.[1,3] The upper trace shows the oscillatory return of M_z to its equilibrium, $M_z=+M_0$, value. The peaks of M_z coincide with these of H_1^2 as required by conservation of energy considerations. It was found that as long as $T_1<T_2$ which is the start oscillation condition for a two-level maser oscillator, T_2 had a negligible effect on the shape of the curves and could be assumed to be infinite. The behavior of H_1^2 bears a close resemblance to the experimental results—especially those of the Westinghouse Group.[2] A significant difference remains—the time interval between power peaks in Fig. 1 is $\sim$0.1 μsec while the observed results give $\sim$1 μsec. This difference may be due to the actual inhomogenous nature of the line, in contrast to the homogenous line assumed in our analysis. The envelope curve, traced through the successive oscillation peaks, decays with a characteristic time corresponding to the cavity Q, i.e.,

$$T_{\text{envelope}}\approx Q/\omega.$$

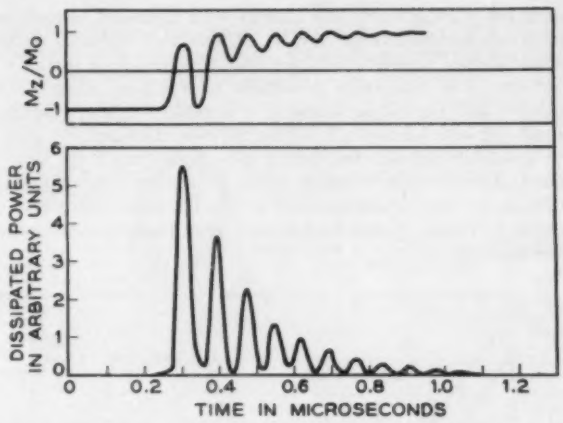

FIG. 1. Upper trace: $M_z(t)/M_0$ vs t following spin inversion at $t=0$. $M_0=5\times10^{-4}$. Lower trace: $(H_r^2+H_i^2)/M_0^2$ which is proportioned to the power coupled out of the cavity is shown as a function of the time following the spin inversion, $M_0=5\times10^{-4}$.

This feature is retained regardless of the magnitude of M_0. The interval between peaks depends on M_0. This dependence is not very strong and using a value of M_0 which is smaller by a factor of 15 than that used in Fig. 1 yielded a value of $\sim$0.3 μsec which is closer to the experimentally observed values.

The author is indebted to J. P. Gordon for some helpful discussions and to Miss J. Liu for carrying out the numerical computation.

[1] G. Feher, J. Gordon, E. Buehler, E. Gere, and C. Thurmond, Phys. Rev. **109**, 221 (1958).
[2] P. F. Chester, P. E. Wagner, and J. G. Castle, Jr., Phys. Rev. **110**, 281 (1958).
[3] N. Bloembergen and R. V. Pound, Phys. Rev. **95**, 8 (1954).
[4] A. Yariv, J. R. Singer, and J. Kemp, J. Appl. Phys. **30**, 265 (1959).

Backscattering of Carbon-14 Beta Radiation

GEORGE L. GAINES, JR.
General Electric Research Laboratory, Schenectady, New York
(Received November 12, 1959)

IN connection with studies of radiostearic acid monolayers,[1] we have been concerned about the backscattering of C^{14} β-particles by various substrates. It is commonly stated[2] that the percentage saturation backscattering of β-particles is independent of β-energy for radiation of sufficiently high energy ($E_{max}>0.6$ Mev). Zumwalt[3] has shown that the same saturation backscattering results are obtained with Geiger-Müller counters for radiation of lower energy if the observed results are corrected for air- and window-absorption of the scattered radiation. Glendenin and Solomon[4] have pointed out that the same sort of correction brings results for S^{35} β-particles (0.17 Mev) into line with those for more energetic radiation.

It is reasonable to suppose that the same results would be obtained with C^{14} (0.15 Mev), but we have found no reported experimental verification of this. Because of the considerable importance of this isotope in chemical and biological studies, it seems desirable to record the results which we have obtained. Yaffe and Justus[5] have reported some results for C^{14} β-radiation with Geiger-Müller counters. Beischer[6] has found that autoradiographic observations lead to similar backscattering results for C^{14} and more energetic radiation. In the present experiments we have compared the backscattering of β-radiation from C^{14} and Tl^{204} (0.76 Mev) with a mica end-window Geiger-Müller counter under conditions of similar geometry, and have measured the absorption (in aluminum) of the backscattered radiation.

The sources were evaporated deposits of C^{14} labelled stearic acid ($\sim$10 mC/g) and $TlNO_3$ ($\sim$50 mC/g) on vinylite films of

thickness $<25\ \mu g/cm^2$.[7] The sources were extended, in each case occupying a circular area of $\sim 8\ cm^2$, and were centered under a Geiger-Müller counter (1.29 mg/cm^2 window) at a distance of 1.25 cm. The aluminum absorbers were placed close to the counter, and the entire assembly was housed in a conventional aluminum and Lucite rack within an iron chamber. No part of the assembly beneath the source was closer than 5 cm from it. Backscatterers thick enough to assure saturation ($\frac{1}{4}$ in. Al and Cu, 0.020 in. Pt) were placed as close as possible to the film (certainly within 0.2 mm). Usual background and dead-time corrections were applied.

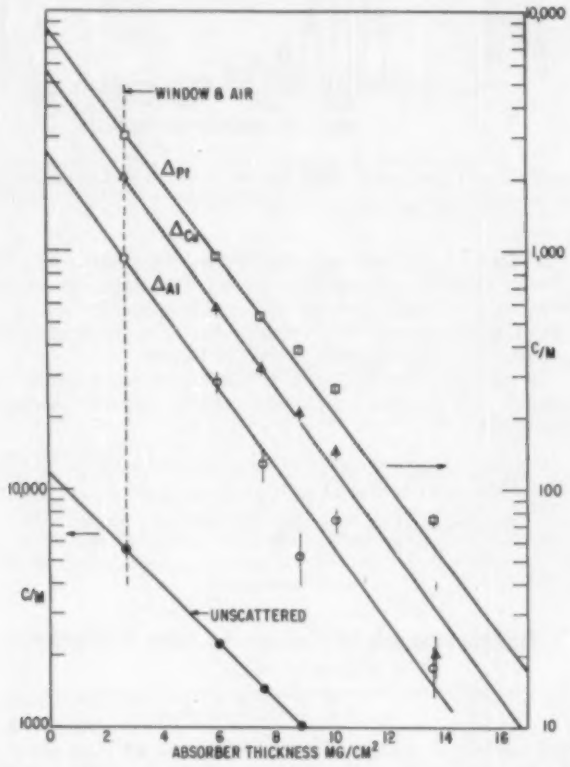

FIG. 1. Absorption (in aluminum) of C^{14} β-radiation, unscattered and backscattered from various metals. (Points for Al, Cu, and Pt represent differences between observed count rates with and without backscatterer.) (Count rate standard deviations indicated.)

Figure 1 illustrates the results for C^{14}. The results obtained for the two sources, with no correction and after extrapolation to zero absorber are shown in Table I. It is apparent that, while the uncorrected results for C^{14} are appreciably lower than those for Tl^{204}, correction for absorption brings them into reasonable agreement.

TABLE I. Increase in count rate due to backscattering.

	C^{14}		Tl^{204}	
Substrate	Uncorr. %	Corr. for absorption %	Uncorr. %	Corr. for absorption %
Al	16	21	24	23
Cu	36	46	41	42
Pt	54	68	75	71

These significant corrections are due to the different absorption behavior of the scattered radiation, which is degraded in energy. As has been observed before,[8,9] this degradation is extremely dependent on the angle of scattering. For this reason it must be emphasized that backscattering corrections must be evaluated under conditions of very carefully controlled geometry. Even very slight variations in the geometry of the source or counting arrangement may lead to significant differences in the observed backscattering, especially with low-energy radiation.

I am indebted to Miss C. P. Rutkowski for experimental assistance.

[1] G. L. Gaines, Jr., submitted to J. Phys. Chem.
[2] See, e.g., G. Friedlander and J. W. Kennedy, *Nuclear and Radiochemistry* (John Wiley & Sons, Inc., New York, 1955), p. 203.
[3] L. R. Zumwalt, Oak Ridge National Laboratory Rept. MonC-397 (1949); (obtainable from the U. S. Government Printing Office as Document AECU-567).
[4] L. E. Glendenin and A. K. Solomon, Science **112**, 623 (1950).
[5] L. Yaffe and K. M. Justus, J. Chem. Soc. (1949).
[6] D. E. Beischer, J. Phys. Chem. **57**, 134 (1953); U. S. Navy School of Aviation Medicine, Naval Air Station, Pensacola, Florida, Project NM 001 059.16, Rept. No. 6, 1951.
[7] B. Pate and L. Yaffe, Can. J. Chem. **33**, 15 (1955).
[8] H. H. Seliger, Phys. Rev. **88**, 408 (1952).

CW Millimeter Wave Maser Using Fe^{3+} in TiO_2*

S. FONER AND L. R. MOMO
Lincoln Laboratory, Massachusetts Institute of Technology, Lexington, Massachusetts
(Received December 21, 1959)

A CW 3-level maser,[1] employing Fe^{3+} ions in a TiO_2 dielectric,[2,3] has been operated at signal frequencies from 26 to 39 kMcps. In contrast with the *pulsed-field* millimeter wave maser,[4] which can use paramagnetic materials with various zero-field splittings, the characteristics of the cw millimeter wave maser material are dictated mainly by technical limitations of available millimeter wavelength pump sources. In this letter, the characteristics of the cw maser are briefly summarized and some of the useful properties of the paramagnetic material are described. Despite the narrow tuning range of the 4-mm wavelength pumping source, maser operation over a wide range of signal frequencies and magnetic fields was attained at 4.2°K. The present results indicate that this maser material will be useful far above and below the frequency range investigated here.

The high dielectric constant of TiO_2 [5] simplified the maser cavity design. Any convenient dimensions of the dielectric assured many suitable modes for both the signal frequency f_s and the pump frequency f_p; the maximum dielectric volume was limited mainly by the available pump power. The cavity was an adjustable rectangular brass box,[6] which contained the dielectric (0.026 in. by 0.15 in. by 0.35 in. for most of the experiments). The dimensions of the rectangular box and the filling factor were not critical. Loaded Q's were a few thousand at both f_p and f_s. The signal and pump waveguide polarizations were mutually orthogonal, and energy was coupled to the cavity through slots. The TiO_2 was oriented so that the c axis was parallel to the rf magnetic field of the f_p waveguide, but the rf field orientations in the multimode dielectric cavity could not be accurately specified. The applied magnetic field H was rotated in a (100) plane.

Pump power[7,8] of 2 to 10 mw was sufficient for maser operation either as an amplifier or as an oscillator at 4.2°K. By carefully adjusting the dimensions of the signal coupling iris, oscillations were observed at f_s. Amplification was then obtained when proper external loading was supplied. With f_p fixed, f_s could be varied over a wide range by simply changing the magnitude of H and the angle θ between H and the c axis. The high density of signal modes permitted almost continuous coverage of f_s from 33.7 to 36.1 kMcps to be obtained by this procedure. As an example, Fig. 1 shows f_s vs θ, where H (approximately 3000 gauss for all the data), θ, and the external loading were varied while f_p was fixed at 70.4 kMcps. By decreasing f_p to 68.4 kMcps, the range of f_s has been increased to 39.2 kMcps at larger values of θ. Maser operation at values of f_s spaced within 300 Mcps of each other was observed over this range. Gain-bandwidth products from 10 to 40×10^6 cps have been measured over the operating range. Signal saturation effects were noted at input powers

greater than about 10^{-8} w. Decreased maser operation could be found in a small region near $f_s = f_p/2$, probably because of cross-relaxation effects.[9] Simultaneous amplification at two frequencies separated by about 30 Mcps has been observed for some operating points e.g., Fig. 1, $\theta = -7.2°$. Thus further bandwidth improvements can be expected with larger dielectric cavities or a traveling wave structure.

The oscillations showed a pulsating character similar to those described previously.[10,11] The repetition rate could be varied from less than 10^3 per sec to over 2×10^5 per sec by changing pump power, f_s, H, θ, or external loading. Oscillations at more than one frequency are frequently observed, and oscillation could be detected simultaneously at f_s or at frequencies near f_s while amplifying at f_s.[12] Employing f_p near 70 kMcps, oscillations have also been observed for various other energy levels. Oscillations at $f_s \leqslant 26.5$ kMcps have been attained at about 4 kilogauss, and a number of other operating points with $H \leqslant 16.5$ kilogauss are indicated. Because sufficiently accurate energy level diagrams were not available for these experiments, the maser oscillation characteristics were used to examine feasible regions for maser operation. When f_s was less than the signal waveguide cut-off frequency (21.1 kMcps), evidence of signal oscillations was indirectly indicated by pulsating demands on the pump power.

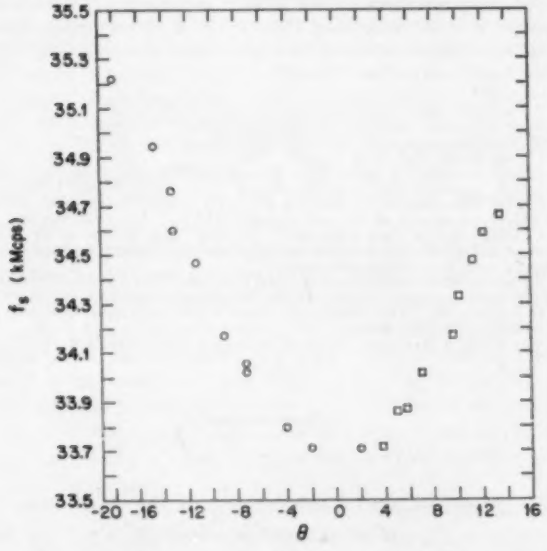

FIG. 1. Maser signal frequency f_s vs θ, the angle between the magnetic field H, and the c axis of the TiO_2 crystal. H was in the (100) plane for this experiment. The pump frequency was 70.4 kMcps, and H was adjusted slightly for the various operating points. Note that the miltimode dielectric cavity permits almost continuous tuning of f_s. The squares and circles correspond to different experiments.

The maser characteristics of Fe^{3+} in TiO_2 are well suited for operation in the millimeter wavelength region. The high dielectric constant and good mechanical properties permit construction of a small volume, multimode cavity. Tuning of f_s can then be accomplished by varying the magnitude and direction of H. Operation in the 8 mm wavelength region can easily be attained with superconducting solenoid magnets now available,[13] and the small maser cavity will also permit superconducting magnets with ferromagnetic cores[12] to be employed for maser operating points over the entire field range so far investigated. The large zero field splittings of Fe^{3+} in TiO_2, and the large E term[14] in the spin Hamiltonian permit efficient operation over a very wide range of frequencies. The low pumping powers required, and relatively low signal saturation level indicate a long spin-lattice relaxation time for this material. At present, higher operating frequencies appear to be limited by availability of suitable pumping frequency sources.

We wish to thank Dr. Benjamin Lax and Dr. Gerald S. Heller for suggesting this problem, and for encouragement during the course of this work. We also wish to thank Professor W. Low of the Hebrew University, Jerusalem, Israel, for suggesting the possibilities of the paramagnetic material Fe^{3+} in TiO_2, Mr. E. P. Warekois for his valuable assistance in finding a suitable crystal and aid with preparation of maser test samples, and Dr. S. H. Autler for several valuable discussions.

* The work reported in this paper was performed at Lincoln Laboratory, a center for research operated by Massachusetts Institute of Technology with the joint support of the U. S. Army, Navy, and Air Force.

[1] N. Bloembergen, Phys. Rev. **104**, 324 (1956).

[2] Supplied by the National Lead Company, South Amboy, New Jersey. The starting material contained 0.2% by weight Fe^{3+} (added as Fe_2O_3) in TiO_2. The final concentration of Fe^{3+} is estimated to be from 0.5 to 0.1 of the starting ratio.

[3] W. Low (private communication) suggested the use of this particular material.

[4] L. R. Momo, R. A. Myers, and S. Foner, J. Appl. Phys. (to be published); S. Foner, L. R. Momo, A. Mayer, and R. A. Myers, "Quantum electronics conference," Shawanga Lodge (September 12–14, 1959) (to be published).

[5] $\epsilon = 160$ parallel to the c axis, $\epsilon = 86$ perpendicular to the c axis at 25°C. See A. von Hippel, *Dielectric Materials and Applications* (The Technology Press of Massachusetts Institute of Technology, p. 302; and John Wiley & Sons, Inc., New York, 1954).

[6] The initial cavity design, intended for use with materials of much lower dielectric constant, was similar to that of W. From, 1959 PGMTT National Symposium, Cambridge, Massachusetts (June 1–3, 1959).

[7] The pump power was furnished by a Philips Laboratory DX151, kindly loaned to us by the millimeter wave group under the direction of Dr. G. S. Heller.

[8] Power measurements were made by J. B. Thaxter and J. McGowan of the millimeter wave group.

[9] N. Bloembergen, S. Shapiro, P. S. Pershan, and J. O. Artman, Phys. Rev. **114**, 445 (1959).

[10] G. Makhov, C. Kikuchi, J. Lambe, and R. W. Terhune, Phys. Rev. **109**, 1399 (1958).

[11] S. Foner, L. R. Momo, and A. Mayer, Phys. Rev. Letters **3**, 36 (1959).

[12] The simultaneous amplification and/or oscillation at frequencies near or equal to f_s suggest several possibilities for maser gain stabilization for radiometry. The simultaneous oscillations may also be used as a local oscillator which tracks the nearby maser amplication channel.

[13] S. H. Autler, Bull. Am. Phys. Soc. Ser. II, **4**, 413 (1959); Rev. Sci. Instr. (to be published).

[14] W. Low, "Symposium on millimeter waves," Polytechnic Institute of Brooklyn, Brooklyn, New York (April 1, 1959).

Dislocation Etch Pits on the {111} and {$\overline{111}$} Surfaces of InSb*

HARRY C. GATOS AND MARY C. LAVINE
Massachusetts Institute of Technology, Lincoln Laboratory, Lexington, Massachusetts

(Received October 5, 1959)

DISLOCATION etch pits were observed on InSb {111} surfaces terminating with Sb atoms; these surfaces are often designated as {$\overline{111}$} or B surfaces. Previous investigators[1–4] have observed the formation of dislocation etch pits only on the {111} surfaces of III–V intermetallic compounds terminating with group III atoms (A surfaces).

The authors[5] have demonstrated experimentally that in oxidizing media the B surface atoms (triply bonded group V atoms) are ordinarily more reactive than the A surface atoms (triply bonded group III atoms). They have interpreted this behavior on the basis of bonding considerations and attributed the formation of dislocation etch pits only on the A surface to differences in reactivity between the A and B atoms.[6]

By altering the relative reactivities of the triply bonded A and B atoms, it was possible to develop dislocation etch pits on the B surfaces as well as on the A surfaces of InSb, as discussed below. The etch pits on the B surfaces were considered to be dislocation etch pits because they could be followed by successive grinding and etching and also because they were observed at low angle boundaries.

1. By employing a preferential inhibitor (stearic acid) in an oxidizing etchant, the etching rate of the B surfaces was inhibited to the extent that it became comparable to the etching rate of

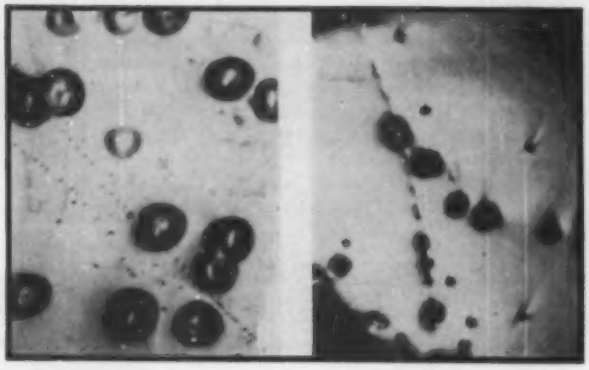

I II

FIG. 1. Dislocation etch pits on the A (I) and B surface (II) of an {111} wafer of InSb. Etchant composition in parts by volume: 2 conc HNO_3; 1 conc HF; 1 glacial CH_3COOH. Temperature 8°C. The etchant was saturated with stearic acid which is only slightly soluble. 30×.

the A surfaces.[7] The observed dislocation etch pits on the B surface (Fig. 1) could form at the termination of dislocations with a row of A atoms (α dislocations) and/or dislocations with a row of B atoms (β dislocations). Actually, dislocation etch pits of two distinct sizes appear on the A surface of InSb (Fig. 1-I). One type of etch pits may correspond to α dislocations, and the other to β dislocations. The possibility that the pits may correspond to edge and screw dislocations is not excluded. Work is in progress to clarify the origin of these dislocation etch pits.

2. At 95°C, the etchant consisting of 0.2*N* Fe^{+++} in 6*N* HCl leads to the formation of dislocation etch pits on the B surfaces as well as on the A surfaces of InSb (Fig. 2). At temperatures below 82°C, dislocation etch pits appear only on the A surfaces. The factors responsible for the observed etching behavior at 95°C are being investigated.

3. The presence of group IV atoms in InSb led to the formation of dislocation etch pits on the B surfaces under etching conditions which ordinarily develop dislocation etch pits only on the A surfaces. Figure 3 shows the A and B surfaces of InSb containing approximately 0.4% Pb or Ge. It is seen that on the B surfaces the density and size of the pits are less than on the A surfaces. Group IV atoms generally replace both group III and group V atoms in III-V compounds.[8] Substitution with group IV atoms leads to the formation of dislocation etch pits either because the relative reactivities of the A and B atom sites are altered or

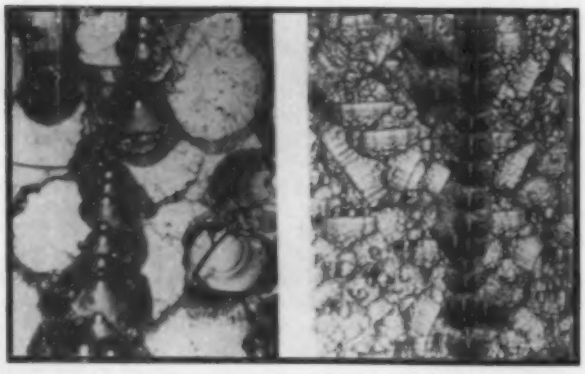

I II

FIG. 2. Dislocation etch pits on the A (I) and B surface (II) of an {111} wafer of InSb. Etchant: 0.2*N* Fe^{+++} in 6*N* HCl. Temperature 95°C. 50×. The identical row of dislocations running across the wafer is shown on both sides.

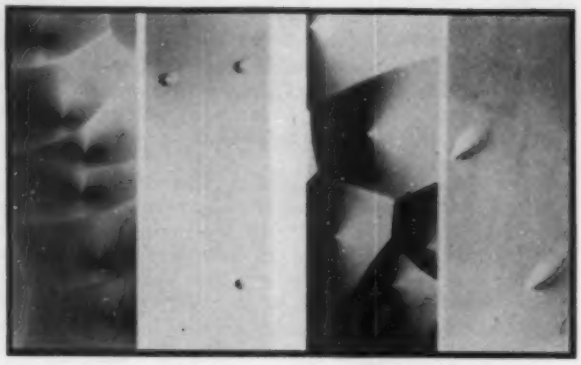

A B A B

I II

FIG. 3. Dislocation etch pits on the two faces of {111} wafers of InSb containing approximately 0.4% Pb (I) and 0.4% Ge (II). A and B designate the A and B surfaces, respectively. Etchant in parts by volume: 1 30% H_2O_2; 1 conc HF; 2 H_2O. 157.5×.

because segregation takes place in the vicinity of the dislocations. Since, however, only a small amount of the group IV element is present it is not surprising that on the B surfaces only a small number of dislocation etch pits are formed and that their size is less than those on the A surface.

* The work reported in this paper was performed by Lincoln Laboratory, a center for research operated by Massachusetts Institute of Technology with the joint support of the U. S. Army, Navy, and Air Force.

[1] J. W. Allen, Phil. Mag. **2**, 1475 (1957).
[2] R. E. Maringer, J. Appl. Phys. **29**, 1261 (1958).
[3] E. P. Warekois and P. H. Metzger, J. Appl. Phys. **30**, 960 (1959).
[4] J. G. White and W. C. Roth, J. Appl. Phys. **30**, 946 (1959).
[5] H. C. Gatos and M. C. Lavine, submitted to J. Electrochem. Soc.
[6] Elastic strains associated with the edge dislocations in the III-V compounds do not seem to play a significant role under the experimental etching conditions being considered.
[7] Dissolution of InSb in 2 conc HNO_3 + 1 conc HF + 1 glacial CH_3COOH at 0°C in the presence of stearic acid: A surface 0.44 mg/cm²/sec; B surface 0.38 mg/cm²/sec. In the absence of stearic acid: A surface 0.5 mg/cm²/sec; B surface 7.8 mg/cm²/sec.
[8] C. Kolm, S. A. Kulin, and B. A. Averbach, Phys. Rev. **108**, 965 (1957).

Monte Carlo Calculations of the Motions of Electrons in Helium

T. ITOH AND T. MUSHA
Electrical Communication Laboratory, Musashino-shi, Tokyo, Japan
(Received November 30, 1959)

FOR the investigation of a gas discharge, it is important to know the behavior of electrons under the influence of an electric field. The parameters such as the ionization coefficients and the energy distributions of electrons, however, have not yet been calculated from the more fundamental quantities, except when the electric field is weak and uniform.[1,2] In the present note are described Monte Carlo calculations of the ionization and the excitation coefficients of electrons in a uniform electric field. This method can be applied similarly when the electric field is strong and not uniform.

In a uniform electric field an electron moves on a parabolic orbit until it collides elastically or inelastically with a gas molecule. After the collision, the electron moves in another parabolic orbit, repeating the same process. These processes were simulated on the electronic digital computor "M-1" in our laboratory[3] as follows:

(1) The initial conditions specified were: a magnitude of the velocity of electron, an angle between the direction of velocity and the z axis (which is antiparallel to the direction of electric

field), a position on the z axis, and a certain time. From this, the orbit of the electron was calculated.

(2) The collision cross section of the electron with a gas molecule varies along the orbit as the electron changes its energy. The orbit was divided into small sections in which the probability that the electron collides with a gas molecule is just 0.1. In every section, whether the electron collides or not was decided by a pseudo-random number which was provided by a subroutine stored in the computor. The procedure described above was repeated until a collision occurred.

(3) When a collision occurred, the kind of collision had to be specified. The three kinds of collision cross sections, namely, exciting, ionizing, and elastic, were calculated (corresponding to any electron energy). The formulas were good approximations to the experimental results[4] up to the electron energies of 200 ev. The probability 0.1 was divided into parts proportional to these cross sections, respectively. The kind of collision was determined according to the part in which the random number previously provided fell. When it was elastic, the electron changed only its direction of motion. If excitation occurred, however, the electron lost a certain amount of energy. Especially in the case of the ionization collision, a part of the energy of the primary electron is shared with the secondary one, so that the energy lost by the primary electron could be determined using another random number. The probability distributions of the energy of the secondary electrons were known from experiments.[5] As to the angle of scattering, it was assumed that in any kind of collision, the incident electron was scattered isotropically. This assumption had to be introduced from the capacity of the memories in our computor. Thus a new orbit of the electron after the collision was calculated, and these processes were repeated.

In this manner the motion of one electron was traced throughout the calculations. The positions on the z axis and the times were recorded as the outputs of the computor whenever an inelastic collision occurred. Drift velocities of the electrons and coefficients of ionization and excitation were calculated from them.

Information of the velocity of one electron was sampled for every constant time interval in the above process. This electron may be taken arbitrarily among the ensemble of electrons under the same physical conditions. Then this sequence of samples can be taken as an ensemble and, according to the "ergodic hypothesis," this new ensemble is statistically equivalent to the original one. Therefore, the energy distribution of electrons and the angular distribution of their velocities were obtained from the information about one electron.

Our calculations were performed in the case of He for $E/P=40$, 80, and 160 v/cm/mmHg, where E is the strength of the electric field and P is the gas pressure at constant temperature. The results of these calculations are shown in Fig. 1 and Table I. The details will be discussed in a later paper.

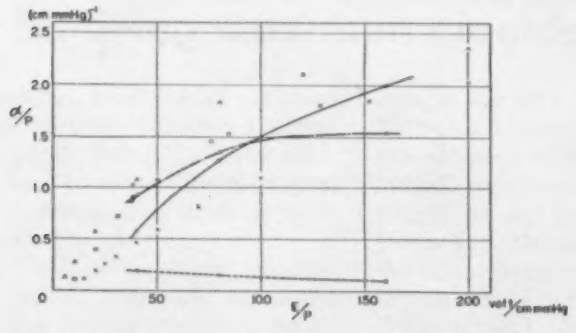

FIG. 1. Coefficients of inelastic collisions of electrons in helium as a function of E/P. α is the number of inelastic collisions per cm and open circles are the calculated values. ———, ionization; - - - -, excitation to 2^3S_1 metastable level; - · - · -, excitation to the other levels. For comparison the observed values are also plotted: Δ and □, Gill and Pidduck, and ×, Townsend and McCallum.[6]

TABLE I. Calculated values of the drift velocity and the mean energy of electrons in helium.

E/P (v/cm/mmHg)	Drift velocity (cm/sec ×10⁷)	Mean energy (ev)
40	2.6	14.35
80	5.6	22.24
160	12.0	48.50

[1] I. Abdelnabi and H. S. W. Massey, Proc. Phys. Soc. (London) **A66**, 288 (1953).
[2] S. J. B. Corrigan and A. von Engel, Proc. Phys. Soc. (London) **A71**, 786 (1958).
[3] S. Muroga and K. Takashima, IRE Trans. on Electronic Computers **EC-8** (1959).
[4] C. E. Normand, Phys. Rev. **35**, 1217 (1930); P. T. Smith, *ibid.* **36**, 1293 (1930); H. Maier-Leibnitz, Z. Physik **95**, 489 (1935); *Handbuch der Physik* edited by S. Flugge (Springer-Verlag, Berlin, 1956), Vol. 36, p. 360; G. J. Schulz and R. E. Fox, Phys. Rev. **106**, 1179 (1957).
[5] M. Goodrich, Phys. Rev. **52**, 259 (1937).
[6] E. W. B. Gill and F. B. Pidduck, Phil. Mag. **16**, 280 (1908); **23**, 837 (1912); J. S. Townsend and S. P. McCallum, *ibid.* **17**, 678 (1934).

Transistor with Base Containing a Dispersed Colloidal Phase*

B. R. GOSSICK
Arizona State University, Tempe, Arizona
(Received September 24, 1959)

IT appears worthwhile to attempt the fabrication of transistors with an n-type base containing colloidal p-type particles (or a p-type base with colloidal n-type particles) in the anticipation of extending the gain-bandwidth product. The presence of such particles in the base decreases the conductivity of majority carriers by a factor[1] $(1-f)/(1+f/2)$, and increases the mobility of minority carriers by a factor $(1+2f)/(1-f)$,[2] with f the fraction of volume occupied by colloidal particles and the surrounding double layers. An impurity content of 1 part in 10^5 under representative conditions localized in particles of radius ~100 A would make f equal about 10%.[3] The manner in which these variations could simultaneously increase both the gain and the band width is explained by the following argument, which applies to a simple junction transistor with a uniform n-type base.

The dc current gain α is given approximately by the relation

$$1-\alpha=\frac{\sigma_b w_b}{\sigma_e L_e}+\frac{w_b^2}{2L_b^2} \qquad (1)$$

in which subscripts b and e refer respectively to the base and emitter, σ to electrical conductivity, w to width and L to diffusion length of minority carriers. Hence, if the deviation of α from unity were divided equally between the two terms in (1), a value of f of 10% would decrease $1-\alpha$ by 27%. At the same time, the cutoff frequency would be increased by 40% as it is proportional to the drift mobility of minority carriers.

A dispersed colloidal phase of tin in n-type germanium deserves consideration, because it should not interfere with standard procedures of impurity doping. The segregated particles of tin should behave like a colloidal p-type phase,[3] while the individual tin atoms would replace germanium substitutionally as a neutral impurity with little effect on electrical properties.[4]

If this suggestion were followed, then the optical extinction by the colloidal phase[3] might be effectively employed in techniques of development and production.

* Work assisted by U. S. Atomic Energy Commission contract.
[1] J. H. Crawford, Jr., and B. R. Gossick (paper in preparation).
[2] B. R. Gossick, J. Appl. Phys. p. 648, this issue.
[3] E. H. Borneman, R. F. Schwarz, and J. J. Stickler, J. Appl. Phys. **26**, 1021 (1955).
[4] W. Crawford Dunlap, Jr., *Progress in Semiconductors*, edited by A. F. Gibson (John Wiley & Sons, Inc., New York, 1957), Vol. 2.

Books Reviewed

Prompt, noncritical reviews appear in this column. Critical reviews of many of the books described here will appear in Physics Today, The Review of Scientific Instruments, *or* American Journal of Physics.

Solid State Physics, Volume 9. F. SEITZ AND D. TURNBULL, editors. Pp. 548. Academic Press, Inc., New York, 1959. Price $14.50.

This volume consists of seven articles continuing the admirable review work of the series. In addition to two works on spectra—Wolf on aromatics and McClure on ionic crystals—there are contributions by Scanlon on polar semiconductors (mostly PbS), Montgomery on static electrification, Heer and Novey on angular distribution of nuclear radiations, Kahn and Frederikse on oscillatory susceptibility and conductivity, and Guenier on heterogeneities in metallic solid solutions. The articles and the press work are of uniform high quality.

Advances in Chemical Physics, Volume II. I. PRIGOGINE, editor. Pp. 412. Interscience Publishers, Inc., New York, 1959. Price $11.50.

Ten experts give comprehensive, personal evaluations of progress in 8 research fields of chemical physics. Contributions are by van der Waals and Platteeuw on clathrates, Pitzer on molecular polarizability, Rowlinson and Richardson on solutions of solids in compressed gases, Oriani on the thermodynamics of metallic solutions, Szwarc on polymers, Duchesne on quadrupole resonance in irradiated crystals, Löwdin on correlation effects, and E. Bright Wilson on internal rotation in molecules. In addition, there is a 40-page bibliography compiled by Yoshizumi on the correlation problem. The articles are rigorous but not so sophisticated as to be unintelligible to the nonexpert.

Announcements

1960 Cryogenic Engineering Conference, August 23, 24, and 25, 1960 Boulder, Colorado

The 1960 Cryogenic Engineering Conference will be cosponsored by the Universtiy of Colorado and the National Bureau of Standards and will be held in Boulder, Colorado on August 23, 24, and 25.

Papers for presentation at the 1960 Cryogenic Engineering Conference dealing with the technical aspects of cryogenic engineering in the field below 150°K are now being solicited. The deadline for abstracts (not over 200 words) will be *May 15, 1960.* Since the acceptance of papers will be handled by an editorial board appointed by the Cryogenic Engineering Conference Committee, it will be essential also to set a deadline for preliminary manuscripts by *May 15, 1960.* K. D. Timmerhaus, *Secretary,* University of Colorado, Boulder, Colorado.

1960 Metallurgical Society Conference on Response of Materials to High Velocity Deformation

A conference on "The Response of Materials to High Velocity Deformation" has been announced by the Physical Metallurgy Committee, Institute of Metals Division, The Metallurgical Society of AIME, to be held July 11 and 12 in Estes Park, Colorado. The Society is a constituent organization of the American Institute of Mining, Metallurgical, and Petroleum Engineers.

Papers will have to do largely with the crystallographic, metallographic, and basic metallurgical phenomena that occur in metals under high strain rate.

Further information concerning the Conference can be obtained from Douglas Johnston, AIME or from N. F. Brown, Naval Research Laboratory.

Optical Society of America Announces the Russian Journal Optika i Spektroscopiya

This monthly journal of the USSR Academy of Sciences commenced publication in 1956, and publishes the work of leading Russian scientists in all branches of optics and spectroscopy, including x-ray, ultra-violet, visible infrared and microwave, thin layer optics, filters, detectors, diffraction gratings, electroluminescence, thermal radiation backgrounds, infrared polarizers, and their many other applications in science and industry. The English translation, which is being published with a grant-in-aid from the National Science Foundation starts from Volume 6, January 1959, and it is the aim of the Society that *Optics and Spectroscopy,* will appear within four months of the Russian original.

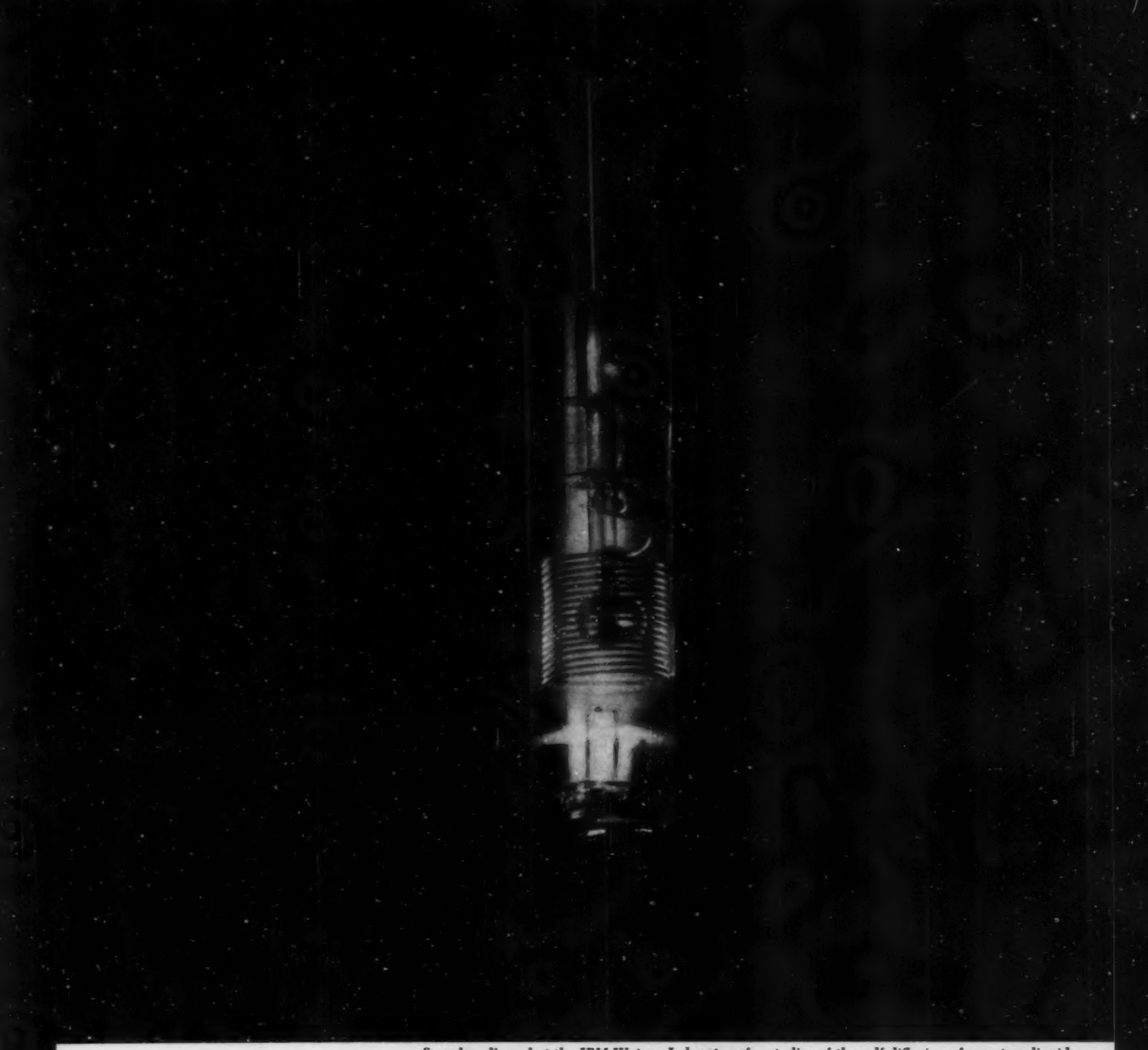

Sample cell used at the IBM Watson Laboratory for studies of the self-diffusion of quantum liquids.

Studying Quantum Liquids to Observe Nuclear Theory

Atomic nuclei are dense systems composed of identical particles which obey Fermi-Dirac statistics. Using these statistics, scientists have computed the theoretical behavior of the particles which compose heavy nuclei.

Helium^3, a quantum liquid, provides scientists with an extremely convenient model of this nuclear matter – a model readily accessible to research. A cryogenic liquid, He^3 permits the investigation of quantum effects. This makes it possible to compare nuclear behavior with theoretical predictions.

Research in quantum liquids is being done at the IBM Watson Laboratory at Columbia University. Direct spin-echo measurements of diffusion and nuclear relaxation were made on He^3 atoms in the pure liquid, and also in dilute solutions of He^3 in He^4. Measurements were made in the temperature range 0.5°K to 4.2°K, at pressures up to 67 atmospheres.

Experiments on the pure quantum liquid revealed diffusion persisting to the lowest temperatures. However, it was apparent that the diffusion was not thermally activated as in an ordinary liquid, or in a gas. Diffusion persisted for two reasons: (1) because of the zero-point energy of the atoms, and (2), because of the atoms' long wave length as compared with the thickness of the potential barriers which inhibited their motion. The results of the experiments on dilute solutions of He^3 in He^4, in accord with expectations, showed that the He^3 diffusion coefficient increased rapidly with decreasing temperature.

This study will help to increase our understanding of quantum systems, and consequently, help to increase our familiarity with nuclear matter.

IBM® RESEARCH

Investigate the many career opportunities available in exciting new fields at IBM.
International Business Machines Corporation, Dept. 579P, 590 Madison Avenue, New York 22, New York

NOW— 15,000°F. PLASMA FLAME SPRAY IN YOUR OWN PLANT

Apply coatings of high melting point materials such as tungsten, tungsten carbide, molybdenum, chromium carbide, titanium oxides, calcium zirconate, rare earth oxides. Operates at 10,000°-15,000°F.

Plasma flame spraying hi-temperature crucible

Now any material that can be melted without decomposing can be sprayed. Despite high melting temperature, object sprayed stays cool.

High fluidity of particles and high velocity of impingement bond the particles together to produce high density coatings semi-fused to work. Absence of air eliminates oxidation.

The METCO Plasma Flame Spray Gun is a valuable new tool for the metalworking research department or production line. Operates on inexpensive inert gases with high electrical power conversion efficiency, long component life. Continuous gas streams, as high as 30,000°F., with accurate control of temperature, generated at costs of ⅛ to ½ those of oxygen-fuel gas equipment for equivalent heat output. No combustion—uses inert gases. No flashback or explosion hazards—push-button operation.

Write today for free bulletin describing the METCO Plasma Flame Gun.

METCO

Metallizing Engineering Co., Inc.
Flame Spray Equipment and Supplies
1143 Prospect Avenue, Westbury, Long Island, N. Y.
In Great Britain METALLIZING EQUIPMENT CO., Ltd.
Chobham-near-Woking, England

Please send me free bulletin on the Metco Plasma Flame Spray Gun.

Name _____ Title _____

Company _____

Address _____

City _____ Zone _____ State _____

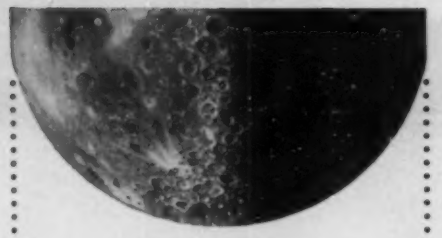

ROCKETDYNE

announces immediate openings in

ELECTRICAL PROPULSION

for

PHYSICISTS

Rocketdyne, the nation's leader in Research and Development of high and low thrust propulsion systems, is expanding its Electrical Propulsion Activities in Southern California.

PROJECT LEADER to direct experimental research and development of electrical thrust devices. A PhD in experimental physics and experience with ion sources, ion acceleration and collimation, ion-electron recombination and charged particle detection, desirable.

SENIOR PHYSICIST plan and conduct experimental research on such electrical propulsion devices as ion and plasma jet engines. Work includes development and testing of ion sources, accelerating-electrode arrangements, beam neutralization devices, and measurement of such parameters as the current, power and thrust of the ion beam. PhD or MS in experimental physics, and experience with high vacuums, and with the acceleration and detection of charged particles, desirable.

SENIOR PHYSICIST. Plan and conduct theoretical research, such as the design of accelerating and collimating electrode systems, and analysis of space missions, using large digital computers. PhD or MS in Physics, and advanced study in celestial mechanics and electrostatics, desirable.

Address inquiries to:
Mr. J. C. Peck, Dept. 596 S.D.
6633 Canoga Avenue
Canoga Park, California

ROCKETDYNE
A DIVISION OF NORTH AMERICAN AVIATION, INC.
First with Power for Outer Space

WANTED!

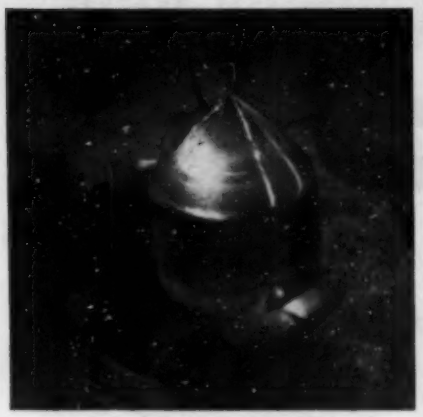

BRAIN

to direct these hands

CRYSTAL GROWING: physicist or physical chemist for senior position in currently growing research and development activity in solid-state materials with present emphasis on scintillation crystals. Require experience in crystal-growing techniques and materials-purification and some knowledge of scintillation spectroscopy. Desire leadership, initiative, and imagination in generating and carrying out new programs to expand present activities.

Combined with the opportunity to assume high-level responsibilities are the advantages of a full program of health benefits, life insurance, and participation in a profit-sharing plan.

Plant is located in Stanford Industrial Park, Palo Alto, in an outstanding center of science and technology. The climate is one of the most favorable in the world. The area offers the best in housing, recreation, and technical stimulation.

For more information, telephone DAvenport 6-1640 or write today, including your resume, to Dr. Elliott C. Levinthal at:

LEVINTHAL ELECTRONIC PRODUCTS

STANFORD INDUSTRIAL PARK · PALO ALTO 5, CALIFORNIA

SUBSIDIARY OF **RADIATION** INCORPORATED

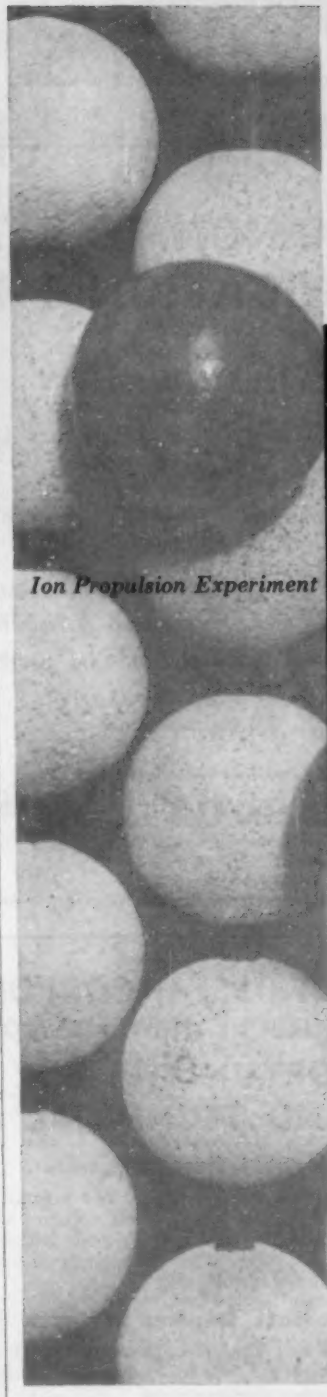

Ion Propulsion Experiment

An announcement of importance to PHYSICISTS

Only occasionally do *truly* outstanding professional opportunities with a vital, growing organization become available. New and expanding programs in the Fluid Physics Division of EOS* have created positions of this exceptional caliber for both theoretical and applied physicists.

These rewarding appointments on the technical staff will be concerned with pioneering efforts in the fields of . . .

Magnetohydrodynamics
Electrically Exploding Wires
Electromagnetics
Nuclear and Molecular Physics
Ion and Plasma Propulsion

Creative scientists — men with ideas and curiosity — who hold an advanced degree and have pertinent research experience, are invited to write in confidence to the Senior Technical Staff Placement Director for additional information.

*Founded in 1956, Electro-Optical Systems is conducting advanced research and development programs in solid state devices, energy research and advanced power systems, fluid physics, advanced electronics and space defense systems.

ELECTRO-OPTICAL SYSTEMS, INC.
MUrray 1-0408

E
O
S

150 NORTH VINEDO AVE.
PASADENA, CALIFORNIA

Just Published . . .

AN INTRODUCTION TO STATISTICAL COMMUNICATION THEORY

by

DAVID MIDDLETON

McGraw-Hill International Series of Pure and Applied Physics
1134 pages, $25.00

This book covers important mathematical aspects of large-scale, complex automatic control systems. It discusses, in excellent detail, the following:

Feedback Theory
Matrix Methods
Numerical Analysis
Linear Integral Equations
Basic Statistical Theory
Systems Analyses in Phase Space
Analysis of Sampled-Data Systems

and much more

Send for Your On-Approval Copy

McGRAW-HILL BOOK COMPANY, INC.

330 West 42nd Street **New York 36, N. Y.**

ACF INDUSTRIES, INCORPORATED

ALBUQUERQUE, NEW MEXICO

OPPORTUNITIES FOR ENGINEERING AND TECHNICAL PERSONNEL

Theoretical Stress Analysts

M.S. in engineering or engineering mechanics with three- to five-years direct experience in application of theory of elasticity to structural members, thin- and thick-walled pressure vessels. Some experience in plastic range analysis and nuclear reactor connected experience desirable but not necessary. Individuals selected will be expected to originate solutions to unique problems in the analysis of vessel structures and to participate in testing programs for the resolution of design problems.

Senior Heat Transfer Engineer

M.S. in chemical or mechanical engineering and three- to five-years experience. Familiarity with two dimensional and transient systems most desirable. Must be able to originate analytic solutions to unusual problems demanding advanced mathematical treatment.

Mathematician

A.B., B.S. or M.S. in mathematics with working knowledge of IBM 650 and 704 programming methods. Must assist engineering personnel in formulation of analytic solutions to problems in stress analysts and heat transfer, for subsequent programming on IBM and Bendix Computor equipment.

ACF Industries, Incorporated, Albuquerque Division, is a prime contractor for the Atomic Energy Commission. Albuquerque is located in the rapidly expanding Southwest with a high, dry, mountainous climate, adequate schools, churches, and recreational facilities. U. S. Citizenship required.

Send resume to: **R. L. Hansen**

P. O. Box 1666 **Employment Section** **Albuquerque, New Mexico**

need high vacuum components?

Stokes Series H Microvacs were designed by vacuum specialists . . . are industry engineered to meet your needs . . . give you more pumping capacity per dollar. The integral construction includes dynamic balancing, valves, motor, belt guard, and automatic lubrication—there are no extras to buy. A complete line of Microvacs include capacities from 17 to 500 cfm. For fast, efficient pump-down—you can depend on Stokes Microvac Series H Pumps.

STOKES makes a complete line of vacuum components . . . advance-designed and engineered to help make your vacuum systems more productive. Each unit reflects Stokes' unparalleled experience, pioneering leadership and wealth of basic vacuum technology.

The product list includes: Diffusion Pumps, Vapor Booster Pumps, Mechanical Pumps, Mechanical Booster Pumps, Vacuum Gages, and Valves.

Send for technical data on any or all . . . without obligation.

High Vacuum Division
F. J. STOKES CORP.
5565 Tabor Road, Phila. 20, Pa.

STOKES

NOW AVAILABLE

FROM THE PUBLISHERS OF SEMICONDUCTOR PRODUCTS MAGAZINE

BOUND VOLUME

Proceedings of the 2nd Conference on Nuclear Radiation Effects on Semiconductor Devices, Materials and Circuits.

Limited Edition of this Once-A-Year Symposium

AVOID DISAPPOINTMENT—RESERVE YOUR COPIES NOW! Contains the Following 23 Papers, Complete with Illustrations, by the Foremost Authorities in the Field. Don't Miss Out on This Invaluable Information—Only $4.50 a Copy.

- High Energy Electron Irradiation of Germanium and Silicon
- The Nature of a Non-equilibrium Excess Conductance Induced in Silicon by Nucleon Irradiation
- Transient Radiation Effects in Semiconductors
- Positive Ion Bombardment of Metals with Radioactive Kr-85
- Radiation Effects in Compound Semiconductors
- Electron Irradiation Effects in CdS
- Minority Carrier Lifetime of Neutron Bombarded Germanium
- Correlation of Theoretical and Experimental Behavior of Silicon Junction Diodes During Neutron and Gamma Irradiation
- Study Directed Toward Improving the Radiation Tolerance of Silicon Diodes
- Preliminary Study of the Effects of Exposure of Electronics Components to 2-Mev Electrons and Other Kinds of Radiation
- Radiation Effects on Semiconductors
- The Effects of Nuclear Radiation on Some Selected Semiconductor Devices
- Semiconductor Devices as Charged Particle Detectors and Energy Spectrometers
- Gamma Irradiation Effects on Infrared Detectors
- On the Neutron Bombardment Reduction of Transistor Current Gain
- Analysis of Simple Rectifying and Magnetic Amplifier Circuits During Irradiation
- Transistor Circuit Behavior at Exposures Greater than 10^{15} Fast Neutrons/CM^2
- Radiation Resistant Digital Computer Circuitry
- The Use of Diffused Junctions in Silicon as Fast Neutron Dosimeters
- A Transistor Scaler Circuit For A Megarad Gamma Ray Environment
- Problems of Correlating Radiation Environments
- The Effect of Intermittent Irradiation of the Magnetic Remanence of a Ferrite
- A Brief Resume of Radiation Effects on Semiconductor Materials and Devices

SEND FOR A SAMPLE COPY OF SEMICONDUCTOR PRODUCTS MAGAZINE—$1.00 TO COVER COSTS

SEMICONDUCTOR PRODUCTS, DEPT. MG JAP-4
300 West 43rd Street
New York 36, N. Y.

Send .... copy(ies) of 'Proceedings' @ $4.50 each.
Send .... copy(ies) of Semiconductor Products @ $1.00 each.
Remittance Enclosed ....
Name .....
Home Address .....
City ..... Zone ..... State .....
Company ..... Title .....
Address .....
City ..... Zone ..... State .....

New York residents add 3% Sales Tax

Since final quality of your production of ferrites, electronic cores, and magnetic recording media depends on proper use of 3 specialized groups of magnetic materials . . . you'll find it mighty helpful to have all the latest, authoritative technical data describing the physical and chemical characteristics of each. This information is available to you just for the asking. Meanwhile, here are highlights of each product group.

PURE FERRIC OXIDES—For the production of ferrite bodies, we manufacture a complete range of high purity ferric oxide powders. These are available in both the spheroidal and acicular shapes, with average particle diameters from 0.2 to 0.8 microns. Impurities such as soluble salts, silica, alumina and calcium are at a minimum.

MAGNETIC IRON OXIDES—For magnetic recording—audio, video, instrumentation etc.—we produce a group of special magnetic oxides with a range of controlled magnetic properties. Both the black ferroso-ferric and brown gamma ferric oxides are available.

MAGNETIC IRON POWDERS—For the fabrication of magnetic cores in high-frequency, tele-communication, and other magnetic applications, we make a series of high purity iron powders.

If you have problems involving any of these materials, please let us go to work for you. We maintain fully equipped laboratories for the development of new and better inorganic materials. Write . . . stating your problem . . . to C. K. Williams & Co., Dept. 38, 640 N. 13th St., Easton, Penna.

WILLIAMS
COLORS & PIGMENTS
C. K. WILLIAMS & CO.
E. ST. LOUIS, ILL. • EASTON, PA. • EMERYVILLE, CAL.

High Performance ELECTROMAGNETS and Power Supplies

ECONOMY
7" Electromagnet Type E (7" pole diameter).
Fields up to 8,000 gauss.
Homogeneity of at least 4 parts in 10^5 in ½ cc.

ROTATION
Rotating Base Type AE.
360° scale.
Positive friction lock.

STABILITY
Current-Stabilized Power Supply Unit Type B.
Two models:
B.4—Stability 1 part in 10^4.
B.5—Stability 1 part in 10^5.

Also available:—
1½" Electromagnet Type C—for Teaching purposes.
4" Electromagnet Type A—for all purposes.
8" Electromagnet Type D—for Electron Resonance and Nuclear Magnetic Resonance work.
Direct Reading Magnetometer Type G.
Proton Resonance Magnetometer Type P.

NEWPORT INSTRUMENTS
(Scientific & Mobile) Ltd.
NEWPORT PAGNELL, BUCKS, ENGLAND
Telephone: NEWPORT PAGNELL 401/2

NEW LOW COST GETTERING VACUUM PUMP

Cartridge only $135

Complete assembly including metal gaskets $215

- For use in ultra-high vacuum or continuously pumped closed systems.
- Pumps through chemical action — no fluids to contaminate system.
- Operating range 10^{-1} -10^{-9}mm. Hg. Speed approx. 5 l/s.
- No backing pump or expensive power supply needed.

Gases are removed by chemical reaction with titanium film which is intermittently deposited by low voltage filament.

Available either as a cartridge for mounting directly in vacuum chamber, or with stainless steel housing where deposits of titanium are objectionable or for external mounting. Write today for technical details on NRC Model 2202-02 Titanium Adsorber Pump.

NRC
EQUIPMENT CORPORATION
A subsidiary of National Research Corporation
Dept. P-4. 160 Charlemont St., Newton 61, Massachusetts • DEcatur 2-5800

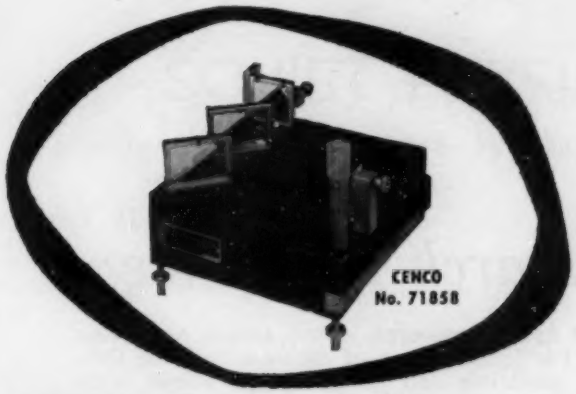

NOW! *a low cost Michelson*
INTERFEROMETER

This precision instrument is ingeniously designed to provide .2% accuracy at minimum cost. Directly calibrated in inches. Clear, well defined fringes are observable and measurable. Refractive properties of transparent materials can be easily studied. Sturdily constructed for classroom or laboratory research.

Complete with monochromatic mercury light and illustrated experiment manual . . . only $209.95

cenco

CENTRAL SCIENTIFIC CO.
A Subsidiary of Cenco Instruments Corporation
1718-A Irving Park Road • Chicago 13, Illinois
Branches and Warehouses—Mountainside, N. J.
Boston • Birmingham • Santa Clara • Los Angeles • Tulsa
Houston • Toronto • Montreal • Vancouver • Ottawa

MS-9 SERIES
PACKAGED
Helium
Mass Spectrometer
LEAK DETECTORS

Finds leaks in hermetically sealed components

WITH/WITHOUT AUTOMATIC ROUGHING STATION, BACKFILL CONSOLE

This is the most accurate, trouble-free
LEAK DETECTOR
you can buy

fast...simple...safe

- **Quick and Easy to Operate**
  Flip a switch and the built-in automatic station does the work for you, electrically (no air supply required) ...lets you make up to 120 tests per hour...safety interlocks eliminate operator error, permits use of non-technical personnel.
- **Guaranteed Accurate and Safe**
  Constant 10^{-10} cc/sec accuracy guaranteed by the patented VEECO VEETUBE®...it cleans itself...uses safe, inert helium as tracer gas.
- **Thoroughly Tested**
  Each MS-9 undergoes a full week (168 hrs) of test run and inspection before shipment.

FREE MS-9 BROCHURE contains full details on performance, specifications, operation and advantages. There is an MS-9 series Leak Detector to fill your exact need. Write Department A-1435.

Veeco
VEECO VACUUM CORP.
86 J Denton Avenue, New Hyde Park
Long Island, New York
HIGH VACUUM & LEAK DETECTION EQUIPMENT

MASSACHUSETTS INSTITUTE OF TECHNOLOGY
OPERATIONS EVALUATION GROUP

The M.I.T. OPERATIONS EVALUATION GROUP enjoys an enviable position within the Naval Establismment, with which they have been associated since early 1942. This position of mutual respect and confidence is a prime factor underlying OEG's continued growth and success as a scientific advisory group.

The problems dealt with are operational in nature and range from the evaluation of newly developed weapons systems or operational strategy to the formulation of new requirements and the correlation of research and development with Fleet needs.

To the graduate mathematician or physical scientist possessing the ability to envision and solve complex operational problems outside conventional fields of specialization, we offer a stimulating professional atmosphere and the opportunity to participate at the highest level in the solution of problems directly concerned with the national defense.

In addition, we are currently extending our activities into the area of technological research that lies midway between the research conducted in the nation's laboratories and that traditionally conducted by groups such as OEG in the purely operational field.

OPERATIONS EVALUATION GROUP
Office of the Chief of Naval Operations
Navy Department
Washington 25, D.C.

U. S. Citizenship Required

HONEYWELL

senior research physicists

Conduct pure and applied research in magnetism and computer components. Particular areas of interest include thin films, ferrimagnetic materials and ferromagnetic alloys with emphasis on high temperatures. Studies involve alternating field responses, domain patterns, hysteresis properties, resonance phenomena, etc. Proposals are encouraged for original research in other areas of magnetism.

Positions are also open in the areas of molecular scale electronic components, geometrical and physical optics and plasma physics.

Candidates should have a doctor's degree or its equivalent. Further experience is desirable.

For a personal interview at the Honeywell basic research laboratories in suburban Minneapolis, send your resumé to F. W. Miller, Dept. 532, 2753 Fourth Avenue South, Minneapolis 8, Minnesota.

Honeywell
RESEARCH CENTER

NEW ULTRA-HIGH VACUUM GAUGE

- Direct Reading to 10^{-10} mm Hg
- Indirect Reading to 10^{-12} mm Hg
- Improved Stability and Sensitivity
- Facilitates Flash Filament Studies

This new gauge offers you three advantages over other Bayard-Alpert type gauges. Increased stability and sensitivity result from addition of elements which prevent space charge build-up on the envelope, and which increase ion collection efficiency. Extra filaments facilitate gas desorption studies.

This new NRC Model 2205-01 Nottingham Gauge can be used with standard UHV ionization controls or with the new, highly stable NRC Model 2207-03 control. Write for complete information today.

NRC
EQUIPMENT CORPORATION

A subsidiary of National Research Corporation
Dept. P-4, 160 Charlemont Street, Newton 61, Massachusetts • DEcatur 2-5800

LONG RANGE VISIBILITY

The NEW CENCO Lecture Room Meter

Now—a combination galvanometer, four-range voltmeter and four-range ammeter with figures and graduations on a large 17″ scale that is plainly seen from both sides over any distance in the classroom. An accurate, versatile lecture meter with a modern, shielded movement. All parts and circuits clearly visible.

Cenco No. 82140 complete with shunts and multipliers $260.00

cenco
Serving education since 1889.

CENTRAL SCIENTIFIC CO.
A Subsidiary of Cenco Instruments Corporation
1718-A Irving Park Road • Chicago 13, Illinois
Branches and Warehouses—Mountainside, N. J. Boston • Birmingham • Santa Clara • Los Angeles • Tulsa Houston • Toronto • Montreal • Vancouver • Ottawa

SOVIET PHYSICS JOURNALS

Published in English by the American Institute of Physics

Soviet Physics—JETP

A translation, beginning with 1955 issues of "Journal of Experimental and Theoretical Physics" of the USSR Academy of Sciences. Leading physics journal of Soviet Union. Similar to "The Physical Review" in quality and range of topics. Outstanding new work is most likely to appear in this journal.

*Twelve issues, approx. 4,000 pages, $75 domestic, $79 foreign. Libraries * $35 domestic, $39 foreign. Single copies, $8.*

Soviet Physics—SOLID STATE

A translation, beginning with 1959 issues of "Fizika Tverdogo Tela" of the USSR Academy of Sciences. Offering results of theoretical and experimental investigations in the physics of semiconductors, dielectrics, and on applied physics associated with these problems. Also publishes papers on electronic processes taking place in the interior and on the surface of solids.

*Twelve issues, approx. 2,000 pages. $55 domestic, $59 foreign. Libraries * $25 domestic, $29 foreign. Single copies, $8.*

Soviet Physics—TECHNICAL PHYSICS

A translation, beginning with 1956 issues of "Journal of Technical Physics" of the USSR Academy of Sciences. Contains work on plasma physics and magnetohydrodynamics, aerodynamics, ion and electron optics, and radio physics. Also publishes articles in mathematical physics, the physics of accelerators and molecular physics.

*Twelve issues, approx. 2,000 pages. $55 domestic, $59 foreign. Libraries * $25 domestic, $29 foreign. Single copies, $8.*

Soviet Physics—ACOUSTICS

A translation, beginning with 1955 issues of "Journal of Acoustics" of USSR Academy of Sciences. Devoted principally to physical acoustics but includes electro, bio, and psycho acoustics. Mathematical and experimental work with emphasis on pure research.

Four issues, approx. 500 pages. $12 domestic, $14 foreign. Single copies, $4.
(No library discounts)

Soviet Physics—DOKLADY

A translation, beginning with 1956 issues of "Physics Sections" of Proceedings of USSR Academy of Sciences. All-science journal offering four-page reports of recent research in physics and borderline subjects.

*Six issues, approx. 1,500 pages. $35 domestic, $38 foreign. Libraries * $15 domestic, $18 foreign. Single copies Vols. 1 and 2, $5; Vol. 3 and later issues, $7.*

Soviet Physics—CRYSTALLOGRAPHY

A translation, beginning with 1957 issues of the journal "Crystallography" of USSR Academy of Sciences. Experimental and theoretical papers on crystal structure, lattice theory, diffraction studies, and other topics of interest to crystallographers, mineralogists, and metallurgists.

*Six issues, approx. 1,000 pages. $25 domestic, $27 foreign. Libraries * $10 domestic, $12 foreign. Single copies, $5.*

SOVIET ASTRONOMY—AJ

A translation, beginning with 1957 issues of "Astronomical Journal" of USSR Academy of Sciences. Covers various problems of interest to astronomers and astrophysicists including solar activity, stellar studies, spectroscopic investigations of radio astronomy.

*Six issues, approx. 1,100 pages. $25 domestic, $27 foreign. Libraries * $10 domestic, $12 foreign. Single copies, $5.*

Soviet Physics—USPEKHI

A translation, beginning with September, 1958 issue of "Uspekhi Fizicheskikh Nauk" of USSR Academy of Sciences. Offers reviews of recent developments comparable in scope and treatment to those carried in "Reviews of Modern Physics." Also contains reports on scientific meetings within the Soviet Union, book reviews, and personalia.

*Six issues, approx. 1,700 pages. (Contents limited to material from Soviet sources.) $45 domestic, $48 foreign. Libraries * $20 domestic, $23 foreign. Single copies, $9.*

* For libraries of non-profit academic institutions.

Subscription prices subject to annual variation depending on size of Russian originals.

Please send orders and inquiries to

American Institute of Physics
335 East 45 Street, New York 17, N. Y.

American Institute of Physics

A Federation of Professional Societies in Physics

The American Institute of Physics was founded to assist in "the advancement and diffusion of knowledge of the science of physics and its application to human welfare." All of the societies listed below are members, associate members, or affiliates of the Institute. Eight journals are published by the Institute for the Member Societies. These, together with fourteen journals owned by the Institute, constitute a coordinated publishing program of high standards, efficiency and economy.

The Institute also carries on other activities designed to advance physics and to serve the public interest through physics. Its education program is concerned with strengthening education in physics at all levels, and its public relations program is directed toward promoting a wider public understanding of physics. The Institute works with the Societies in seeking cooperation with other fields of science, with departments of the Federal Government, with educational institutions, and with industrial organizations. In addition, the Institute maintains a free Placement Service for the use of employers and of physicists seeking jobs.

Corporate Associates: A special class of membership is available to corporations, institutions and laboratories who pay annual dues in accordance with a graduated scale ranging from $350 to $3500. Through their membership the Corporate Associates contribute to the support of the work of the Institute. With membership they may receive certain journals, programs of meetings of societies, and other privileges.

Student Sections: College physics students may form local organizations which may, upon application and approval, become Student Sections of the Institute. The Student Sections provide an opportunity for students to obtain official status in the Institute and thus establish their members as part of the physics profession.

Information: Address Wallace Waterfall, Secretary, 335 East 45 Street, New York 17, N. Y. for information about the Institute and its activities. For information about any member society, address its Secretary.

Member Societies:

AMERICAN PHYSICAL SOCIETY

The Society has as its object the advancement and diffusion of the knowledge of physics. All branches of fundamental and applied physics are generally included in its scope. Both experimental and theoretical researches are reported in its journals and meetings.

Dues: Members, $15; Fellows, $25.

Address: Karl K. Darrow, Secretary, Columbia University, New York 27, New York.

OPTICAL SOCIETY OF AMERICA

The Society devotes itself to the advancement of optics, pure and applied, in all its branches. Its scope includes research in fundamental optics as well as problems concerned with design and production of optical instruments.

Dues: Associate Members, $13.00; Regular Members and Fellows, $17.00; Student Members, $2.00; Corporation Members, $125.00 minimum; Patrons, $1000.

Address: Mary E. Warga, Executive Secretary, 1155 16th Street, N.W., Washington 6, D. C.

ACOUSTICAL SOCIETY OF AMERICA

The Society's purpose is to increase and diffuse the knowledge of acoustics and promote its practical applications. The scope includes fundamental researches on the intensity, transmission, and absorption of sound; also on noise, reverberation in rooms, the processes of speech and hearing, the performance and reproduction of music, etc.

Dues: Associate Members, $10; Members and Fellows, $15; Sustaining Members, not less than $100.00.

Address: Wallace Waterfall, Secretary, 335 East 45 Street, New York 17, New York.

AMERICAN ASSOCIATION OF PHYSICS TEACHERS

Whereas the other Societies are mainly concerned with research, this Association has provided a much needed forum for the discussion of the problems of teaching. In cooperation with the other groups, the Association promotes the advancement of physics and emphasizes its place in the general culture.

Dues: Members, $7.50; Junior Members, $4.00; Sustaining Members, $200.00.

Address: Frank Verbrugge, Secretary, Univ. of Minnesota, Minneapolis 14, Minnesota.

SOCIETY OF RHEOLOGY

This small but active society is composed of physicists, chemists, and engineers interested in "rheology," which is defined as the science of deformation and flow of matter.

Dues: Members, $6.00; Sustaining Members, $25.00.

Address: W. R. Willets, Secretary-Treasurer, Titanium Pigment Corp., 99 Hudson Street, New York 13, N. Y.

Associate Member Societies:

American Crystallographic Association

Address: Leroy E. Alexander, Secretary, Mellon Institute, 4400 Fifth Avenue, Pittsburgh 13, Pennsylvania.

American Astronomical Society

Address: J. Allen Hynek, Secretary, Smithsonian Astrophysical Observatory, 60 Garden Street, Cambridge 38, Massachusetts.

Affiliated Societies:

American Society for Metals • Cleveland Physics Society • Electron Microscope Society of America • Foundation for Instrumentation Education and Research, Inc. • Philosophical Society of Washington • Physical Society of Pittsburgh • Physics Club of Chicago • Physics Club of Lehigh Valley • Physics Club of Philadelphia • Sigma Pi Sigma

Inquiries regarding membership in the Affiliated Societies may be sent to the American Institute of Physics, 335 East 45 Street, New York 17, New York. Such inquiries will be forwarded to the respective secretaries.

NEW VACUUM METALLIZER

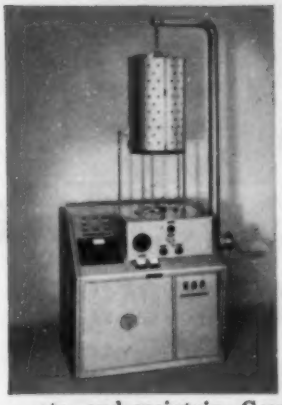

- For research or small scale deposition of metals and salts on metals, glass, plastics, ceramics, etc.
- Permits multiple source evaporations and close control of filament voltage from 0 – 40 V.
- Power, high voltage, thermocouple, work positioning, etc. feed-throughs are easily relocated at any of 17 points.

Packaged 35″ x 48″ x 112″ unit is easy to install, operate, and maintain. Geared hoist takes work out of raising 18″ shielded Pyrex or 24″ O.D. mild or stainless 30″ high bell jar. Vibration-isolated, 6″ pumping system with optical baffle cold trap gives fast, "clean" pump-down to 10^{-6} mm. Hg. Write today for details on NRC Model 3144.

NRC
EQUIPMENT CORPORATION

A subsidiary of National Research Corporation
Dept. P-4, 160 Charlemont St., Newton 61, Massachusetts • DEcatur 2-5800

←This unit is ⅛ actual size

Another NEW
LECTURE ROOM
PERIODIC TABLE
LARGER • EASY TO READ • COLORFUL
INCLUDES ATOMIC DATA

Includes all elements and number of naturally occurring radioactive and stable isotopes. Shows atomic number in large type, also weight, density, boiling and melting points, electronic configuration, half-life, and important atomic constants for physics and chemistry. New large lecture room size, 62″ x 52″, in 4-colors on heavy plastic coated stock.

No. 12056 with wood strips and eyelets.....each $ 7.50
No. 12057 mounted on spring roller with brackets.... $12.50

cenco®

CENTRAL-SCIENTIFIC CO.
A Subsidiary of Cenco Instruments Corporation
1718-A Irving Park Road • Chicago 13, Illinois
Branches and Warehouses—Mountainside, N. J. Boston • Birmingham • Santa Clara • Los Angeles • Tulsa Houston • Toronto • Montreal • Vancouver • Ottawa

---

EPLAB

PYRHELIOMETER
For the Measurement of SOLAR RADIATION

Eppley Pyrheliometers are used for solar radiation measurements at ninety-eight weather stations in the continental United States, Canada, Alaska, Greenland, Iceland, Caribbean Sea, and the Pacific Ocean. Sixty-two of these stations are under the direction of the United States Weather Bureau.

The Eppley Pyrheliometer was adopted as standard equipment by the Weather Bureau after considerable experimentation. It was found to be the best instrument so far tested by the Bureau.

Used in conjunction with a suitable recorder, the Eppley Pyrheliometer will provide an accurate and reliable record of total solar and sky radiation on a horizontal surface.

Bulletin No. 2 On Request

THE EPPLEY LABORATORY, INC.
Scientific Instruments
6 Sheffield Ave.
Newport, Rhode Island, U.S.A.

INDEX TO ADVERTISERS

Name	*Page*
A.C.F. INDUSTRIES, INC.	xxviii
BECKMAN & WHITLEY, INC.	Cover 2
BELL TELEPHONE LABS.	v
C.B.S. ELECTRONICS	xix
CENTRAL RESEARCH LABS.	xxiii
CENTRAL SCIENTIFIC CO.	xxxi, xxxii, xxxv
COLLINS RADIO CO.	xxi
CORNELL-DUBILIER ELECTRIC CORP.	xviii
COWAN PUBLISHING CO.	xxix
ELECTRO-OPTICAL SYSTEMS, INC.	xxvii
EPPLEY LABORATORY	xxxv
ERIE RESISTOR CORP.	x
GENERAL MAGNETICS, INC.	Insert at pages iii, iv
GENERAL MOTORS CORP.	
DELCO RADIO DIV.	vi
OLDSMOBILE DIV.	xiii
GENERAL RADIO CO.	Cover 3
HUGHES AIRCRAFT CO.	xxii
I.B.M. CORPORATION	xxv, xxxvi
KEITHLEY INSTRUMENTS, INC.	xvii
LEVINTHAL ELECTRONIC PRODUCTS	xxvii
LOCKHEED MISSILES & SPACE DIV.	viii, ix
LOS ALAMOS SCIENTIFIC LAB.	xv
McGRAW-HILL BOOK CO., INC.	xiv, xxviii
METALLIZING ENGINEERING CO., INC.	xxvi
MINNEAPOLIS-HONEYWELL REGULATOR CO.	xxxii
N.R.C. EQUIPMENT CORP.	xxx, xxxii, xxxv
NEWPORT INSTRUMENTS LTD.	xxx
NEW YORK UNIVERSITY	xii
OPERATIONS EVALUATION GROUP	xxxi
PHILIPS ELECTRONICS, INC.	xi
R.C.A. LABORATORIES	vii
RAMO-WOOLDRIDGE	Cover 4
REPUBLIC AVIATION	xviii
ROCKETDYNE, DIV. OF NORTH AMERICAN AVIATION	xxvi
STOKES CORP., F. J.	xxix
SYLVANIA ELECTRONIC SYSTEMS	xvi
UNITED AIRCRAFT CORP.	xx
VEECO VACUUM CORP.	xxxi
WELCH SCIENTIFIC CO., W. M.	xxiv
WILLIAMS & CO., C. K.	xxx

Outstanding opportunity for scientists and engineers in

SOLID STATE DEVICES

If you are a Physicist, Chemist, Metallurgist or Electrical Engineer, and have experience or interest in solid state development, or in related fields, you are invited to investigate the several excellent positions now open at IBM.

We are greatly expanding our development work in the theory, design and technology of solid state devices for use in new advanced computer systems.

This is an outstanding opportunity for experienced scientists and engineers who wish to undertake new and interesting work in this field.

Recent graduates are also invited to apply.

Please write, outlining briefly your qualifications and experience, to:

Mr. B. N. Slade, Dept. 579P1
Product Development Laboratory
IBM Corporation, Box 390
Poughkeepsie, N. Y.

IBM®

INTERNATIONAL BUSINESS MACHINES CORPORATION

POSITIONS OPEN

GRADUATE STUDENT TEACHING AND RESEARCH ASSISTANTSHIPS IN MATERIALS SCIENCE

Available to students with degrees in science or engineering. Pay for ½ time is $285 per month and up depending on experience and ability. Apply to Department of Materials Science, The Technological Institute, Northwestern University, Evanston, Illinois.

Sweep Oscillator System

with Plenty of Frequency Coverage

By merely substituting basic oscillator units in this system, you can cover, in narrow or wide sweeps, segments of the frequency range from 500 kc to 2000 Mc. More than this, you can control sweep speed, center frequency and frequency span over wide ranges by simple knob adjustments.

The Type 1263-A Regulated Power Supply is designed to power the Unit Oscillator as well as to keep the oscillator's output constant over wide ranges of frequency. It does this by comparing the rectified r-f output of the oscillator against an internal reference voltage, and applying any necessary corrections to the oscillator through its plate voltage supply. With this setup output is maintained within 2% over the oscillator's entire frequency range.

Write For Complete Information

★ Sweep Drive's claw-like arm attaches to knobs and dials up to 4 inches in diameter, and to ¼- and ⅜-inch shafts to convert oscillators, signal generators, and receivers to sweep operation.

★ Sweep-speed, sweep-arc, and sweep-center frequency are completely adjustable even while the Drive is in motion.

★ Wide range of sweep speeds . . . reciprocating motion, adjustable from 0.5 to 5 cps.

★ Sweep arc adjustable from 30° to 300°. At sweep speeds below 1 cps, arc can be increased by coupling Drive directly to Oscillator dial rather than to control Knob attached to vernier reduction-drive.

★ Rated maximum torque is 24 ounce-inches. Limit-switch circuit disconnects and brakes motor should limits of shaft travel be accidentally exceeded.

★ Generates a horizontal deflection voltage proportional to shaft angle for scope displays and x-y recorders.

★ Blanking circuit shorts out CRO trace during return portion of cycle and produces a reference base line.

GENERAL RADIO COMPANY

WEST CONCORD, MASSACHUSETTS

NEW YORK, WOrth 4-2722 District Office in Ridgefield, N. J. WHitney 3-3140	CHICAGO Oak Park Village 8-9400	PHILADELPHIA Abington HAncock 4-7419	WASHINGTON, D.C. Silver Spring JUniper 5-1088	SAN FRANCISCO Los Altos WHitecliff 8-8233	LOS ANGELES Los Angeles HOllywood 9-6201	IN CANADA Toronto CHerry 6-2171

At The Ramo-Wooldridge Laboratories... integrated programs of research & development of electronic systems and components.

The new Ramo-Wooldridge Laboratories in Canoga Park provide an environment for creative work in an academic setting. Here, scientists and engineers seek solutions to the technological problems of today. The Ramo-Wooldridge research and development philosophy places major emphasis on the imaginative contributions of the members of the technical staff. ■ There are outstanding opportunities for scientists and engineers. *Write* Dr. Richard C. Potter, Head, Technical Staff Development, Department 16-D.

THE RAMO-WOOLDRIDGE LABORATORIES
8433 FALLBROOK AVENUE, CANOGA PARK, CALIFORNIA

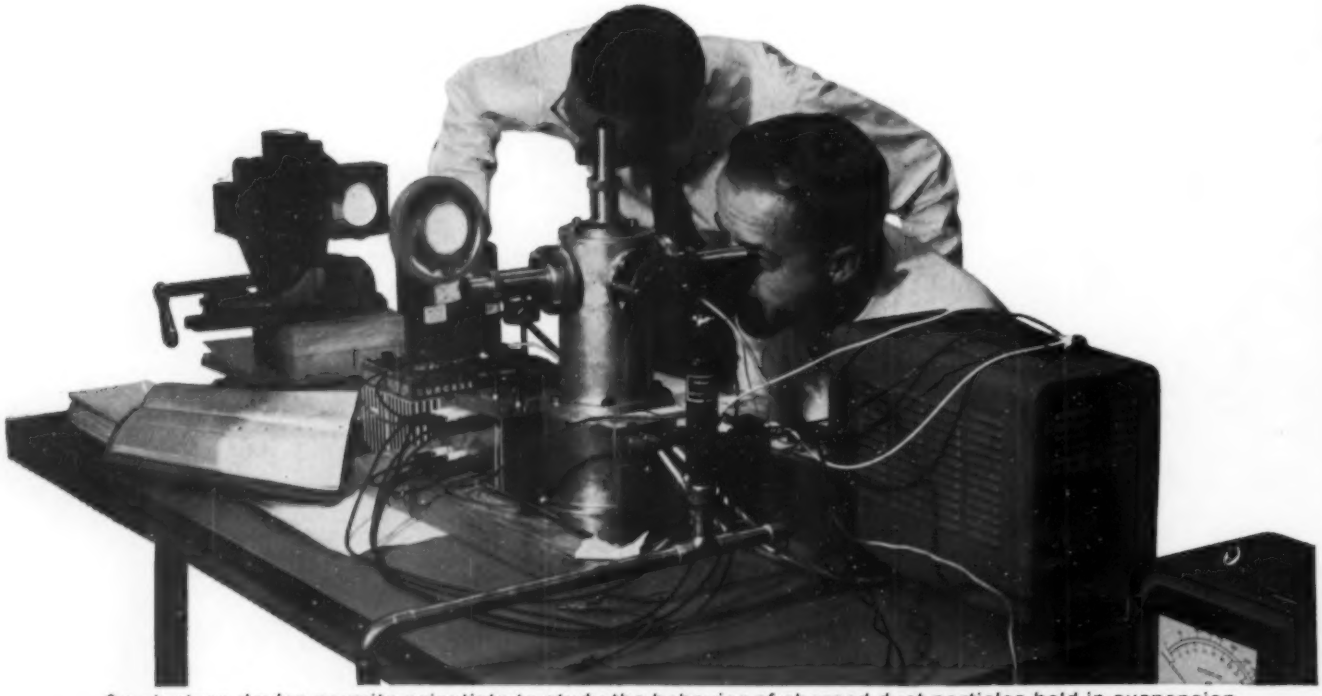

An electron device permits scientists to study the behavior of charged dust particles held in suspension.